Dynamics of Active Filament Systems

- The Role of Filament Polymerization and Depolymerization -

Dissertation

zur Erlangung des akademischen Grades
Doctor rerum naturalium (Dr. rer. nat.)
vorgelegt
der Fakultät Mathematik und Naturwissenschaften
der Technischen Universität Dresden
von

Alexander Zumdieck

geboren am 31.10.1975 in Bielefeld

angefertigt
an der Fakultät für Mathematik und Naturwissenschaften
der Technischen Universität Dresden
und am Max-Planck-Institut für Physik komplexer Systeme

Dresden · 2005

Abstract

Active filament systems such as the cell cytoskeleton represent an intriguing class of novel materials that play an important role in nature. The cytoskeleton for example provides the mechanical basis for many central processes in living cells, such as cell locomotion or cell division. It consists of protein filaments, molecular motors and a host of related proteins that can bind to and cross-link the filaments. The filaments themselves are semiflexible polymers that are typically several micrometers long and made of several hundreds to thousands of subunits. The filaments are structurally polar, i.e. they possess a directionality. This polarity causes the two distinct filament ends to exhibit different properties regarding polymerization and depolymerization and also defines the direction of movement of molecular motors. Filament polymerization as well as force generation and motion of molecular motors are active processes, that constantly use chemical energy. The cytoskeleton is thus an active gel, far from equilibrium.

We present theories of such active filament systems and apply them to geometries reminiscent of structures in living cells such as stress fibers, contractile rings or mitotic spindles. Stress fibers are involved in cell locomotion and propel the cell forward, the mitotic spindle mechanically separates the duplicated sets of chromosomes prior to cell division and the contractile ring cleaves the cell during the final stages of cell division. In our theory, we focus in particular on the role of filament polymerization and depolymerization for the dynamics of these structures. Using a mean field description of active filament systems that is based on the microscopic processes of filaments and motors, we show how filament polymerization and depolymerization contribute to the tension in filament bundles and rings. We especially study filament treadmilling, an ubiquitous process in cells, in which one filament end grows at the same rate as the other one shrinks. A key result is that depolymerization of filaments in the presence of linking proteins can induce bundle contraction even in the absence of molecular motors. We extend this description and apply it to the mitotic spindle. Starting from force balance considerations we discuss conditions for spindle formation and stability. We find that motor binding to filament ends is essential for spindle formation.

Furthermore we develop a generic continuum description that is based on symmetry considerations and independent of microscopic details. This theory allows us to present a complementary view on filament bundles, as well as to investigate physical mechanisms behind cell cortex dynamics and ring formation in the two dimensional geometry of a cylinder surface. Finally we present a phenomenological description for the dynamics of contractile rings that is based on the balance of forces generated by active processes in the ring with forces necessary to deform the cell. We find that filament turnover is essential for ring contraction with constant velocities such as observed in experiments with fission yeast.

Zusammenfassung

Aktive Filament-Systeme, wie zum Beispiel das Zellskelett, sind Beispiele einer interessanten Klasse neuartiger Materialien, die eine wichtige Rolle in der belebten Natur spielen. Viele wichtige Prozesse in lebenden Zellen wie zum Beispiel die Zellbewegung oder Zellteilung basieren auf dem Zellskelett. Das Zellskelett besteht aus Protein-Filamenten, molekularen Motoren und einer großen Zahl weiterer Proteine, die an die Filamente binden und diese zu einem Netz verbinden können. Die Filamente selber sind semifexible Polymere, typischerweise einige Mikrometer lang und bestehen aus einigen hundert bis tausend Untereinheiten, typischerweise Mono- oder Dimeren. Die Filamente sind strukturell polar, d.h. sie haben eine definierte Richtung, ähnlich einer Ratsche. Diese Polarität begründet unterschiedliche Polymerisierungs- und Depolymerisierungs-Eigenschaften der beiden Filamentenden und legt außerdem die Bewegungsrichtung molekularer Motoren fest. Die Polymerisation von Filamenten sowie Krafterzeugung und Bewegung molekularer Motoren sind aktive Prozesse, die kontinuierlich chemische Energie benötigen. Das Zellskelett ist somit ein aktives Gel, das sich fern vom thermodynamischen Gleichgewicht befindet.

In dieser Arbeit präsentieren wir Beschreibungen solcher aktiven Filament-Systeme und wenden sie auf Strukturen an, die eine ähnliche Geometrie wie zellulare Strukturen haben. Beispiele solcher zellularer Strukturen sind Spannungsfasern, kontraktile Ringe oder mitotische Spindeln. Spannungsfasern sind für die Zellbewegung essentiell; sie können kontrahieren und so die Zelle vorwärts bewegen. Die mitotische Spindel trennt Kopien der Erbsubstanz DNS vor der eigentlichen Zellteilung. Der kontraktile Ring schließlich trennt die Zelle am Ende der Zellteilung. In unserer Theorie konzentrieren wir uns auf den Einfluß der Polymerisierung und Depolymerisierung von Filamenten auf die Dynamik dieser Strukturen. Wir zeigen, dass der kontinuierliche Umschlag (d.h. fortwährende Polymerisierung und Depolymerisierung) von Filamenten unabdingbar ist für die kontraktion eines Rings mit konstanter Geschwindigkeit, so wie in Experimenten mit Hefezellen beobachtet. Mit Hilfe einer mikroskopisch motivierten Beschreibung zeigen wir, wie “filament treadmilling”, also Filament Polymerisierung an einem Ende mit der gleichen Rate wie Depolymerisierung am anderen Ende, zur Spannung in Filament Bündeln und Ringen beitragen kann. Ein zentrales Ergebnis ist, dass die Depolymerisierung von Filamenten in Anwesenheit von filamentverbindenden Proteinen das Zusammenziehen dieser Bündel sogar in Abwesenheit molekulare Motoren herbeiführen kann.

Ferner entwickeln wir eine generische Kontinuumsbeschreibung aktiver Filament-Systeme, die ausschließlich auf Symmetrien der Systeme beruht und von mikroskopischen Details unabhängig ist. Diese Theorie erlaubt uns eine komplementäre Sichtweise auf solche aktiven Filament-Systeme. Sie stellt ein wichtiges Werkzeug dar, um die physikalischen Mechanismen z.B. in Filamentbündeln aber auch bei der Bildung von Filamentringen im Zellkortex zu untersuchen. Schließlich entwickeln wir eine auf einem Kräftegleichgewicht basierende Beschreibung für bipolare Strukturen aktiver Filamente und wenden diese auf die mitotische Spindel an. Wir diskutieren Bedingungen für die Bildung und Stabilität von Spindeln.

Acknowledgment

I would like to thank Frank Jülicher for accepting me into his group, his ongoing interest in my work and availability for many fruitful discussions. A constant fountain of ideas, you enhanced and sharpened my physical thinking in many ways.

This thesis in its present form would have never come into existence without the continuous and ongoing support of Karsten Kruse. Thank you.

Also I was fortunate to enjoy working with Marileen Dogterom and Bela Mulder whom I would like to thank for our fruitful collaboration and their hospitality at the AMOLF in Amsterdam. Marco Cosentino Lagomarsino and Catalin Tanase were fun to work and discuss with and are behind some of the most memorable moments of my thesis. Thank you.

I thank Ewa Paluch for reading this manuscript and her support throughout my time in Dresden. Her and Cecile Leduc I thank for sharing their manuscripts prior to publication. Furthermore, I would like to acknowledge the hospitality of Institute Curie and especially thank Cecile Sykes, who hospitably shared her office with me several times.

Michael C. Cross taught me a novel style of doing physics. I very much enjoyed our collaboration and discussions.

Nadine Baldes is the invaluable soul of the group. Thank you for all support concerning everyday survival, not only administratively.

Further I would like to thank Nils Becker, Tobias Bollenbach, Peter Borowski, Andreas Buchleitner, Ralf Everaers, Elisabeth Fischer, Stefan Günther, Andrea Jimenez-Dalmaroni, Florian Mintert, Gernot Klein, Andreas Hilfinger, Giovanni Meacci, Björn Nadrowski, Romain Nguyen Van Yen, Ingmar Riedel, Thomas Risler, Christian Simm, and Martin Zaptocky for the time we spent together.

Hubert Scherrer provided competent support in all questions regarding computers. This thesis would not have come into existence without you.

I would also like to thank Heidi Näther for providing me with even the most hidden journal articles. You always found a way to get them very rapidly.

Last but not least I would like to thank my parents and grandparents for all kinds of support during my studies. Without you my studies and hence this thesis would not have been possible. Thank you.

I acknowledge support by the German National Merit Foundation (Studienstiftung des Deutschen Volkes) and financial support by the European Union, NATO and the Max-Planck-Society.

Contents

Acknowledgment **vii**

1 Introduction and Overview **1**
1.1 Overview of this Manuscript . . . 2

2 The Cytoskeleton **5**
2.1 Filaments and Molecular Motors . . . 6
2.2 Actin and Actin Binding Proteins . . . 7
2.2.1 G-actin and F-actin . . . 8
2.2.2 Actin Polymerization and Treadmilling . . . 9
2.2.3 Actin Binding Proteins . . . 12
2.2.4 Myosin: The Actin Motor . . . 14
2.2.5 Actin and Cell Locomotion . . . 18
2.3 Microtubules and Microtubule Associated Proteins . . . 20
2.3.1 Microtubules and Dynamic Instability . . . 21
2.3.2 Microtubule Associated Proteins . . . 22
2.3.3 Microtubule Motors: Kinesin and Dynein . . . 23
2.4 Dynamics of Individual Filaments . . . 25
2.4.1 Nucleation, Polymerization and Treadmilling . . . 25
2.4.2 Force Generation by Polymerization and Depolymerization . . . 26
2.4.3 Force Generation by End-Tracking Proteins . . . 28
2.5 Cytoskeletal Structures . . . 29
2.5.1 Mitotic and Meiotic Spindles . . . 32
2.5.2 The Contractile Ring . . . 38
2.5.3 The Pre-Prophase-Band in Plant Cells . . . 43
2.5.4 Stress Fibers and Myofibrils . . . 46

3 Physics of Active Filament Systems **49**
3.1 From Molecular Properties to Coarse Grained Descriptions . . . 49
3.1.1 Motors and Other Cross-Linkers . . . 49
3.1.2 Dynamics of Filament Pairs with Cross-Linkers . . . 52
3.1.3 Mean Field Description of Active Filament Systems . . . 56
3.2 Minimal Model of Active Filament Bundles . . . 60
3.2.1 Bundles of Stabilized Filaments . . . 61
3.2.2 Treadmilling and Molecular Motors . . . 63
3.2.3 Passive End-Tracking Cross-Linkers . . . 66
3.2.4 Polymerization of Entire Filaments . . . 70
3.2.5 Tension . . . 72
3.3 Stochastic Simulation of Active Filament Bundles . . . 75
3.3.1 Stochastic Simulation . . . 75
3.3.2 Stochastic Filament Dynamics in Bundle Geometry . . . 79
3.3.3 Currents in the Stochastic Simulations . . . 81
3.4 Stochastic Simulations and Mean Field Description . . . 83

3.5 Discussion 84

4 Stability of the Mitotic Spindle 87

4.1 Introduction 87
  4.1.1 From Filament Bundles to the Mitotic Spindle 87
  4.1.2 Computer Simulations of Interacting Asters 88
4.2 Mean Field Description of Mitotic Spindles 90
  4.2.1 Spindle Geometry 90
  4.2.2 Spindle Dynamics, Stability and Length 91
  4.2.3 Force on Asters 92
  4.2.4 Interaction between Filament Pairs 92
  4.2.5 Microtubule Length Distributions 95
4.3 Results 99
  4.3.1 Spindle Stability 99
  4.3.2 Spindle Length 100
  4.3.3 State Diagrams 102
  4.3.4 Comparison to Computer Simulations 104
  4.3.5 Generality of Our Results 105
  4.3.6 Microtubule Dynamics, Chromosomes and Motor Transport 106
4.4 Discussion 107

5 Continuum Theory of the Cytoskeleton 109

5.1 Phenomenological Description of Active Fluids 110
  5.1.1 Dynamic Equations 110
  5.1.2 Order Parameters 111
5.2 Active Filament Bundles 113
  5.2.1 Fully Polar Fibers 114
  5.2.2 Non-Polar Fibers 117
  5.2.3 Partial Polarization 117
  5.2.4 Polymerization and Depolymerization of Filaments 118
  5.2.5 Filament Treadmilling 120
  5.2.6 Connection to the Minimal Model 121
5.3 Active Fluid in Cortical Geometry 122
  5.3.1 Continuum Description in 2D 122
  5.3.2 Rotationally Invariant Equations 123
  5.3.3 Stability and Phase Diagram 125
  5.3.4 Stationary and Oscillating Rings 133
5.4 Discussion 134

6 Dynamics of the Contractile Ring 137

6.1 Structure of the Contractile Ring 137
6.2 Force Balance and Material Exchange During Ring Contraction 138
6.3 Ring Dynamics 139
  6.3.1 Contraction of the Ring 140
  6.3.2 Numerical Analysis of Ring Contraction 142
  6.3.3 Estimate of Parameter Values 143
  6.3.4 Parameter Dependence of Ring Dynamics 144
6.4 Generality of the Description 149
6.5 Stresses and Ring Contraction 151
  6.5.1 Radial Stress and Normal Force 151

6.5.2 Forces of Arbitrary Stress Tensor 152
6.5.3 Generic Condition for Radial Contraction 152
6.6 Discussion 153

7 Summary and Perspectives 155
7.1 Summary of the Results 155
7.2 Outlook and Perspectives 156

A Supplementary Analytic Calculations 159
A.1 Minimal Model: Linear Stability Analysis 159
A.1.1 Parameter Dependence of the Critical Alpha 159
A.1.2 Polymerization of Entire Filaments 161
A.2 Minimal Model: Interaction Integrals 162
A.3 Continuum Limit of the Minimal Model 162

B Numerical Methods 167
B.1 Numerical Integration of the Mean Field Description 167
B.2 Numerical Integration of the Continuum Theory 169
B.2.1 Description with Nematic Order 169
B.2.2 Boundary Conditions 170

C Supplementary Calculations to the Spindle 173
C.1 Forces between Asters 173
C.1.1 Motors Bound to the Bulk 173
C.1.2 Motors at the $\oplus$-Ends 176
C.1.3 Motors at the $\ominus$-Ends 178
C.1.4 Example: Forces Between two Half Asters 179
C.1.5 Overview of Force Contributions from Ensembles of Motors 182
C.2 Existence and Stability of Spindles 184
C.2.1 Half Asters 184
C.2.2 Full Asters 187
C.3 Generality of Our Description 190
C.3.1 Various distributions of $\ominus$-ends 190
C.3.2 Homogenous Half Asters 191
C.4 Microtubule Distributions in 2D 193
C.5 Additional Force Contributions of Motor Dimers 195
C.5.1 Motors bound in the Bulk 195
C.5.2 Forces due to Interactions between Bulk and $\oplus$-end 196
C.5.3 Forces due to Interactions between Bulk and $\ominus$-end 198

D Stability of the Contractile Ring 201

Bibliography 203

1 Introduction and Overview

> There is a biologist word for “stable”. It is “dead”.
> Jack Cohen

The concept of the cell as the smallest living unit was a major advance of our understanding of living organisms. Scientists have always been interested in identifying fundamental units of structure, such as the atom as the basic unit of matter. The cell is not only the basic structural unit of all living organisms, but also the basic functional unit of life. In this sense the cell truly qualifies as the atom of biology (Nurse, 2003).

Besides identifying and classifying objects, we also want to understand how they work, i.e. what they do, when and why. The range of actions biological cells can take is absolutely amazing. Many cells are specialized to accomplish certain tasks, such as the translation of acoustic stimuli into nerve pulses by hair cells in the inner ear (Hudspeth, 2005), the fast transmission of electrical signals by neurons in the brain (Hodgkin and Huxley, 1952) and central nervous system, or the rapid contraction of muscle cells (Huxley and Niedergerke, 1954). But despite such specializations, most cells are made of comparable constituents and share common features, such as the ability to control the directed intracellular transport of cargo, or to duplicate and separate their DNA and divide their cytoplasm. Hence there are processes in the cellular world, which may be governed by general principles underlying the diversity. All of the common processes mentioned above are mediated by the cytoskeleton, an active material far from equilibrium that consists mainly of protein filaments and molecular motors. Molecular motors are proteins that convert chemical energy into directed motion and mechanical force. The cytoskeleton is furthermore responsible for active cell locomotion and also determines the cell shape. From the physical point of view the cytoskeleton is a paradigmatic example of a novel class of active materials, that require a wide range of techniques for their analysis.

Cytoskeletal protein filaments are typically several micrometers long. Their persistence length is often of the same order, making them semiflexible polymers. They are polymerized from hundreds to thousands of polar subunits and are structurally polar themselves, i.e. they possess a directionality like e.g. a ratchet. These filaments interact with numerous related proteins that bind and cross-link them or influence their polymerization dynamics. The resulting physical gel can thus be effectively polar and exhibit complex dynamics. The polymerization of filaments as well as the action of molecular motors takes place using chemical energy provided in the form of adenosine triphosphate (ATP) or guanine triphosphate (GTP). The energy is liberated when a an inorganic phosphate group is cleaved of the molecule. Consecutively the energy is partially converted into mechanical work (Howard, 2001). The resulting aggregate is thus an active gel, that provides the mechanical basis for many fascinating cellular behaviors such as locomotion and division, that have captured the attention of biologists and physicist alike.

The action of molecular motors and their effect on the collective cytoskeletal dynamics has been the topic of many physical investigations, see e.g. (Jülicher and Prost, 1995; Nédélec et al., 1997; Kruse and Jülicher, 2000, 2003; Liverpool and Marchetti, 2003;

Kruse et al., 2004). Recent experiments have revealed that the polymerization and depolymerization of filaments also generate forces at the sub-cellular level (Dogterom et al., 2005) and contribute to the observed cellular behavior. In this thesis we theoretically investigate the ubiquitous process of filament polymerization and depolymerization and focus on its consequences for macroscopic intracellular dynamics.

An essential cellular structure is the contractile ring that cleaves the cell during the final stages of cell division. It consists of filaments of the cytoskeletal protein actin, the corresponding myosin motors as well as many associated proteins. Together they form an equatorial band around the cell. After the DNA has been separated and distributed to the two prospective daughter cells, the band condenses into a ring and starts to contract. This causes a radial movement of the cell membrane and finally cleavage of the cell. Recent experiments have shown that this cleavage is slower when actin polymerization is inhibited (Pelham and Chang, 2002) and that under certain circumstances cells can divide even in the absence of myosin (Gerisch and Weber, 2000). How the contractile ring forms in the cell cortex, is another open question at the forefront of cell biology.

The contractile ring forms part of the group of filament bundles in the cell. Other prominent members are stress fibers, that are involved in cell locomotion. Theoretical investigations have shown that the action of motor dimers bound to filament pairs can give rise to stress in such bundles and thereby lead to interesting dynamics ranging from bundle contraction to traveling density profiles (Kruse et al., 2001). Microscopically the dimers induce relative sliding of the filaments they are bound to. Besides motors, filament polymerization and depolymerization also contribute to bundle dynamics. Filament treadmilling, i.e. polymerization of one end and depolymerization of the other end at the same rate is a ubiquitous process in the cytoskeleton. We show that the disassembly of filaments can also contribute to tension in bundles and rings. This effect is especially obvious when this depolymerization takes place in the presence of cross-linkers that are able to stay attached to filament ends.

Prior to cell cleavage by the contractile ring the duplicated DNA has to be distributed to the designated daughter cells. Mechanically this is accomplished by an apparatus called the mitotic spindle. The spindle is a bipolar arrangement of microtubules (another type of cytoskeletal filaments besides actin) around the condensed DNA in its middle. At the spindle poles there are microtubule organizing centers, the centrosomes. How the spindle forms, how its length is determined and what precisely triggers DNA separation are all open questions. Besides molecular motors and microtubules, many other regulating proteins have been localized in the spindle. The microtubules are attached to the chromosomes at one end and to the centrosomes at the other while undergoing so called pole-ward flux (Mitchison and Salmon, 2001), i.e. a constant treadmilling motion of the monomers in the microtubules towards the spindle poles. Filament polymerization and depolymerization thus evidently plays an important role in this structure as well.

1.1 Overview of this Manuscript

In this thesis we consider two main issues that arise when investigating cytoskeletal dynamics. One is the role of polymerization and depolymerization in cytoskeletal systems. These processes provide a way of generating dynamics in cytoskeletal systems, as important as the action of molecular motors. But the effects of polymerization and depolymerization on the dynamics of macroscopic cytoskeletal structures have been largely neglected in theoretical descriptions of the dynamics of complex filament structures. Here we investigate their role in the generation of stress and induction of dynamics in filament rings and bundles by extending a microscopic theory with the appropriate processes.

The analysis of cytoskeletal systems despite the fact that not all proteins involved or the details of their interactions are known is the second big topic we address. To this end we develop a generic continuum description of active cytoskeletal systems that allows us to unveil generic physical properties independent of microscopic details. As the description is based on symmetries only, it is readily extended to higher dimensions, making it applicable to a wide variety of biologically more realistic geometries.

The organization of the thesis is as follows: in chapter 2 we introduce the cytoskeleton, its main constituents, substructures and functions. We also briefly discuss the dynamics of polymerizing filaments as well as molecular motors. Our results are presented in the following four chapters. In chapter 3 we present a description of filament bundles based on microscopic processes such as filament treadmilling. Using this framework explicitly discuss the contribution of polymerization of filaments to the collective dynamics in the bundle. The following chapter 4 introduces a theory for the formation of the mitotic spindle based on force balance considerations. In chapter 5 we then introduce the complementary generic continuum description, which we use to analyze filament bundles. Furthermore, we apply it to investigate physical mechanisms of ring formation in the cell cortex. Finally, we present our analysis of the contraction dynamics of the contractile ring in chapter 6 and highlight the importance of filament turnover for the dynamics observed in experiments. The main part concludes with a summary and perspectives for future research in chapter 7. Supplementary calculations and methods are presented in the appendices.

2 The Cytoskeleton

Cells are the smallest units of live. This concept was a major advance for our understanding of living organisms. It allows us to ask more precise questions regarding how cells work, what they do, when and why. Many of these questions involve mechanical aspects, such as e.g. the division of cells or cell locomotion. All cellular mechanic functions are based on the cytoskeleton. For a long time it was believed that the cytoskeleton was exclusive to eucaryotic cells, i.e. cells that have a nucleus, such as animal or plant cells. Then it was discovered that bacteria also possess cytoskeletal proteins and form a cytoskeleton (Lutkenhaus, 2003; Moller-Jensen and Lowe, 2005).

The cytoskeleton is a complex system of dynamic protein filaments, molecular motors, and other proteins. It provides the basis for many important cellular processes such as cell locomotion or morphogenesis, i.e. changes in cell shape. While cellular motility is important for example for wound healing, fertilization of egg cells, development and plays a crucial role in cancer dissemination, cell division or cytokinesis is one of the most prominent instances of a change in cell shape. Here one cell actively divides itself into two. The cytoskeleton also enables cells to regulate the organization of their internal components. Many cellular organelles like e.g. the Golgi apparatus need to be rearranged e.g. when cells divide, react to changes in the external environment or simply grow. As all of these processes depend on the cytoskeleton, understanding of these key cellular processes inevitably requires a thorough understanding of the cytoskeleton.

Despite their apparently different strategies for life, animals and plants share the same cytoskeletal proteins. Although they do make different use of them – their strategies for cell division is vastly different for example. The cytoskeleton of bacteria on the other hand involves different proteins, that however seem to be related to those found in animal and plant cells. Until now no molecular motors have been found in bacteria, which poses the interesting question how their cytoskeleton achieves the necessary forces and movements. Polymerization and depolymerization as discussed in this thesis could give rise to the observed dynamics. Moreover, while the biological details and functions of the cytoskeleton may vary between different cells, the underlying physical principles are likely to be generic.

In this chapter we discuss the function of the cytoskeleton starting with a description of its basic components: protein filaments and molecular motors in section 2.1. One of the most prominent cytoskeletal proteins actin and proteins related to it are discussed in section 2.2. Section 2.3 presents microtubules, the other class of cytoskeletal filaments important for this thesis. The most important dynamical processes in the cytoskeleton are movement of filaments induced by the action of molecular motors as well as filament polymerization and depolymerization. We discuss the polymerization and depolymerization dynamics of biopolymers and the forces generated in these processes in section 2.4. Section 2.5 concludes the chapter by presenting four cytoskeletal structures that are central for this thesis in greater detail: the contractile actin ring that cleaves the cell during cell division, stress fibers which are important for cell motility, meiotic and mitotic spindles that separate chromosomes during mitosis, and the pre-prophase band, a microtubule ring around plant cells that marks the division plane prior to cytokinesis but does not itself contract.

2.1 Filaments and Molecular Motors

The cytoskeleton is made up of different kinds of protein filaments, their corresponding molecular motors and other associated proteins. Molecular motors use the protein filaments as tracks along which they walk. In this thesis we will explore various processes that rely on this kind of motility. The protein filaments themselves are also dynamic. They are polymers made of many subunits that constantly polymerize and depolymerize. Three different kinds of filaments have been identified: actin filaments, microtubules and intermediate filaments. An overview of these three polymers, their composition and function is given in table 2.1.

Eucaryotic cytoskeletal polymers

Polymer	Actin filament	Microtubule	Intermediate filament
Protein subunit	Actin monomer	Tubulin heterodimer	Various proteins
Diameter	7 nm	25 nm	10 nm
Persistence length	17 μm	5 mm	2 μm
Structurally polar	Yes	Yes	No
Polymerization	Yes	Yes	Probably
Bound nucleotide	ATP	GTP	None
Nucleotide hydrolysis	Yes	Yes	No
Treadmilling	Yes	Yes	No
Dynamic instability	No	Yes	No
Track for motors	Yes, myosins	Yes, dyneins and kinesins	No
Electron micrographs of polymers		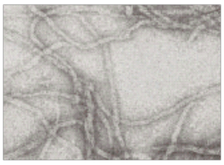	
Fluorescence micrographs of cells with stained polymers	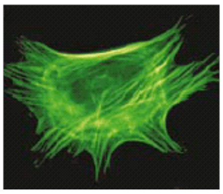	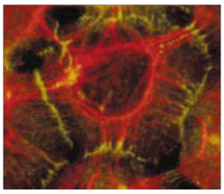	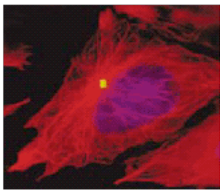

Table 2.1: Overview of eucaryotic cytoskeletal polymers. Compiled from (Pollard, 2003; Bray, 2001; Alberts et al., 2002).

Intermediate filaments are important for cell structure and integrity. They are rather flexible and gels of intermediate filaments tolerate forces that cause actin and myosin gels to rupture (Janmey et al., 1991). The filaments themselves seem not to be very dynamic. They do not bind nucleotides and no associated motors have been found. In this thesis we focus on active filament motor systems and the role of filament polymerization and depolymerization for the systems' dynamics in particular. We will thus describe the actin-myosin system as well as microtubules with dyneins and kinesins in greater detail.

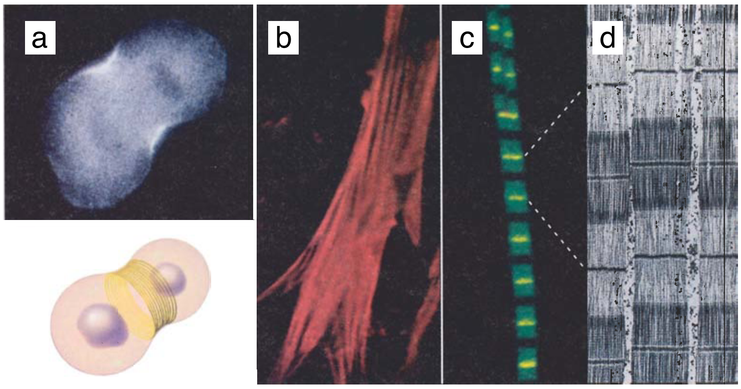

Figure 2.1: Contractile bundles of actin filaments in cells. (a) Actin filaments in the contractile ring of a normal rat kidney cell. (b) Stress fibers in cultured endothelial cells. (c) Myofibril isolated from skeletal muscle. Actin is stained green and α-actinin, which localizes to the Z-disks, yellow. (d) Electron micrograph of a myofibril. Figure modified from (Pollard and Earnshaw, 2002).

Although they are frequently analyzed and described separately, there is growing evidence that the actin and tubulin systems work together in a coordinated way in many cellular processes (Kodama et al., 2004).

2.2 Actin and Actin Binding Proteins

Actin is ubiquitous in all eukaryotes. It is a small (43 kDa) globular protein that spontaneously assembles into polymers. The actin protein is ancient and highly conserved. Very similar proteins to actin are found even in bacteria and sequences of actin isoforms are generally more than 90 % identical. Different isoforms are coded for by different genes, e.g. 6 in Humans, 1 in yeast and more than 10 in *Dictyostelium* (Pollard and Earnshaw, 2002). The degree of conservation is illustrated by the fact that only 15 of the 375 aminoacids differ between actin of mammals and that of *Acanthamoeba*, furthermore the sequence of muscle actin is absolutely identical in all endotherm vertebrates (Bray, 2001). This unusually high degree of conservation is often explained by the large host of actin binding proteins that regulate actin dynamics (see section 2.2.3 below). A mutation might have a positive effect on one of those interactions, but at the same time it would probably affect many others negatively and thus be an overall disadvantage (Alberts et al., 2002). Besides being highly conserved, actin is abundant: often up to 15 % of all protein in nonmuscle cells is actin, with actin binding proteins accounting for up to 10 % on top of that. In muscle cells actin and myosin comprise up to 60 % of the cell's total protein content (Pollard and Earnshaw, 2002).

Actin filaments and myosin motors form together the so called actomyosin system, that is at the basis of many cellular processes. One of the main functions of the actomyosin system is the **active generation of stress.** Typical structures for stress generation are contractile bundles, Fig. 2.1. Actin filaments and myosin filaments form stress fibers that generate tension, which, transmitted via adhesive junctions, permits the cell to move. Another linear contractile actin structure is the contractile ring which cleaves cells during cell division (see section 2.5.2 below). While these two structures are temporary, actin and myosin also form sarcomers, i.e. the repetitive units of myofibrils, the permanent, highly organized, contractile apparatus of muscle cells. Actin filaments furthermore transmit

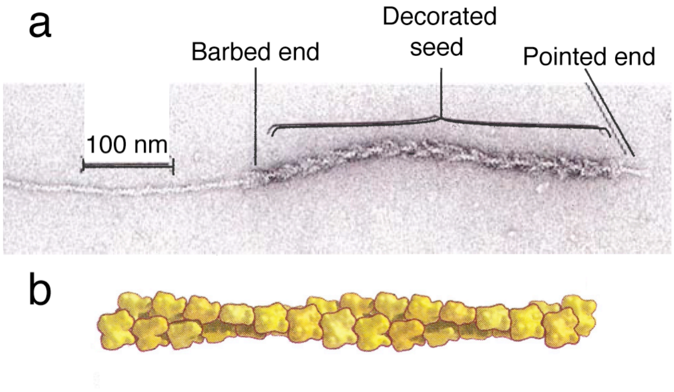

Figure 2.2: Structure of actin filaments. (a) Electron micrograph of an actin filament dressed with myosin II heads revealing the structural polarity. (b) Schematic drawing of an actin filament, clearly exhibiting the doubel helix. Figure modified from (Pollard and Earnshaw, 2002).

forces and contribute to spatial organization in the cell by restricting the movement of organelles. Networks of cross-linked actin filaments resist deformations: the cell's plasma membrane is reinforced by the actin cortex, a dynamic network of actin filaments that can be up to $1\,\mu$m thick. Finally actin structures facilitate cell motility by polymerization and depolymerization of filaments as well as by providing tracks for the myosin family of motor proteins. Polymerization and depolymerization of actin filaments e.g. drive the extension of lamellipodia during cell locomotion or the engulfment of extracellular material by phagocytosis.

2.2.1 G-actin and F-actin

The structure of the actin molecule has been solved by K. Holmes et. al. in 1990 (Holmes et al., 1990; Kabsch et al., 1990). The 375 aminoacids of a monomeric actin protein fold in two similar domains.

The whole molecule is globular and thus often called G-actin. Between the two actin domains lies an adenine nucleotide binding site. The nucleotide stabilizes the two domains. Actin binds adenosine triphosphate (ATP) or adenosine diphosphate (ADP) together with a divalent cation. Actin has a higher affinity for ATP than for ADP. In cells ATP is more abundant and thus unpolymerized actin monomers are saturated with ATP. The exchange of bound nucleotides is relatively slow. Thus most actin in extract of Xenopus eggs for example is in its ATP form (Rosenblatt et al., 1995).

Actin monomers are polar, i.e. they possess a structure that allows them to bind to other actin monomers only in a certain orientation. Actin monomers may spontaneously assemble to form actin filaments or F-actin, which is then also structurally polar. These filaments are semiflexible with a persistence length of $17\,\mu$m (compare with 5 mm for microtubules, (Alberts et al., 2002), see section 2.3). They possess a double-helical structure of two parallel protofilaments. The monomers in the two protofilaments are oriented in the same sense. This is the basis of the overall structural polarity of actin filaments.

This polarity can be visualized with an electron microscope when the filaments are dressed with heads of myosin II (fragment S1), i.e. fragments of the corresponding molecular motor that bind under a specific angle with the filament (Huxley, 1963; Woodrum et al., 1975). This results in an arrow-like structure as shown in Fig. 2.2a. The end towards

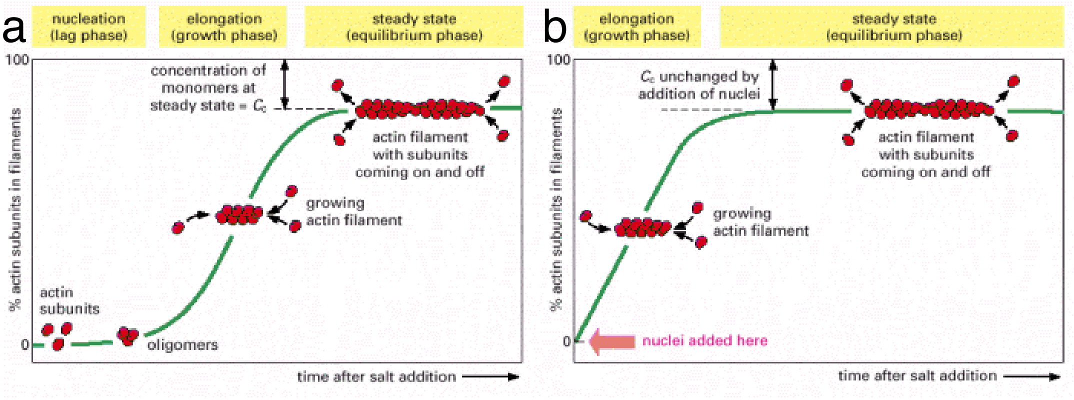

Figure 2.3: Schematic time course of actin polymerization in a test tube. (a) Polymerization is begun by raising the salt concentration in a solution of pure actin subunits. (b) Polymerization is begun in the same way, but with preformed fragments of actin filaments present to act as nuclei for filament growth. Modified from (Alberts et al., 2002).

which the arrows point is called the pointed end, the opposite end is the barbed end. This structural polarity gives rise to the interesting polymerization dynamics of actin filaments that is essential for many cellular processes.

2.2.2 Actin Polymerization and Treadmilling

Actin filaments self-assemble from actin monomers via a series of bimolecular reactions (Pollard and Earnshaw, 2002). From in vitro experiments it seems that actin monomers form first dimers and then trimers. These trimers consecutively serve as the nuclei for new actin filaments. The reactions necessary for filament polymerization are more favorable than trimer formation, so that nucleation is the rate limiting step in polymerizing new actin filaments. This shows up as a lag phase when filament polymerization is induced, Fig. 2.3a. Cells use regulating proteins to overcome these limitations either by severing existing filaments (e.g. via gelsolin) in order to provide several short filaments as nuclei or by enhancing nucleation of filaments from monomeric actin (e.g. Formin, Arp2/3 complex). In in vitro experiments the lag phase is eliminated when small filament fragments are added to the solution, Fig. 2.3b.

Once nucleated, a filament starts to grow by adding monomers at both ends. This process is reversible: filaments may shrink by loosing monomers from the ends as well. Filament growth is determined by the balance of polymerization and depolymerization at both ends:

$$\frac{\mathrm{d}n_\mathrm{b}}{\mathrm{d}t} = k_{\mathrm{on,b}}\, c - k_{\mathrm{off,b}} \tag{2.1}$$

$$\frac{\mathrm{d}n_\mathrm{p}}{\mathrm{d}t} = k_{\mathrm{on,p}}\, c - k_{\mathrm{off,p}} \quad . \tag{2.2}$$

where $\mathrm{d}n_\mathrm{b}/\mathrm{d}t$ and $\mathrm{d}n_\mathrm{p}/\mathrm{d}t$ denote the rates of monomer addition at the barbed end and at the pointed end respectively. The on- and off- rates for monomers at both ends are given by k_on and k_off and c is the concentration of monomeric actin in the surrounding solution. The polymerization rate is given by $k_\mathrm{on} \times c$ and depends on the monomer concentration. Note that we assume that the depolymerization rate k_off is independent of the monomer concentration.

When a filament polymerizes, it diminishes the concentration of free monomers in the solution until the critical concentration $c_\mathrm{c} = k_\mathrm{off}/k_\mathrm{on}$ is reached. At the critical concentration the growth and shrinkage of the filament exactly balance, the filament has reached a stationary length. If one starts out with filaments and a monomer concentration $c < c_\mathrm{c}$ the filaments will depolymerize until $c = c_\mathrm{c}$.

Due to the structural polarity of filaments, polymerization and depolymerization occur with different rates at both ends (Pollard, 1986). While subunit dissociation is relatively slow at both ends (between 1 and 10 subunits per second) filament growth is diffusion limited at the barbed end and slower at the pointed end (Pollard and Borisy, 2003). The barbed end thus is more dynamic than the pointed end and grows more rapidly. That is why it is also called the plus end while the pointed end is called the minus end. Nonetheless in the absence of an external energy supply the equilibrium constant $K_{eq} = k_\mathrm{on}/k_\mathrm{off} = 1/c_\mathrm{c}$ is the same for both ends, see Fig. 2.4.

As already pointed out above, monomeric actin binds the nucleotide adenosine triphosphate (ATP) and possesses the capacity to hydrolyze it to adenosine diphosphate (ADP) and an inorganic phosphate P_i. This process frees about $20\,k_\mathrm{B}T \simeq 20 \times 4.1\,\mathrm{pN\,nm}$ per molecule and is irreversible (Carlier et al., 1988). Nucleotide hydrolysis is slow for individual monomers but accelerated in actin filaments with a half time of 2 s (Blanchoin and Pollard, 2002). Phosphate dissociation is much slower with a half time of 350 s (Carlier and Pantaloni, 1986), so that ADP-P_i-actin is relatively long-lived in assembled actin filaments. Because monomeric actin in the cell is saturated with ATP, filaments will generally incorporate ATP-actin. This results in a filament with a comparatively short actin-ATP cap and an actin-ADP tail in which phosphate is bound to some actin subunits but not to others. Due to the nucleotide hydrolysis it is energetically more favorable to dissociate an ADP-actin monomer than an ATP-actin monomer from the filament, cf. Fig 2.4a.

Filament Treadmilling

In the previous section we motivated, why the equilibrium constants at both ends are not equal in the presence of ATP. Typical values are $c^{-}_\mathrm{c,ATP} = 0.6\,\mu\mathrm{M}$ for the minus end of a filament in solution with globular ATP-actin and $c^{+}_\mathrm{c,ATP} = 0.12\,\mu\mathrm{M}$ for the plus end with ATP-actin in vitro (Pollard, 1986; Pollard and Borisy, 2003), cf. Fig. 2.4a. So for a concentration of ATP monomers $c^{+}_\mathrm{c,ATP} < c_\mathrm{ATP} < c^{-}_\mathrm{c,ATP}$, the filament will grow at the plus end while shrinking at the minus end. This is often called the treadmilling regime (blue range in Fig. 2.4c). Under these conditions a monomer of ATP-actin is incorporated into a filament at the plus end, then its nucleotide is hydrolyzed. Some time later the inorganic phosphate is released, and finally the now ADP-actin monomer reaches the minus end and dissociates. While there is a whole range of concentrations for which the plus end grows and the minus end shrinks, there is only one value for which these processes occur at precisely the same rates. In this thesis we use the term treadmilling only for filaments that polymerize and depolymerize with equal rates at both ends. Taking the values reported in (Pollard, 1986) for actin filaments in vitro, we find a critical treadmilling concentration $c_\mathrm{tm,ATP} \simeq 0.14\,\mu\mathrm{M}$ where the polymerization rate for ATP-actin at the plus end exactly matches the depolymerization rate for ADP-actin at the minus end, taking into account that in a cell monomeric actin is typically saturated with ATP, i.e. $c_\mathrm{ADP} \simeq 0$. A filament at this critical treadmilling concentration retains its length while continuously exchanging monomers with the solution. The total turnover time for a $1\,\mu\mathrm{m}$ long filament consisting of 370 monomers is about 20 min. This turnover time is greatly increased in lamellipodia of motile cells or in the actin comets of bacterial pathogens where a $3\,\mu\mathrm{m}$ long filament

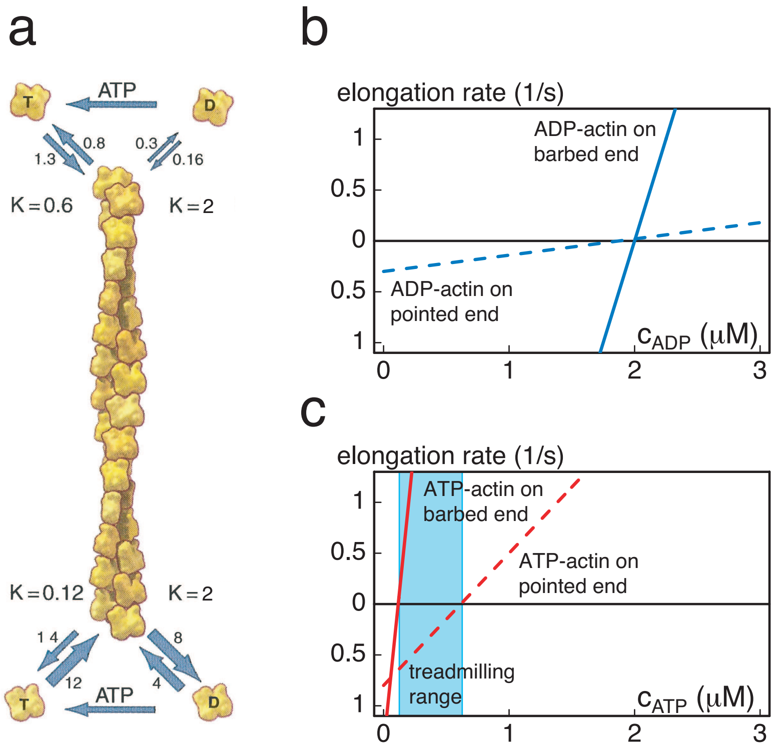

Figure 2.4: Actin filament dynamics and filament elongation rates versus monomer concentration c.
(a) Elongation rate constants for actin in vitro. The association rate constants have units of $\mu\mathrm{M}^{-1}s^{-1}$ and the dissociation rate constants of s^{-1}. The ratio of the dissociation rate to the association rate gives the critical concentration c_c in units of μM. Note that the critical concentration for ATP actin differs at both ends while it is the same for ADP actin. Figure modified and corrected from (Pollard and Borisy, 2003).
(b,c) Elongation rates of actin filaments in vitro versus concentration of free monomers of ADP-actin (b) and ATP-actin (c). The barbed end (continuous line) is more dynamic than the pointed end (dashed line) which is reflected by the greater slope. For ADP-actin (b) both ends either shrink or grow depending on c_ADP. The critical concentration is $c_\mathrm{c,ADP} = 2\,\mu$M for both ends. (c) In the presence of ATP-actin the critical concentration at the barbed end (continuous line) is smaller than the critical concentration at the pointed end (dashed line). The barbed end may thus grow while the pointed end shrinks, the filament treadmills. The range of treadmilling concentrations is marked by the blue rectangle. Data plotted from (Pollard and Borisy, 2003).

typically turns over in 1 min (Pantaloni et al., 2001). This increase is attributed to a host of regulating factors, see section 2.2.3.

Filament treadmilling has been demonstrated to occur in the bulk cytoplasm of cells but it also occurs in the linear strucures of microvili, filopodia and stereocilia (Lin et al., 2005).

2.2.3 Actin Binding Proteins

The concentration of free actin monomers in cells was reported to be around 100 μM (Pollard et al., 2000; Plastino et al., 2004), i.e. two to three orders of magnitude larger than the critical concentrations measured in vitro. Furthermore cell movement, which to a large extend is driven by filament polymerization and depolymerization, can occur with velocities up to 10 $\mu\mathrm{m}\,\mathrm{min}^{-1}$ (Safer and Nachmias, 1994) and hence about two orders of magnitude faster than filament treadmilling in vitro (Bray, 2001; Pollard and Borisy, 2003). The presence of regulatory proteins explains these differences.

Actin binds a substantial number of proteins collectively called actin binding proteins (ABPs). These proteins fall into more than 60 classes (Kreis and Vale, 1999) and recently more than 162 distinct and separate proteins were counted, without including their many synonyms or isoforms (dos Remedios et al., 2003). These proteins influence actin dynamics in various ways. They can:

1. bind to G-actin (e.g. profilin, thymosin-β4, DNase) sometimes sequestering it and preventing its polymerization
2. nucleate actin filaments (Arp2/3, formin)
3. depolymerize filaments (e.g. CapZ, ADF/cofilin)
4. cap the ends of F-actin, preventing the exchange of monomers (e.g. gelsolin, CapZ)
5. sever actin filaments by binding to their sides and cutting them (e.g. gelsolin)
6. cross-link filaments, thus forming gels and bundles (e.g. Arp2/3, α-actinin)
7. stabilize filaments by binding along their sides (e.g. tropomyosin)
8. actively walk along filaments using them as tracks (e.g. the myosin family of motor proteins, cf. section 2.2.4)

Here we briefly introduce some of the most common ABPs that are important for the main part of this thesis. These include the five proteins that can reconstitute bacterial motility in purified systems (i.e. ADF/cofilin (Bamburg et al., 1999), capping protein (Cooper and Schafer, 2000), Arp2/3 complex (Pollard and Beltzner, 2002), an activator of Arp2/3 complex (Weaver et al., 2003), and profilin (Schluter et al., 1997)) as well as formin, which binds to filament plus ends and α-actinin that cross-links filaments in bundles. Comprehensive lists and descriptions of actin binding proteins can be found in (Sheterline et al., 1998; Kreis and Vale, 1999; dos Remedios and Thomas, 2001) and also online at http://www.bms.ed.ac.uk/research/others/smaciver/Encyclop/encycloABP.htm. Here we stress the biochemical function of these components. Recent reviews highlight their implications e.g. for actin based motility in cells and bacterial pathogens (Plastino and Sykes, 2005; Rafelski and Theriot, 2004; Gruenheid and Finlay, 2003; Pollard and Borisy, 2003; Pantaloni et al., 2001).

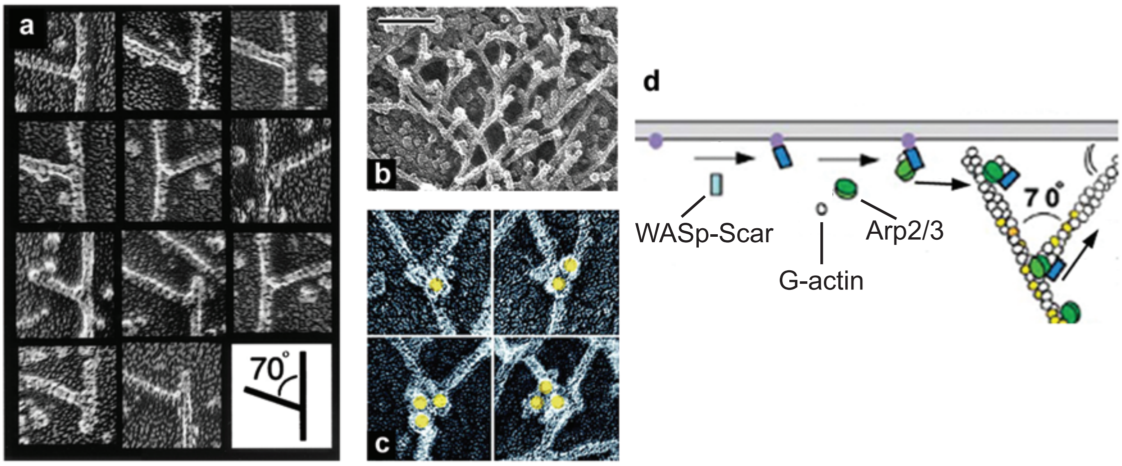

Figure 2.5: (a) Electron micrographs of actin branches nucleated by Arp2/3. Taken from (Mullins et al., 1998) (b,c) Electron micrographs of actin filaments in the lamellipodium of a keratocyte. The yellow dots in (c) mark the positions of the Arp2/3 complex. Figures from (Svitkina and Borisy, 1999). (d) Model for dendritic actin nucleation by Arp2/3, adapted from (Pollard and Borisy, 2003).

ABPs often possess many ways of interaction with the actin system. Gelsolin for example has been shown to cap and also to sever filaments (dos Remedios et al., 2003). The following list thus can only include some of the most prominent features of the selected ABPs.

Profilin & thymosins bind and buffer actin monomers. Practically all monomers in the cell are sequestered by thymosin and profilin which effectively controls their concentration and prevents spontaneous nucleation of actin filaments. The competition between profilin and thymosin-β 4 provides two important actin buffering systems. Profilin also works as a nucleotide exchange factor for monomeric actin (Rosenblatt et al., 1995; Vinson et al., 1998). Furthermore profilin binds monomeric actin at its barbed end. This allows actin-profilin to elongate filaments at the barbed end at rates similar to those of actin monomers but prevents binding to the pointed ends of filaments. Profilin seems to be expressed in all eucaryotes. While the concentration of profilin and its affinity for actin are sufficient to maintain the pool of unpolymerized ATP-actin in amoeba, in human platelets and leukocytes thymosin-β 4 is necessary to control the concentration of ATP-actin monomers (Safer and Nachmias, 1994; De La Cruz et al., 2000).

The Arp2/3 complex nucleates new filaments that branche off the sides of existing filaments at an angle of 70°. This leads to a cross-linked gel of actin filaments similar to that found at the leading edge of fish keratocytes, see Fig. 2.5a. It is generally believed that the Arp2/3 complex by itself is inactive and relies on activating factors such as ActA (Welch et al., 1998), a surface protein of Listeria, or WASp/Scar proteins (Machesky et al., 1999). Actin filaments are coactivators of the Arp2/3 complex (Machesky et al., 1999; Pantaloni et al., 2000). Filament growth thus enhances the nucleation of new filaments and the reaction continues autocatalytically.

WASp/Scar proteins are activators of the Arp2/3 complex. They are usually localized at the leading edge of moving keratocytes or on the membrane of bacterial pathogens such as *Shigella* (Gruenheid and Finlay, 2003).

Formin processively binds to filament barbed ends and promotes filament elongation (Kovar et al., 2003). Formins are nucleators of unbranched actin filaments and involved in dynamic processes such as cell migration (Watanabe et al., 1997; Koka et al., 2003) or cell cleavage (Pelham and Chang, 2002; Wu et al., 2003). Formin can increase the rate constant for profilin-actin association at the barbed end 15-fold (Romero et al., 2004) but differences between different members of the formin family appear to be important (Kovar and Pollard, 2004).

CapZ and Gelsolin are capping proteins that hinder monomer binding and unbinding at filament barbed ends. They limit the lengths of actin filaments and the number of growing barbed ends in a gel. Short filaments are stiffer than long filaments, e.g. making the resulting gel more efficient in pushing the membrane in the lamellipodium. The concentration of CapZ in the cytoplasm is about $1\,\mu$M (Cooper and Schafer, 2000) and its rate constant for binding barbed ends accounts for a capping half time of about 1 s (Schafer et al., 1996). Filaments that grow at velocities of $0.3\,\mu\mathrm{m\,s}^{-1}$ for about 1 s reach a length comparable to that of filaments found at the leading edge (Svitkina et al., 1997). Gelsolin is found mainly in higher eucaryotes (Sun et al., 1999).

ADF/cofilin promotes the disassembly of actin filaments by several mechanisms. It severs filaments (Maciver et al., 1991, 1998; Blanchoin and Pollard, 1999; Ichetovkin et al., 2000), promotes phosphate dissociation in filaments (Blanchoin and Pollard, 1999) and exhibits a higher affinity for ADP-actin monomers than for ADP-actin filaments. Furthermore it changes the twist of actin filaments (McGough et al., 1997), which can induce rupture and may debranche filaments (Pollard and Borisy, 2003). ADF/cofilin increases the off-rate at the pointed ends of filaments 30-fold (Ressad et al., 1998) without changing the rates at barbed ends. As dissociation at the pointed ends of filaments is the rate limiting step in filament treadmilling, ADF increases the treadmilling velocity. This effect is further increased in the presence of profilin. The rate of pointed end disassembly is then increased 125-fold by the combined action of ADF/cofilin and profilin (Didry et al., 1998).

α-actinin cross-links parallel actin filaments. Filament bundles linked by α-actinin are rather loosely packed, so that e.g. myosin-II can enter the bundle and contract it. α-actinin is a major component of the Z-disk in muscle cells (Bray, 2001). Fimbrin is another bundling protein that however forms tightly packed filament bundles that are not contractile (Alberts et al., 2002). Besides these proteins that link filaments parallel to each other and thus promote the formation of bundles, other cross-linkers such as spectrin or filamin or the Arp2/3 complex discussed above, link filaments at an angle and lead to the formation of gels. A review of actin cross-linkers is given in (Revenu et al., 2004).

2.2.4 Myosin: The Actin Motor

Besides the cross-linkers described above, myosin motors can also bind to and cross-link filaments. The cross-linkers are passive, i.e. they do themselves not consume energy. Motors on the other hand possess the ability to convert chemical energy, freed by the hydrolysis of ATP, into directed motion. From a physics point of view, molecular motors

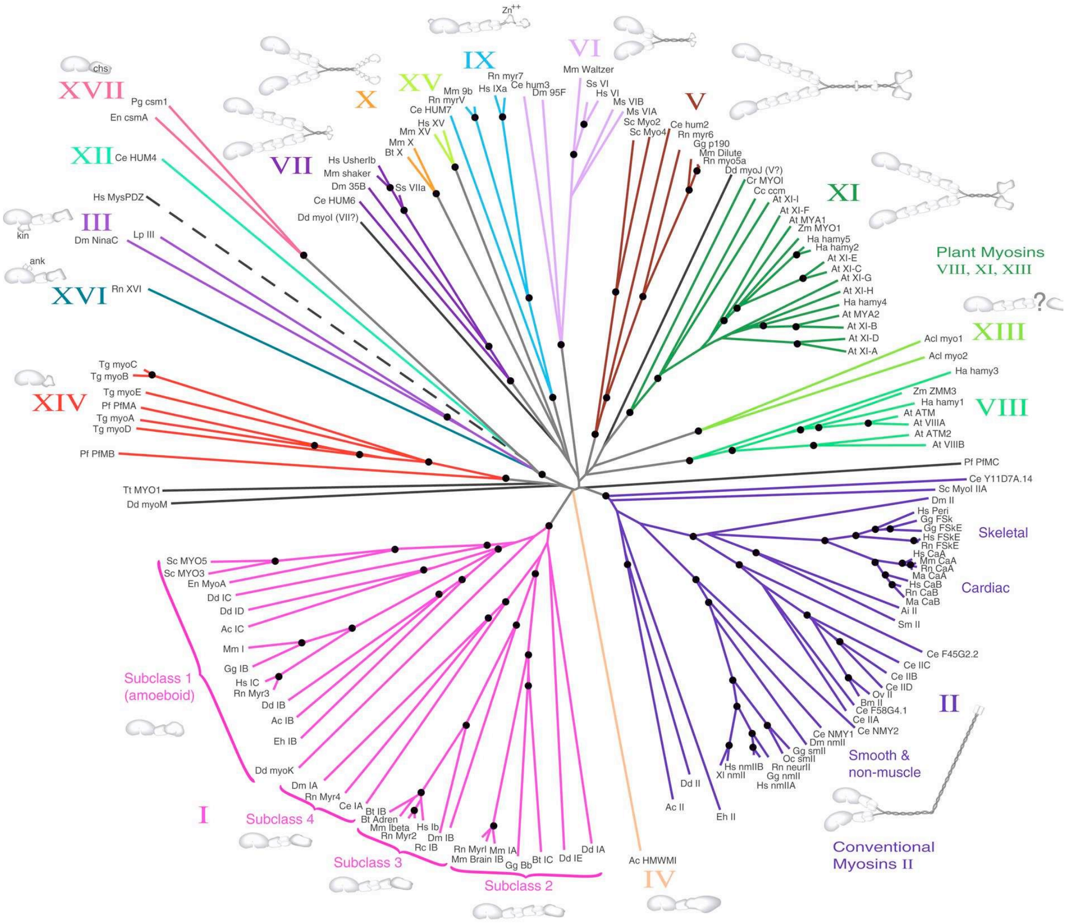
Zn++
chs
XVII
Pg csm1
En csmA
XII
Ce HUM4
Hs MysPDZ
kin
III
Dm NinaC
Lp III
ank
XVI
Rn XVI
X
VII
Hs UsherIb
Mm shaker
Dm 35B
Ss VIIa
Ce HUM6
Dd myoI (VII?)
XV
Bt X
Mm X
Mm XV
Hs XV
Ce HUM7
Rn myrV
Mm 9b
IX
Hs IXa
Rn myr7
Ce hum3
Dm 95F
VI
Mm Waltzer
Ss VI
Hs VI
Ms VIB
Ms VIA
Sc Myo2
Sc Myo4
V
Ce hum2
Rn myr6
Gg p190
Mm Dilute
Rn myo5a
Dd myoJ (V?)
Cr MYOI
Cc ccm
XI
At XI-I
At XI-F
At MYA1
Zm MYO1
Ha hamy5
Ha hamy2
At XI-E
At XI-C
At XI-G
At XI-H
Ha hamy4
At MYA2
At XI-B
At XI-D
At XI-A
Plant Myosins
VIII, XI, XIII
?
XIII
Acl myo1
Acl myo2
Ha hamy3
Zm ZMM3
Ha hamy1
VIII
At ATM
At VIIIA
At ATM2
At VIIIB
Pf PfMC
Ce Y11D7A.14
Sc MyoI IIA
Dm II
Hs Peri
Gg FSk
Gg FSkE
Hs FSkE
Rn FSkE
Skeletal
Hs CaA
Mm CaA
Rn CaA
Ma CaA
Hs CaB
Rn CaB
Ma CaB
Cardiac
Ai II
Sm II
Ce F45G2.2
Ce IIC
Ce IIB
Ce IID
Ov II
Bm II
Ce F58G4.1
Ce IIA
II
Ce NMY1
Ce NMY2
Dm nmII
Gg smII
Oc smII
Rn neurII
Gg nmII
Hs nmIIA
Hs nmIIB
Xl nmII
Smooth &
non-muscle
Dd II
Ac II
Eh II
Conventional
Myosins II
Ac HMWMI
IV
Tg myoC
Tg myoB
XIV
Tg myoE
Pf PfMA
Tg myoA
Tg myoD
Pf PfMB
Tt MYO1
Dd myoM
Sc MYO5
Sc MYO3
En MyoA
Dd IC
Dd ID
Ac IC
Mm I
Gg IB
Hs IC
Rn Myr3
Dd IB
Ac IB
Eh IB
Subclass 1
(amoeboid)
Dd myoK
Dm IA
Rn Myr4
Ce IA
I
Subclass 4
Bt IB
Bt Adren
Mm Ibeta
Rn Myr2
Hs Ib
Dm IB
Rc IB
Subclass 3
Rn MyrI
Mm IA
Mm Brain IB
Gg Bb
Bt IC
Dd IE
Dd IA
Subclass 2

Figure 2.6: The Myosin Tree. From (Hodge and Cope, 2000).

can e.g. be understood as machines that rectify Brownian motion (Jülicher et al., 1997; Duke, 2002a; Reimann, 2002). The dynamics of many motors acting collectively as is frequently the case in the cytoskeleton displays a variety of surprising phenomena (Jülicher and Prost, 1995, 1997; Duke, 1999; Badoual et al., 2002; Duke, 2002b).

Here we will concentrate on the effect of molecular motors on cytoskeletal dynamics. The intrinsic activity of protein filaments (i.e. polymerization, depolymerization, treadmilling) as well as the action of molecular motors are crucial for many cellular processes. Both are active, i.e. energy consuming, non-equilibrium processes. Gels of filaments, cross-linkers, regulating proteins and molecular motors are hence called active gels.

Myosins are motors, that are able to move along actin filaments. They are ubiquitous and new members of the myosin super-familiy of actin motors are constantly discovered (Hodge and Cope, 2000), cf. Fig. 2.6. Myosins are large proteins that bind actin with a globular head, possess ATPase activity and move along actin filaments by coupling ATP hydrolysis to conformational change. The most studied myosin is the two-headed myosin II, also called conventional myosin. It was renamed myosin II for two-headed after the discovery of a one-headed myosin, which was called myosin I. The numbers of the other myosin subfamilies roughly reflect the time sequence of their discovery. Myosins perform a multitude of functions in many different cells. They are involved in vesicle transport in the cell (myosin V), in hearing (myosins VI and VII are present in the stereocilia in

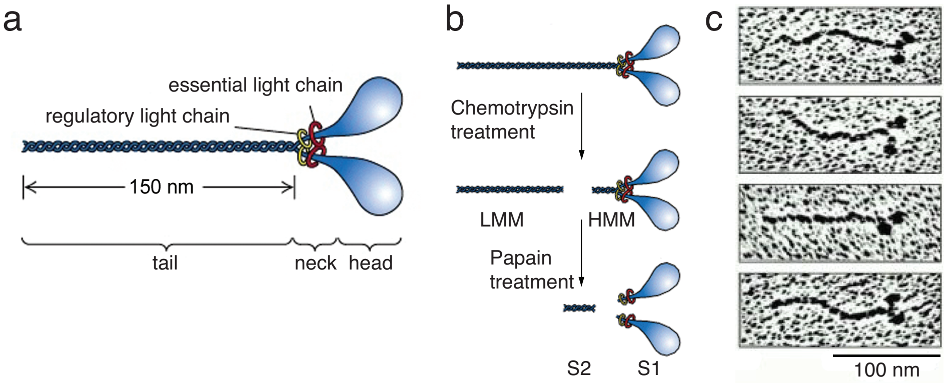

Figure 2.7: (a) Schematic representation of the structure of myosin II. (b) A myosin molecule can be split up into Heayy Meromyosin (HMM) that is still an active ATPase and Light Meromyosin (LMM). HMM can be further dissected into subfragments S1 and S2, of which only S1 is an ATPase. (c) Electron micrographs of of myosin II. Figures adapted from Alberts et al. (2002).

the inner ear, the graded distribution of myosin XVa seems to be responsible for length dependent treadmilling rates in stereocilia (Lin et al., 2005; Rzadzinska et al., 2004)) or in vision (myosin III). Myosin I is able to link actin filaments to phospholipids such as those in the cell membrane. All myosins are unidirectional and move towards the barbed (plus) end, except for myosin VI which moves towards the minus end. Here we focus on myosin II, the member of the myosin family involved in muscle contraction, cell motility and - generally, see discussion in section 2.5.2 - cell division.

Myosin II molecules are made up from two identical heavy chains, and two identical pairs of light chains. The N-terminal of the heavy chains folds to form the globular head that binds to actin. The C-terminal halves of the chains assemble into a ca. 150 nm long coiled-coil rod of α-helices, see Fig. 2.7. These coiled-coils feature binding sites that allow myosin II molecules to form bipolar filaments. These so called thick filaments were first discovered in muscle cells, where they interdigitate with the thinner actin filaments. The heads of myosin II can be isolated and still glide along filaments in vitro, which proves that they contain the mechanism for force generation (Toyoshima et al., 1987). Each head is associated with a pair of light chains. Each pair consists of an “essential light chain” and a “regulatory light chain” that is the substrate for several kinases, which regulate the activity of myosin II.

Myosin proteins generate force, e.g. to walk along a filament, by converting the energy from ATP hydrolysis into conformational change. In order to advance one step, the motor head has to let go of the filament, undergo a conformational change, rebind to a new site on the filament and generate the force in order to get back into the old conformation. Figure 2.8 elucidates these basic steps of a myosin head in greater detail:

1. Attached In the absence of a bound nucleotide, the myosin molecule is bound to the actin filament in the so called rigor conformation (named so because it is responsible for *rigor mortis*, the rigidity of death). In actively contracting muscle this state is relatively short lived, because of rapid binding of an ATP molecule.

2. Released An ATP molecule binds to the myosin in the cleft and causes a slight change in conformation. This reduces the affinity of the actin binding site and allows the head to move along the filament.

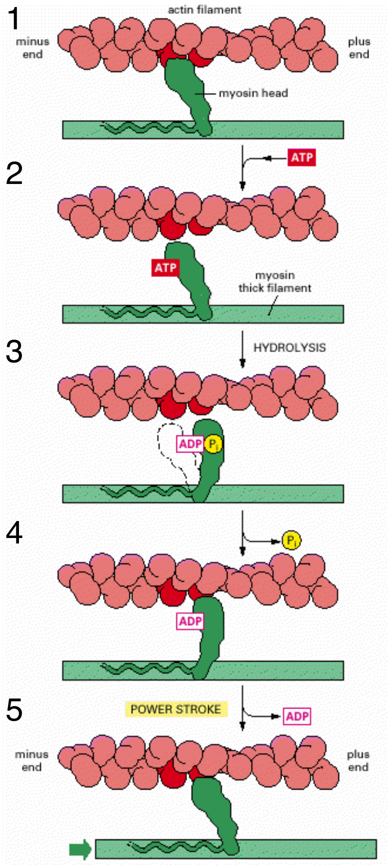

Figure 2.8: Schematic representation of the working steps of a molecular motor. See text for explanation. Figure adapted from (Alberts et al., 2002).

3. COCKED The cleft closes around the ATP molecule, causing a big conformational change. This causes the head to be displaced along the filament by 5 nm. ATP is hydrolyzed but ADP and P_i remain closely bound to the myosin.

4. FORCE-GENERATING The head binds weakly to the new site along the actin filament which causes the release of the inorganic phosphate P_i. This induces tighter binding between head and actin filament and triggers the power stroke, i.e. the force generating conformational change in the cycle. Here the head regains its original conformation albeit linked to a different site on the actin filament and looses its bound ADP.

5. ATTACHED The myosin head is again locked tightly to the actin filament in a rigor configuration and the cycle can start anew.

Individual myosins are not processive, i.e. they only bind briefly to an actin filament and detach after less than 20 μm (Finer et al., 1994). They generate forces around 3-4 pN independent of the ATP concentration. When assembled in filaments, on the other hand, heads of myosin II collectively can become processive as is for instance the case in muscle fibers, where thick filaments of myosin slide actin filaments with respect to each other.

It was shown in the 1940s by Albert Szent-Gyorgyi et. al. that myosin can contract artificial fibrils. This gave rise to the **filament sliding hypothesis**, in which a myosin

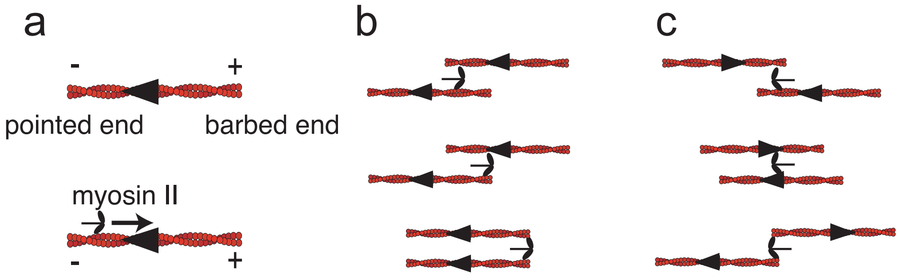

Figure 2.9: (a) The polarity of actin filaments determines the direction of movement of myosin motors. Myosin II moves towards the barbed or plus end (indicated by the wide side of the wedge). (b,c) The direction of relative filament motion depends on the orientation of filaments. Myosin II always works to align the barbed ends of filaments. For parallel filaments (b) this means also aligning pointed ends, while for anti-parallel filaments (c) pointed ends will move to maximize their distance.

simultaneously binds to two filaments and induces relative motion in the pair. This hypothesis has been proven right subsequently by electron micrographs of muscle cells that feature polymers of myosin II molecules, so called heavy myosin filaments. In vitro studies have shown that Heavy Meromyosin (HMM), i.e. a myosin II molecule that has lost most of its coiled coil and thus cannot form bipolar assemblies (such as e.g. thick filaments, cf. Fig. 2.7), also leads to contraction of bundles of filaments (Takiguchi, 1991). Thus neither aggregation nor processivity are necessary for an ensemble of myosin motors to induce filament sliding. The direction of filament sliding generally depends on the relative position and orientation of filaments, see Fig. 2.9b and c.

2.2.5 Actin and Cell Locomotion

Cell locomotion is understood as a three step process. A prominent example is provided by thelamellipodium as found e.g. in fish keratocytes, Fig. 2.10. The figure shows the dense actin network that is involved in pushing the lamellipodium forward. The lamellipodium is extended mainly by the polymerization forces generated in the actin rich region (Plastino and Sykes, 2005; Rafelski and Theriot, 2004). This part of cell motility is called protrusion, see Fig. 2.11. The next step is attachment, i.e. the actin cytoskeleton connects to the substratum, forming adhesions. The subsequent motion of the cell body, called traction, is driven by stress fibers, i.e. bundles of actin filaments that terminate in focal adhesions, see section 2.5.4.

For many years the main focus was on molecular motors to drive motion. In recent years however alternative concepts of biological motility have received some attention.Molecular motors are certainly involved in the traction phase of cell locomotion. Cells deficient of myosin II move slower while still protruding their lamellipodium at the same speed. Myosin could furthermore weaken old focal adhesions by contraction of the actin cortex at the back of the cell. Myosin II could then transport components of the cell body along a polar array of actin filaments. For cell migration the focus has widened to also include controlled polymerization and depolymerization of filaments as a driving mechanism besides molecular motors.

For the lamellipodium it is known that actin polymerization is crucial for protrusion. It has been shown also that depolymerization of polymers can generate contractile forces in locomotion (Miao et al., 2003). Dynamic actin patterns consistent with this general framework of cell motility have been observed by TIRF microscopy in migrating dictyostelium

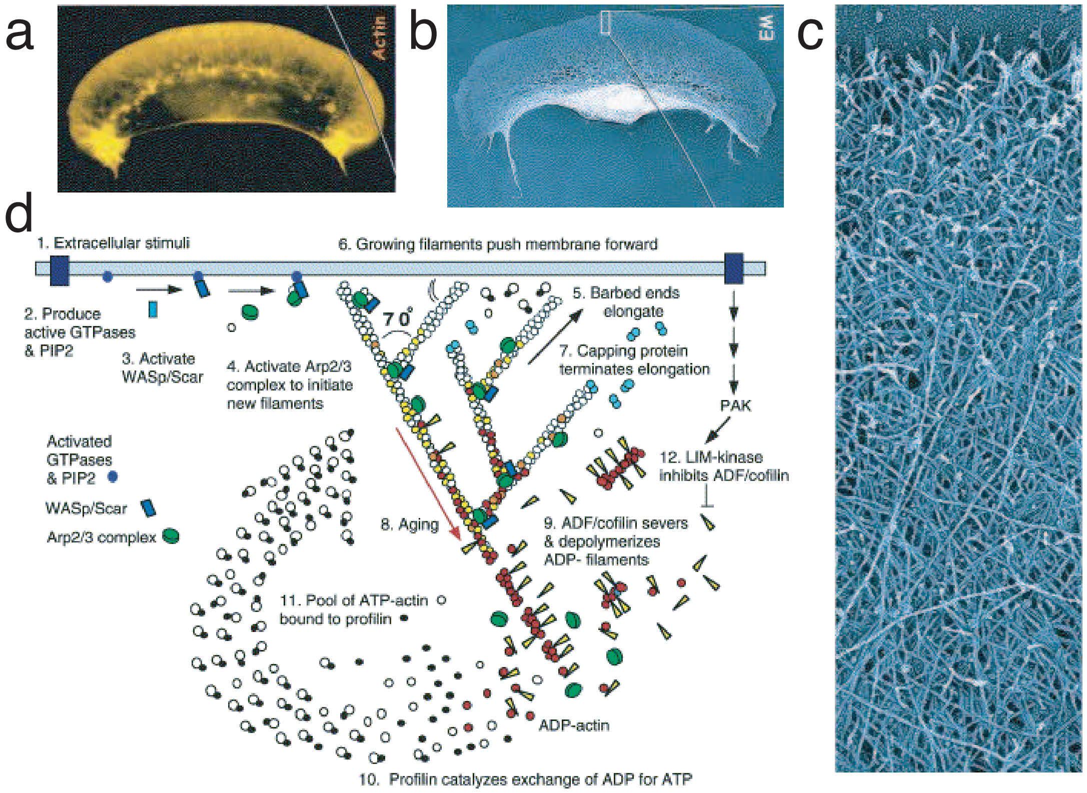
a
Actin
b
EM
c
d
1. Extracellular stimuli
6. Growing filaments push membrane forward
2. Produce active GTPases & PIP2
3. Activate WASp/Scar
4. Activate Arp2/3 complex to initiate new filaments
70°
5. Barbed ends elongate
7. Capping protein terminates elongation
PAK
12. LIM-kinase inhibits ADF/cofilin
Activated GTPases & PIP2
WASp/Scar
Arp2/3 complex
8. Aging
9. ADF/cofilin severs & depolymerizes ADP- filaments
11. Pool of ATP-actin bound to profilin
ADP-actin
10. Profilin catalyzes exchange of ADP for ATP

Figure 2.10: Actin structures and cell locomotion. Fluorescence micrograph (a) and transmission electron micrograph (b) of a keratocyte. The box in (b) indicates the region of the actin gel in the lamellipodium enlarged in (c).

(d) Model for how actin treadmilling drives lamellipodium protrusion.

(1) Extracellular signals activate receptors.

(2) The associated signal transduction pathways activate Rho-family GTPases and PIP2 that in turn

(3) activate WASp/Scar proteins.

(4) WASp/Scar proteins bring together Arp2/3 complex and an actin monomer on the side of a preexisting filament to form a branch.

(5) Rapid growth at the barbed end of the new branch

(6) pushes the membrane forward.

(7) Capping protein terminates growth within a second or two.

(8) Filaments age by hydrolysis of ATP bound to each actin subunit (white subunits turn yellow) followed by dissociation of the inorganic phosphate (subunits turn red).

(9) ADF/cofilin promotes phosphate dissociation, severs ADP-actin filaments and promotes dissociation of ADP-actin from filament ends.

(10) Profilin catalyzes the exchange of ADP for ATP (turning the subunits white), returning subunits to

(11) the pool of ATP-actin bound to profilin, ready to elongate barbed ends as they become available.

(12) Rho-family GTPases also activate PAK and LIM-kinase, which phosphorylates ADF/cofilin. This tends to slow down the turnover of the filaments.

Composed from (Pollard and Borisy, 2003).

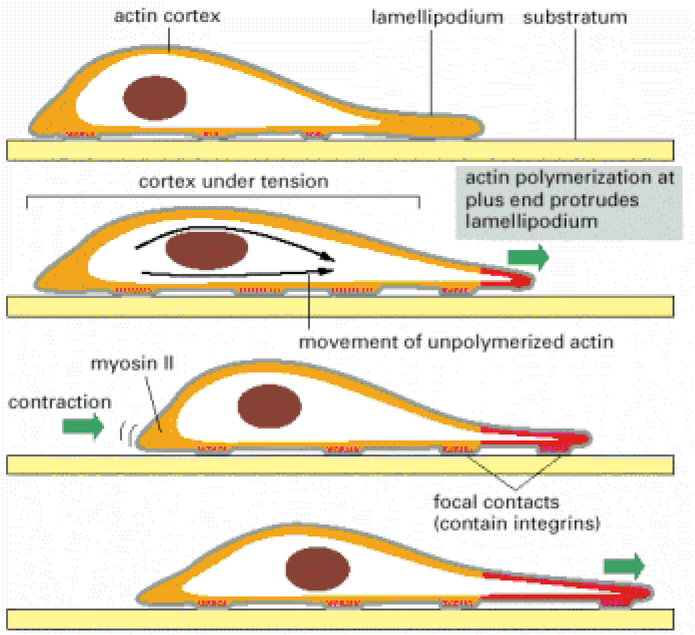
actin cortex
lamellipodium
substratum
cortex under tension
actin polymerization at plus end protrudes lamellipodium
movement of unpolymerized actin
myosin II
contraction
focal contacts (contain integrins)

Figure 2.11: Model for cell locomotion driven by forces generated in the actin rich cell cortex. The actin polymerization protrusion of the lamellipodium moves the cell forward (green arrow at the front) and stretches the cortex. Contraction at the rear of the cell drags the cell body forward (green arrow at the back) New focal contacts are made in the front while old ones at the back are weakened. Newly polymerized actin is shown in red. Figure from (Alberts et al., 2002).

cells (Bretschneider et al., 2004). These patterns include traveling waves that are based on recruitment of the Arp2/3 complex. The cortical network also exhibits foci with a lifetime of 7-10 s that also depend on Arp2/3. These structures form even in the absence of myosin II. Figure 2.10 shows a schematic model for polymerization driven cell motility and the ABPs involved in the process. In this thesis we show that polymerization can play a role also for traction in cell locomotion, as the contraction of stress fibers, usually believed to be driven by motors, can also be driven by filament polymerization and depolymerization, cf. section 3.2.3.

2.3 Microtubules and Microtubule Associated Proteins

Microtubules are another class of filaments found in cells. They provide the basis for directed cellular transport, influence the cell's shape and determine the positions of membrane enclosed organelles. Mitotic and meiotic spindles as well as the pre-prophase band in higher plant cells are among the most prominent microtubule structures. Like actin, microtubules are also polymerized from smaller units hydrolyzing a tri-phosphate bond. Many of the principles governing actin polymerization dynamics presented above also apply to microtubules. In this section we will thus only briefly introduce microtubule structure and highlight differences in the polymerization dynamics. Then we briefly introduce two families of microtubule motors, kinesins and dyneins.

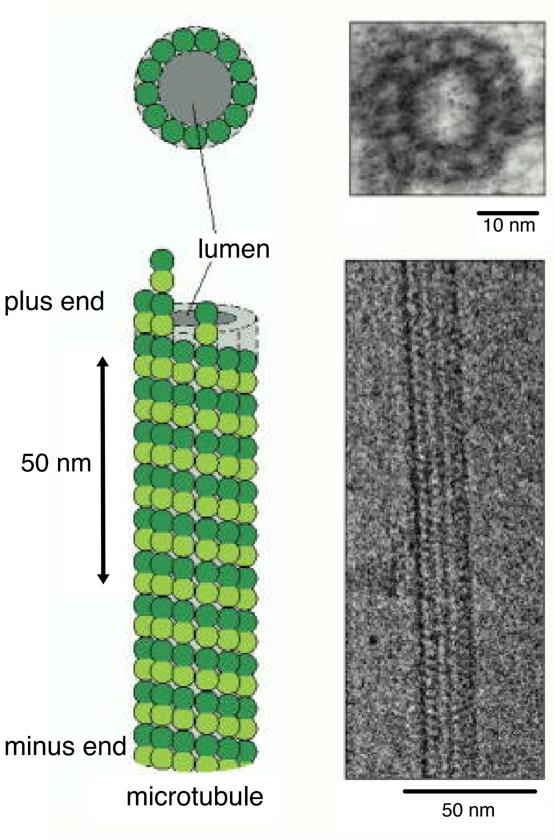

Figure 2.12: Microtubules are stiff hollow tubes formed from 13 protofilaments. The tube has an outer diameter of about 25 nm. Shown is a cross section and short segments of microtubules. Figure modified from (Alberts et al., 2002).

2.3.1 Microtubules and Dynamic Instability

Microtubules (MTs) are hollow cylinders with an outer diameter of 25 nm, Fig. 2.12. With a persistence length of about 5 mm they are a lot more rigid than actin filaments. They often form long structures that help to define the cell shape. MTs are made of tubulin heterodimers that consist of globular proteins, α- and β-tubulin. Each MT is a hollow cylindrical structure constructed from usually 13 protofilaments of alternating α- and β-tubulin units, see Fig. 2.12. As all tubulin heterodimers are aligned in a microtubule, the structural polarity of the subunits thus directly gives rise to the structural polarity of the whole microtubule: at one end the MT exposes only α-tubulin and at the other only β-tubulin, Fig. 2.12. The end exposing β-tubulin is the fast growing plus end and the other is the slow growing minus end.

Each α- and β-tubulin binds a molecule of guanosine triphosphate (GTP). The nucleotide bound to the α-molecule is never hydrolyzed or exchanged, it may thus be considered as an integral part of the tubulin heterodimer. The GTP bound to the β-tubulin on the other hand can be hydrolyzed and exchanged and plays a similar role for the polymerization dynamics of microtubules as ATP does for actin filaments. We will refer to a tubulin heterodimer with a GTP(GDP) molecule bound to its β-tubulin as GTP(GDP)-tubulin respectively. Actin filaments as well as microtubules have been observed to treadmill in vitro as well as in cells (Rodionov and Borisy, 1997a). It is believed that **dynamic instability** is the predominant behavior of microtubules in cells.

Dynamic instability refers to the sudden switching of a MT from steady growth to rapid shrinkage and then back to steady growth. The basis for this abrupt change is again nucleotide hydrolysis. If a microtubule is surrounded by a tubulin concentration between the critical concentrations for the GDP- and the GTP-form of tubulin respectively (i.e. the concentration range where treadmilling is possible), any end exposing GDP-tubulin will shrink while any end exposing GTP-tubulin will grow. If the rate of subunit addition is of the same magnitude as the rate of hydrolysis in the microtubule, growth may start out with GTP-tubulins, but eventually the hydrolysis can catch up with the addition of GTP-units and thus the microtubule would expose GDP-tubulin at its end. But now the concentration of tubulin is below the critical concentration for GTP elongation and the end will start to depolymerize. This rapid depolymerization takes place until the microtubule is completely anihilated or regains its GTP-cap and starts to grow again. The rapid shrinking is called a catastrophe, while the change to growth is called a rescue event.

Another reason for the rapid depolymerization of microtubules upon loss of their GTP-caps besides the kinetic arguments described above is the structural difference between GTP- and GDP-tubulin(Mahadevan and Mitchison, 2005) and their different bending flexibility (Wang and Nogales, 2005). GTP-tubulin forms straight protofilaments that make strong and regular lateral contacts with other protofilaments. Hydrolysis of GTP to GDP induces a little structural change in the heterodimers which leads to curved protofilaments. A GTP-cap on a fast growing microtubule constrains the curvature of the protofilaments made of GDP-tubulin. When it is lost, e.g. by hydrolysis, the curvature is not restrained anymore and the protofilaments curve apart, see Fig. 2.13. The individual filaments then peel off rapidly.

2.3.2 Microtubule Associated Proteins

Like actin, microtubules interact with a large group of other proteins, collectively called microtubule associated proteins (MAPs). Two important functions of MAPs are the stabilization or destabilization of microtubules, thus promoting or hindering MT depolymerization. Other MAPs mediate the interaction of MTs with other cellular components. In neurons stabilized bundles of microtubules form the core of axons and dendrites. These bundles are held together by MAPs such as MAP2 or tau. Bundles packed by different MAPs have different characteristics. MAP2 bundles for example feature bigger spaces between the microtubules while tau bundles are tightly packed. MAPs can also serve as nucleation cores in solutions of tubulin, as they bind tubulin dimers and thus stabilize the oligomers necessary to induce microtubule polymerization.

A very interesting class of MAPs is represented by XMAP215, a MAP found in the frog *Xenopus* whose molecular weight is 215 kDa, hence the name. XMAP215 has close homologs in many organisms that range from yeast to humans. XMAP215 binds to the side of microtubules, but it also has the ability to stabilize free microtubule ends, preventing catastrophes. This activity can be inhibited by phosphorylation of XMAP215. It has been shown that this phosphorylation contributes to the ten-fold increase in MT dynamic instability during mitosis (see also section 2.5.1). XMAP215 is one member of a large class of MT end binding or tracking proteins (Akhmanova and Hoogenraad, 2005). Other members of this class may processively depolymerize microtubules (Wordeman, 2005), such as the Mitotic Centromere-Associated Kinesin/kinesin family 2 (MCAK/kif2) (Wordeman

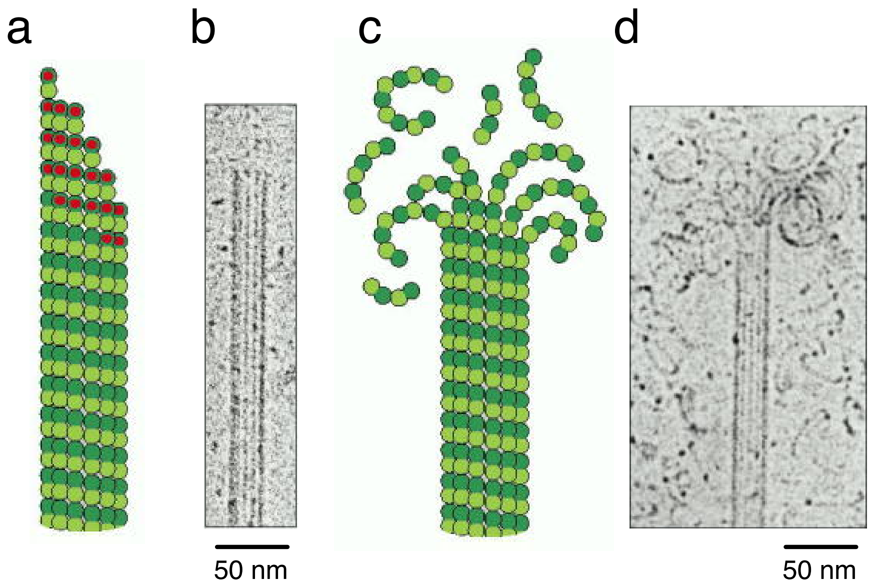

Figure 2.13: Dynamics instability due to structural differences of a growing (a,b) and shrinking (c,d) microtubule end.
(a) Sketch of an intact microtubule with a GTP-cap, indicated by red dots. The GTP-tubulin subunits in the protofilaments are forced into straight configurations.
(b) Electron micrograph of an intact microtubule.
(c) When the GTP-cap is lost, the GDP-protofilaments assume a curved configuration, destabilizing the end. This leads to a catastrophe, a rapid depolymerization of the microtubule.
(d) Electron micrograph of a microtubule end with bent protofilaments.
Figure modified from (Alberts et al., 2002).

and Mitchison, 1995), recently named kin-13 family (Lawrence et al., 2004). Kinesins found in the mitotic spindle can also change the structure of microtubules (Bringmann et al., 2004). Generally the mitotic spindle abounds with MAPS, especially those acting at the end of microtubules. Members of the kin-13 family for example are found both on the centromere and on the centrosome, contributing to spindle morphology and dynamics. Interestingly not only spindle function but also spindle positioning depend on end acting MAPs (Grill et al., 2005, 2003). An extensive list of MAPs and their role during mitosis is discussed in (Maiato et al., 2004).

2.3.3 Microtubule Motors: Kinesin and Dynein

Contrary to actin for which only one class of motors (myosin) is known, there are two types of microtubule motor proteins: kinesins and dyneins. Kinesins are generally plus-end directed while dyneins mostly walk towards minus ends. Dyneins reach speeds up to $14\,\mu$m/s and are thus faster than kinesins that move with $0.02-2\,\mu$m/s (Mallik and Gross, 2004; Vale, 2003). Compare this to myosin motors that move along actin filaments with velocities between $0.2-60\,\mu$m/s.

Kinesin

Kinesins were first discovered in the squid giant axon where they walk away from the cell body towards the plus end of the MTs, carrying membrane-enclosed organelles. Kinesins also play a role in mitosis, meiosis, transport of DNA and proteins, and MT polymerization dynamics. In in vitro experiments kinesins have been shown to be strong enough to pull membrane tubes from vesicles (Roux et al., 2002; Leduc et al., 2004; Leduc, 2005)

Kinesin is structurally similar to myosin II, as it also forms a dimer, having two globular motor domains, possessing one heavy and two light chains each. These strucutral similarities hint to a common evolutionary origin (Alberts et al., 2002). Like myosin, kinesin is a member of a large protein superfamily - humans have 40 different kinesins for example. Most members of the at least 10 families of kinesin that make up the super family have their motor domain at the N-terminus of the heavy chain and walk towards the MT plus end. There is however at least one family that has the motor domain at the C-terminus and walks towards the minus end. Many kinesins are homo- or hetero-dimers; Kinesin-5 (BimC) is a KRP family, whose members can associate and form bipolar motors. They can then slide two microtubules with respect to each others, similar to myosin II on actin filaments. Most kinesins have binding sites for membrane-enclosed organelles or microtubules in their tails. Besides providing intracellular transport, kinesins have specific roles in mitotic and meiotic spindle formation and dynamics. It has recently been shown that for example the mitotic kinesin Eg5, which is important for spindle integrity, can simultaneously move along two microtubules and even stay attached to MT plus ends (Kapitein et al., 2005).

Kinesins generally walk on one protofilament towards the MT plus end making 8 nm steps. They hydrolyze one molecule of ATP per step and average about 125 steps before unbinding from the MT without any external force applied. The average velocity is on the order of μm/s at 1 mM ATP (Howard et al., 1989; Block et al., 1990). The stall force at which the motor stops to advance is about 6 pN (Svoboda and Block, 1994) and depends on the ATP concentration (Block et al., 2003). Kinesin seems to walk in a bipedal manner, i.e. it walks like a person (Asbury, 2005).

Dynein

Dyneins are a family of minus end directed microtubule motors that are unrelated to the kinesin superfamily. The dynein family has two branches: cytoplasmic and axonemal dyneins. Cytoplasmic dyneins are heavy chain homodimers (the heavy chain of dyneins contains the motor domain) and are the more ancient form of dyneins. They are responsible e.g. for vesicle transport in the cell. As microtubules tend to originate with their minus ends close to the nucleus and their plus ends radiating outwards, dyneins will usually transport cargo towards the center of the cell. One particular example is the localization of the Golgi apparatus close to the nucleus.

The other family are axonemal dyneins. They represent heavy chain heterodimers or heterodimers with two or three motor domains respectively. They are responsible and optimized for the sliding motion of microtubules in beating cilia and flagella (Gibbons, 1981; DiBella and King, 2001).

Dyneins are the largest known molecular motors and they are also among the fastest. Dynein structure and function are not as well understood as those of myosin and kinesin, e.g. as there is no crystal structure of dynein yet (Oiwa and Sakakibara, 2005). Dyneins have been observed to take steps of 8 nm or 32 nm, depending on applied load and ATP

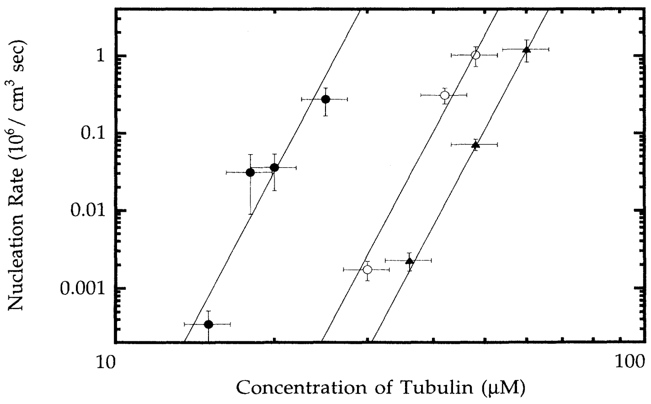

Figure 2.14: Nucleation rate per unit volume versus concentration under conditions of marginal nucleation at three different temperatures: $T = 30°\text{C}$ (solid circles), $T = 22°\text{C}$ (open circles), and $T = 20°\text{C}$ (triangles). The lines represent $1/\tau \propto c^{12}$. The error bars allow for an error ±2 in the exponent. Figure taken from (Kuchnir Fygenson et al., 1995).

concentration (Mallik et al., 2004). As seems useful for motors involved in directed transport over long distances, dyneins are highly processive.

2.4 Dynamics of Individual Filaments

2.4.1 Nucleation, Polymerization and Treadmilling

Cytoskeletal filaments such as actin filaments or microtubules are formed from many protein subunits. They can thus polymerize and depolymerize depending on the conditions. Generally nucleation of new filaments is the rate limiting step in polymerization dynamics. The physical basis of nucleation and polymerization of filaments from subunits is given e.g. in (Oosawa and Asakura, 1975; Hill, 1987). Here we will briefly present the basic ideas and demonstrate how quantitative analysis of polymerization data can reveal details about nucleation events.

Quantitative experiments on microtubule nucleation (Voter and Erickson, 1984) together with a careful analysis based on a physical model for the nucleation mechanism have led to a measurement of the size of the critical nucleus and shown that the nucleus is assembled by different pathways depending on conditions (Kuchnir Fygenson et al., 1995). Direct observation of microtubules in a regime where nucleation and polymerization are slow shows that the density of MT ends increases linearly with time before leveling off. The time between two nucleation events per unit volume, τ, obtained from these measurements is very sensitive to changes in the tubulin concentration c: measurements show $\tau^{-1} \propto c^{12\pm2}$ at three different temperatures, see Fig. 2.14.

These results can be explained in terms of a simple model: a subcritical aggregate of size x grows or shrinks by one dimer at a time with probabilities g and s. As subcritical aggregates are unstable and larger aggregates grow, s and g have to depend on x. The simplest assumption is $g < s$ for $x < N_c$ and $g > s$ for $x > N_c$, where N_c is the critical size of the nucleus. A reasonable assumption is that g is proportional to c while s is independent of c. The critical size N_c thus can decrease for higher c. Assuming $g/s(N)$

to be a step function and ignoring events involving more than one aggregate, a constant nucleation rate leads to a steady state of subcritical aggregates captured by

$$g\,n(N) = s\,n(N+1) \quad \text{for} \quad N < N_c - 1 \tag{2.3}$$

where $n(N)$ is the number density of aggregates of size N. The nucleation rate in a Volume V is then given by

$$\frac{1}{\tau} = g\,n(1)\left(\frac{g}{s}\right)^{N_c-2} \propto c^{N_c}, \tag{2.4}$$

where $n(1) = c$ is the concentration of dimers. The exponent $N_c = 12 \pm 2$ obtained from measurements thus implies a critical size of 12. The model only demands subsequent aggregation, not instantaneous condensation of 12 dimers.

In the other extreme regime of abundant nucleation microtubules are dense and cannot be observed directly by light microscopy. It also turns out that the population of subcritical aggregates is not steady state and that growth and shrinking depend on the size N. A modified model to interpret the obtained measurements suggests that in he abundant regime nucleation takes place in three to four steps and the nucleus comprises 12 to 15 dimers (Kuchnir Fygenson et al., 1995).

Once a filament is nucleated, new subunits can be added to its ends with rate k_{on} and removed with rate k_{off}. The gain in length of a filament due to addition of a subunit is denoted by a. It will be in general equal to or smaller than the length $\tilde{a}$ of an individual subunit. For simplicity we assume that $a = \tilde{a}$ for the remainder of this thesis. The velocities of a polymerizing (plus) and a depolymerizing (minus) end of a filament are given by

$$\begin{aligned} v^+ &= a\,(k^+_{\text{on}} - k^+_{\text{off}}) = a\,k^+ \qquad (2.5)\\ v^- &= a\,(k^-_{\text{on}} - k^-_{\text{off}}) = a\,k^- \quad . \qquad (2.6)\end{aligned}$$

Here we have chosen to denote velocities towards the plus end with positive values. If $k_{\text{on}} > k_{\text{off}}$ the respective filament end will grow. We define $k^{\pm} = k^{\pm}_{\text{on}} - k^{\pm}_{\text{off}}$. If $k^+ \neq k^-$ the length will increase. Typically we have $k^+ > k^-$ as the faster growing, more dynamic end is termed the plus end. If the concentration of subunits is constant, the filament grows with velocity

$$v_g = v^+ - v^- = a(k^+ - k^-) \quad . \tag{2.7}$$

If the rates k^+ and k^- are of the same magnitude but have opposites signs, so that the velocities of both ends obey

$$v = v^+ = -v^- \quad , \tag{2.8}$$

the filament does not change its length. If $v > 0$ the filament center of mass as well as both ends dislocate in space while the filament length remains constant. This type of filament dynamics is called treadmilling, cf. section 2.2.2. The velocity v is called the treadmilling speed.

2.4.2 Force Generation by Polymerization and Depolymerization

Forces in the cytoskeleton can be generated by molecular motors but also by the polymerization and depolymerization of protein filaments (Oosawa and Asakura, 1975; Hill, 1987). Due to their greater structural stability (e.g. greater persistence length) microtubules seem to be better suited to transmit pulling as well as pushing forces than individual actin filaments. In this section we concentrate on microtubules. The general ideas behind the analysis do of course usually also apply to actin filaments. Examples of how the polymerization forces are used to achieve important functions in cells have been reviewed recently (Dogterom et al., 2005). In this section we will briefly review possible physical mechanisms for this type of force generation.

Depending on the exact conditions MTs gain $\Delta G = 5 - 10\,k_\mathrm{B}T$ per addition of a GTP-tubulin dimer. So in principle a microtubule that grows $a = 8\,\mathrm{nm}$ by adding one tubulin dimer to each of the $N = 13$ protofilaments, could generate $\sim 50\,\mathrm{pN}$ force ($F \simeq N\Delta G/a$) (Inoue and Salmon, 1995; Desai and Mitchison, 1997). After hydrolysis of the tri-phosphate, the disassembly of GTP-tubulin from a microtubule also releases $5-10\,k_\mathrm{B}T$ per dimer (Desai and Mitchison, 1997). Assembly and disassembly of microtubules are thus processes that release energy. This energy stems from the GTP-hydrolysis and can be harnessed to do mechanical work. In addition to that, the GTP hydrolysis itself could also contribute to force generated by a microtubule. Forces due to polymerization and depolymerization can be transmitted to other structures by proteins that track filament ends. The efficiency of these end-tracking proteins in transmitting forces might also depend on GTP-hydrolysis (Dickinson et al., 2004).

The polymerization forces of microtubules *in vitro* have been measured directly (Dogterom and Yurke, 1997). The stall force for microtubule growth is at least 5 pN, comparable to the stall force of molecular motors, e.g. 8 pN for kinesin (Verkhovsky et al., 1999). The force-velocity curves of polymerizing microtubules depend on the concentration of free tubulin (Janson and Dogterom, 2004a). Pushing on growing microtubules *in vitro* increases the rate of catastrophes and slows growth (Janson et al., 2003).

These observations suggest a thermal or Brownian ratchet mechanism for MT force generation by polymerization (Peskin et al., 1993). If a filament grows against an applied force (cf. Fig. 2.15a) thermal fluctuations of the target will occasionally allow the addition of new subunits to the filament. The filament will thus grow despite the applied force. Increasing the force decreases the amplitude of the fluctuations and consequently the rate of addition of new subunits (Mogilner and Oster, 1999). The stall force is the force at which the rates of subunit addition and removal are exactly equal and no net growth takes place (van Doorn et al., 2000). An important extension of this model was the elastic Brownian ratchet (Mogilner and Oster, 1996), which also takes into account the fluctuations due to bending of the filament.

In terms of thermodynamics the observation that applied forces influence the polymerization dynamics can be understood as the presence of an external force F_ext modifies the on- and off rates by a Boltzmann factor $\exp(F_\mathrm{ext}a_1/k_BT)$ (Dogterom and Yurke, 1997; Kolomeisky and Fisher, 2001). Here $F_\mathrm{ext}a_1$ is the most probable work needed to add a subunit against the force F_ext and k_BT is the thermal energy. The length a_1 is a parameter which has to be determined experimentally. This give rise to a force dependent growth velocity, i.e. Eq. (2.7) becomes

$$v_g(F_\mathrm{ext}) = a\left(k_\mathrm{on}\exp\left(q\frac{F_\mathrm{ext}a_1}{k_BT}\right) - k_\mathrm{off}\exp\left((1-q)\frac{F_\mathrm{ext}a_1}{k_BT}\right)\right) \quad . \tag{2.9}$$

Here q is a parameter that characterizes the relative strength of influence of the external force on the on- and off-rate respectively. The stall force for which $v_g(F_\mathrm{s}) = 0$ is given by

$$F_\mathrm{s} = \frac{k_BT}{a_1}\ln\frac{k_\mathrm{on}}{k_\mathrm{off}} \tag{2.10}$$

and independent of q and a.

These results have also been obtained by applying a generalized version of this Brownian ratchet model to multi-filament microtubules (cf. Fig. 2.15b), which showed that the force

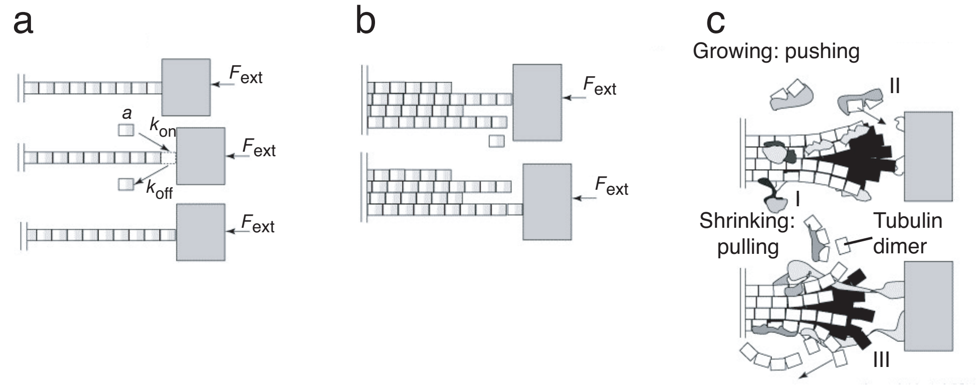

Figure 2.15: Force generation by polymerizing protein filaments.
(a) The Brownian ratchet model for a single filament. Thermal fluctuations of the target (gray box) allow the addition of subunits of length a with rates k_{on} even in the presence of an external force F_{ext}. Subunits detach with a constant rate k_{off}.
(b) Multi-filament polymers such as microtubules can be described by a generalized Brownian ratchet model. The example shows four protofilaments that grow independently.
(c) Schematic representation of the ends of real growing and shrinking microtubules. MT dynamics is regulated by end binding proteins that are present in the cell. This influences force generation as well as the interaction with cellular sites. A few processes are schematically displayed: (I) delivery of regulating factors by molecular motors (II) MT polymerization assisted by microtubule associated proteins (III) linking between the depolymerizing end of a MT and a target. Figure adapted from (Dogterom et al., 2005).

velocity relation (Kolomeisky and Fisher, 2001) but not the stall force (van Doorn et al., 2000) depends on the details of MT growth. When the microtubule growths regularly, i.e. each added subunit pushes the target a small, equal distance, the force generation is optimal, i.e. the velocity decrease per applied force is smallest. Irregular growth means that not every addition of a subunit performs work, then the growth velocity decreases faster with the force. Available data on growing MTs *in vitro* suggest that in the absence of microtubule associated proteins growth is not optimal (Janson and Dogterom, 2004b; Dogterom et al., 2002).

The disassembly of protein filaments can also generate forces and perform work (Lombillo et al., 1995). These forces are more difficult to determine *in vitro* because they can only be measured if a persistent link with the depolymerizing end can be established, see next section 2.4.3. At the moment no quantitative measurements are available (Dogterom et al., 2005).

2.4.3 Force Generation by End-Tracking Proteins

The action of the force generated by polymerization and depolymerization of filaments can be transmitted directly by pushing of polymerizing filament ends on an object, such as the cell membrane in a lamellipodium. As argued in the previous section, exerting pulling forces by depolymerizing ends is dependent on establishing a durable link between the filament end and the object. Links of this kind could be established by proteins that are attached to an object while simultaneously tracking filament ends.

Such proteins are present in cells and their action is not limited to the depolymerizing end. Experiments have also identified many proteins that seem to link objects to polymerizing ends: on the surface of *Listeria monocytogenes* for example ActA binds VASP which links it to actin filaments in the comet (Niebuhr et al., 1997). In many cellular structures, such as the contractile ring, formins are located at the plus ends of actin filaments, blocking capping proteins but allowing polymerization (Zigmond et al., 2003). In bacteria the polymerization of the actin-like protein ParM generates the mechanical force that drives separation of plasmids while being continuously attached to them. The situation in eucaryotic cells is similar: microtubules in the mitotic spindles whose plus ends are bound to kinetochores polymerize and exhibit poleward flux despite being attached firmly enough to push and drag chromosomes (Dewar et al., 2004; Kline-Smith et al., 2005).

Proteins involved in this kind of force transduction have to be located at filament ends. These end-tracking proteins can generate forces using three different ways of converting energy. They may passively follow the filament end or harness the energy freed by triphosphate hydrolysis in the filament or themselves hydrolyze chemical fuel to exert forces. Molecular motors are an example for this last class. If end-tracking proteins follow the end passively, i.e. without converting energy themselves in order to exert forces or advance on the filament, the force they transmit is based on the free energy of subunit addition or loss, $\Delta G^{+}_{\text{add}}$ and $\Delta G^{-}_{\text{loss}}$ respectively. The third type are proteins that do not themselves hydrolyze nucleotide tri-phosphate (NTP) but harness the free energy released by NTP hydrolysis in the filament. A detailed estimate of the free energy steps in a treadmilling cycle reveals that for actin the largest energy decrease is the hydrolysis of ATP which frees about $14\,k_BT$, while energy changes due to addition and removal of monomers are clearly smaller with $\Delta G^{+}_{\text{add}} \simeq 1-2\,k_BT$ and $\Delta G^{-}_{\text{loss}} \simeq 6\,k_BT$ (Dickinson et al., 2004). These three steps account for the lion's share of the $\sim 20\,k_BT$ freed per hydrolysis cycle. Given these circumstances it comes as no surprise that this second kind of end-tracking proteins that harness energy from NTP hydrolysis in the filament can be more efficient in transmitting forces (Dickinson et al., 2004).

Molecular motors which themselves hydrolyze NTPs and convert chemical energy into mechanical force, can also serve as end-tracking proteins. A plus end directed motor that advances with a velocity greater than the polymerization velocity for example will eventually reach the filament's plus end. If the motor does not fall off, it will always advance when new subunits are added and thus track the plus end. An example is the motor Eg5 which is able to stay attached to filament ends (Kapitein et al., 2005).

2.5 Cytoskeletal Structures

In this section we introduce four structures of the cytoskeleton that are central to this thesis. They are crucial for two important cellular processes: cell division and locomotion. Three of the structures are involved in cell division: the mitotic spindle, the contractile ring and the pre-prophase band in plant cells. The fourth structure, stress fibers, is involved in cell locomotion.

After the DNA of a cell has been duplicated, it is separated and distributed to the new nuclei by the **mitotic spindle**. Spindles also are responsible for separating DNA during meiosis in order to create haploid[1] cells. We start by introducing these bipolar microtubule structures first. Then we present the **contractile ring**, a band of actin, myosin and many other proteins which constricts and cleaves most eucaryotic cells during cytokinesis. Cytokinesis is the mechanical separation of a cell into two daughter cells. It occurs through a series of stereotypical shape changes (Rappaport, 1996). Initially cells round up and then elongate due to major rearrangements of the cytoskeleton. Consecutively the cleavage

---

[1] Cells that contain only one set of chromosomes, as in a sperm cell or a bacterium. Distinct from diploid cells (having two sets of chromosomes).

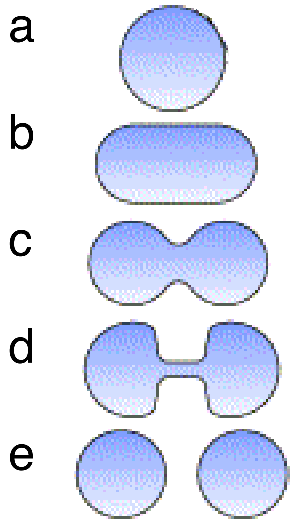

adapted from Current Opinion in Cell Biology

Figure 2.16: Morphological changes during cytokinesis in animal cells. (a) The cell is rounded up. (b) The cell elongates into a cylindrical shape. (c) The cleavage furrow starts to invaginate the cell cortex. (d) The cell has taken on a dumb-bell shape, with a discrete midbody connecting the two daughter cells to be. (e) The bridge is severed and two daughter cells are produced. Modified from (Robinson and Spudich, 2004).

furrow constricts, often driven by a contractile ring, until the midbody, a cylindrical bridge forms between the two cell domains. This bridge thins and severs, the separation of the two daughter cells is complete. Mechanical aspects of cytokinesis are extensively studied experimentally and theoretically (Reichl et al., 2005; Robinson and Spudich, 2004) and theories how cytokinesis works mechanically are plentiful[2].

While cell cleavage by a contractile ring is the dominant mechanism of cytokinesis in many cells (Fig. 2.17b-d), plant cells divide differently, Fig. 2.17a. Plant cells possess a hard outer wall and do not divide by cell cleavage but by forming first a so called or phragmoplast and then the cell plate between the two daughter nuclei, see e.g. (Guertin et al., 2002; Jurgens, 2005) for recent reviews. They do however also exhibit a ring like structure that determines the site of cell division prior to prophase, the so called **pre-prophase band** (PPB) consisting mainly of aligned microtubules. The PPB marks the future division site, the phragmoplast seems to always form in the plane of the PPB.

Like the contractile ring, **stress fibers** are linear contractile structures of actin and myosin. They are important for cell locomotion, as they participate in cell body retraction by coupling to the substrate via adhesions. We compare them to **muscle myofibrils** that are responsible for muscle contraction and also are linear structures based on actin an myosin motors.

---

[2] "Usually, it is easier to invent a new theory of cell division than to test an old one.", L.V. Heilbrunn, The Colloid Chemistry of Protoplasm (p. 256).

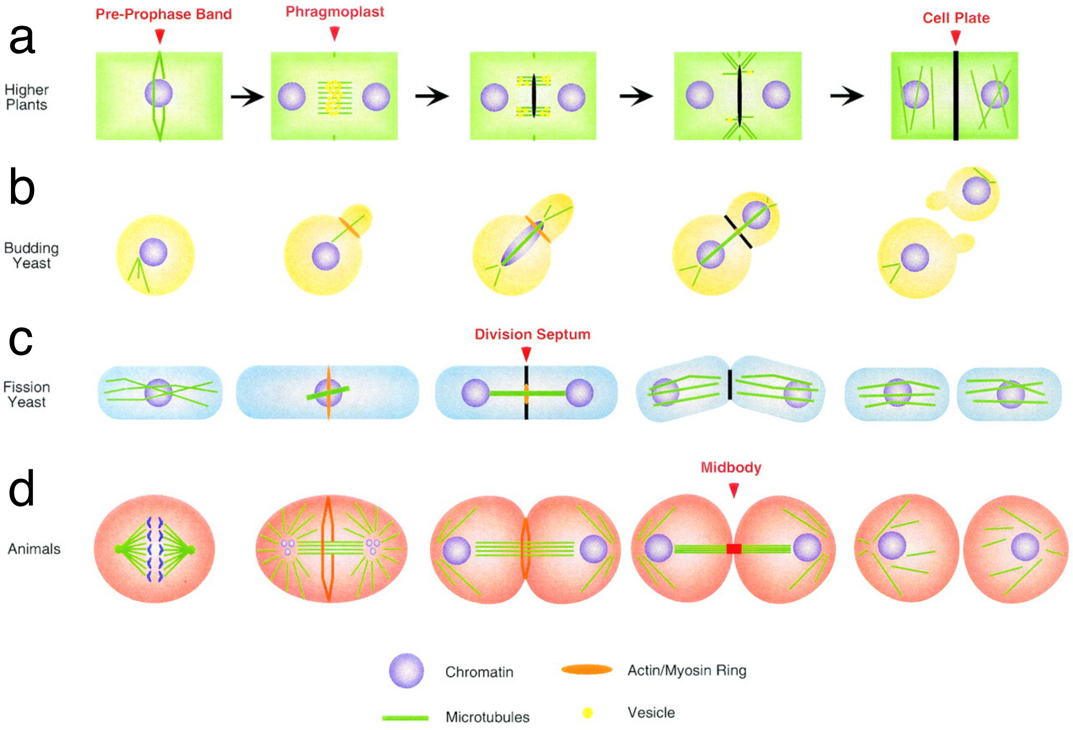
a
Higher Plants
Pre-Prophase Band
Phragmoplast
Cell Plate
b
Budding Yeast
c
Fission Yeast
Division Septum
d
Animals
Midbody
Chromatin
Actin/Myosin Ring
Microtubules
Vesicle

Figure 2.17: General mechanisms of cytokinesis in eukaryotes. While the process of cytokinesis results in the physical partition of a mother cell into two daughter cells, the approach to cell division differs between several model organisms. (a) Higher plants mark the division site by a pre-prophase band, a ring of microtubules around the equator of the cell. After separating the nuclei, they use microtubules to deliver Golgi-derived vesicles to the equatorial region. Vesicles fuse to form the phragmoplast, which, through continued vesicle fusion, grows outward to the cell cortex, ultimately building a physical barrier between daughter cells called the cell plate. (b and c) Yeast and animal cells, unlike plant cells, divide through use of an actomyosin-based contractile ring. (b) In budding yeast cells, the ring is positioned at the interface between the mother cell and daughter bud, termed the bud neck. (c) In fission yeast and animal cells, the contractile ring is centrally placed, as both cell types divide by medial fission. Both budding and fission yeasts synthesize a division septum behind the leading edge of the constricting ring, which is eventually degraded, resulting in physical cell separation. (d) In animals, the ingressing furrow constricts the spindle midzone components into a dense structure called the midbody. Taken from (Guertin et al., 2002).

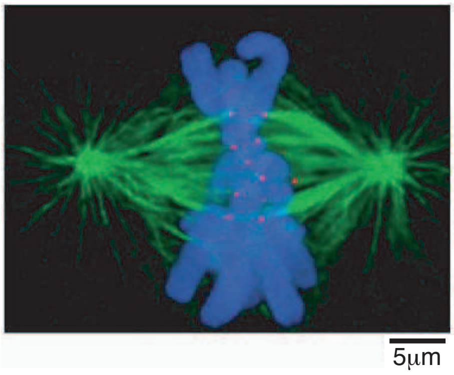

Figure 2.18: Mitotic spindle in a vertebrate cell during metaphase. Microtubules are labeled in green, kinetochores in red, and chromosomes in blue. Taken from (Desai, 2000).

2.5.1 Mitotic and Meiotic Spindles

Prior to cytokinesis, i.e. the division of the cytoplasm of the cell, each nascent daughter cell needs to be equipped with one of the two identical sets of chromosomes. The cell's DNA thus has to be duplicated and then distributed to the two newly formed nuclei. In all eucaryotic cells this distribution is achieved by a bipolar spindle during mitosis. Spindles are composed of microtubules and various other proteins such as molecular motors, kinases that interact with them and hundreds of other MAPs (Maiato et al., 2004). The typical spindle is formed by two microtubule asters that become the spindle poles. These asters are linked to the chromosomes via kinetochores, Fig. 2.18. Microtubules of both asters also reach out into the cytoplasm and can make contact with MTs from the other aster as well as the cell walls. Microtubules then shorten and spindle poles move away from the center thus separating the chromosomes. Spindles are also involved in meiosis, i.e. the cell division in which haploid sperm cells and eggs are produced. In this case they are referred to as meiotic spindles.

The typical life cycle of a spindle is depicted in Fig. 2.19. Spindles generally start to form outside the nuclear membrane during prophase while the chromosomes condense. The centrosomes are duplicated and then separate. They start nucleating microtubules, forming the nascent poles of the future spindle. After nuclear envelope breakdown at prometaphase these microtubules can capture the condensed chromosomes. The chromosomes become aligned between the poles in the metaphase plate perpendicular to the spindle axis. During anaphase-A the chromosomes separate and move towards opposite spindle poles. Anaphase-B marks the further separation of the spindle poles from each other. In mammalian cells, the spindle elongates up to 2-fold during anaphase. In some plant cells however, spindle length hardly changes at all while some protozoa represent the other extreme: here the chromosomes become separated 15 times their distance in the metaphase spindle (Bray, 2001).

Spindle Structure

The spindle microtubules (several thousands in mammalian cells) can be grouped into three classes depending on their properties: astral microtubules radiate from the spindle pole in all directions and are involved in force transmission between the pole and the cell membrane (Grill et al., 2003, 2001). These forces are responsible for spindle positioning and orientation (Grill and Hyman, 2005), spindle pole separation and spindle oscillations (Grill

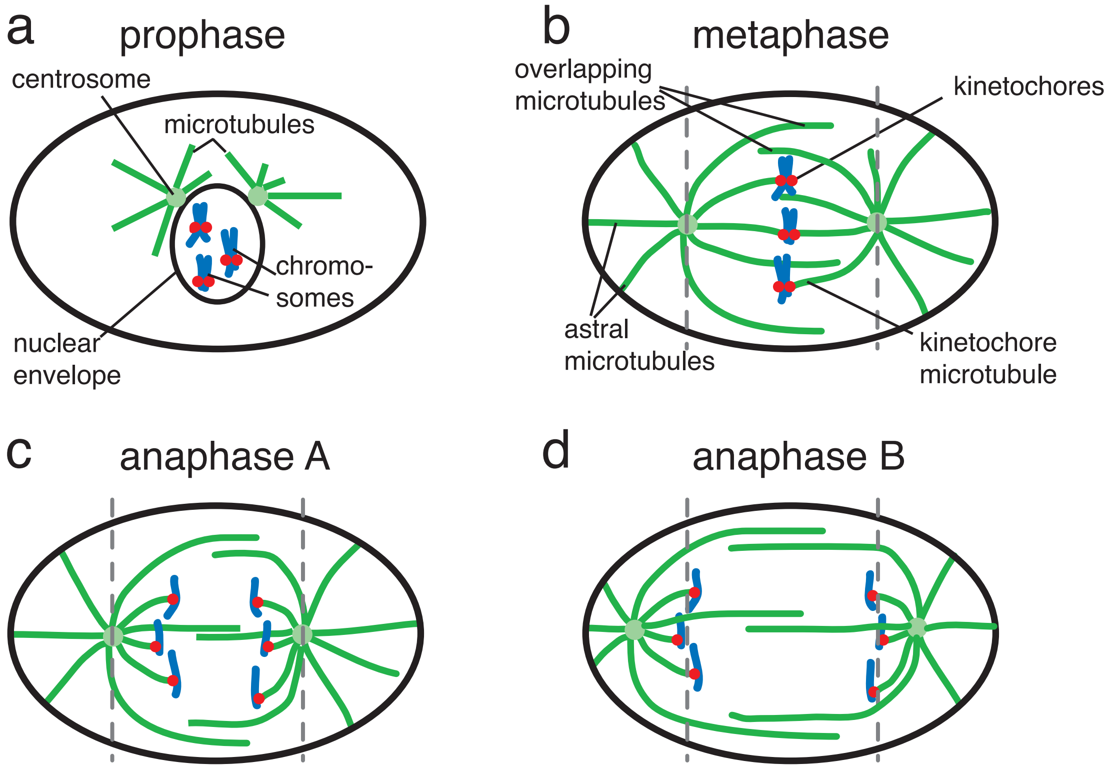

Figure 2.19: Schematic formation and dynamics of the mitotic spindle. (a) During prophase the centrosomes separate outside the nuclear envelope and start nucleating microtubule asters. (b) In metaphase the nuclear envelope has dissolved. Microtubules attach to the kinetochores on the chromosomes and align them in the metaphase plate. Dashed lines mark the horizontal position of spindle asters during metaphase. (c) The kinetochore microtubules shorten during anaphase A and separate the sister chromatids. The distance between the spindle poles remains constant. (d) During anaphase B the spindle elongates, further separating chromosomes and spindle poles.

et al., 2005). Kinetochore microtubules link the spindle poles to the kinetochores, a region on the centromeres of the duplicated chromosomes. Each kinetochore links several tens of microtubules that form a kinetochore bundle. Overlap microtubules from both poles interdigitate and are responsible for spindle bipolarity and structure. All these microtubules have their minus ends at the centrosomes and their plus ends pointing away from the pole.

During metaphase the microtubules are a lot more dynamic than during interphase. At the same time the centrosomes appear to nucleate more microtubules, so that overall fewer, long, and rather stable microtubules during interphase change into more, shorter and highly dynamic microtubules during metaphase. This change can be due to an increase in the frequency of catastrophes, a decrease in the microtubule polymerization rate, or both. The increase in the catastrophe frequency can be mediated by a class of proteins called catastrophins. On the other hand microtubule-associated proteins (MAPs) can stabilize microtubules. In *Xenopus* egg extract the catastrophe rate and the average length of microtubules is set by the balance between the catastrophin XKCM1 and XMAP215 (Tournebize et al., 2000).

Yet another balance, i.e. **the balance between plus end directed kinesins and minus end directed dyneins, is important for spindle formation and length,**

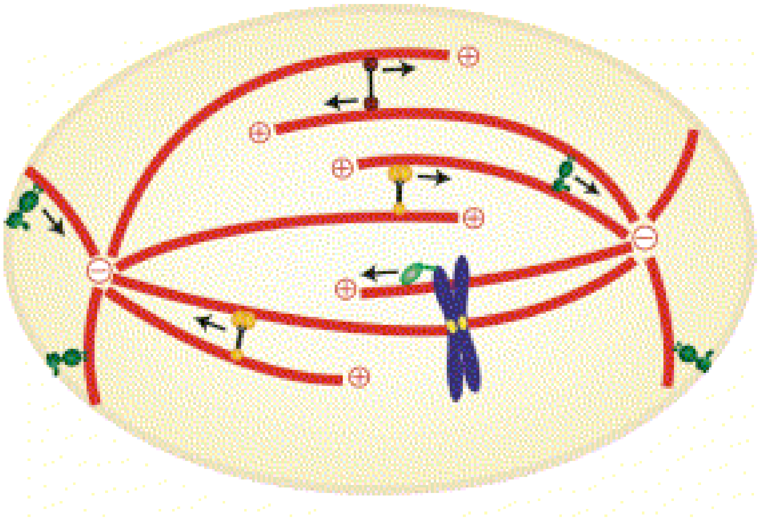

Figure 2.20: Motor balance determines spindle pole separation. Microtubules orient their minus ends at the spindle poles with the plus ends radiating out. Plus-end directed cross-linking motors (red) increase and minus end directed motors (yellow) decrease spindle pole distance. Chromokinesins (light green) can link chromosomes to microtubules and move them towrards the plus end. Cytoplasmic dynein (dark green) in the cortex can pull on astral microtubules or focus microtubule minus-ends into poles. Figure modified from (Gadde and Heald, 2004).

Fig. 2.20. Because microtubules point their plus ends away from the poles, overlap microtubules have opposite polarity. Plus end directed motors that link MTs such as kinesin dimers (or polymers, of course) bound to a pair of overlap microtubules work to align the plus ends of both MTs and thus push the spindle poles apart, leading to spindle elongation (Hyman and Karsenti, 1996). Minus-end directed cross-linking motors (e.g dyneins) can balance this movement by pushing the poles towards the middle. Dyneins can also be involved in pole formation, e.g. when a spindle forms in the absence of centrosomes, see below.

Motor types are abundant in the spindle. At least seven members of the kinesin familiy have been localized in the spindle. A recent RNAi scan in *Drosophila* yielded nine motors with mitotic functions (Goshima and Vale, 2003). The function of related motors in several systems seem to be remarkably conserved. Here we discuss some examples for motor action in the spindle demonstrated in experiments.

In budding yeast, overexpression of the minus end directed motor Kar3p leads to shorter, overexpression of Cin8p, a plus-end directed motor, to longer spindles (Saunders et al., 1997). In cell free *Xenopus* egg extracts the inhibition of dynein/dynactin has been shown to increase spindle lengths, Fig 2.21 (Gaetz and Kapoor, 2004). This treatment suppresses MT depolymerization at the poles while pole-ward flux persists. Dynein is found to be involved in targeting Kif2a, a MT depolymerizing kinesin, to the poles but does not interfere with the localization of MCAK. In the same system it has been shown that inhibition of MCAK perturbs the pole structure but does not lead to longer spindles (Mitchison et al., 2005). Cytoplasmic dynein/dynactin complexes on the cell cortex can orient the spindle when bound to astral MTs and plus-end directed kinesins at the kinetochores held chromosome movement towards the metaphase plate (Gadde and Heald, 2004). Another important class of motors in the spindle is the BimC/Eg5-familiy (tetrameric, plus end directed kinesins), which is involved in spindle pole separation and spindle bipolarity. It

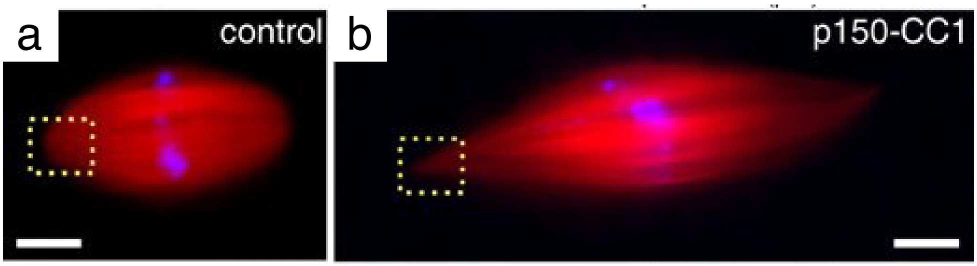

Figure 2.21: Inhibition of dynein/dynactin increases spindle length in *Xenopus* egg extract. Spindles fixed 8 min after addition of control buffer (a) or p150-CC1, a dynein/dynactin inhibitor. Scale bars 10 μm. Figure from (Gaetz and Kapoor, 2004).

has been found that dynein/dynactin and Eg5 play antagonistic roles in spindle formation (Mitchison et al., 2005). Inhibition of dynactin leads to spindles without focussed poles. Additional inhibition of Eg5 rescues bipolarity.

Spindle Formation

Various mechanisms have been proposed for spindle formation. The main difference between them concerns spindle microtubule nucleation: MTs can be nucleated by the centrosomes or by the chromosomes. It has been found however that higher eucaryotes require MTs nucleated at the chromosomes in order to form fully functional bipolar spindles (Karsenti and Nédélec, 2004), while lower eucaryotes such as yeast can form fully functional spindles with MTs only nucleated from centrosomes. Both mechanisms thus seem to be at work simultaneously in most cases.

Microtubules nucleated and grown from the centrosomes are highly dynamic and undergo catastrophes and rescue events probing the cytoplasm. They seem to "search" for the kinetochores of the chromosomes. When they are "captured" by these, they seem to become stabilized. This mechanism is often referred to as the **"search and capture"** mechanism, Fig 2.22a. The attachment of microtubules to kinetochores is a dynamic process (Kline-Smith et al., 2005). Kinetochores are often observed to bind to the side of MTs and then slide to the plus end. This kind of transport is probably mediated by plus-end directed kinesins. The search and capture goes on until all kinetochores are attached to MTs so that sister chromatids are attached to one pole each and chromosomes are bi-oriented. The chromosomes then oscillate back and forth along the spindle axis, eventually forming a metaphase plate in the middle between the spindle poles.

Spindles can also form in the absence of kinetochores or even chromosomes, Fig 2.22b. In *Xenopus* egg extract spindle formation can be induced by adding DNA-coated beads (Heald et al., 1996). Sometimes spindles can even form in the complete absence of chromosomes. Some mutants of *Drosophila* form secondary spermatocytes that completely lack chromosomes. These cells do however contain robust asters, form bipolar spindles and even undergo a morphologically normal-looking anaphase (Bucciarelli et al., 2003).

Spindles have also been observed to form **in the absence of centrosomes**, e.g. in female meiosis, where microtubules polymerize in a disorganized way without common focal nucleation sites. The subsequent formation of spindle poles depends on molecular motors. Similar spindles form in cells in which the centrosomes have been ablated using a laser (Khodjakov et al., 2000). Spindles without centrosomes are however more often misoriented, probably due to loss of astral microtubules, which can decrease fidelity of

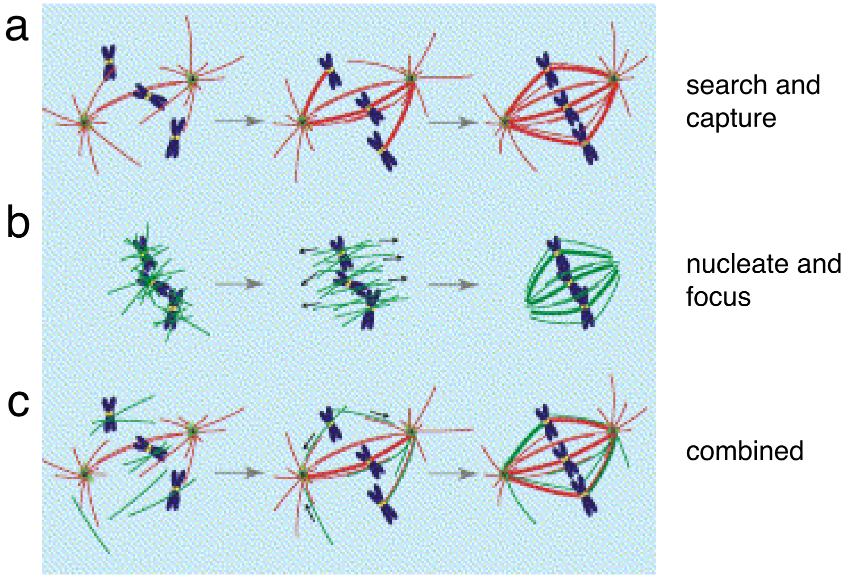

Figure 2.22: Different pathways of spindle assembly. (a) "Search and capture" model: microtubules nucleate from the centrosomes and capture chromosomes at their kinetochores by chance. Chromosomes stabilize the microtubules upon attachment and by a gradient of stabilizing factors. (b) "Nucleate and focus" model: chromosomes nucleate randomly oriented microtubules which are organized into a bipolar spindle by molecular motors. (c) Combined action of both pathways. Microtubules are labeled in red when nucleated at centrosomes, in green when nucleated at chromosomes. Figure modified from (Gadde and Heald, 2004).

cytokinesis. This pathway has been named "Self organization" in distinction to the "search and capture" pathway. Self-organization phenomena in a physical sense (i.e. out-of-equilibrium organization in which a system continuously dissipates energy, cf. (Nédélec et al., 2003)) are certainly at work in both ways of spindle formation. We call this second pathway of spindle formation **"nucleate and focus"**, as microtubules are nucleated by the chromosomes and then focused into two spindle poles by molecular motors. It is an interesting observation that a bundle of microtubules nucleated from chromosomes will almost always evolve towards a bipolar structure since MTs in the bundle generally have two orientations and thus are pushed into exactly two directions when molecular motors are at work (Karsenti and Nédélec, 2004).

These observations suggest multiple simultaneous mechanisms for bipolar spindle formation in living cells. Studies of the distribution of MT plus ends in cells during the transition from prophase to prometaphase suggest that MTs are nucleated all around the nucleus and not only at the centrosomes (Piehl and Cassimeris, 2003). They are stabilized in the vicinity of the nucleus in a dynein dependent way. At prometaphase the spindle is dense with growing MT tips. Similar nucleation and plus end patterns have been observed in plant cells (Chan et al., 2005), where the pre-prophase band was clearly shown to be involved in determining spindle orientation. Besides stabilization of MTs, microtubule motors are responsible for the generation of many of the forces involved in spindle generation. A prominent example is cytoplasmic dynein, which is present at many sites of the mitotic spindle (Karki and Holzbaur, 1999). It is e.g. responsible for microtubule focussing in *Xenopus* egg extracts. When dynein is blocked, the poles splay apart - even in the presence of centrosomes (Heald et al., 1997). These observations suggest that the action of molecular motors, that cross-link microtubules and move them depending on their polarity, is essential for proper spindle bi-polarity and function (Heald and Walczak, 1999).

As bipolarity is a crucial feature of mitotic spindles, it is elucidating to study **bipolar assemblies made of microtubule asters**. There are at least three different pathways for aster formation (Nédélec et al., 2003). The first is nucleation as e.g. performed by centrosomes. The second is bundling and aster formation of microtubules under motor action such as observed in spindles formed in the absence of centrosomes in the presence of dynein. Another pathway was observed in fish melanophores (Rodionov and Borisy, 1997b). In these cells pigment granules seem to nucleate MTs. These granules are coated with dynein and are thus transported to the MT minus end. The microtubules are not moved (Vorobjev et al., 2001) but the nucleators are. It has been shown in in vitro experiments that mixtures of motors and microtubules can produce asters by self-organization (Surrey et al., 2001). The dynamics of aster formation have also been studied in computer simulations (Surrey et al., 2001; Cytrynbaum et al., 2004). Furthermore it has been shown experimentally (Piel and Bornens, 2001; Faruki et al., 2002; Zhang and Nicklas, 1995) and in numerical simulations (Nédélec, 2002a,b) that the interaction of microtubule asters (usually nucleated from centrosomes) in the absence of chromosomes can lead to stable bipolar structures.

Spindle Dynamics

The microtubules in the metaphase spindle are highly dynamic. All MTs except the kinetochore MTs undergo dynamic instability. Speckle microscopy has revealed that kinetochore and overlap microtubules exhibit poleward flux of tubulin (Mitchison, 1989; Mitchison and Salmon, 2001), i.e. these microtubules continuously treadmill so that individual monomers in the filament move towards the spindle pole. Typical flux velocities are around $2\,\mu$m/min (Waterman-Storer et al., 1998). The attachment of microtubules to the kinetochores thus has to be dynamic, allowing at least the polymerization of microtubules. At the same time microtubules in the spindle are under tension as shown by laser ablation experiments (Gonczy et al., 2001). Recently many molecular mechanisms involved in kinetochore capture, transport and attachment have been reveiled (Tanaka et al., 2005). Kinetochores are also known to depolymerize MTs, e.g. by means of mitotic centromere-associated kinesin (MCAK) (Wordeman and Mitchison, 1995; Moore and Wordeman, 2004; Wordeman, 2005). The active depolymerization of microtubules at the kinetochores as well as the pole-ward flux contribute to chromosome segregation and spindle shortening (Rogers et al., 2004; Gadde and Heald, 2004).

The dynamics of the spindle microtubules are influenced by many molecular factors and MAPs, such as katanin, which severs MTs, KinI and Op18 (stathmin) that depolymerize MTs and sequester tubulin dimers (Andersen, 2000), γ-TURCs that promote nucleation at the centrosomes and many others (Maiato et al., 2004; Gadde and Heald, 2004). A particularly interesting class in this context are the end-located groups of cytoplasmic linker proteins (CLIPs) that promote MT growth and regulate dynein localization as well as CLIP associated proteins (CLASPs) that can stabilize microtubules (Galjart, 2005). The abundance of factors that are often believed to have very similar influence suggests that the spatial control of these factors within the cell is key to understanding the process of spindle formation and dynamics.

Many properties of spindles have been analyzed and characterized, many open questions remain. A spindle matrix, i.e. a scaffold not made of MTs for example has been suggested but its existence is not clear. Studies in *Drosophila* for example have identified a protein named Skeletor that forms a spindle-shaped structure prior to the microtubule spindle (Walker et al., 2000). Imaging of Eg5 in spindles in Xenopus extract has shown that Eg5 is stationary with respect to MTs that undergo pole-ward flux (Kapoor and Mitchison, 2001). This hints towards the existence of a spindle matrix also in this system.

Furthermore an amusing parallel has been drawn between the dynamics of the mitotic spindle and a treadmilling actin gel in cell motility (Karsenti and Nédélec, 2004). The actin comet polymerized by *Listeria* could be compared with microtubules nucleated from chromosomes in a mitotic spindle. The chromatin thus corresponds to the bacterium. Like the actin comet the microtubules treadmill away from the chromosomes as indicated by pole-ward flux. This can exert forces on the chromosomes either directly or by action of plus end directed molecular motors such as kinesin. The most striking difference between the two systems is their symmetry. While symmetry breaking and formation of a monopolar structure in actin gels is essential for motility, the spindle is only functional when it assumes a bipolar configuration.

2.5.2 The Contractile Ring

Once chromosome separation and distribution onto the two future daughter cells is completed, most eucaryotic cells (the exception being higher plant cells as discussed in section 2.5.3 below) divide their cytoplasm by constriction of a contractile actomyosin bundle. This ring is often located at the cell's equator. In many cases such as the fission yeast *S. pombe* (Pelham and Chang, 2002; Wu et al., 2003), *Arbacia* eggs (Schroeder, 1972), human HeLa cells (Schroeder, 1970; Maupin and Pollard, 1986) and many more, the bundle forms a contractile ring which encircles the cell, see Fig. 2.23. There is experimental evidence that the location of the ring is dependent on microtubule structures (Pardo and Nurse, 2003; Glotzer, 2004) that in turn depend on the actin ring (Murthy and Wadsworth, 2005). In chapter 5 we show that self-organization phenomena can also be sufficient for ring formation and positioning.

Electron microscopy suggested that contractile rings consist of many filaments (Schroeder, 1970). These filaments can be arranged in several distinct, closely packed filament bundles, close to each other near the cell membrane (Maupin and Pollard, 1986). The filaments were found to be actin (Schroeder, 1970, 1973) and myosin (Fujiwara and Pollard, 1976; Otto and Schroeder, 1990). These findings provided further arguments for a muscle like, sliding filament contraction mechanism of the cleavage furrow. The structure of the cleavage furrow could support this theory (Sanger and Sanger, 1980), but uncontroversial evidence for structure and mechanism are still lacking (Schroeder, 1990). The orientation of actin filaments in the ring has been studied (Fishkind and Wang, 1993) during metaphase and anaphase. During metaphase the filaments have a slight orientation along the spindle axis, while during anaphase the filaments in the furrow become oriented along the equator. The degree of orientation seems to be largest in regions where the cell adheres to a substrate or other cells.

Besides actin and myosin the ring contains many other proteins (Robinson and Spudich, 2000; Feierbach and Chang, 2001). Prior to ring formation actin and a large number of associated proteins are recruited to an equatorial domain of the cell cortex (Wu et al., 2003; Glotzer, 2005), seemingly in a precisely timed sequence. These proteins include myosin motor proteins and tropomyosin that is highly concentrated in muscles and stabilizes F-actin. These proteins could play a role for the generation of contractile forces, bundling proteins and cross-linkers such as alpha-actinin. Proteins can also be responsible for the link between actin filaments in the ring and the cell's plasma membrane (Satterwhite and Pollard, 1992). Furthermore, several proteins are recruited that regulate the nucleation, polymerization and depolymerization of actin filaments (cf. section 2.2.3). These include

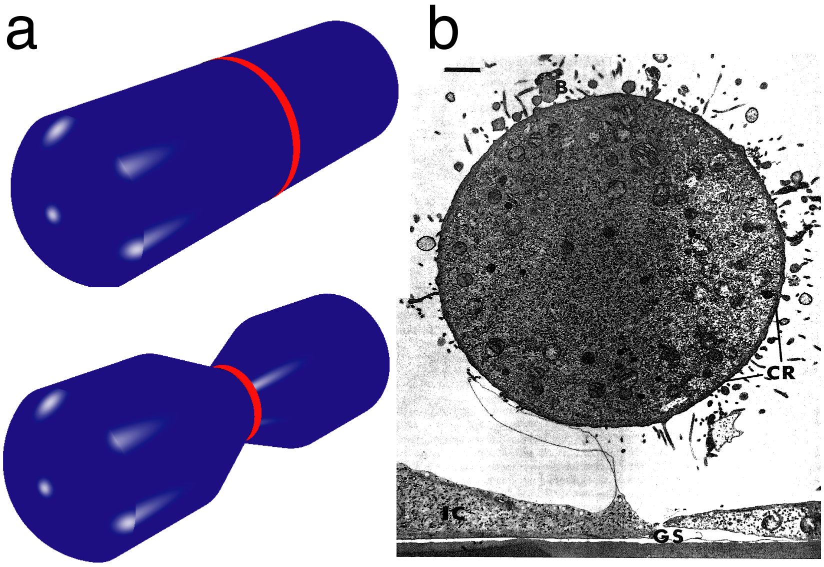

Figure 2.23: (a) Schematic representation of a contractile ring at the equator of an elongated cell. The ring is formed beneath the cell membrane and constricts the cell when contracting. (b) Electron micrograph of a section through the contractile ring of a dividing HeLa cell. CR marks the contractile ring, GS the growth surface, B blebs, and IC a neighboring interphase cell. This is the first published illustration showing the annular continuity of the contractile ring around an entire cell circumference. Scale bar 1 μm. Taken from (Schroeder, 1970).

capping proteins, that stabilize polymerizing ends, formins which nucleate and polymerize actin filaments, Arp2/3 that nucleates filament branches, and ADF/cofilin which accelerates depolymerization. This ring assembly is directed by the RhoA GTPase that induces actin nucleation and activates myosin. The concerted action of these proteins leads to the formation of actin bundles in the mature contractile ring. At the end of mitosis, the mature ring begins to contract, in response to a cellular signal. The precise nature of this signal is still unclear but a lot of progress has been made in recent years uncovering key players in ring assembly and constriction (Wolfe and Gould, 2005).

The concept as well as the terminology of the "contractile ring" was first formulated by Marsland in his contractile gel theory of cell furrowing (Marsland and Landau J.V., 1954; Marsland, 1970). It was further developed by Wolpert (1960). This theory was successful in accounting for many experimental observations regarding contractility during cytokinesis, but based on the language of "sol-gel transitions"[3] it did not specify concrete structures of the cleavage furrow. Inspired by the mechanics of muscle cells, similar sarcomer-like mechanisms based on the filament sliding hypothesis were proposed to apply to the contractile ring (Schroeder, 1990); see also (Schroeder, 1975) for a detailed discussion of prerequisites for this hypothesis. This "standard model" of cell division that developed subsequently has been investigated using more rigorous physical descriptions and considering chemical reactions as well as the different properties of the solvent and a network phase of cytoskeletal filaments (He and Dembo, 1997). Recently Zhang and Robinson (2005) proposed a physical theory to explain the characteristic cell shapes observed in cytokinesis, based on active stresses and passive elements, such as the Laplace pressure. Furthermore, Biron et al. (2005) investigated the influence of actin polymerization and depolymerization for the dynamics. They suggest that the actin concentration within the ring and thus the power the ring exerts both increase during contraction.

---

[3] The transition of a substance from a liquid (sol) to an apparently solid, jelly-like phase (gel).

In this thesis we focus on the physical properties and mechanics of the contractile ring. We aim at analyzing key mechanisms involved in ring contraction. Although the contractile ring occurs in cells that are very different in character such as protozoa, squid eggs or tissue culture cells, many ultrastructural features are very similar, even when the surrounding circumstances vary (Schroeder, 1975). And although details of ring formation differ even between budding yeast *S. cerevisiae* and fission yeast *S. pombe*, many aspects are similar all the way from yeast to animal cells (Balasubramanian et al., 2004). While the radius varies according to cell size, a "typical" contractile ring is a band about 5-10 μm wide (extreme cases beeing 20 μm in large amphibean eggs and 3 μm in tiny algal cells) and 0.1-0.2 μm thick, see Fig. 2.24. It thus resembles a sheet (or a band) of microfilaments wrapped around the cell's equator. The microfilaments are 5 nm thick, spaced ca 15 nm apart. In a cross section there are about 5000 of them (Schroeder, 1990). The thickness, width and microfilament spacing are constant during ring contraction (Schroeder, 1972). The ring has been measured to exert a force on the order of 10 nN (Schroeder, 1975; Rappaport, 1967; Burton and Taylor, 1997), but these measurements only provide an upper bound of the force generation and not necessarily the force employed during ring constriction. The contraction velocity depends on the cell type: the ring constricts with a velocity $\simeq 0.07\,\mu$m/min in fission yeast (Pelham and Chang, 2002) and $\simeq 0.6\,\mu$m/min in Swiss 3T3 fibroblasts (DeBiasio et al., 1996).

How exactly the ring constricts is still a mystery (Alberts et al., 2002). It seems not to operate by a simple "purse-string" mechanism in which the actomyosin ring simply constricts by filament sliding due to myosin II motors such as in muscles. Electron micrographs of meridional cross-sections through the ring show that the area of the cross-section is conserved during ring constriction (Schroeder, 1972). As the density of material in the ring does not change, this implicates that the ring looses material while constricting. The ring thus appears as a dynamic structure that is not only assembled prior to and disassembled after use, but also constantly reorganized while cleaving the cell. It has been shown that an actin gel solates or disassembles if a pressure is applied to it (Condeelis and Taylor, 1977). The tension generated by the ring itself could thus be a cause for partial ring disassembly, similar to mechanisms proposed for the cell cortex (Paluch et al., 2005; Paluch, 2005).

In chapter 6 we study a mechanism for ring contraction that besides the action of molecular motors also can be driven by filament polymerization and depolymerization. The dynamics of the constituents of the ring, especially the turnover of actin, could thus be directly contributing to ring contraction. Here we present some experimental results concerning ring dynamics. The view of the contractile ring as a highly dynamic structure has been strengthened by investigation of ring dynamics in fission yeast cells (Pelham and Chang, 2002). The formation of the ring depends on actin asssembly either from preexisting actin cables or de novo nucleation and polymerization. This polymerization depends on Arp2/3, formin, profilin or WASp, but not myosin II. It was shown that Arp3 colocalizes with actin in an equatorial ring, Fig. 2.25. During the time course of ring contraction ($\sim$ 25 min for wild type *S. pombe*), many components of the ring (such ase tropomyosin or a myosin light chain) are exchanged with a half time of usually less than one minute. F-actin in particular is completely turned over about every minute. Similar rates have been measured in LLCPK1 epithelial cells (Murthy and Wadsworth, 2005). In normal rat kidney cells the turnover time of actin in the equatorial region was doubled to about 30 s after cells had been exposed to blebbistatin, a myosin II inhibitor (Guha et al.,

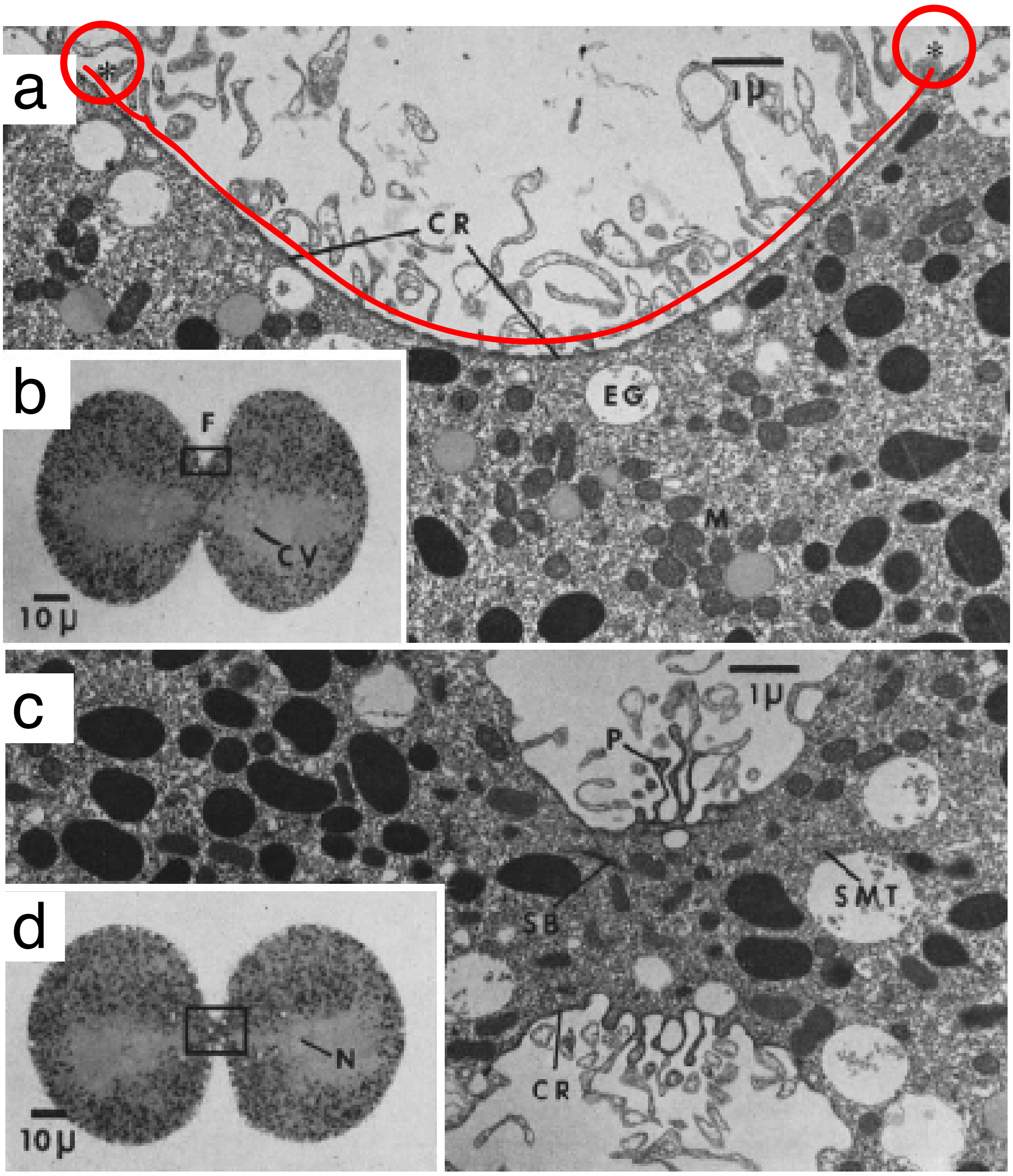

Figure 2.24: Section through a contractile ring or arbaccia eggs at two different times during cytokinesis. (a) Detail (×9500) of a ring about 4 min after onset of cleavage. The contractile ring spans the concave surface between the asterisks (marked in red). The ring prevents cytoplasmic particles, yolk, mitochondria (M) and echinochrome granules (EG) from coming into direct contact with the plasma membrane. (b) Section through entire cell (×490). Clusters of chromosomal vesicles (CV) characterize the reforming nuclei at this stage. The cleavage furrow (F) is clearly visible. The box indicates the location of the detail shown in (a) (not the same specimen). (c) Section about 5 min after cleavage (×9500). The contractile ring is about to disappear. Complex protrusions (P) occur at this stage. Stem bodies (SB) and a few spindle microtubules (SMT) are remnants of the mitotic apparatus. (d) Full cell at same time as in (c). Daughter nuclei (N) are now completely reformed. Figures modified from (Schroeder, 1972).

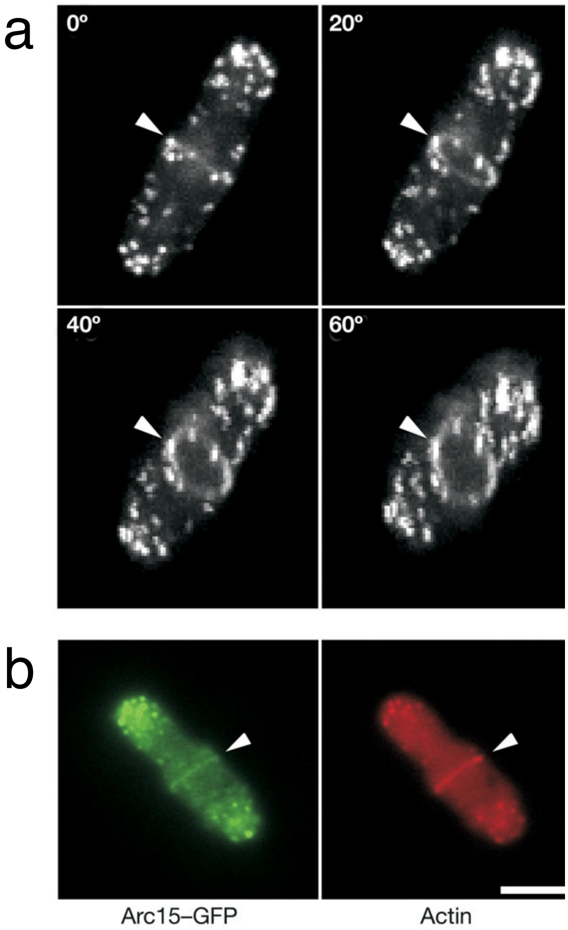

Figure 2.25: The contractile ring in a fission yeast cell *S. pombe*. (a) Three-dimensional confocal images of a contractile ring (arrow head, visualized by Arc15-GFP, a component of the Arp2/3 complex that localizes to the contractile ring) (b) Cell expressing Arc15-GFP (green) stained for F-actin with rhodamine phalloidin (red). Scale bar 5 μm. Taken from (Pelham and Chang, 2002).

2005). The motor myosin II thus seems to be involved in actin turnover in the ring. Ring assembly on the other hand did not seem to be affected by this treatment. In all cases, the site of the ring remains an active site of actin assembly even after initial ring formation. The rate of actin polymerization can furthermore influence the contraction velocity of the ring (Pelham and Chang, 2002; Wu et al., 2003). When actin polymerization is attenuated the ring still closes but the velocities are significantly reduced, see Fig 2.26. Polymerization is inhibited (i) by adding the drug Latrunculin A (ii) in $wsp1\Delta$ mutants, that lack WASp, or (iii) in $cdc12-112$ mutants, i.e. cells with a temperature sensitive formin activity.

Some cells can divide without motors.

Although contractile rings are found in most eucaryotic cells, some cells are able to divide without myosin II (Gerisch and Weber, 2000). Besides *Dictyostelium* this has also been observed in budding yeast *Saccharomyces cerevisiae* (Bi et al., 1998). In both cases division is less efficient and depends on the genetic background or on attachment to a substrate. Non-adherend myosin II deficient *Dictyostelium* cells are able to elongate but do not form

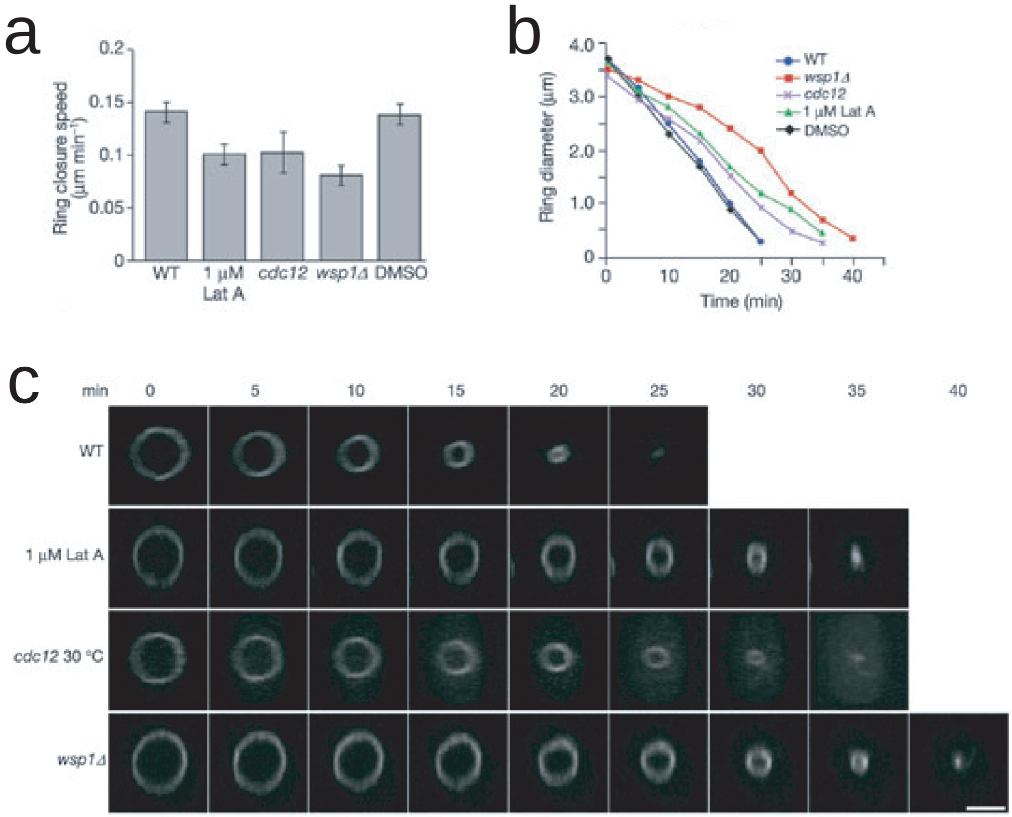

Figure 2.26: (a) Actin polymerization influences the velocity of ring closure. (b) Kinetics of ring closure. (c) Time-lapse images of GFP-Cdc4 rings. Scale bar 2.5 μm. Figure modified from (Pelham and Chang, 2002).

an ingressing cleavage furrow. When attached to a solid surface however, myosin-II-null cells form cleavage furrows that are scarcely distinguishable from those in wild-type cells. The precise mechanics of this ingression mechanism are not known, but it could be based on forces generated from the disassembly of F-actin gels (Weber, 2001).

Bacteria also possess a contractile ring.

Although the contractile ring in eucaryotes consists mainly of actin, a protein that is not present in bacteria, ring like structures also form in bacteria: prior to binary division a distant tubulin homologue (FtsZ), localizes to the midcell division site and forms a cytokinetic ring. This ring constricts the membrane during septation (Moller-Jensen and Lowe, 2005). Additionally FtsZ filaments are essential for the recruitment of all other cell division proteins to the division site. The Z-ring has furthermore been shown to be highly dynamic, with half time of about 30 s in *E. coli* (Stricker et al., 2002) and $\sim$ 8 s in *B. subtilis* (Anderson et al., 2004).

2.5.3 The Pre-Prophase-Band in Plant Cells

Because of their rigid cell wall, higher plant cells do not divide by mechanically cleaving the cell membrane and cytoplasm, Fig. 2.27 (Smith, 2001). That's why unlike yeast or animal cells (Balasubramanian et al., 2004), higher plant cells do not form a contractile actomyosin

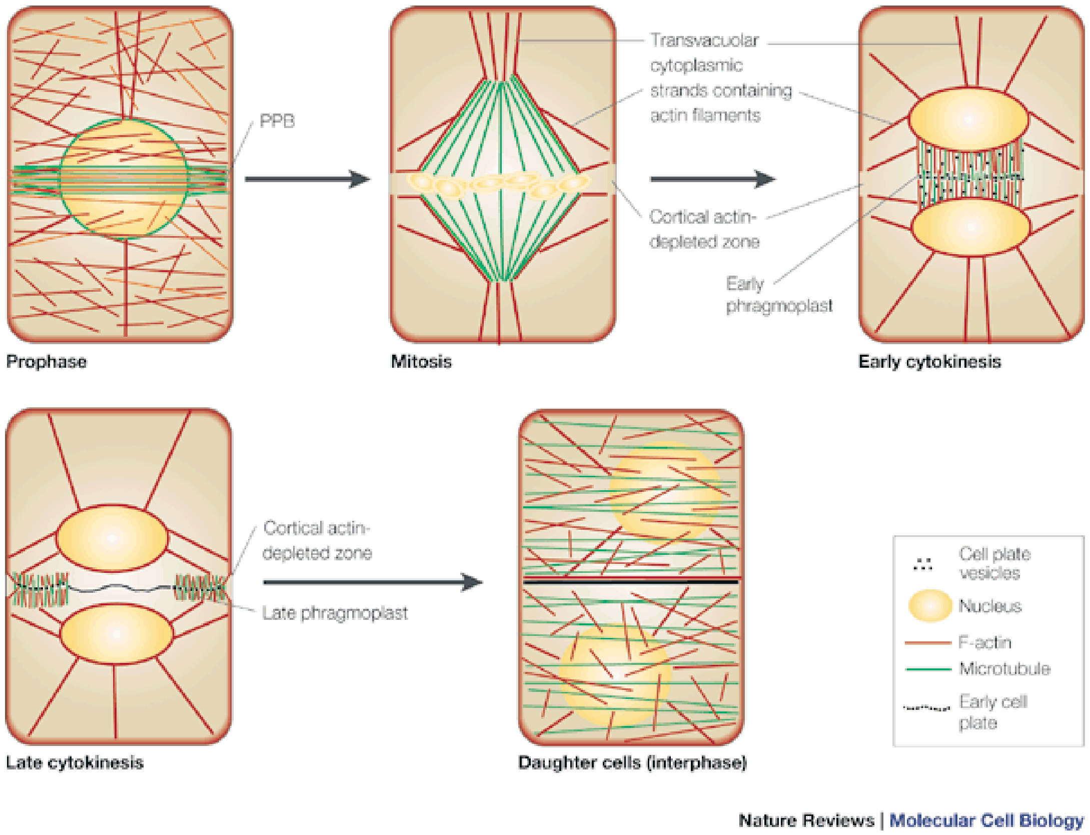
PPB
Transvacuolar cytoplasmic strands containing actin filaments
Cortical actin-depleted zone
Early phragmoplast
Prophase
Mitosis
Early cytokinesis
Cortical actin-depleted zone
Late phragmoplast
Late cytokinesis
Daughter cells (interphase)
Cell plate vesicles
Nucleus
F-actin
Microtubule
Early cell plate
Nature Reviews | Molecular Cell Biology

Figure 2.27: Cytoskeletal organization in dividing plant cells. Drawings for prophase and interphase cells represent projections of a three-dimensional view showing both the cell surface and internal features. Drawings for cells in mitosis and cytokinesis represent mid-plane, cross-sectional views showing only the outlines of the cell cortex. At all stages of the cell cycle, cytoplasmic strands containing actin filaments span the vacuole, linking the cytoplasm surrounding the nucleus with the cortical cytoplasm. During prophase, a cortical preprophase band (PPB) of microtubules circumscribes the future plane of cell division. Actin filaments are distributed throughout the cell cortex during prophase, but some are clearly aligned together with the microtubules of the PPB. When the microtubule PPB is disassembled on entry into mitosis, the actin component of the PPB also disappears, leaving behind an actin depleted zone in the cell cortex that persists and marks the division site throughout mitosis and cytokinesis. After completion of mitosis, a phragmoplast of microtubules and actin filaments is initiated between daughter nuclei, which guides the movement of Golgi-derived vesicles containing cell wall materials to the cell plate. As cytokinesis proceeds, the phragmoplast expands centrifugally until it fuses with the parental plasma membrane and cell wall at the cortical division site previously occupied by the PPB. Figure taken from (Smith, 2001).

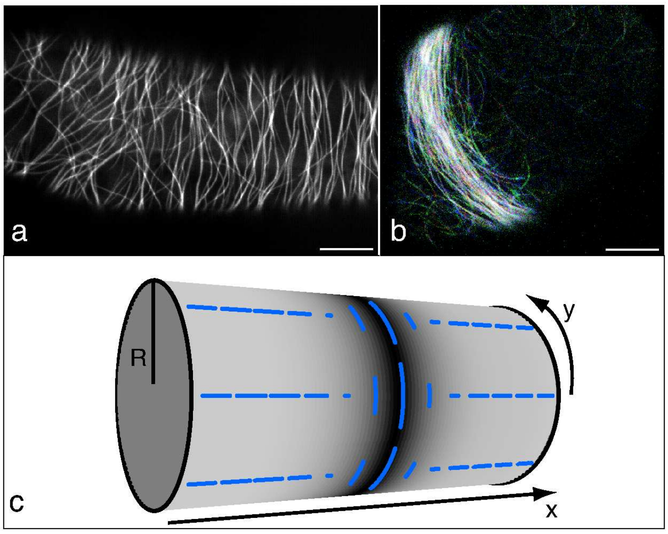

Figure 2.28: (a) Cortical array (CA) and (b) Pre-prophase band (PPB) of microtubules in Tobacco BY2 suspension cells made visible by fluorescence microscopy. (c) Schematic representation of a state of an active gel on a cylinder as discussed in chapter 5, resembling a PPB. The blue bars indicate the nematic order of filaments by their orientation and length. Figure taken from (Zumdieck et al., 2005a).

ring (Jurgens, 2005). Instead of they form an equatorial structure of aligned microtubules and actin (Alberts et al., 2002), that appears before the beginning of prophase, the so called pre-prophase band (PPB) (Wasteneys, 2002). The PPB is a circumferential band around the cell that marks the future division site. It does not constrict and cleave the cell, unlike the contractile ring. It becomes thinner during prophase and vanishes completely before metaphase. Yet it has somehow marked the division site (Smith, 2001). The mitotic spindle is held by cytoplasmic strands (filament fibers that contain actin) so that its mid-plane coincides with the plane of the PPB, Fig. 2.27. First the phragmoplast and then the cell plate, which divides the plant cell, grows for in this plane, and then grow outwards to fuse with the cell wall exactly where the PPB was.

During interphase in higher plant cells microtubules form cortical arrays (CAs) with a preferred orientation in the azimuthal direction (Wasteneys, 2002), see also Fig. 2.28a. Experimental evidence indicates that in the CA filaments orient in a non-polar way (Chan et al., 2003), i.e. in a small volume there are equally many filaments pointing in each direction. It has been suggested, that this holds for the PPB as well (Tian et al., 2004; Dhonukshe and Gadella, 2003). During the transition from the cortical array to the PPB the total mass of polymerized microtubules is conserved (Vos et al., 2004). Figure 2.28b shows an electronmicrograph of a PPB in tobacco cells. All these transitions usually take place in an essentially two dimensional geometry, because in vacuolated plant cells microtubules appear to be confined to a thin cortical region about $200 - 500\,\mathrm{nm}$ thick between the plasma membrane and the vacuole. Self-organization of microtubules in confined geometries has been studied in vitro Cosentino-Lagomarsino (2004).

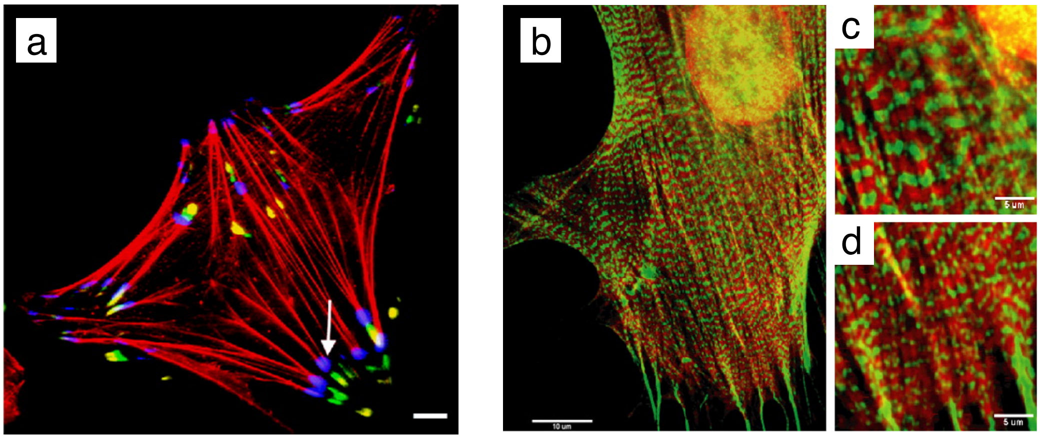

Figure 2.29: (a) Stress Fibers and moving focal adhesions in a fibroblast. F-actin is labeled in red. Focal adhesions are shown for three different times (8 minute intervals, yellow for earliest time, then green, then purple). Figure from (Smilenov et al., 1999). (b,c,d) Stress fiber banding pattern in a gerbil fibroma cell. Myosin light chains (red) and α-actinin (green) show complementary periodic localization along the fibers. Stripes in the bulk (c) are wider than in the peripheral region (d). Figure from (Peterson et al., 2004). Scale bars $5\,\mu$m in (a,c,d) and $10\,\mu$m in (b).

2.5.4 Stress Fibers and Myofibrils

Stress fibers are involved in propelling (dragging) the cell body forward during the traction phase of cell locomotion, cf. Fig. 2.11. The necessary forces seem to be generated mainly by myosin motor proteins, especially myosin II (Hinz and Gabbiani, 2003; Peterson et al., 2004). The dislocation of the cell body of myosin II deficient *Dictyostelium* cells is significantly slower than in normal cells, although they are able to extend their lamellipodium at equal speed. This result can be explained assuming that myosin II is necessary to contract the stress fibers that link a focal adhesion in the front of the cell to its back, cf. Fig 2.29. These results underline the importance of myosin II in cell locomotion.

Furthermore, stress fibers have been shown to possess a structure of alternating filament orientations, similar to that of myofibrils (Cramer et al., 1997), suggesting that they act like small muscles inside the cell. This is consistent with the striped patterns obtained in staining experiments in stress fibers and muscles (compare Fig. 2.29b and Fig. 2.1c). In chapter 5 we discuss a physical mechanisms of that also gives rise to striped patterns in a fiber of active filaments.

Myofibrils are regular periodic structures of actin and myosin filaments in muscle cells, Fig. 2.1. One repetitive unit of this structure is called a sarcomere in which thin actin filaments and thick myosin filaments interdigitate, Fig. 2.30. Myofibrils appear to be more controlled structurally than stress fibers. The actin filaments are of the same length and are stabilized by associated proteins like troponin and tropomyosin. They are attached to structuring components called Z-disks with their plus ends. No Z-disks have been reported from stress fibers. Action of the myosin motors in the resulting bipolar structure leads to bundle contraction.

Despite the structural similarities, there are **important differences between stress fibers and myofibrils.** Recent studies revealed that unlike muscle cells, stress fibers do

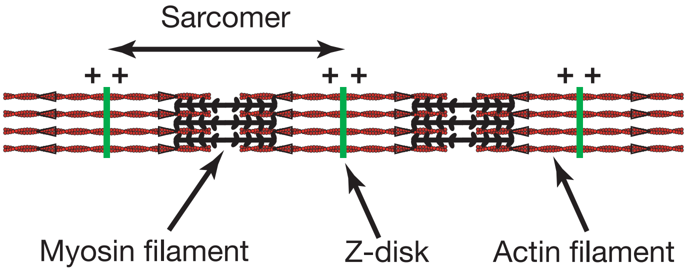

Figure 2.30: A sketch of a myofibril from muscle cells. Actin thin filaments and myosin thick filaments form a periodic pattern. The elementary unit between two Z-disks where the filaments interdigitate is called a sarcomere. Active movement of the myosin motors will lead to contraction. Figure modified from (Kruse, 2005).

not contract uniformly along their length (Peterson et al., 2004). Furthermore actin and myosin are continuously exchanged in stress fibers, which seems not to be the case muscle cells. It seems that the length of actin filaments in muscle cells is well controlled Alberts et al. (2002). This is unlikely in stress fibers as no structuring elements as Z-disks have been reported.

3 Physics of Active Filament Systems

In this chapter we present physical descriptions for the dynamics of active filament systems. Our theory is based on considerations regarding microscopic processes, which distinguishes it from the generic continuum description presented in chapter 5 that are based on symmetry considerations only. With a focus on dynamics driven by filament polymerization and depolymerization, we also consider the action of molecular motors. Starting out by presenting microscopic descriptions of cytoskeletal dynamics in section 3.1, we discuss the details and properties of processes driven by de-/polymerization as well as by molecular motors. Central processes are filament treadmilling in the presence of cross-linking proteins such as end-tracking cross-linkers or molecular motor dimers.

In active filament bundles all filaments are aligned along a common axis. We analyze the collective dynamics due to filament polymerization and depolymerization, especially filament treadmilling, with help of a microscopic mean field description for filament bundles in section 3.2. We discuss bundle contraction and present state diagrams for active filament bundles that show the conditions for stationary and localized as well as oscillating density profiles to exist. Furthermore, we study the dynamics induced by polymerization and depolymerization of entire filaments. Moreover, we derive an analytical expression for the tension generated in an active bundle, which allows us to discuss the contribution of different processes to bundle tension. Then we investigate the action of these processes in active filament bundles by stochastic simulations and present some typical dynamics in section 3.3. Furthermore in section 3.4 we link the mean field description to the stochastic simulations quantitatively.

3.1 From Molecular Properties to Coarse Grained Descriptions

Here we present descriptions of cytoskeletal dynamics based on microscopic processes that occur in the cytoskeleton. We start out by considering cross-linker binding and unbinding from filaments and the motion of molecular motors in section 3.1.1. Then in section 3.1.2 we turn to dynamics of filament pairs linked by such cross-linkers and the ensuing collective dynamics. Finally we present a general framework for coarse grained, mean field descriptions of cytoskeletal dynamics based on microscopic processes and apply it to active filament bundles in section 3.1.3.

3.1.1 Motors and Other Cross-Linkers

Proteins that link cytoskeletal filaments to other cytoskeletal filaments such as molecular motor dimers or cross-linkers are indispensable to generate and transmit forces in filament systems. They provide the basis for collective effects that determine important characteristics of cytoskeletal dynamics. If these cross-linkers do not themselves move along the filaments, we call them passive cross-linkers. These proteins thus do not themselves induce filament motion or dynamics. A more interesting case is the presence of a molecular motor that actively walks along filaments using chemical fuel such as ATP.

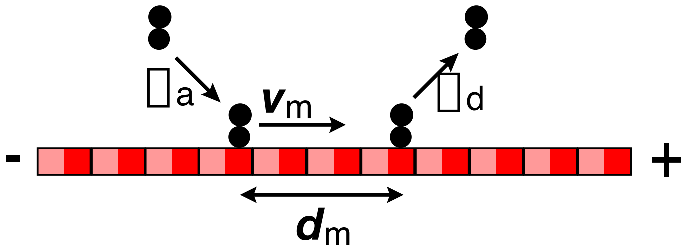

Figure 3.1: Cross-linkers in solution (black) can bind to a filament with rate ω_a, actively move a distance $\boldsymbol{d}_\mathrm{m}$ along the polar filament (red) with velocity $\boldsymbol{v}_\mathrm{m}$ and then detach with rate ω_d. Passive cross-linkers are described by $\boldsymbol{v}_\mathrm{m} = 0$ and unbind from the site on the filament where they attach.

Binding Dynamics of Cross-Linkers

Cross-linkers in solution can bind to a single filament in the system with rate ω_a and unbind from a filament with rate ω_d, see Fig 3.1. The binding rate ω_a will generally depend on the concentration of cross-linkers in the solution as well as the length l of the filaments. Here we assume the concentration to be homogenous and length and concentration to be constant, so that ω_a is an effective rate including these dependences. The unbinding rate can be influenced e.g. by the application of a force or by other proteins that either influence the cross-linker directly or change the properties of the filament. The probability of a cross-linker to be bound is given by

$$p_b = \frac{\omega_\mathrm{a}}{\omega_\mathrm{a} + \omega_\mathrm{d}} \quad . \tag{3.1}$$

Moreover, the average time till detachment is given by $\tau_\mathrm{d} = \omega_\mathrm{d}^{-1}$. If the cross-linker, e.g. a molecular motor, moves with a velocity $\boldsymbol{v}_\mathrm{m}$ along the filament it will thus cover a distance

$$\boldsymbol{d}_\mathrm{m} = \boldsymbol{v}_\mathrm{m} \tau_\mathrm{d} \tag{3.2}$$

on the filament before detaching. A cross-linker that does not actively move along the filament is described by $\boldsymbol{v}_\mathrm{m} = 0$.

The attachment and detachment rates at the end of filaments Ω_a and Ω_d respectively will generally be different from those in the bulk. End-tracking proteins that do not detach from the filament ends have $\Omega_\mathrm{d} = 0$.

Now we turn to cross-linker binding to filament pairs. We assume the following sequence of events as they appear to be the most likely: A motor binds to a filament with rate $\omega_a N$, where N is the number of filaments in the system and ω_a is the attachment rate as introduced in the previous section. For low filament densities the probability for this assembly of a filament and a cross-linker to encounter another filament is proportional to the number of neighboring filaments within a suitable distance. The unbinding events are assumed to be independent of filament concentration and occur with rate ω_d. The typical binding time is again given by $\tau_\mathrm{d} = \omega_\mathrm{d}^{-1}$. Passive cross-linkers that do not move on the filaments will stabilize the relative positions of the two filaments. Active cross-linkers such as molecular motors on the other hand will induce relative sliding of the filaments with respect to each other.

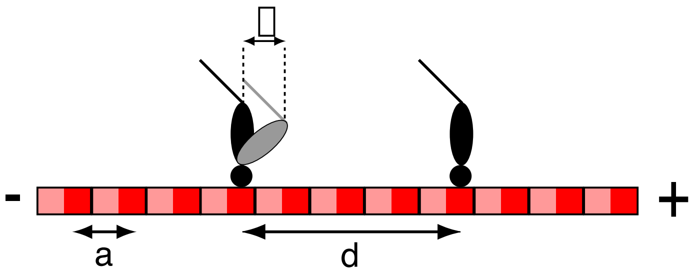

Figure 3.2: Schematic working distance δ and path distance d for a molecular motor. The length of a filament subunit is a. In this example the path distance is $d = 4\,a$.

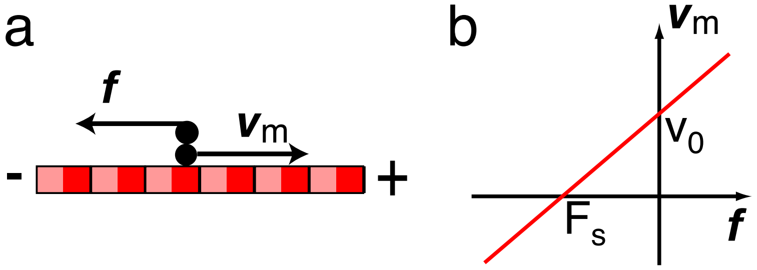

Figure 3.3: Force-velocity relation of a motor. (a) A motor moves with velocity v_m towards the plus end of a filament against an applied force f. (b) The resulting motor velocity v_m is often to a good approximation a linear function in f (Howard, 2001). Without any force appliied the motor moves with velocity v_0. It stops when f reaches the stall force F_s.

Molecular Motors

While a phenomenological model of advancement of molecular motors has been presented in section 2.2.4, here we will focus on the physical quantities characterizing a motor bound to filaments.

The smallest length scale characterizing motor action is the working distance $\boldsymbol{\delta}$. For this thesis we assume that the working distance is equal to the power stroke distance, see (Howard, 2001) for the distinction. The working distance is the distance covered by a configurational change during ATP hydrolysis, cf. Fig. 3.2. For skeletal muscle myosin the working distance has been measured to be 5 nm, and for conventional kinesin it is 8 nm.

The path distance $\boldsymbol{d}$ is the distance between two consecutive binding sites of a motor head. Although the discrete structure of the subunits of the filament is responsible for the discrete steps a motor can take, the path distance can be larger thanthe length of a filament subunit a, as motor binding can be hindered e.g. by filament twist in an actin filament. The path distance is not well defined, if the motor moves irregularly. The path distance for skeletal muscle myosin is $d = 36\,\text{nm}$ and for conventional kinesin $d = 8\,\text{nm}$.

When motors are not moving freely, but are subject to a load, their behavior can often be described by a linear force-velocity curve (Howard, 2001):

$$v_m = v_0 + \chi f \quad , \tag{3.3}$$

where v_m denotes the resulting velocity of the motor with respect to the orientation of the microtubule it is walking on (v_m positive if the motor moves towards the $\oplus$-end), f is the applied force and v_0 is the motor speed without any force applied, both defined with

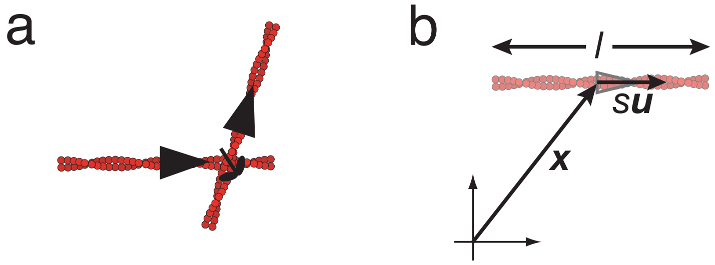

Figure 3.4: (a) A filament pair bound by a cross-linker. The filaments are polar, indicated by the open arrow heads. (b) Filaments are of length l. The position of their center is given by $\boldsymbol{x}$. Every point along the filament can be referenced by $\boldsymbol{x} + s\boldsymbol{u}$, where $\boldsymbol{u}$ is a unit vector pointing along the filament towards its plus end and $l/2 \leq s \leq l/2$ is the position along the filament. Figure adapted from (Kruse, 2005).

respect to the microtubule orientation, $\chi > 0$ is a coefficient ($\chi = -v_0/F_s$, with F_s the stall force), see Fig. 3.3.

End-Active Motors and End-Tracking Proteins

As end-tracking proteins we term any kind of protein that is able to processively follow a filament end. Examples include formin for actin filaments or mitotic centromere-associated kinesin (MCAK) for microtubules. Another example could be a plus end directed motor, that moves slightly faster than the polymerization speed $v_\mathrm{m} > v_g$ and does not fall off at the end. It would always advance on the newly added subunit thus tracking the plus end.

A main difference between the above example is the activity of the motion. While e.g. formins themselves do not use energy and hydrolyze ATP, and thus move passively along with the end of polymerizing filament, molecular motors move actively along filaments converting chemical energy into conformational changes. End-active motors could represent an interesting class in between those two extremes of active and passive motion. We can imagine them as binding to the filament bulk and sitting there passively until depolymerization has brought a filament end into their vicinity. This may trigger the motor to become active and cause it to stay attached to the depolymerizing end.

In this thesis we assume that motors that follow ends always move in steps of size a, i.e. the length of a filament subunit. We thus neglect fluctuations of the cross-linker around the filament end and possible additional movement dynamics. Proteins that are attached to the polymerizing (plus) end thus move with a velocity $v^+ = a\,k^+$ and proteins at the depolymerizing minus end move with $v^- = a\,k^-$.

3.1.2 Dynamics of Filament Pairs with Cross-Linkers

General Description

In this section we consider two filaments in solution that are connected by an active cross-linker, Fig. 3.4a. The filaments are assumed to be rigid rods of length l. Their center of mass is given by $\boldsymbol{x}_i$ where $i = 1, 2$ indexes the two filaments. Points on the filaments are referenced by $\boldsymbol{x}_i + s_i\boldsymbol{u}_i$. Here $\boldsymbol{u}_i$ is a unit vector ($\boldsymbol{u}_i^2 = 1$) pointing along the filament to its plus end and s_i is a coordinate on the filament with $-l/2 \leq s_i \leq l/2$, see Fig. 3.4b. The size of the cross-link is assumed to be much smaller than the filament length. It is thus exactly located at the point where the two filaments overlap. Assuming that $v_\mathrm{m}(s)$, the velocity of a motor along a filament as a function of the position on the filament is known, the motion of the filaments was calculated by Liverpool and Marchetti (2005). Motion is overdamped ($Re \simeq 10^{-6}$) and filament friction with the surrounding fluid is assumed to be local.

In the absence of external forces momentum is conserved and force balance between two filaments 1 and 2 requires

$$\boldsymbol{\eta}(\boldsymbol{u}_1)\boldsymbol{v}_1 = -\boldsymbol{\eta}(\boldsymbol{u}_2)\boldsymbol{v}_2 \quad , \tag{3.4}$$

where

$$\boldsymbol{\eta}(\boldsymbol{u}_i) = \left[\eta_{\|}\boldsymbol{u}_i\boldsymbol{u}_i + \eta_{\perp}(1 - \boldsymbol{u}_i\boldsymbol{u}_i)\right] \tag{3.5}$$

is the friction tensor of the rod. Here, $\eta_{\|}$ and $\eta_{\perp}$ are the friction coefficients for motion parallel and perpendicular to the filament axis respectively. The center-of-mass velocities of the two filaments are denoted by $\boldsymbol{v}_i$, $i = 1, 2$. For point-like cross-linkers there is no rotation of the filaments with respect to their center of mass. The relative velocity between the filaments

$$\boldsymbol{v}_{12} = \boldsymbol{v}_1 - \boldsymbol{v}_2 = v_{\mathrm{m}}(s_2)\boldsymbol{u}_2 - v_{\mathrm{m}}(s_1)\boldsymbol{u}_1 \tag{3.6}$$

and the velocity of the center of mass of the two filaments

$$\begin{aligned} \boldsymbol{V}_{12} \;&=\; A(\eta,\varphi)\,\{(1-2\eta)[v_{\mathrm{m}}(s_1)\boldsymbol{u}_2 + v_{\mathrm{m}}(s_2)\boldsymbol{u}_1] \qquad (3.7)\\ &\quad -[1-\eta-\eta\cos^2(\varphi)][v_{\mathrm{m}}(s_1)\boldsymbol{u}_1 + v_{\mathrm{m}}(s_2)\boldsymbol{u}_2]\} \quad . \qquad (3.8) \end{aligned}$$

Here φ is the angle between the two filaments, $\eta = (\eta_{\perp} - \eta_{\|})/2\eta_{\perp}$, and $A(\eta,\varphi) = \eta/2[(1-\eta)^2 - \eta^2\cos^2(\varphi)]$. The center of mass moves due to the anisotropic friction of the rods. This motion is not present if $\eta_{\perp} = \eta_{\|}$. It also vanishes for aligned filaments with $\varphi = 0$ or $\varphi = \pi$.

Here we have assumed that the velocity $v_{\mathrm{m}}(s)$ of the cross-linkers along the filaments is independent of the applied force but depends on the position s of the motor on the filament. This dependence could be due to properties of the filament that vary along its axis, e.g. a coating with other proteins. Furthermore filament ends can have different properties than the bulk. Sticky ends, i.e. filament ends to which motors remain attached for some time before unbinding, have been proposed to be important for spindle formation (Hyman and Karsenti, 1996). When motors are abundant, excluded volume effects of motors on filaments can also lead to position dependent velocities (Kruse and Sekimoto, 2002).

Aligned Filaments

In a bundle all filaments are aligned along a common axis. This simplifies the dynamics of cross-linked pairs of filaments in such structures. We explicitly discuss the processes central to this chapter in this linear geometry.

Motor induced filament sliding. A motor dimer can link two filaments and slide them with respect to each other. In the absence of external forces the total momentum of the filament pair is conserved. This implicates that in the frame of reference in which the center of mass of the entire system does not move the two filaments move in opposite directions due to the force exerted by the motor, Fig. 3.5. We always choose this reference system unless noted otherwise. The action of a motor dimer always works towards aligning the filament ends that the motor is directed to (e.g. the plus ends for a plus end directed motor). This means that the midpoints of parallel filaments are always moved towards each other and the maximal distance between filament ends in the pair shrinks until the pair

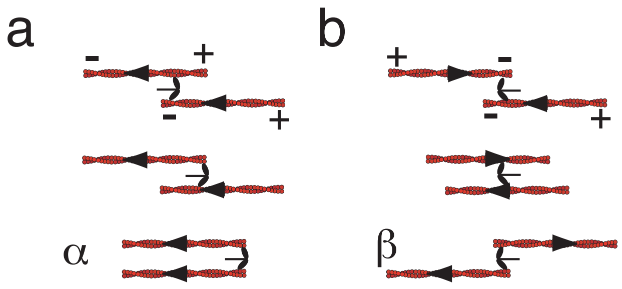

Figure 3.5: Motor action on filament pairs in an active bundle. Filaments can assume two orientations along the bundle axis, depending on where they point their plus ends (also called barbed ends, marked by wide side of the arrowhead). (a) A plus end directed motor dimer induces relative filament sliding between two parallel filaments. The filament ends are aligned in the end. The parameter for this type of interaction in the mean field description is α. (b) The same motor dimer between antiparallel filaments leads to a maximal extension of the minus ends. The strength of this interaction in the mean field description is given by β.

has reached a configuration of maximal overlap, see Fig. 3.5a. For antiparallel filaments the tendency to align ends of the same polarity may also lead to shortening of the end to end distance. Under the action of a plus-end directed motor this is only the case when the filament minus ends are closer to each other than the filament plus ends, see first two steps in Fig. 3.5b. Ultimately the action of a motor between antiparallel filaments leads to an increase in the distance between the filament centers until only the ends towards which the motor walks overlap. The strength of this interaction is characterized by a coefficient β.

A motor bound to parallel filaments induces relative sliding between them only when it walks with different velocities on each filament. For a motor dimer with two identical heads this is the case for example when one head reaches a filament end and remains attached to it while the other head walks along its filament (Fig. 3.5a). In this case the action of motor dimers between parallel filaments can be seen as an end effect. The strength of this effect is characterized by a coefficient α. Another way to achieve different velocities could be proteins bound along the filament that influence the motor speed. Motors between antiparallel filaments on the other hand induce relative filament sliding irrespective of their position along the filament. The exception to this rule being that if the motor dimer has reached the end on both filaments it cannot advance and thus does not induce relative sliding anymore. This obviously holds as well for motors between parallel filaments.

Treadmilling. A treadmilling filament loses monomers at its minus end and gains monomers at its plus end at equal rates so that the overall filament length is conserved while the center of mass as well as both filament ends move in the direction of the plus end Fig. 3.6a. The treadmilling velocity v of these ends is usually much greater than the velocity of monomers in the bulk of the filament, i.e. the monomers between the ends. To zeroth order approximation each monomer in the bulk of a treadmilling filament is stationary in the absence of external forces.

Filament sliding due to passive cross-linkers. Passive cross-linkers are proteins that can link two filaments. Unlike molecular motors, they do not actively (i.e. converting chemical energy such as provided by ATP or GTP into directed motion) move along the filaments. Generally they stabilize a bundle by hindering relative sliding of the filaments. When

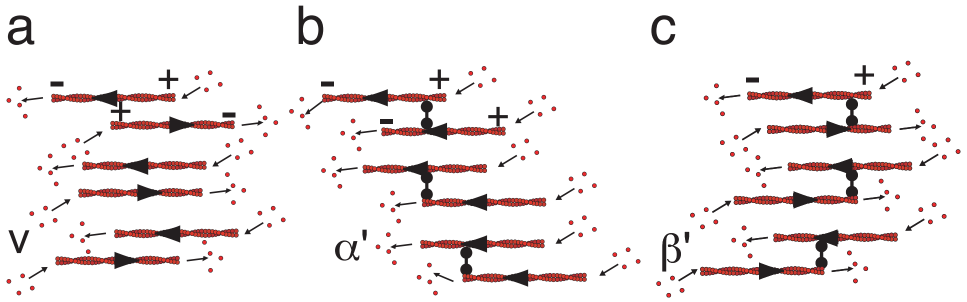

Figure 3.6: Treadmilling of filaments and action of end-tracking cross-linkers. (a) Subunits are added to the filaments plus ends and removed from the minus ends at equal rates. The length of the filament does not change. Both ends as well as the center are dislocated with velocity v though. The direction of filament treadmilling depends on filament orientation, indicated by the arrowheads. (b,c) A passive cross-linker that does not itself move actively along the filaments but stays attached to the ends of treadmilling filaments induces relative sliding between filament pairs. (b) Linking two parallel treadmilling filaments will ultimately lead to pairwise alignment of ends of the same orientation. The parameter for this type of interaction is α'. (c) Antiparallel filaments will only align their minus ends, with their plus ends maximally distant. The parameter is β'. Note that these figures display a superposition of the currents due to treadmilling as displayed in (a) and due to the action of passive cross-linkers.

attached to at least one polymerizing or depolymerizing end of filaments in a pair, passive crosslinkers can also induce relative filament sliding. Their contribution to the collective dynamics differs depending on if the cross-linkers are attached to the polymerizing plus-ends or the depolymerizing minus-ends.

The action of passive cross-linkers that bind to minus-ends in the presence of treadmilling can be similar in nature to that of molecular motors (Fig. 3.6b and c): starting bound to a particular monomer in the bulk of one filament, treadmilling will eventually make that monomer the minus end of the filament. If the cross-linker now stays attached to this minus end (at least for a little while) while the filament treadmills, the cross-linker is displaced in space and can exert a force on the second filament in the pair. Microscopically we could imagine that the cross-linker binds to the next monomer in the bulk when the monomer at the end falls off.

The contribution of passive cross-linkers that bind to filament plus-ends and stay attached to them while the filament treadmills to the dynamics of the pair is different, Fig. 3.7. A detailed discussion of their dynamics is given in section 3.2.3.

Our considerations illustrate the similarity between the action of motor dimers and passive cross-linkers. But there are also important differences: passive cross-linkers always have to be attached to one filament *end* in order to induce relative motion in the filament pair. This is reminiscent of the requirement for a motor with identical heads between two parallel filaments that also only slides the filaments with respect to each other when it has reached exactly one end. However, as described above the action of motors between antiparallel filaments is independent of their location along the filaments in contrast to that of passive cross-linkers that depend on filament ends to move. In both cases all motion stops when motors or cross-linkers have reached the ends of both filaments. Note also that passive cross-linkers cannot have any effect in the absence of treadmilling. They can only “modulate” the treadmilling currents. Figures 3.6b,c and 3.7 thus display the outcome of a superposition of the currents due to treadmilling alone (as displayed in 3.6a) and the currents due to the action of passive cross-linkers.

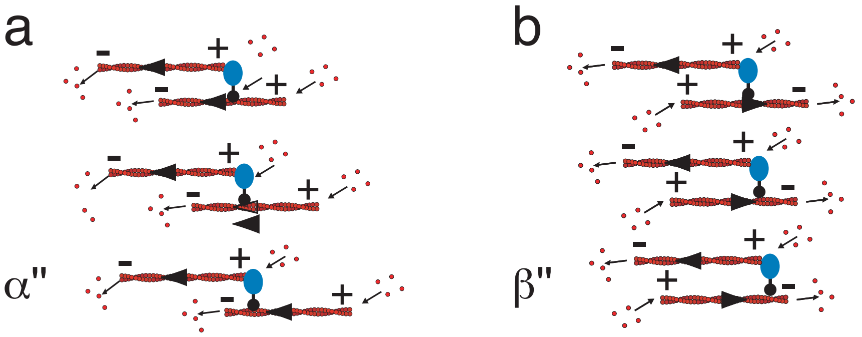

Figure 3.7: Dynamics due to plus-end tracking cross-linkers in the presence of treadmilling. The cross-linkers possess a domain that allows them to processively follow the filaments plus end (blue ellipse) while another domain is linked to the bulk of the second filament (black dot). The resulting dynamics is strikingly different from that found for minus-end tracking cross-linkers, cf. Fig. 3.6b and c. (a) Between parallel filaments the action of cross-linkers leads to a maximal separation of the filament centers. (b) Antiparallel filaments on the other hand tend to get aligned under the action of these cross-linkers. The associated parameters are α'' and β'' respectively.

3.1.3 Mean Field Description of Active Filament Systems

An analytical description of systems of many individual filaments and cross-linkers is not to feasible because these are many body systems with complicated interactions. This side of the challenge is more successfully tackled by computer simulations, cf. section 4.1.2. Mean field descriptions do provide a way to gain analytical insight into the exciting dynamics of active filament systems despite this complexity (Nakazawa and Sekimoto, 1996; Sekimoto and Nakazawa, 2000; Kruse and Jülicher, 2000; Liverpool and Marchetti, 2003). These descriptions are based on densities of filaments and cross-linkers, whose evolution is described in equations that neglect higher order correlations. A general framework for the derivation of such descriptions in one spatial dimension has been presented by Kruse and Jülicher (2003). Here we report the generalization to arbitrary dimension as given in (Kruse, 2005).

General Description

The description is centered around the interaction of filament pairs that move with respect to a non-moving background. As before filaments are described as thin, rigid rods. Filament bending and rotation around the longitudinal axis are ignored. The density of filaments that have their center at $\boldsymbol{x}$ and orientation $\boldsymbol{u}$ is given by $\Psi(\boldsymbol{x},\boldsymbol{u})$. Motors are assumed to be small compared to filaments and are treated as point particles. The number density of motors bound to filaments is denoted by m. The two densities evolve according to

$$\partial_t\Psi - \nabla\cdot\left[D_\parallel\boldsymbol{uu}+D_\perp(1-\boldsymbol{uu})\right]\cdot\nabla\Psi - D_\mathrm{r}\mathcal{R}\cdot\mathcal{R}\Psi+\nabla\cdot\boldsymbol{J}_a+\mathcal{R}\cdot\boldsymbol{J}_\mathrm{r} \;=\; S \tag{3.9}$$

$$\partial_t m - D_\mathrm{m}\Delta m+\nabla\cdot\boldsymbol{J}_\mathrm{m} \;=\; S_\mathrm{m} \quad , \tag{3.10}$$

where $\mathcal{R}=\boldsymbol{u}\times\partial/\partial\boldsymbol{u}$ is the rotation operator. The filament currents $\boldsymbol{J}_a$ (translational) and $\boldsymbol{J}_\mathrm{r}$ (rotational) as well as the motor current $\boldsymbol{J}_\mathrm{m}$ are generated by the active interaction between motors and filaments. The diffusion terms with diffusion constants $D_{\|}$, $D_{\perp}$, $D_{\rm r}$, and $D_{\rm m}$ account for fluctuations in the dynamics. The major source of these fluctuations are the stochastically applied forces during filament motor interactions and not thermal noise. For a one dimensional bundle the following argument motivating this statement has been given in (Kruse and Jülicher, 2003): Thermal diffusion would lead to a diffusion coefficient $D \simeq kT/\eta_{\|} l$. Active interactions between filaments that do not generate a net current in the homogenous state lead to an effective diffusion coefficient $D \simeq d_{\rm m}^2 \omega_a^{(2)}$, where $d_{\rm m}$ is the run length of a motor on a filament introduced in Eq. (3.2) and $\omega_a^{(2)} \sim l$ is the rate of cross-link generation.The effective diffusion constant thus scales like $D \sim l$ while thermal contributions scale like $\sim l^{-1}$ and for long filaments the diffusion is dominated by fluctuations due to active cross-linkers. All diffusion constants are thus effective diffusion coefficients that in general do not satisfy an Einstein relation.

Nucleation and annihilation of filaments is described by the source term S. In the following we will mostly consider $S = 0$ which corresponds e.g. to *in vitro* experiments with stabilized filaments. The source term $S_{\rm m}$ describes the exchange of motors with the surrounding solvent. Motors in the solvent are assumed to be abundant so that their concentration is homogenous and constant.

Here again the dynamics take place in the regime of low Reynolds number, i.e. inertia effects are negligible. Momentum conservation imposes a force balance everywhere along each filament (parametrized by $\boldsymbol{x} + s\boldsymbol{u}$):

$$\boldsymbol{u}\partial_s\sigma(\boldsymbol{x},\boldsymbol{u},s) - \boldsymbol{f}_{\rm int}(\boldsymbol{x},\boldsymbol{u},s) = \boldsymbol{f}_{\rm fl}(\boldsymbol{x},\boldsymbol{u},s) + \boldsymbol{f}_{\rm m}(\boldsymbol{x},\boldsymbol{u},s) + \boldsymbol{f}_{\rm ext}(\boldsymbol{x},\boldsymbol{u},s) \quad . \tag{3.11}$$

Here, σ denotes the line tension along the filament. The internal force density $\boldsymbol{f}_{\rm int}$ describes all active filament interactions through cross-linkers, $\boldsymbol{f}_{\rm fl}$ describes the force density resulting from friction with the surrounding fluid, $\boldsymbol{f}_{\rm m}$ the force density due to the action of motors moving along a single filament that do not form cross-links between different filaments, and $\boldsymbol{f}_{\rm ext}$ is the density of external forces.

In a stationary solvent friction is local:

$$\boldsymbol{f}_{\rm fl}(\boldsymbol{x},\boldsymbol{u},s) = \left[\eta_{\|}\boldsymbol{u}\boldsymbol{u} + \eta_{\perp}(1-\boldsymbol{u}\boldsymbol{u})\right]\cdot \boldsymbol{J}_a(\boldsymbol{x},\boldsymbol{u})R(s) + \eta_0 s\boldsymbol{J}_{\rm r} \times \boldsymbol{u}R(s) \quad . \tag{3.12}$$

Here, $\eta_{\|}$ and $\eta_{\perp}$ are friction coefficients per unit length, parallel and perpendicular to the filament axis. The coefficient η_0 describes the friction of a filament subunit. The function $R(s)$ describes dissipation of energy along a moving filament. It also captures the distribution of filament lengths. When all filaments have the same length l, a simple choice is $R(x) = 1$ on the filament for $|x| \leq l/2$ and $R(x) = 0$ otherwise.

For the force density of motors we write

$$\boldsymbol{f}_{\rm m}(\boldsymbol{x},\boldsymbol{u},s) = \eta_{\rm m}\Gamma\boldsymbol{u}m(\boldsymbol{x}+s\boldsymbol{u})\Psi(\boldsymbol{x},\boldsymbol{u})R(s) \quad . \tag{3.13}$$

Here $\eta_{\rm m}$ is the motor friction coefficient and Γ is the average velocity of motors moving on a filament. If we neglect steric exclusion between motors and in the limit of pairwise filament interaction we obtain

$$\Gamma = v_{\rm m} \quad . \tag{3.14}$$

The active translational and rotational currents in Eqs. (3.9) and (3.10) can be expressed in terms of the internal, the motor and the external force densities. For simplicity, we will assume that $\boldsymbol{f}_{\rm ext} = 0$. Furthermore the friction of motors is assumed to be small compared to the filament friction, i.e. the contribution of $\boldsymbol{f}_m$ can be neglected. Integration of Eq. (3.11) with respect to s then yields

$$\begin{aligned} -\int \mathrm{d}s\, \boldsymbol{f}_{\mathrm{int}}(\boldsymbol{x},\boldsymbol{u},s) &= \int \mathrm{d}s\, \boldsymbol{f}_{\mathrm{fl}}(\boldsymbol{x},\boldsymbol{u},s) && (3.15)\\ &= l\left[\eta_{\|}\boldsymbol{u}\boldsymbol{u}+\eta_{\perp}(1-\boldsymbol{u}\boldsymbol{u})\right]\cdot \boldsymbol{J}_a(\boldsymbol{x},\boldsymbol{u}) \quad . && (3.16)\end{aligned}$$

Here we have used $\int \mathrm{d}s\, R(s) = l$ and assumed $R(s) = R(-s)$ so that

$$\boldsymbol{J}_a(\boldsymbol{x},\boldsymbol{u}) = -\frac{1}{l}\left[\frac{1}{\eta_{\|}}\boldsymbol{u}\boldsymbol{u}+\frac{1}{\eta_{\perp}}(1-\boldsymbol{u}\boldsymbol{u})\right]\cdot\int \mathrm{d}s\, \boldsymbol{f}_{\mathrm{int}}(\boldsymbol{x},\boldsymbol{u},s) \quad . \tag{3.17}$$

Integrating Eq. (3.11) with $\int$ ds $s\boldsymbol{u}\times$ yields

$$\boldsymbol{J}_{\mathrm{r}}(\boldsymbol{x},\boldsymbol{u}) = -\frac{1}{\eta_0\chi^2}\int \mathrm{d}s\, s\boldsymbol{u}\times \boldsymbol{f}_{\mathrm{int}}(\boldsymbol{x},\boldsymbol{u},s) \quad . \tag{3.18}$$

Here we have introduced $\chi^2 = \int \mathrm{d}s\, s^2 R(s)$ and used $\boldsymbol{J}_{\mathrm{r}}(\boldsymbol{x},\boldsymbol{u}) \perp \boldsymbol{u}$.

The internal force density $\boldsymbol{f}_{\mathrm{int}}$ depends on the densities of filaments and cross-linkers. We assume the cross-linkers to be point-like particles so that filaments can only be cross-linked when they cross. The internal force density acting at point s on a filament with orientation $\boldsymbol{u}$ and center at $\boldsymbol{x}$ is then given by

$$\boldsymbol{f}_{\mathrm{int}}(\boldsymbol{x},\boldsymbol{u},s) = \int \mathrm{d}\boldsymbol{x}'\int \mathrm{d}\boldsymbol{u}'\int \mathrm{d}s'\Psi(\boldsymbol{x},\boldsymbol{u})\Psi(\boldsymbol{x}',\boldsymbol{u}')C^{\boldsymbol{x}',\boldsymbol{u}',s'}_{\boldsymbol{x},\boldsymbol{u},s}\, m(\boldsymbol{x}+s\boldsymbol{u})\boldsymbol{F}(\boldsymbol{x},\boldsymbol{u},s,\boldsymbol{x}',\boldsymbol{u}',s') \quad . \tag{3.19}$$

Here $C^{\boldsymbol{x}',\boldsymbol{u}',s'}_{\boldsymbol{x},\boldsymbol{u},s} = R(s)R(s')\delta(\boldsymbol{x}+s\boldsymbol{u}-\boldsymbol{x}'-s'\boldsymbol{u}')$ restricts the integration to filaments that cross. The function $\boldsymbol{F}$ captures the average force between two filaments depending on their position and orientation. While the precise form of $\boldsymbol{F}$ is not determined, it has to fulfill some symmetry requirements. Due to translation invariance, $\boldsymbol{F}$ can only depend on the relative positions of the filament centers

$$\boldsymbol{F}(\boldsymbol{x},\boldsymbol{u},s,\boldsymbol{x}',\boldsymbol{u}',s') \equiv \boldsymbol{F}(\boldsymbol{x}-\boldsymbol{x}',\boldsymbol{u},s,\boldsymbol{u}',s') \quad . \tag{3.20}$$

Under rotation $\boldsymbol{F}$ has to transform like a vector (i.e. $\boldsymbol{F}$ is covariant)

$$\boldsymbol{F}(\mathbf{R}\boldsymbol{x},\mathbf{R}\boldsymbol{u},s,\mathbf{R}\boldsymbol{u}',s') = \mathbf{R}\boldsymbol{F}(\boldsymbol{x},\boldsymbol{u},s,\boldsymbol{u}',s') \quad , \tag{3.21}$$

where $\mathbf{R}$ denotes the rotation operator.

Newton's law *actio = reactio* requires

$$\boldsymbol{F}(\boldsymbol{x},\boldsymbol{u},s,\boldsymbol{u}',s') = -\boldsymbol{F}(-\boldsymbol{x},\boldsymbol{u}',s',\boldsymbol{u},s) \quad . \tag{3.22}$$

And covariance under reflections imposes

$$\boldsymbol{F}_{\|}(\boldsymbol{x}_{\|}+\boldsymbol{x}_{\perp},\boldsymbol{u}_{\|}+\boldsymbol{u}_{\perp},s,\boldsymbol{u}'_{\|}+\boldsymbol{u}'_{\perp},s') = \boldsymbol{F}_{\|}(\boldsymbol{x}_{\|}-\boldsymbol{x}_{\perp},\boldsymbol{u}_{\|}-\boldsymbol{u}_{\perp},s,\boldsymbol{u}'_{\|}-\boldsymbol{u}'_{\perp},s') \tag{3.23}$$

$$\boldsymbol{F}_{\perp}(\boldsymbol{x}_{\|}+\boldsymbol{x}_{\perp},\boldsymbol{u}_{\|}+\boldsymbol{u}_{\perp},s,\boldsymbol{u}'_{\|}+\boldsymbol{u}'_{\perp},s') = -\boldsymbol{F}_{\perp}(\boldsymbol{x}_{\|}-\boldsymbol{x}_{\perp},\boldsymbol{u}_{\|}-\boldsymbol{u}_{\perp},s,\boldsymbol{u}'_{\|}-\boldsymbol{u}'_{\perp},s') \tag{3.24}$$

where the subscripts $\|$ and $\perp$ denote vector components along and perpendicular to the reflection axis, respectively. In the following section we will apply this description to a filament bundle.

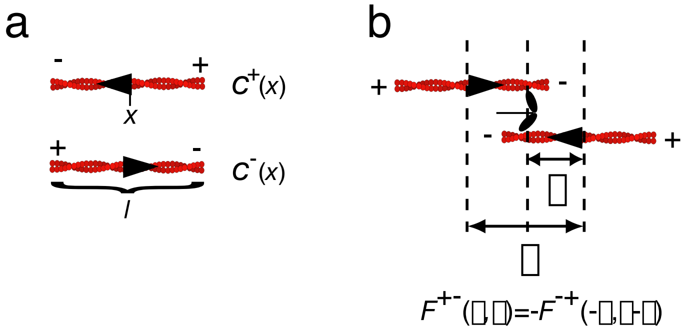

Figure 3.8: (a) Filaments of length l in a bundle can be described by two filament densities c^+ and c^- depending on their orientation. (b) An active cross-link (i.e. a motor dimer) exerts a force on a filament pair with opposite orientations, see text for explanations. The motor moves towards the plus end on each filament.

Filament Bundles

Since linear cytoskeletal structures are important in live cells we will now derive a microscopic description of active filament bundles. In a bundle all filaments are aligned along a common axis. This represents an effectively one dimensional geometry in which filaments can only have one of two orientations, depending on where they point their plus end. *In vitro* experiments on such systems have shown that bundles of filaments with molecular motors can contract and elongate and that filaments can be sorted due to their polarity and depending on their orientation (Takiguchi, 1991; Tanaka-Takiguchi et al., 2004). One dimensional structures in living cells include stress fibers, the contractile ring, and myofibrils in muscle cells.

For the physical description of the bundle we choose the x-axis along the bundle axis. All filaments have the same length l. As only two orientations are possible, the filaments are characterized by two densities c^+ and c^-, for filaments that point their plus or minus end along the positive x-axis respectively, see Fig 3.8a. The internal force densities acting on plus and minus filaments are composed of contributions from interactions between parallel and anti-parallel filaments:

$$f^+_{\text{int}} = f^{++}_{\text{int}} + f^{+-}_{\text{int}} \tag{3.25}$$

$$f^-_{\text{int}} = f^{--}_{\text{int}} + f^{-+}_{\text{int}} \tag{3.26}$$

Here f^{+-}_{int} denotes the forces on plus filaments due to the interaction with minus filaments. The expression for the internal force (Eq. (3.19)) then becomes

$$f^{\pm\mp}_{\text{int}}(x,s) = \int \mathrm{d}x' c^{\pm}(x)c^{\mp}(x')R(s)R(x+s-x')m(x+s)F^{\pm\mp}(x'-x,s) \tag{3.27}$$

and corresponding expressions for $f^{\pm\pm}_{\text{int}}$. Here, $F^{+-}(\xi,\zeta)$ is the average force on a plus-filament applied at a distance ζ from its center, exerted by minus-filaments located a distance ξ from the first, see Fig 3.8b. The symmetry relations (3.20)- (3.24) become in one dimension

$$F^{\pm\pm}(\xi,\zeta) = -F^{\pm\pm}(-\xi,\zeta-\xi) \tag{3.28}$$

$$F^{\pm\mp}(\xi,\zeta) = -F^{\mp\pm}(-\xi,\zeta-\xi) \tag{3.29}$$

$$F^{++}(\xi,\zeta) = -F^{--}(-\xi,-\zeta) \tag{3.30}$$

$$F^{+-}(\xi,\zeta) = -F^{-+}(-\xi,-\zeta) \quad . \tag{3.31}$$

Here we have analyzed the symmetry of such a bundle with pairwise filament interaction. It is independent of the precise nature of the forces acting on the filaments and the currents they induce. The following section provides a simple choice that obeys all relations derived here.

3.2 Minimal Model of Active Filament Bundles

A simple example for the dynamics of a bundle of polar filaments in the presence of active cross-linkers such as molecular motors is presented in (Kruse and Jülicher, 2000). It represents a minimal model of active bundle contraction in the sense that it is based on strongly simplifying assumptions and strives to bring out clearly the key mechanisms involved in stress generation in bundles. It is contained in the general framework presented above and corresponds to a set of filaments with length l for which $R(x) = 1$ for $|x| < l/2$ and $R(x) = 0$ otherwise. Furthermore the forces are chosen as follows

$$\begin{aligned} F^{\pm\pm}(\xi,\zeta) &\sim \operatorname{sgn}(\xi) && (3.32)\\ F^{\pm\mp}(\xi,\zeta) &\sim \mp 1 \quad . && (3.33) \end{aligned}$$

Here $\operatorname{sgn}(\xi) = 1$ for $\xi > 0$ and -1 otherwise, so that the symmetry requirements Eq. (3.28)-(3.31) are fulfilled. Motors are taken to be point-like cross-linkers that move with the same speed everywhere on both filaments they link. The motor distribution is taken to always be homogenous and thus its dynamics can be neglected.

So far only interactions of pairs of stable, i.e. non-polymerizing filaments have been studied in this context. Here we present an extension of this framework to include polymerizing and depolymerizing filaments. We especially focus on the dynamics caused by treadmilling in the presence of motor proteins and passive cross-linkers as outlined in section 3.1 but also consider the generation and destruction of entire filaments.

The description is formulated in terms of filament number densities c^+ and c^- for plus and minus filaments respectively that have their center at position x. The number of filaments in the interval $[x, x + \mathrm{d}x]$ is thus given by $c(x)\mathrm{d}x$ and $N = \int_0^L c(x)\mathrm{d}x$ is the total number of filaments in a system of length L. Filaments are of length l and polymerize from monomers that diffuse freely in the surrounding fluid. The monomer number density is denoted by c_m. These densities satisfy continuity equations of the form

$$\begin{aligned} \partial_t c^+ &= D\partial_x^2 c^+ - \partial_x J^+ - k_{\mathrm{d}}^+ c^+ + k_{\mathrm{p}}^+ c_m && (3.34)\\ \partial_t c^- &= D\partial_x^2 c^- - \partial_x J^- - k_{\mathrm{d}}^- c^- + k_{\mathrm{p}}^- c_m && (3.35)\\ \partial_t c_m &= D_{\mathrm{m}}\partial_x^2 c_m + \mu k_{\mathrm{d}}^+ c^+ + k_{\mathrm{d}}^- c^- - \mu(k_{\mathrm{p}}^+ + k_{\mathrm{p}}^-)c_m \quad . && (3.36) \end{aligned}$$

Here, D is an effective diffusion coefficient as discussed in section 3.1.3, $k_d^\pm$ and $k_p^\pm$ denote rates of filament polymerization and depolymerization of plus and minus filaments respectively, μ is the number of monomers in a filament of length l, and D_{m} is the diffusion coefficient of monomers in solution. Note that k_d and k_p describe the creation and annihilation of entire filaments. Interactions between filaments as well as filament treadmilling induce active filament currents $J^\pm$ describing the rate at which filaments slide locally. For pairwise interactions of filaments, these active currents depend quadratically on the local densities $c^\pm(x)$. They are proportional to the interaction strengths $\alpha, \beta, \alpha', \beta', \alpha''$ and β'' as well as to the treadmilling speed v, which correspond to the processes indicated in Figs. 3.5, 3.6 and 3.7.

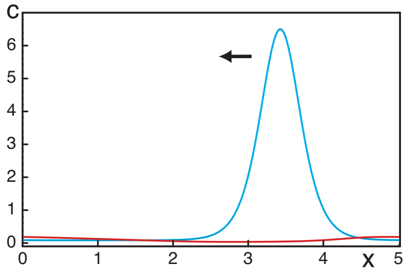

Figure 3.9: Example of a solitary wave obtained by numerically integrating Eqs. (3.44) and (3.45) with periodic boundary conditions in x. Shown are the density profiles of the plus filaments (blue) and minus filaments (red). Parameters are $\alpha = 1.3$, $\beta = 0.5$, $v = 0$, $L = 5$. Initial condition was a sinusoidal perturbation on the homogenous state with $c_0^+ = 1$ and $c_0^- = 0.1$.

3.2.1 Bundles of Stabilized Filaments

In this thesis we focus on the contribution of filament polymerization and depolymerization. The minimal model however has first been studied for stabilized filaments in the absence of any kind of filament polymerization dynamics (Kruse and Jülicher, 2000; Kruse et al., 2001; Kruse and Jülicher, 2003). The interesting results obtained in this simplified setting reveal some generic properties of the dynamics of active filament bundles.

When only molecular motors are present and no other active processes influence the dynamics, the active currents can be decomposed into two contributions

$$J^+ = J_\alpha^{++} + J_\beta^{+-} \tag{3.37}$$

$$J^- = J_\alpha^{--} + J_\beta^{-+} \tag{3.38}$$

reflecting the filament sliding due to motors between parallel and antiparallel filaments. For simplicity we use dimensionless coordinates for space $\tilde{x} = x/l$, time $\tilde{t} = tD/l^2$, and concentration $\tilde{c} = cl$. The parameters α and β that characterize the active processes are then dimensionless as well. We drop the tildes for better readability, understanding that all parameters and quantities in this section are dimensionless. The currents in ±-filaments due to motors between parallel filaments

$$J_\alpha^{\pm\pm}(x) = \alpha \int_0^1 \mathrm{d}\xi \, \left[c^\pm(x+\xi) - c^\pm(x-\xi)\right] c^\pm(x) \tag{3.39}$$

and the currents in ±-filaments due to motors between antiparallel filaments

$$J_\beta^{\pm\mp}(x) = \mp\beta \int_{-1}^1 \mathrm{d}\xi \, c^\mp(x+\xi) c^\pm(x) \tag{3.40}$$

were introduced in (Kruse and Jülicher, 2000).

Analysis of the ensuing description reveals that in a filament bundle the interaction between parallel filaments (α) drives tension generation and pattern formation. The homogenous state in which the filament density is constant everywhere in the bundle is stable for $\alpha \leq \alpha_c$, where the critical value α_c depends on β, the coupling parameter between filaments of opposite orientations. The value of α_c is always positive, although it decreases with increasing β. This indicates that in the absence of interactions between filaments of the same orientation (i.e. $\alpha = 0$), the homogenous state is always stable. Similar results

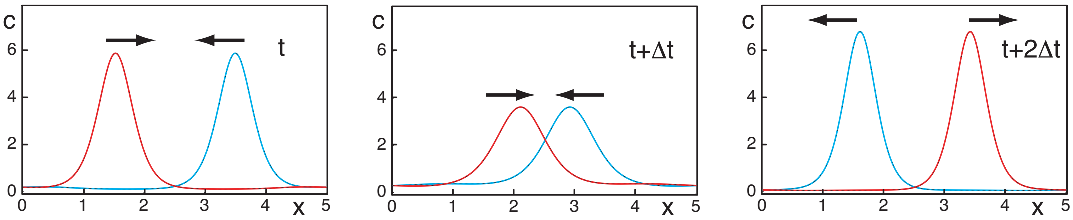

Figure 3.10: Example of an oscillatory wave obtained by numerically integrating Eqs. (3.44) and (3.45) with periodic boundary conditions in x. Shown are the density profiles of the plus filaments (blue) and minus filaments (red) at three consecutive points in time (from left to right, $\Delta t = 1.6$). Parameters are $\alpha = 1.3$, $\beta = 0.5$, $v = 0$, $L = 5$. Initial condition was a sinusoidal perturbation on the homogenous state with $c_0^+ = 1$ and $c_0^- = 1$.

have been obtained by Nakazawa and Sekimoto (1996). The authors studied the dynamics of filament bundles in the absence of a motor-induced coupling between filaments of the same orientation and only found an instability when they took into account friction between the filaments, which effectively leads to a coupling between filaments of the same orientation.

For periodic boundary conditions and $\beta \neq 0$ the homogenous state always loses stability through a Hopf-bifurcation (Kruse et al., 2001), i.e. for $\alpha > \alpha_c$ oscillatory states appear. These states are solitary waves advancing with velocity v_s such that $c^\pm(x,t) = u^\pm(x - v_s t)$, where $u^\pm(x)$ is the corresponding stationary density profile. This wave-form u is the sum of a localized distribution of filaments of one orientation and an extended distribution of filaments of the opposite orientation. The moving wave can thus be pictured as a localized distribution of filaments of one orientation gliding on a carpet of filaments of the opposite orientation (cf. Fig. 3.9).

Interestingly two solitary waves moving in opposite directions can coexist if the concentrations of plus- and minus-filaments in the system are not too different and the interaction β is comparatively small (compared to α). One can think of this as two oriented bundles, both exhibiting coexistence of the homogenous and a localized distribution (Kruse and Jülicher, 2003). Solitary waves are unstable for values of α beyond a second critical value, where oscillatory waves are generated. The name stems from the fact that while the shape of the density profiles is constant for solitary waves, it oscillates for oscillatory waves, see Fig. 3.10. For oscillatory waves the density profile of both orientations is peaked and the peaks are moving in opposite directions. When they encounter each other, they deform due to the interaction with filaments of the opposite orientation. The peaks form again after passing "through" each other and continue to travel around the ring. Note that even though the profile of the total filament density $c^+ + c^-$ moves along the system, in the absence of polymerization dynamics the total current

$$I = \int \mathrm{d}x (J^+ + J^-) = 0 \tag{3.41}$$

vanishes due to conservation of momentum. Cytoskeletal waves have been found in several cells (Vicker, 2002; Bretschneider et al., 2004; Giannone et al., 2004; Dubin-Thaler et al., 2004; Döbereiner et al., 2004).

An oriented bundle in which all filaments have the same orientation allows the explicit calculation of the critical value α_c. In this case the dynamics is given by only one equation for a density c which represents either c^+ or c^-. Given a system of length L with periodic boundary conditions, linear stability analysis of the homogenous state $c(x) = c_0$ reveals the critical value α_c explicitly:

$$\alpha_c = \frac{2\pi^2}{c_0 L^2(1-\cos(2\pi/L))} \quad . \tag{3.42}$$

Its critical mode has wave number $k_c = 2\pi/L$. The critical mode is thus determined by the system size alone and not by features intrinsic to the dynamics. The critical value α_c decreases with increasing c_0 and L. Beyond the instability, the homogenous state evolves into a stationary, localized, inhomogenous state. In this state the density distribution has a clear peak, so that most of the filaments are centered around one point. With increasing values of α, this peak sharpens. For a range of parameter values $\alpha_d \leq \alpha \leq \alpha_c$ an inhomogenous, stationary state coexists with the homogenous state.

3.2.2 Treadmilling and Molecular Motors

As filament polymerization is central to many cellular processes, we extend the minimal model to include such dynamics. We start out with filament treadmilling in the presence of molecular motors but without passive end-tracking cross-linkers. We investigate the influence of filament treadmilling alone, i.e. we do not consider polymerization and depolymerization of entire filaments ($k_\mathrm{p} = 0$, $k_\mathrm{d} = 0$). Treadmilling induces only an orientation dependent drift in an individual filament. The dynamics become more interesting when interactions between filaments, e.g. via cross-linkers are taken into account.

Treadmilling gives rise to active currents of the form

$$J_v^\pm(x) = \pm v c^\pm(x) \quad , \tag{3.43}$$

which have to be added to the active currents $J^\pm$ as introduced in Eqs. (3.37)-(3.38). We note that these currents, like the currents due to interactions between antiparallel filaments, Eq. (3.40), depend on the orientation of the filaments. The sign of the currents is fixed by the fact that filaments grow at their plus end and shrink at their minus end. The dynamical equations are then explicitly (in dimensionless form):

$$\begin{aligned} \partial_t c^+(x) &= \partial_x^2 c^+(x) - \alpha\partial_x \int_0^1 \mathrm{d}\xi \, \left[c^+(x+\xi) - c^+(x-\xi)\right] c^+(x) \qquad (3.44) \\ &\quad + \beta\partial_x \int_{-1}^1 \mathrm{d}\xi \, c^-(x+\xi)c^+(x) - v\partial_x c^+(x) \\ \partial_t c^-(x) &= \partial_x^2 c^-(x) - \alpha\partial_x \int_0^1 \mathrm{d}\xi \, \left[c^-(x+\xi) - c^-(x-\xi)\right] c^-(x) \qquad (3.45) \\ &\quad - \beta\partial_x \int_{-1}^1 \mathrm{d}\xi \, c^+(x+\xi)c^-(x) + v\partial_x c^-(x) \end{aligned}$$

In the following we will see, that although the treadmilling current introduced by Eq. (3.43) seems just a minor change to the whole set of equations, it has a major impact on the system. In particular treadmilling (i) destabilizes the homogenous state, (ii) allows bundle contraction even in the absence of interactions between parallel filaments (i.e. $\alpha_c < 0$, where α_c is the critical value below which the homogenous bundle is stable), (iii) can change the type of bifurcation by which the homogenous state loses stability and finally (iv) increases the contractile tension in a bundle. We will now analyze the stability of the homogenous state on a filament bundle with length $L > 1$, which sheds light on how treadmilling achieves the first three points on the list above. The fourth point is discussed in section 3.2.5.

Linear Stability Analysis

The homogenous state $c^{\pm}(x) = c_0^{\pm}(x)$ is a steady state of Eqs. (3.44) and (3.45). Here we analyze its stability against small perturbations up to linear order and calculate the critical value α_c at which the homogenous state loses stability as a function of the treadmilling speed v. In order to determine the development of a small perturbation $\delta c^{\pm}(x)$ around the homogenous state, we expand the perturbation $\delta c^{\pm}(x)$ in Fourier modes

$$\delta c^{\pm}(x) = \sum_{k=-\infty}^{\infty} c_k^{\pm} \exp(ikx) \quad , \tag{3.46}$$

where $c_k^{\pm}$ are coefficients of the Fourier sum. The details of this calculation are given in appendix A.2. The dynamic equations can be written in a compact way in dimensionless quantities:

$$\partial_t \begin{pmatrix} c_k^+ \\ c_k^- \end{pmatrix} = \begin{pmatrix} \Lambda^{++} & \Lambda^{+-} \\ \Lambda^{-+} & \Lambda^{--} \end{pmatrix} \begin{pmatrix} c_k^+ \\ c_k^- \end{pmatrix} \quad , \tag{3.47}$$

where

$$\Lambda^{\pm\pm} = -k^2 - 2\alpha c_0^{\pm}(\cos k - 1) \pm 2i\beta k c_0^{\mp} \mp ivk \tag{3.48}$$

$$\Lambda^{\pm\mp} = \pm 2i\beta c_0^{\pm} \sin k \tag{3.49}$$

are the matrix elements.

Note that if only filaments of one orientation are present stability is given by the real part of the only eigenvalue Λ^{++} (w.o.l.g). In this case treadmilling does not influence the stability of the homogenous state, because it only enters in the imaginary part of $\Lambda^{\pm\pm}$ while the stability is determined by the real part. Thus we still find $\alpha_c = k^2/2c_0(1-\cos k)$, cf. (Kruse and Jülicher, 2000). Here treadmilling just induces a drift with velocity v in the stationary state, be it homogenous or localized. This of course means that the stationary, localized filament distribution found in fully polar bundles ceases to exist, the peak moves with the treadmilling velocity v.

When filaments of both orientations are present, the stability of the modes is determined by the real part of the eigenvalues of the above matrix:

$$\lambda_{1,2} = \frac{\Lambda^{++} + \Lambda^{--}}{2} \pm \sqrt{\frac{(\Lambda^{++} + \Lambda^{--})^2}{4} + \Lambda^{-+}\Lambda^{+-}} \tag{3.50}$$

We use these expressions to numerically determine the critical value $\alpha_c(v)$, at which the homogenous state is unstable. The results are displayed by the thick lines in Fig. 3.11. We find that treadmilling lowers α_c, i.e. it destabilizes the homogenous state. In the presence of treadmilling the homogenous state can become unstable even in the absence of interactions between parallel filaments ($\alpha = 0$). Interactions between antiparallel filaments ($\beta \neq 0$) are still necessary. If the densities of both filament orientations are equal, a new state emerges. For intermediate values of v the bifurcation becomes stationary (solid line in Fig. 3.11b). The resulting inhomogenous state is thus different from the stationary or oscillatory waves observed without treadmilling. Note however, that unequal concentrations of filaments of opposite orientations ($c_0^+ \neq c_0^-$) suppress the stationary bifurcation. We will see below that polymerization and depolymerization of entire filaments also destroy this stationary bifurcation. This is consistent with the results from stochastic simulations where no stationary states are observed in the presence of treadmilling. This stationary, localized state thus seems to be a particularity of the mean field description. The dependence of $\alpha_c(v)$ on the other parameters is discussed explicitly in appendix A.1.

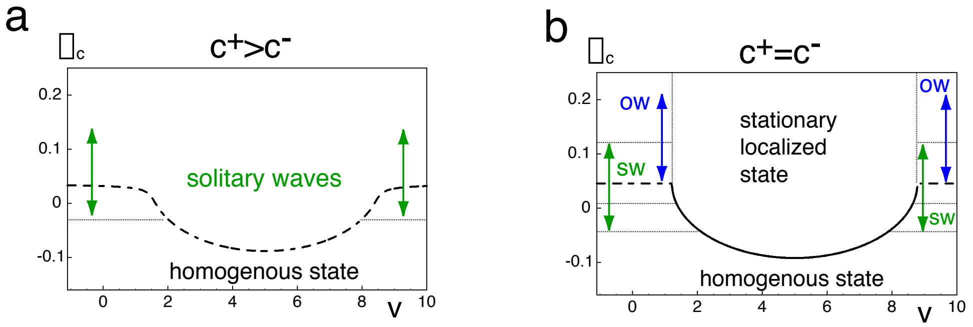

Figure 3.11: State diagram of an active bundle with molecular motors in the presence of treadmilling. Due to treadmilling, the homogenous bundle can be unstable even in the absence of interactions between parallel filaments ($\alpha = 0$). (a) For unequal densities (here $c_0^+ = 32.5, c_0^- = 17.5$) the bifurcation is always of the Hopf kind (thick broken line). The inhomogenous states are always solitary waves. (b) For equal densities of filaments (here $c_0^+ = 25, c_0^- = 25$) stability can be lost via a Hopf bifurcation (broken line) or via a stationary pitchfork bifurcation (solid line). Increasing α causes the solitary waves to undergo another subcritical bifurcation towards oscillatory waves. The interaction strength between antiparallel filaments is β=0.1, the system length is $L = 5$.

State Diagram

While the linear stability analysis reveals the regions where the homogenous state is stable, we need to integrate the dynamic equations (3.44)-(3.45) numerically in order to determine the asymptotic states of the dynamics, i.e. the states the system finally assumes, in the remaining regions. These states are typically stable against perturbations. As already indicated by the linear stability analysis, for unequal densities of plus and minus filaments the phase space features two different regions, Fig. 3.11a. In one region, below the critical $\alpha_c(v)$ the homogenous state is stable against small perturbations. Above the phase boundary solitary waves are the only stable asymptotic solution. While the bifurcation is supercritical in the “valley” of the phase boundary, for small and large values of v it is subcritical, giving rise to regions of coexistence as indicated by the thin dotted lines. An example of a solitary wave is shown in Fig. 3.9. The direction of movement is determined by spontaneous symmetry breaking in the absence of treadmilling and by the orientation of the more abundant type of filaments when treadmilling is present. For $c_0^+ > c_0^-$ for example the peaks will move in the direction of the positive x-axis, the direction of treadmilling of the plus-filaments. Intuitively this solution can be understood as two peaks that are held together by the bundling activity of motor action between parallel filaments (α-term) and run around the ring circumference.

For equal concentrations of plus and minus filaments the phase space is more complex, Fig. 3.11b. Besides the solitary waves, also oscillatory waves and stationary localized states emerge. For small and large treadmilling speeds v, i.e. outside the “valley” the homogenous state loses stability in a series of two subcritical bifurcations, first towards solitary and then towards oscillatory waves. This leads to a region, where all three solutions coexist, as indicated in the figure. For intermediate values of v, i.e. in the valley, stability is lost in a supercritical pitchfork bifurcation towards a stationary, localized state. It corresponds to a ruptured bundle, in which two accumulations of filaments of different orientations are close to each other. Intuitively treadmilling would try to push them through each other

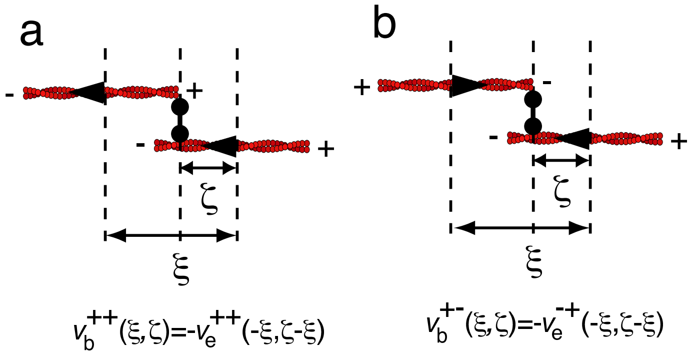
a
-
+
-
+
ζ
ξ
$v_b^{++}(\xi,\zeta)=-v_e^{++}(-\xi,\zeta-\xi)$
b
+
-
-
+
ζ
ξ
$v_b^{+-}(\xi,\zeta)=-v_e^{-+}(-\xi,\zeta-\xi)$

Figure 3.12: Passive cross-linkers bound to at least one depolymerizing end of a filament pair induce relative filament sliding. The velocities of the involved filaments are always of equal magnitude and opposite sign, independent of the relative orientation of filaments which can be (a) parallel or (b) antiparallel.

but the "repulsion" due to motors between antiparallel filaments (β-term) as well as the bundling activity (α-term) do not allow them to pass.

3.2.3 Passive End-Tracking Cross-Linkers

Passive cross-linkers, i.e. proteins that link filaments without actively moving along them, can cause treadmilling to introduce currents in the filament densities beside the treadmilling current itself. One way to achieve this is when these cross-linkers can stay attached to filament ends for some time, cf. Figs. 3.6 and 3.7. Here we derive an expression for these currents and integrate it in our mean field description. We assume again that pairwise interactions dominate. The general symmetry of the forces involved in pairwise filament interactions mediated by cross-linkers has been discussed in section 3.1.3.

Minus-End-Tracking Cross-Linkers

Here we formulate the situation in form of the velocities that passive cross-linkers induce in filaments of length l, as sketched in Fig. 3.6. If the cross-linker is bound to the bulk of both filaments, it does not induce a current. The same is true for a cross-linker at the depolymerizing ends of two parallel filaments. Linked to both minus ends of antiparallel filaments a cross-linker would prevent both filaments from dislocating due to treadmilling - if it does not detach. Here we concentrate on the situation in which a cross-linker is bound to the bulk of one filament (subscript b) and to the depolymerizing end of another (subscript e). The cross-linker then induces a velocity v_e in the filament to whose end it is bound and a velocity $v_\mathrm{b} = -v_\mathrm{e}$ in the other filament, due to conservation of momentum.

Now we derive the currents due to these interactions. For the velocities due to passive cross-linkers the symmetry requirements given in Eqs. (3.28)-(3.31) translate into

$$v_\mathrm{e}^{\pm\pm}(\xi,\zeta) = -v_\mathrm{b}^{\pm\pm}(-\xi,\zeta-\xi) \quad (3.51)$$

$$v_\mathrm{e}^{\pm\mp}(\xi,\zeta) = -v_\mathrm{b}^{\mp\pm}(-\xi,\zeta-\xi) \quad (3.52)$$

$$v_{\{\mathrm{b,e}\}}^{++}(\xi,\zeta) = -v_{\{\mathrm{b,e}\}}^{--}(-\xi,-\zeta) \quad (3.53)$$

$$v_{\{\mathrm{b,e}\}}^{+-}(\xi,\zeta) = -v_{\{\mathrm{b,e}\}}^{-+}(-\xi,-\zeta) \quad . \quad (3.54)$$

where ξ and ζ are the relative distance between the filament centers and the distance to the cross-linker respectively, see Fig. 3.12. Note that due to the distinction between end-bound cross-linkers and those that are bound to the bulk of filaments (subscripts e and b respectively) it is important if the symmetry requirement is due to momentum conservation or space inversion symmetry. Conservation of momentum always links a bulk- to an end-bound cross-linker (Eqs. (3.51) and (3.52)). Space inversion on the other hand changes the sign of all coordinates and orientations, but not the type of attachment (Eqs. (3.53) and (3.54)).

If we assume that the induced velocity is independent of the exact position in the bulk of one filament, ζ, we can furthermore deduce

$$v_{\mathrm{e}}^{\pm\mp}(\xi) = -v_{\mathrm{b}}^{\mp\pm}(-\xi) = v_{\mathrm{b}}^{\pm\mp}(\xi) \quad . \tag{3.55}$$

As for the minimal model outlined in section 3.2, a simple choice for the induced velocities is

$$v_{b,e}^{\pm\pm}(\xi) \sim \mathrm{sgn}(\xi) \tag{3.56}$$

$$v_{b,e}^{\pm\mp}(\xi) \sim \mp 1 \tag{3.57}$$

A filament located at x will be subject to velocities induced by cross-linkers that bind to its bulk as well as cross-linkers that bind to its depolymerizing end. The resulting currents for parallel filaments in dimensionless quantities can then be written as

$$\begin{aligned}
J_{\alpha'}^{++} &= \int_{-1}^{0} \mathrm{d}\,\xi\, c^{+}(x)c^{+}(x+\xi)v_{\mathrm{e}}^{++}(\xi) + \int_{0}^{1} \mathrm{d}\,\xi\, c^{+}(x)c^{+}(x+\xi)v_{\mathrm{b}}^{++}(\xi) \\
&= \int_{0}^{1} \mathrm{d}\,\xi\, c^{+}(x)v_{\mathrm{b}}^{++}(\xi)\left[c^{+}(x+\xi) - c^{+}(x-\xi)\right] \\
&= \alpha' c^{+}(x) \int_{0}^{1} \mathrm{d}\,\xi\, \left[c^{+}(x+\xi) - c^{+}(x-\xi)\right]
\end{aligned} \tag{3.58}$$

$$\begin{aligned}
J_{\alpha'}^{--} &= \int_{0}^{1} \mathrm{d}\,\xi\, c^{-}(x)c^{-}(x+\xi)v_{\mathrm{e}}^{--}(\xi) + \int_{-1}^{0} \mathrm{d}\,\xi\, c^{-}(x)c^{-}(x+\xi)v_{\mathrm{b}}^{--}(\xi) \\
&= \int_{0}^{1} \mathrm{d}\,\xi\, c^{-}(x)v_{\mathrm{e}}^{--}(\xi)\left[c^{-}(x+\xi) - c^{-}(x-\xi)\right] \\
&= \alpha' c^{-}(x) \int_{0}^{1} \mathrm{d}\,\xi\, [c^{-}(x+\xi) - c^{-}(x-\xi)]
\end{aligned} \tag{3.59}$$

where we have used Eq. (3.56) and α' is a dimensionless coupling coefficient.

In conclusion, the action of passive, end-tracking cross-linkers in the presence of treadmilling gives rise to a current exactly equal to the current induced by molecular motors between two parallel filaments, Eq. (3.39). So treadmilling in combination with passive cross-linkers leads to an effective, (generally v-dependent) rescaling of the coupling coefficient α.

The situation is different for antiparallel filaments. A passive cross-linker that is attached to the depolymerizing end of a plus-filament at position x may link to another filament located between $x - l$ and x (x and $x + l$ for a linker attached to a minus filament). If the linker is attached to the bulk of a plus filament at x then it only contributes to the current if it is linked to the end of a minus filament that is located between $x - l$ and

x (x and $x+l$ respectively for a linker in the bulk of a minus filament). This asymmetry is reflected in the integrals of the ensuing currents:

$$\begin{aligned} J_{\beta'}^{+-}(x) &= \int_{-1}^{0} \mathrm{d}\,\xi\, c^{+}(x)c^{-}(x+\xi)v_{\mathrm{e}}^{+-}(\xi) + \int_{-1}^{0} \mathrm{d}\,\xi\, c^{+}(x)c^{-}(x+\xi)v_{\mathrm{b}}^{+-}(\xi) \\ &= \int_{0}^{1} \mathrm{d}\,\xi\, c^{+}(x)c^{-}(x-\xi)(v_{\mathrm{e}}^{+-}(-\xi) + v_{\mathrm{b}}^{+-}(-\xi)) \\ &= -\beta' c^{+}(x) \int_{0}^{1} \mathrm{d}\,\xi\, c^{-}(x-\xi) \qquad (3.60) \\ J_{\beta'}^{-+}(x) &= \int_{0}^{1} \mathrm{d}\,\xi\, c^{+}(x)c^{-}(x+\xi)v_{\mathrm{e}}^{-+}(\xi) + \int_{0}^{1} \mathrm{d}\,\xi\, c^{+}(x)c^{-}(x+\xi)v_{\mathrm{b}}^{-+}(\xi) \\ &= c^{-}(x) \int_{0}^{1} \mathrm{d}\,\xi\, c^{+}(x+\xi)(v_{\mathrm{e}}^{-+}(\xi) + v_{\mathrm{b}}^{-+}(\xi)) \\ &= +\beta' c^{-}(x) \int_{0}^{1} \mathrm{d}\,\xi\, c^{+}(x+\xi) \qquad (3.61) \end{aligned}$$

Here we have used Eq. (3.55) and the simple choice presented in Eq. (3.57). The resulting currents are different from the current due to molecular motors because motors contribute to the current independent of whether they are attached to the ends or the bulk. This leads to a different range of integration from that used in Eq. (3.40) for filaments coupled by motors.

Adding these currents to the minimal model as given by Eqs. (3.44) and (3.45) gives rise to the following dynamic equations:

$$\begin{aligned} \partial_t c^{+}(x) &= \partial_x^2 c^{+}(x) - v\partial_x c^{+}(x) - (\alpha+\alpha')\partial_x c^{+}(x) \int_0^l \mathrm{d}\xi\, c^{+}(x+\xi) - c^{+}(x-\xi) \\ &\quad +\beta'\partial_x \int_0^l \mathrm{d}\xi\, c^{+}(x)c^{-}(x-\xi) + \beta\partial_x \int_{-l}^{l} \mathrm{d}\xi\, c^{+}(x)c^{-}(x+\xi) \qquad (3.62) \\ \partial_t c^{-}(x) &= \partial_x^2 c^{-}(x) + v\partial_x c^{-}(x) - (\alpha+\alpha')\partial_x c^{-}(x) \int_0^l \mathrm{d}\xi\, c^{-}(x+\xi) - c^{-}(x-\xi) \\ &\quad -\beta'\partial_x \int_0^l \mathrm{d}\xi\, c^{-}(x)c^{+}(x+\xi) - \beta\partial_x \int_{-l}^{l} \mathrm{d}\xi\, c^{-}(x)c^{+}(x+\xi) \qquad (3.63) \end{aligned}$$

These equations reflect the fact that the currents due to the interaction between parallel filaments are of equal functional form. In order to simplify the notation we introduce

$$\hat{\alpha} = \alpha + \alpha' \qquad (3.64)$$

the combined coupling coefficient. This is mathematically sensible as both α and α' capture currents of precisely the same form. Their assumed microscopic origin however is different, so that we cannot identify one with the other. So would for instance the absence of treadmilling require that $\alpha' = 0$ while it leaves α unchanged.

Now we investigate how the action of passive cross-linkers influences the dynamics of active filament bundles. We start out by presenting the results regarding the linear stability of the homogenous state under these novel conditions and then briefly discuss the asymptotic dynamics in this setting.

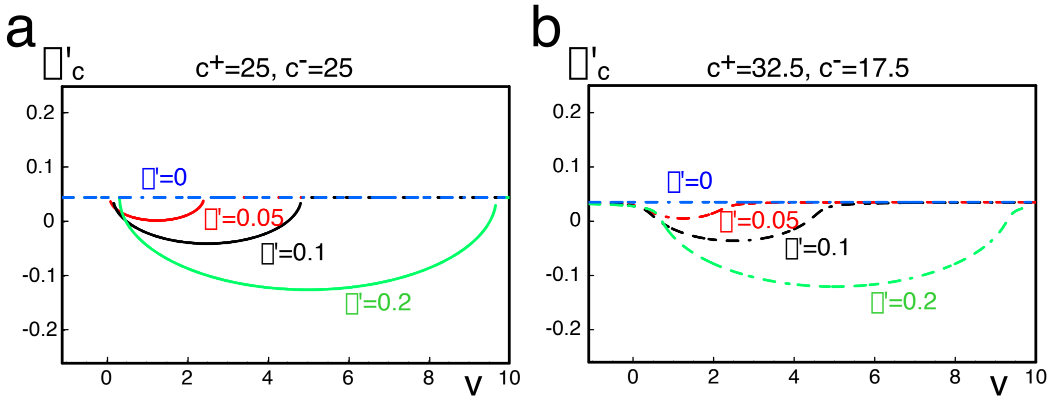

Figure 3.13: Stability boundary of the homogenous state for a bundle with passive cross-linkers in the presence of treadmilling but without molecular motors. Shown is the critical interaction strength $\alpha'_c(v)$ and its dependence on β' for equal concentrations of filaments (a) and for more plus than minus filaments (b). The dependence is very similar to that observed for motors with treadmiling: increasing β' deepens and widens the "valley" in $\alpha'_c(v)$, which for equal concentrations also extends the region of the stationary bifurcation (solid line in (a)), cf. Fig. A.1.

Linear Stability Analysis

Analyzing the stability of the homogenous state up to linear order again leads to Eq. (3.47), but the matrix elements differ. The eigenvalues of the stability matrix are again given by Eq. (3.50). Using the new expressions, we obtain

$$\Lambda^{\pm\pm} = -k^2 \mp ivk - 2\hat{\alpha} c_0^{\pm}(\cos k - 1) \pm (2\beta + \beta')ikc_0^{\mp} \tag{3.65}$$

$$\Lambda^{\pm\mp} = c_0^{\pm}(\pm 2i\beta \sin k - \beta'(e^{\mp ik} - 1)) \tag{3.66}$$

The details of the calculation are given in appendix A.2.

In order to understand the dynamics due to the action of passive cross-linkers, it is instructive to investigate the linear stability of the homogenous state in the absence of molecular motors, i.e. $\alpha = 0$, $\beta = 0$. The resulting function $\alpha'_c(v)$ is displayed in Fig. 3.13. We see immediately that the action of passive cross-linkers gives rise to a qualitatively similar stability boundary, cf. Fig. A.1. Again we find the characteristic "valley" for $\beta' \neq 0$. For equal concentrations of filaments of either orientation the bifurcation in this region is stationary. For unequal concentrations the bifurcation is always of the Hopf kind, i.e. towards oscillating states. Note however that the "valley" is not as wide for a given β' as it would be for β of the same magnitude in the absence of passive cross-linkers, cf. Fig. A.1. It is approximately half as wide and deep for passive cross-linkers between antiparallel filaments. This is intuitively understood as this interaction only applies to filaments that have an overlap with the minus end. Thus we exclude half of the filaments that could interact via motors. It is thus not surprising that the resulting "valley" is only half as big.

The typical shape of $\alpha_c(v)$ also persists, when all interactions are present, Fig. A.3. Note that a "valley" is created for either $\beta \neq 0$ or $\beta' \neq 0$. All other characteristics are unchanged.

State Diagram

The dynamics and state diagram of a bundle with all interactions is qualitatively very similar to the dynamics discussed in section 3.2.2. We again find solitary and oscillatory waves and the overall topology of the state diagram is the same as displayed in Fig. 3.11.‘ In particular stationary localized states are also only found for equal concentrations of plus and minus filaments.

Plus-End-Tracking Cross-Linkers

Until now we have considered the action of cross-linkers that track the minus end of the filaments involved. It is interesting to also consider cross-linkers, that continuously (processively) follow the polymerizing plus end of filament while being bound to another. Some cytoskeletal proteins are know to follow filament ends processively. These include formins that are located at the plus ends of actin filaments, or mitotic centromere-associated kinesin, which has been shown to track the ends of microtubules.

If e.g. formin, while being bound to a filament end links to a second filament, this link together with filament treadmilling will give rise to dynamics sketched in Fig. 3.7. This dynamics is remarkably different from that found for minus-end tracking cross-linkers (3.6b and c). These plus-end tracking cross-linkers tend to align ends of opposite polarity. Parallel filaments are thus driven towards a configuration where their centers are maximally separated, Fig. 3.7a. Antiparallel filaments on the other hand become aligned so that the filament centers coincide. The associated parameters are α'' and β'' respectively.

These intuitive considerations can be formulated in the frame work of the mean field description presented in this section. The corresponding current for parallel filaments is

$$J^{\pm\pm}_{\alpha''} = -\alpha'' c^{\pm}(x) \int_0^1 \mathrm{d}\,\xi \left[c^{\pm}(x+\xi) - c^{\pm}(x-\xi)\right] \tag{3.67}$$

which is exactly the same expression as found for the other currents between parallel filaments, except for the sign. This directly reflects the diametrical action of these plus-end tracking cross-linkers in the presence of filament treadmilling to the action of minus-end tracking cross-linkers considered so far. The current due to interactions between antiparallel filaments is given by

$$J^{\pm\mp}_{\beta''} = \pm\beta'' c^{\pm}(x) \int_0^1 \mathrm{d}\,\xi c^{\mp}(x \pm \xi) \tag{3.68}$$

which is different from the currents in Eqs. (3.60) and (3.61) by sign and range of integration, reflecting the different polarity of the tracked end.

Having obtained these currents it is straightforward to turn the crank and analyze the effects of these novel interactions on the bundle dynamics. We find that these terms stabilize the homogenous state and lower the tension. In fact, an explicit calculation shows that the tension in a homogenous bundle with motors, cross-linkers that track both kinds of ends in the presence of treadmilling is lower than without them (see section 3.2.5).

3.2.4 Polymerization of Entire Filaments

Until now we have considered bundles of filaments in which the the number and orientation of filaments was conserved, as filaments could not entirely (de)polymerize or “flip” their orientation. Now we turn to bundles in which filaments of length l can be generated (polymerized) and destroyed (depolymerized) from a pool of monomers according to the system described by Eqs. (3.34)-(3.36). For simplicity we assume equal polymerization and depolymerization rates for plus and minus filaments, i.e. $k_{\mathrm{d}}^{\pm} = k_{\mathrm{d}}$ and $k_{\mathrm{p}}^{\pm} = k_{\mathrm{p}}$. We first discuss the dynamics of this polymerization and depolymerization from monomers in the absence of treadmilling and molecular motors. Then we describe its influence on the dynamics of an active bundle in which all these effects are present.

Monomer Dynamics

We assume that only whole filaments of length l consisting of μ monomers are polymerized or depolymerized and that the monomers diffuse freely if they are not incorporated in a filament. If filaments of both orientations are polymerized with equal probability, the ensuing description for the dynamics of homogenous filament and monomer distributions in the absence of treadmilling and molecular motors reads:

$$\begin{aligned}
\partial_t c^+ &= k_{\mathrm{p}} c_m - k_{\mathrm{d}} c^+ && (3.69)\\
\partial_t c^- &= k_{\mathrm{p}} c_m - k_{\mathrm{d}} c^- && (3.70)\\
\partial_t c_m &= -2k_{\mathrm{p}}\mu c_m + k_{\mathrm{d}}\mu (c^+ + c^-) && (3.71)
\end{aligned}$$

Thus for any $c_m \in \mathbb{R}^+$ the steady state is given by $c_0^{\pm} = c_m k_{\mathrm{p}}/k_{\mathrm{d}}$. Assume that the total number of monomers M_0 is conserved we write:

$$\begin{aligned}
M_0 &= \mu c^+ + \mu c^- + c_m \\
&= \left(2\mu \frac{k_{\mathrm{p}}}{k_{\mathrm{d}}} + 1\right) c_m && (3.72)
\end{aligned}$$

so that the concentrations of the steady state read

$$m_0 = \frac{k_{\mathrm{d}}}{2\mu k_{\mathrm{p}} + k_{\mathrm{d}}} M_0 \quad \text{and} \quad c_0^+ = c_0^- = \frac{k_{\mathrm{p}}}{k_{\mathrm{d}}} c_m = \frac{k_{\mathrm{p}}}{2\mu k_{\mathrm{p}} + k_{\mathrm{d}}} M_0 \tag{3.73}$$

We consider small small perturbations around this state $c^+ = c_0^+ + \delta c^+$, $c^- = c_0^- + \delta c^-$, $c_m = c_{m,0} + \delta c_m$. The perturbations evolve according to

$$\begin{pmatrix} \delta c^+ \\ \delta c^- \\ \delta c_m \end{pmatrix} = \begin{pmatrix} -k_{\mathrm{d}} & 0 & k_{\mathrm{p}} \\ 0 & -k_{\mathrm{d}} & k_{\mathrm{p}} \\ \mu k_{\mathrm{d}} & \mu k_{\mathrm{d}} & -2\mu k_{\mathrm{p}} \end{pmatrix} \begin{pmatrix} \delta c^+ \\ \delta c^- \\ \delta c_m \end{pmatrix} \tag{3.74}$$

The eigenvalues of this matrix are

$$\begin{aligned}
\lambda_0 &= -k_{\mathrm{d}} && (3.75)\\
\lambda_{1/2} &= \frac{1}{2}\left(-k_{\mathrm{d}} - 2\mu k_{\mathrm{p}} \pm \sqrt{(k_{\mathrm{d}} - 2\mu k_{\mathrm{p}})^2 + 8\mu k_{\mathrm{p}} k_{\mathrm{d}}}\right) = 0 && (3.76)
\end{aligned}$$

so that the steady state is always marginally stable.

Note that the density of free monomers m is a free parameter in this model. For given rates we can thus choose any concentrations $c_0^+ = c_0^- = c_{m,0}\, k_{\mathrm{p}}/k_{\mathrm{d}}$ as steady state. Alternatively we can fix $c_{m,0}$ by assuming conservation of the total monomer concentration M_0 as shown above. This makes M_0 the free parameter. The steady state concentrations of plus and minus filaments can be adjusted separately by choosing the (de)polymerization rates accordingly.

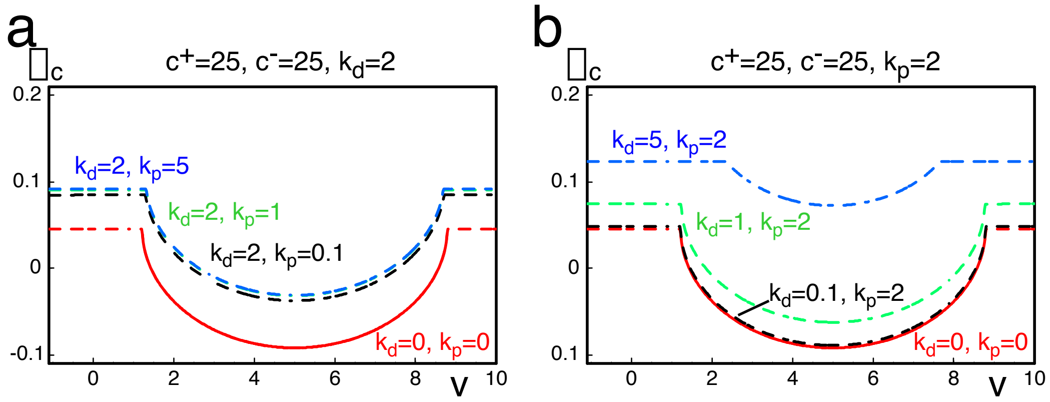

Figure 3.14: Dependence of the stability of the homogenous state on the polymerization and depolymerization rates. Graphs show $\alpha_c(v)$ for (a) a fixed depolymerization rate k_d and varying k_p and (b) a fixed polymerization rate k_p and varying k_d. The red line marks the stability in the absence of any polymerization and depolymerization. Parameters are $c_0^+ = 25$, $c_0^- = 25$, $\beta = 0.1$, $L = 5$.

Linear Stability Analysis

Considering an active bundle with motors, treadmilling and passive cross-linkers in the presence of filament polymerization and depolymerization we obtain for the linear stability of the homogenous state:

$$\partial_t \begin{pmatrix} c_k^+ \\ c_k^- \\ c_{m,k} \end{pmatrix} = \begin{pmatrix} \Lambda^{++} & \Lambda^{+-} & \Lambda^{+m} \\ \Lambda^{-+} & \Lambda^{--} & \Lambda^{-m} \\ \Lambda^{m+} & \Lambda^{m-} & \Lambda^{mm} \end{pmatrix} \begin{pmatrix} c_k^+ \\ c_k^- \\ c_{m,k} \end{pmatrix} \quad . \tag{3.77}$$

The matrix elements are given by

$$\Lambda^{\pm\pm} = -k^2 \mp ivk - 2\hat{\alpha} c_0^{\pm}(\cos k - 1) \pm (2\beta + \beta')ikc_0^{\mp} \tag{3.78}$$

$$\Lambda^{\pm\mp} = c_0^{\pm}(\pm 2i\beta \sin k - \beta'(e^{\mp ik} - 1)) \tag{3.79}$$

$$\Lambda^{mm} = -D_m k^2 - 2\mu k_\mathrm{p} \tag{3.80}$$

$$\Lambda^{m\pm} = \mu k_\mathrm{d} \tag{3.81}$$

$$\Lambda^{\pm m} = k_\mathrm{p} \quad . \tag{3.82}$$

The resulting stability boundaries for equal rates k_d and k_p are displayed in Fig. A.4. Filament turnover stabilizes the homogenous state. This can be credited to the action of depolymerization: large rates of filament depolymerization k_d stabilize the homogenous state by shifting the stability boundary to larger values of α_c, Fig. 3.14b. Due to the faster depolymerization it is more difficult to locally exceed a critical concentration necessary for bundle contraction. Varying $c_0^{\pm}$ has similar effects on the stability boundary. Enlarging the polymerization rate k_p on the other hand has no major effects on the stability of the homogenous state, Fig. 3.14a. The asymptotic dynamics are the same as those found in the absence of polymerization and depolymerization, see above.

3.2.5 Tension

Given the filament distributions in a bundle, the tension Σ in this bundle can be calculated as discussed in (Kruse and Jülicher, 2003). To this end the contributions of all filaments to the tension at a point x are summed up (only filaments that overlap with x can contribute, of course):

$$\Sigma(x) = \int dx' \ \left[\sigma^+(x',x) + \sigma^-(x',x)\right] \quad . \tag{3.83}$$

Here $\sigma^\pm(x',x)$ is the tension at x due to plus- and minus-filaments with centers at x'. Formally these tensions are obtained from the tension defined in Eq. (3.11) through $\sigma^+(x',x) = \sigma(x', \boldsymbol{e}_x, s)$ with $x = x' + s$ and analogously for σ^-.

In the absence of external forces and taking into account momentum conservation one obtains

$$\frac{\mathrm{d}}{\mathrm{d}y}\Sigma(y) = \int \mathrm{d}x \left[f_{\mathrm{fl}}^+ + f_{\mathrm{fl}}^- + f_{\mathrm{m}}^+ + f_{\mathrm{m}}^-\right] \quad , \tag{3.84}$$

which permits the calculation of the tension when the filament currents are known. The total tension in the bundle can be split in parts corresponding to the interaction of parallel filaments $\Sigma_{\rightrightarrows}$ and antiparallel filaments $\Sigma_{\rightleftarrows}$

$$\Sigma(y) = \Sigma_{\rightrightarrows}(y) + \Sigma_{\rightleftarrows}(y) \quad . \tag{3.85}$$

From equation (3.84) it follows

$$\Sigma_{\rightrightarrows}(y) \ = \ -\eta \int \mathrm{d}x (J^{++}(x) + J^{--}(x)) Q(x-y) + \Sigma_{\rightrightarrows}^{(0)} \tag{3.86}$$

$$\Sigma_{\rightleftarrows}(y) \ = \ -\eta \int \mathrm{d}x (J^{+-}(x) + J^{-+}(x)) Q(x-y) + \Sigma_{\rightleftarrows}^{(0)} \quad , \tag{3.87}$$

where $(\mathrm{d}/\mathrm{d}x)Q(x) = R(x)$ with $Q(0) = 0$ and $\Sigma_{\rightrightarrows}^{(0)}$ and $\Sigma_{\rightleftarrows}^{(0)}$are constants of integration. To stress the point that tension is a local quantity, the authors introduce the function $P(x,\xi) = Q(x+\xi) - Q(x)$.

For the microscopic mean field description introduced in this chapter we set $R(x) = 1$ for $|x| < l/2$ and $R(x) = 0$ otherwise. We can thus calculate the contributions from the currents due to molecular motors and treadmilling introduced in Eqs. (3.39)-(3.43) and those due to the interaction via passive cross-linkers, Eqs. (3.58)-(3.61). We obtain as expressions for tension due to the interaction of parallel filaments

$$\begin{aligned}\Sigma_{\rightrightarrows}(y) \ = \ & \frac{1}{2}(\alpha+\alpha')\eta \int_{-l}^{l} \mathrm{d}\xi \int \mathrm{d}x \, c^+(x) c^+(x+\xi) \mathrm{sgn}(\xi) P(x-y,\xi) \\ & + \frac{1}{2}(\alpha+\alpha')\eta \int_{-l}^{l} \mathrm{d}\xi \int \mathrm{d}x \, c^-(x) c^-(x+\xi) \mathrm{sgn}(\xi) P(x-y,\xi)\end{aligned} \tag{3.88}$$

and antiparallel filaments

$$\begin{aligned}\Sigma_{\rightleftarrows}(y) \ = \ & \frac{1}{2}\eta \Bigg[-\beta \int_{-l}^{l} \mathrm{d}\xi \int \mathrm{d}x \, c^+(x) c^-(x+\xi) P(x-y,\xi) \\ & + \beta \int_{-l}^{l} \mathrm{d}\xi \int \mathrm{d}x \, c^-(x) c^+(x+\xi) P(x-y,\xi) \\ & - \beta' \int_{0}^{l} \mathrm{d}\xi \int \mathrm{d}x \, c^+(x) c^-(x-\xi) P(x-y,-\xi) \\ & + \beta' \int_{0}^{l} \mathrm{d}\xi \int \mathrm{d}x \, c^-(x) c^+(x+\xi) P(x-y,\xi) \Bigg] \quad ,\end{aligned} \tag{3.89}$$

where we have dropped constant contributions arising from the boundaries. Note that for periodic boundary conditions these boundary terms must vanish.

The tension in a homogenous bundle $c^{\pm}(x) = c_0^{\pm}$ is given by

$$\Sigma_0 = \frac{1}{2}\eta l^3 \left[(\alpha+\alpha')(c_0^{+2}+c_0^{-2}) + \beta' c_0^+ c_0^-\right] \quad . \tag{3.90}$$

A positive Σ corresponds to contractile tension in the bundle. Note that in a homogenous bundle only motors between parallel filaments (α) contribute to the tension, while passive cross-linkers contribute always (α', β'). This is due to the symmetry of the integrals from $-l$ to l in Eq. (3.89) for the homogenous state. The contributions of the first two terms then exactly cancel. This is not the case for passive cross-linkers as this interaction is intrinsically asymmetric.

It is straightforward to extend the above calculation to include the action of passive, plus-end-tracking cross-linkers (Fig. 3.7). We find that these terms stabilize the homogenous state and lower the tension. Our calculation shows that the tension in a homogenous bundle with motors, cross-linkers that track both kinds of ends in the presence of treadmilling is explicitly given by

$$\Sigma_0 = \frac{1}{2}\eta l^3 \left[(\alpha+\alpha'-\alpha'')(c_0^{+2}+c_0^{-2}) + (\beta'-\beta'') c_0^+ c_0^-\right] \tag{3.91}$$

The action of plus-end tracking cross-linkers thus lowers the tension in homogenous bundles.

In muscle myofibrils the tension generation is due to motors linking antiparallel filaments only. This difference is due to the different symmetries of both structures. In myofibrils the filament position is very well defined and due to the attachment to the Z-disk filament centers never slide past each other. In filament bundles that lack this strict organization, antiparallel filaments will be positioned randomly with respect to each other and thus on average not contribute to the tension. In contractile rings or stress fibers no structuring elements such as Z-disks have been found. Furthermore the density seems to be homogenous along the ring circumference. These observations shed light on motor mediated interactions between parallel filaments for contractility.

Such a bundle may exert contractile forces. A ring can contract radially due to the tension generated along its circumference, see chapter 6. A bundle with two open ends, such as a stress fiber can pull on structures attached to its ends. Consider a homogenous bundle with $c^{\pm}(x) = c_0^{\pm}$ inside a box $0 \le x \le L$ of size L and $c^{\pm}(x) = 0$ elsewhere in the absence of treadmilling. With boundary conditions that immobilize filaments within the intervals $[0, l]$ and $[L-l, L]$, this state is stable for $\alpha < \alpha_c$ on the interval $[l, L-l]$.

The force balance equation (3.11) is only satisfied if a force density

$$f_{\text{ext}}(x) = \eta l (l-x)\left[\alpha(c_0^{+2}+c_0^{-2})\right] \tag{3.92}$$

on $x \in [0, l]$ is applied. Not immobilized filaments on $[0, l]$ would flow according to

$$J^{\pm\pm}(x) = \alpha c_0^{\pm 2}(l-x) \tag{3.93}$$

$$J^{+-}(x) = -\beta c_0^+ c_0^-(l+x) \tag{3.94}$$

$$J^{-+}(x) = \beta c_0^+ c_0^-(l+x) \tag{3.95}$$

These fluxes are due to internal forces (cf. Eq. (3.16)). So the external force density, i.e. the strength with which the bundle pulls on the boundaries is determined by

$$\eta l \left(J^{++}(x) + J^{--}(x) + J^{+-}(x) + J^{-+}(x)\right) = -\int \mathrm{d}y \left[f_{\text{int}}(x,y) + f_{\text{ext}}(x,y)\right] = 0 \quad . \tag{3.96}$$

3.3 Stochastic Simulation of Active Filament Bundles

Stochastic simulations provide an intuitive way of approaching the physics of active bundles. Assuming that filament pairs in the bundle are temporarily cross-linked by motor aggregates that move towards the plus ends of filaments and briefly stay attached at the filament end, we define a simple model for the bundle dynamics, which we study using stochastic simulations. Filaments can interact if they overlap along the bundle axis x. We randomly select pairs of overlapping filaments. At each time-step of duration Δt, an interaction between the two filaments of the pair via a molecular motor occurs with probability $\bar{\alpha}\Delta t$, if filaments are parallel, and $\bar{\beta}\Delta t$, if the filaments are antiparallel. Parameters dressed with a bar correspond to the naked parameters in the mean field description, see section 3.4 for details. If the interaction occurs, both filaments are displaced by a distance δ, the working distance of a molecular motor (cf. Fig 3.2), according to the rules indicated in Fig. 3.5. Assuming that the motors diffuse rapidly, we use a constant and homogenous motor concentration for simplicity. We start our simulations from initially homogenous profiles of filament density $\bar{c}^+(x) = \bar{c_0}^+$ and $\bar{c}^-(x) = \bar{c_0}^-$ along the x coordinate, where $\bar{c}^{\pm}(x)$ denote the number densities of filaments with center at position x and their plus ends pointing in positive and negative x-direction, respectively. In order to capture the dynamics of a filament ring, we impose periodic boundary conditions $\bar{c}(x) = \bar{c}(x + L)$, where $L = 2\pi R$ is the circumference of a ring with radius R. Simulations reveal that for weak interactions between parallel filaments (corresponding to $\bar{\alpha}$ being smaller than a critical value $\bar{\alpha}_c$) the homogeneous bundle is stable. This is independent of the value of $\bar{\beta}$ characterizing the interaction of antiparallel filaments. If $\bar{\alpha}$ exceeds the critical value $\bar{\alpha}_c$, the homogeneous bundle is unstable and develops into an inhomogenous density profile that can be stationary or lead to complex dynamics after long times, which include propagating density profiles. Note, that our stochastic simulations also include fluctuations, captured by an effective diffusion constant $\bar{D}$. Examples of simulation results are shown in Figs. 3.15 and 3.16. If the ring ruptures, stationary density profiles can be attained where the filaments of opposite orientation are localized and completely separated. The homogenous bundle con only contract the ring, when it is stable (see chapter 6 for a detailed discussion of ring contraction). Indeed, filaments are constantly moved relative to each other and motors exert forces on filaments in the stable, homogeneous bundle. As discussed in section 3.2, this generates a net contractile tension in the bundle, which we can estimate with the mean field description (cf. section 3.2.5). In the spirit outlined here we also include filament treadmilling, and the action passive cross-linkers in our simulations. The details of the stochastic simulations are outlined in the next section (3.3.1). Then we present the dynamics of active filament bundles as obtained by stochastic simulations in section 3.3.2. Finally we conclude this section by calculating the filament currents in such bundles in section 3.3.3.

3.3.1 Stochastic Simulation

We study the behavior of N individual filaments of length l along a linear position coordinate x. We impose periodic boundary conditions with period L, corresponding to a ring with circumference L. The position of the center of filament i with $i = 1, .., N$ is denoted by x_i. Its orientation with respect to the positive x-axis is denoted by o_i: this orientation is $o_i = +1$ if the plus end points in positive x-direction, $o_i = -1$ implies that the minus end points in x-direction. At every timestep of duration Δt, each filament is displaced by a distance Δ_i as a result of diffusion, treadmiling, and the interaction with molecular motors and with passive cross-linkers. Furthermore, filaments are removed and created at

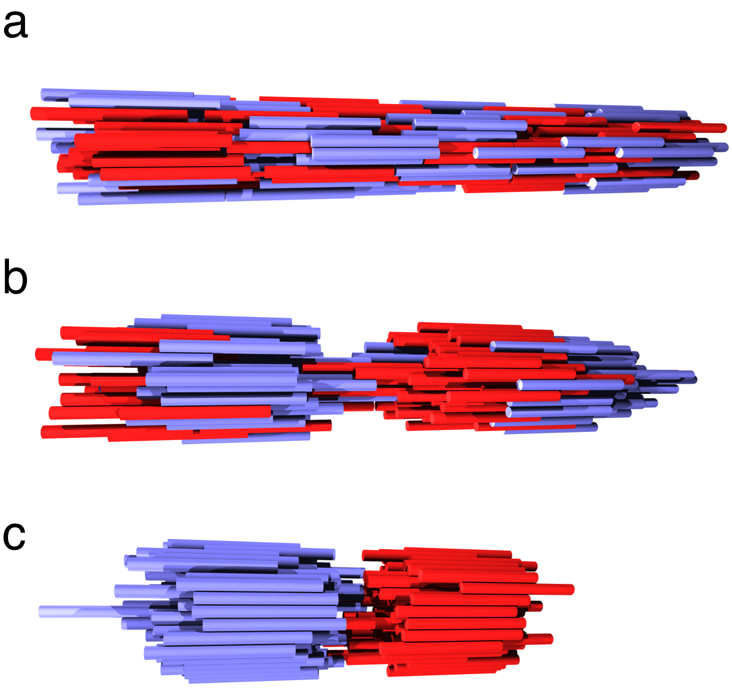

Figure 3.15: Instability of an active filament bundle obtained by a stochastic simulation of 125 plus filaments (blue) and same number of minus filaments (red). Graphs thus represent a total of 250 aligned filaments in one dimension without treadmilling but in the presence of molecular motors. A homogenous bundle (a) can be stable. If the interaction strength of parallel filaments exceeds a critical value, such a state becomes unstable and evolves towards an in-homogeneous filament distribution (a-c). (a) at time $t = 0$, the initial bundle is homogeneous. (b) At $t = 0.75 l^2/\bar{D}$, the bundle becomes unstable and reaches a stable sorted filament configuration at $t = 1000 l^2/\bar{D}$ displayed in (c). Parameters are $\bar{\alpha} l^2/\bar{D} = 40$, $\bar{\beta} l^2/\bar{D} = 40$, $L/l = 5$, $\delta/l = 0.005$ (no treadmilling, i.e. $\bar{v} = 0$, $\bar{\alpha}' = \bar{\beta}' = 0$).

arbitrary position to capture effects of polymerization and depolymerization of filaments. We assume that filaments cannot change their orientation.

Diffusion is described by a random displacement $\Delta_i^{(D)}$ with zero average and Gaussian distribution with variance $\bar{D}\Delta t$:

$$P(\Delta_i^{(D)}) = \frac{1}{\sqrt{2\pi \bar{D}\Delta t}} \exp\left(-\frac{{\Delta_i^{(D)}}^2}{2\bar{D}\Delta t}\right) \tag{3.97}$$

where the parameter $\bar{D}$ is the effective diffusion coefficient of filaments of length l, capturing thermal fluctuations as well as some fluctuations due to active stochastic events, such as the action of molecular motors.

Treadmilling of filaments is characterized by the treadmilling speed $\bar{v}$. Per time step Δt the filaments are displaced by

$$\Delta_i^{(v)} = o_i \bar{v} \Delta t \quad . \tag{3.98}$$

Note that the direction of displacement depends on the filament orientation o_i. If two filaments overlap, i.e. $|x_i - x_j| < l$, they may interact via molecular motors or passive

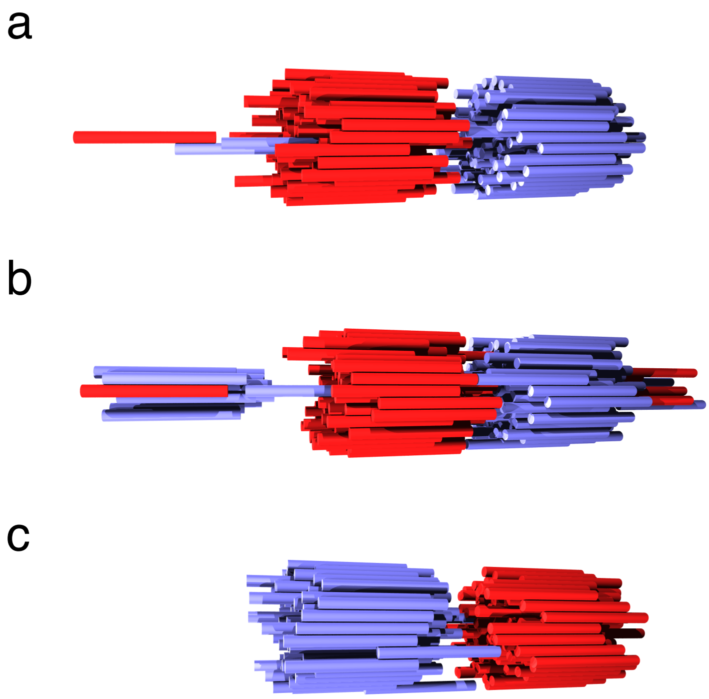

Figure 3.16: The two sorted, concentrated filament groups fluctuate and can pass through each other. Shown are three states of the bundle in Fig. 3.15 at three different times (a) $t = 911 l^2/\bar{D}$, (b) $t = 913 l^2/\bar{D}$ and (c) $t = 915 l^2/\bar{D}$).

cross-linkers. This is captured by determining stochastically for each filament if it interacts with another filament during a given time step.

The interaction between parallel filaments due to motor dimers is described as follows: For each filament i we count all candidates ($n_i^{(c,\alpha)}$) for interaction. Candidates are filaments that have the appropriate orientation and overlap with i. The probability of an interaction between filament i and a candidate filament to take place during the time interval Δt is then given by

$$p_i^{(\alpha)} = \bar{\alpha} n_i^{(c,\alpha)} \Delta t \in [0;1] \quad . \tag{3.99}$$

Here $\bar{\alpha}$ is the rate of interactions between parallel filaments due to molecular motors in the stochastic simulation. The time step Δt has to be chosen small enough, so that p_i is always smaller than 1. If $p_i^{(\alpha)}$ is larger than a random number drawn from a uniform distribution on $[0;1]$, a filament k is chosen at random from the candidate filaments. The displacements for the two parallel filaments i and k then depend on their relative positions (cf. Fig 3.17):

$$\Delta_i^{(\alpha)} = \frac{\delta}{2}, \; \Delta_k^{(\alpha)} = -\frac{\delta}{2} \quad \text{for} \quad x_i < x_k \tag{3.100}$$

$$\Delta_i^{(\alpha)} = -\frac{\delta}{2}, \; x_k^{(\alpha)} = \frac{\delta}{2} \quad \text{for} \quad x_i > x_k \tag{3.101}$$

respecting the conservation of momentum of the filament pair. Here we have assumed that during the time Δt only one motor executes a power stroke, so that δ is the working distance of one motor head (Howard, 2001). Multiple powerstrokes during a time step Δt can be captured by using multiples of δ in Eqs. (3.100) and (3.101).

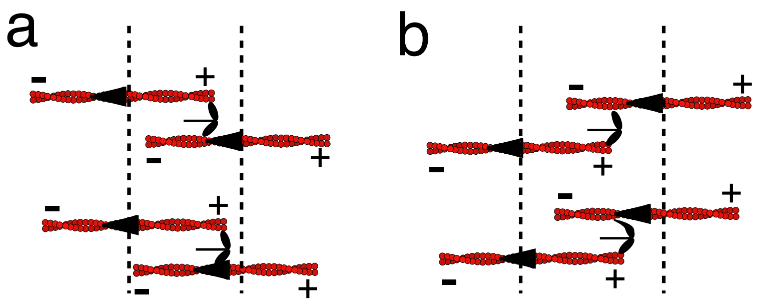

Figure 3.17: For parallel filaments the direction of filament sliding depends on their relative position. The vertical dashed lines mark the initial positions of the filament centers (top). After the action of the molecular motors the filaments have shifted (bottom). Both filaments in a pair move in mutually opposite directions due to conservation of momentum. (a) The top filament is located left of the other filament and moves to the right. (b) The top filament is located right of the other and moves to the left.

The interaction between antiparallel filaments due to molecular motors is very similar. In this case filaments have to be of opposite orientations and the probability for an interaction to occur is given by

$$p_i^{(\beta)} = \bar{\beta} n_i^{(c,\beta)} \Delta t \in [0;1] \quad . \tag{3.102}$$

where $\bar{\beta} \in [0;(N\Delta t)^{-1}]$ is the rate of interactions between antiparallel filaments due to molecular motors in the stochastic simulation, similar to $\bar{\alpha}$ in Eq. (3.99). The change in filament position however now depends on filament orientation and not on the relative position:

$$\Delta_i^{(\beta)} = \frac{\delta}{2},\ \Delta_k^{(\beta)} = -\frac{\delta}{2} \quad \text{for} \quad o_k = 1 \tag{3.103}$$

$$\Delta_i^{(\beta)} = -\frac{\delta}{2},\ \Delta_k^{(\beta)} = \frac{\delta}{2} \quad \text{for} \quad o_k = -1 \quad . \tag{3.104}$$

Passive cross-linkers are described by similar procedures. The dynamics for parallel filaments is identical for motors or passive cross-linkers, so that the stochastic procedures for cross-linkers and motors between parallel filaments are the same. The only difference is that passive cross-linker interaction occurs with rate $\bar{\alpha}'$ and that filaments are moved by the length of a monomer a instead of the working distance δ. For antiparallel filaments the interaction occurs with rate $\bar{\beta}'$. The dynamics is however different from that induced by motors. As a passive cross-linker is only effective when attached to a minus end, the range of positions of candidate filaments $\{j\}$ then depends on the orientation of the reference filament i:

$$0 < x_i - x_j < l \quad \text{for} \quad o_i = 1 \tag{3.105}$$

$$0 < -(x_i - x_j) < l \quad \text{for} \quad o_i = -1 \quad . \tag{3.106}$$

In this position range, only filaments of the opposite orientation $o_i = -o_j$ are candidates.

The filament displacements are similar to those in Eqs. (3.103) and (3.104). Here we replace the motor working distance δ by the monomer length a:

$$\Delta_i^{(\beta')} = \frac{a}{2},\ \Delta_k^{(\beta')} = -\frac{a}{2} \quad \text{for} \quad o_k = 1 \tag{3.107}$$

$$\Delta_i^{(\beta')} = -\frac{a}{2},\ \Delta_k^{(\beta')} = \frac{a}{2} \quad \text{for} \quad o_k = -1 \quad . \tag{3.108}$$

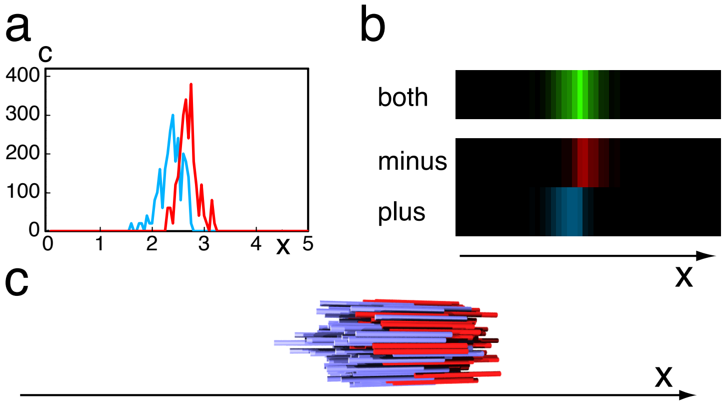

Figure 3.18: Asymptotic state of an active filament bundle with equally many plus and minus filaments in the presence of treadmilling and passive cross-linkers, but without molecular motors. (a) Instantaneous number density of filaments along the bundle axis. Filaments are identified with their centers of mass. (b) Graph displaying fluorescence like representation of this state. The intensity increases proportional to the number of filaments present. All monomers of a filament contribute to the fluorescence at their respective position. (c) Representation of the bundle state by rods. Plus filaments are represented by blue rods, minus filaments by red rods. Parameters are $N^+ = 125$, $N^- = 125$, $\bar{\alpha}' = 40$, $\bar{\beta}' = 40$, $\bar{v} = 1$, $\bar{D} = 1$, $L = 5$.

The new position at time $t + \Delta t$ is finally determined by

$$\begin{aligned} x_i(t + \Delta t) &= x_i(t + \Delta t) + \Delta_i^{(D)} + \Delta_i^{(v)} \\ &\quad + \Delta_i^{(\alpha)} + \Delta_i^{(\beta)} + \Delta_i^{(\alpha')} + \Delta_i^{(\beta')} \end{aligned} \tag{3.109}$$

Besides being displaced individual filaments are depolymerized with rate $\bar{k}_d$ and simply vanish. The steady state number of filaments is given by $N_0 = \bar{k}_p/\bar{k}_d$. During each time step filaments are generated with probability $\bar{k}_p \Delta t$. Their position and orientation are random.

Periodic boundary conditions are modeled by allowing filaments to interact across the 0-L border. This is done by mapping filaments in $[0; l/2]$ to $[L, L + l/2]$ and the other way analogously. Filaments are also allowed to dislocate freely across this boundary. Fixed boundary conditions do not allow interaction nor displacement across 0-L.

Parameters used in the simulations are $L = 5\,l$, $\delta = 0.005\,l$, $a = (1/370)\,l$, $\bar{\alpha} l^2/\bar{D} = 40$, $\bar{\beta} l^2/\bar{D} = 40$, $\bar{\alpha}' l^2/\bar{D} = 40$, $\bar{\beta}' l^2/\bar{D} = 40$, $v l/\bar{D} = 1$, $\bar{k}_p l^2/\bar{D} = 0$, $\bar{k}_d l^2/\bar{D} = 0$, unless stated otherwise.

Experimental measurements reveal a typical value for the distance covered by one powerstroke of a myosin motor of $\delta = 5\,\text{nm}$ (Howard, 2001; Veigel et al., 1999, 1998). One micrometer of actin filament contains 370 monomers (Pollard and Borisy, 2003). For filaments of length $l = 1\,\mu\text{m}$ the values for δ and a thus faithfully reflect the ratios $l/\delta = 200$ and $l/a = 370$ as measured for myosin (Howard, 2001) and actin (Pollard and Borisy, 2003) respectively.

3.3.2 Stochastic Filament Dynamics in Bundle Geometry

We use these stochastic simulations to explore the dynamics of active filament bundles. Here we focus on interactions due to treadmilling and passive cross-linkers. The dynamics caused by molecular motors in the presence of treadmilling is qualitatively identical.

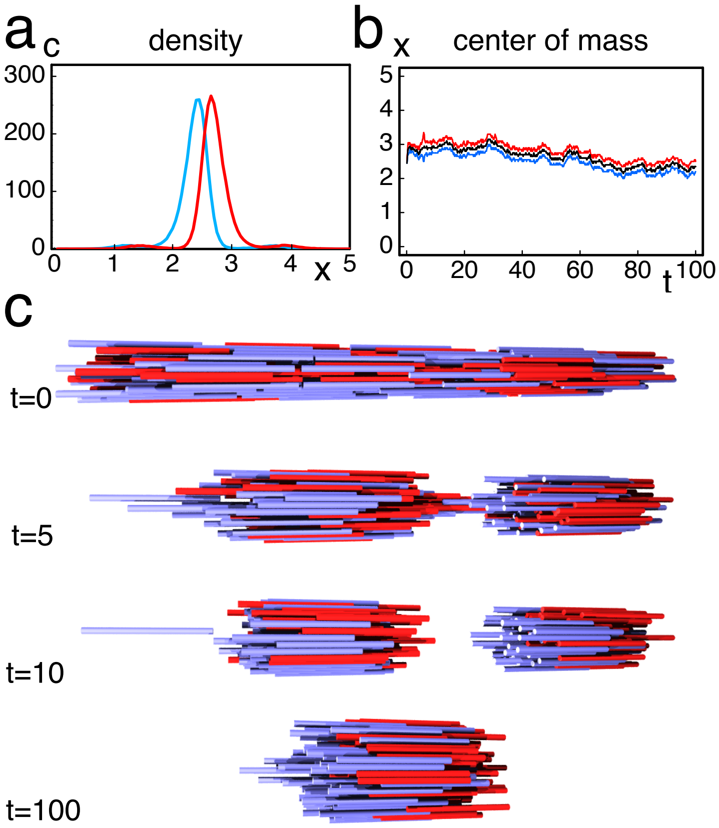

Figure 3.19: Dynamics of the active bundle introduced in Fig. 3.18. (a) Filament density averaged over the whole trajectory. (b) Position of the center of mass of both filament distributions and the whole system as a function of time. (c) Filaments represented by rods (blue corresponds to plus filaments and red to minus filaments) at four time steps showing how the bundle contracts. Parameters are $N^+ = 125$, $N^- = 125$, $\bar{\alpha}' = 40$, $\bar{\beta}' = 40$, $\bar{v} = 1$, $\bar{D} = 1$, $L = 5$.

We consider bundles of length L with periodic boundary conditions, corresponding to filament rings. We study two distinct instructive cases,

- a bundle with an equal number of plus and minus filaments (Fig. 3.18 and 3.19) and
- a bundle with more plus than minus filaments (Fig. 3.20).

We use dimensionless time and space coordinates $\tilde{t} = t\bar{D}/l^2$, $\tilde{x} = x/l$, as well as parameters $\tilde{\bar{\alpha}} = \bar{\alpha} l^2/\bar{D}$, $\tilde{\bar{\beta}} = \bar{\beta} l^2/\bar{D}$, $\tilde{\bar{\alpha}}' = \bar{\alpha}' l^2/\bar{D}$, $\tilde{\bar{\beta}}' = \bar{\beta}' l^2/\bar{D}$, and $\tilde{\bar{v}} = \bar{v} l/\bar{D}$. From here on we drop the tilde for better readability and without fear of confusion.

Independent of the relative number of filaments, both bundles contract under the action of passive cross-linkers and treadmilling, if $\bar{\alpha}'$ is larger than a critical value $\bar{\alpha}'_c$. The bundles evolve from a homogenous random distribution to a compact aggregate of filaments. We analyze the bundle evolution by computing the number density of filaments of each orientation at each time step. Figure 3.18a shows an example of a contracted bundle with an equal number of plus and minus filaments. The density at each time step is not smooth because filaments are discrete. The configuration of the bundle is also displayed by a plot of mock fluorescence in part b and by little rods in part c of the same figure.

Averaging the filament densities over time we gain some insight into the collective dynamics of the bundle. Figure 3.19a shows an example of such filament distributions averaged over a total time of $t = 100$ for the same bundle as displayed in Fig. 3.18. The peaks of the two densities are clearly separated. Part b of this figure shows the position of the center of mass of both distributions and the whole system as a function of time. We observe that the center of mass fluctuates around a mean position. This is different when one filament orientation dominates in the bundle, see below. Figure 3.19c displays representations of the bundle at different points in time, showing how treadmilling and passive cross-linkers contract the bundle. The graphics also indicate that the bundle contracts quickly, so that $t = 100$ is sufficient to attain the asymptotic state of the dynamics. The observed dynamics can be understood intuitively as follows: the action of passive cross-linkers between parallel filaments makes the filaments aggregate in two groups, one for each orientation. These groups would now move depending on their orientation due to treadmilling. The repelling action of cross-linkers between antiparallel filaments however, prevents the two groups of passing through each other. They will thus fluctuate around a mean position due to the stochastic nature of the interactions, but will not pass through each other or show directed movement. This is precisely what we observe in these stochastic simulations.

While the overall contraction dynamics is similar for unequal numbers of filaments of either orientation, the center of mass of the system moves along the x-axis. The direction of this movement is determined by the filament orientation that is more abundant, see below.

The filament densities in such a bundle are different, Fig. 3.20a. The center of mass of the bundle now periodically travels around the ring circumference, as shown in Fig. 3.20b. The direction of motion is determined by the orientation of the bigger number of filaments, in this case the plus filaments, hence the center of mass moves in positive x-direction (note that for periodic boundary conditions we identify $L = 0$). The bundle dynamics is represented also with rods, highlighting the initial contraction phase. Again we can understand this type of dynamics intuitively by considering that of the two unequal aggregates of filaments that are held together by the interaction between parallel filaments and that cannot pass through each other due to the interaction between antiparallel filaments, the bigger one “wins”, i.e. it is potent enough to make its treadmilling direction the direction of motion of the whole system and “push” the smaller aggregate in front of it against its treadmilling direction.

While most aspects of the dynamics found for passive cross-linkers are exactly the same for interactions mediated by motors, there is a difference: passive cross-linkers do not give rise to any dynamics in the bundle in the absence of treadmilling ($\bar{v} = 0$), while motor of course still can do so (Fig. 3.15). Also it seems that the passing of filament aggregates through each other occurs more frequently in the absence of treadmilling.

3.3.3 Currents in the Stochastic Simulations

The dynamic processes described in the previous section lead to filament currents in the ring. In order to describe the currents, it is useful to define the local filament density $\bar{c}$: let $\bar{c}^{\pm}(x)\Delta x$ be the number of plus (minus) filaments in the interval $[x - \Delta x/2, x + \Delta x/2]$. The current due to treadmilling is then given by

$$J_{\bar{v}}^{\pm}(x) = \pm \bar{v} \bar{c}^{\pm}(x) \tag{3.110}$$

For the interaction of pairs of parallel filaments due to molecular motors the current is proportional to the number of filaments times their probability to move. Here we have

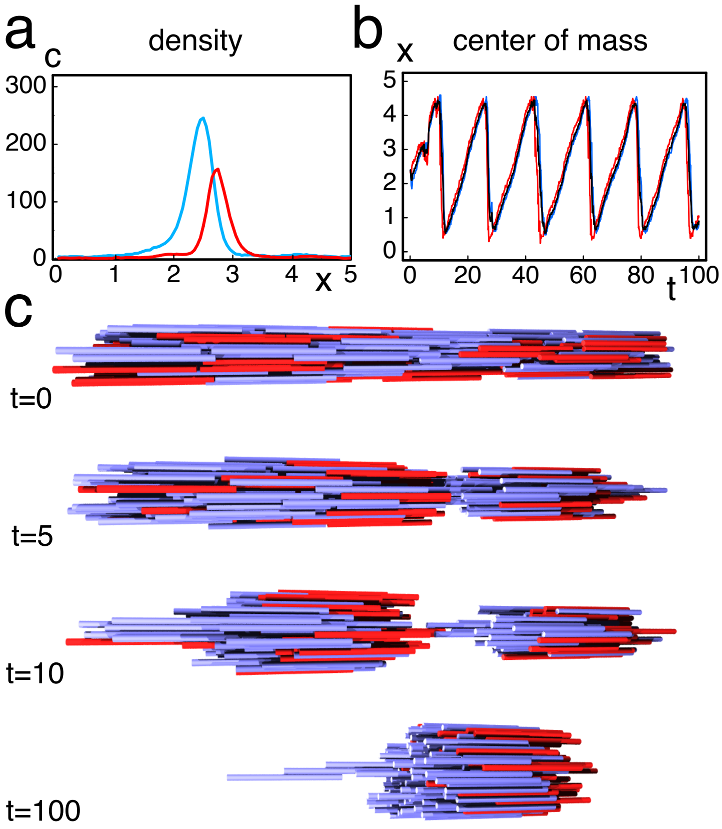

Figure 3.20: Dynamics of the active bundle introduced in Fig. 3.18. (a) Filament density averaged over the whole trajectory. (b) Position of the center of mass of both filament distributions and the whole system as a function of time. (c) Filaments represented by rods (blue corresponds to plus filaments and red to minus filaments) at four time steps showing how the bundle contracts. Parameters are $N^+ = 163$, $N^- = 87$, $\bar{\alpha}' = 40$, $\bar{\beta}' = 40$, $\bar{v} = 1$, $\bar{D} = 1$, $L = 5$.

to exercise some care though, as the direction of motion depends on the relative filament position. The current is thus given by

$$J_{\bar{\alpha}}(x) = \bar{c}(x) \times (p_{\bar{\alpha}}^{(r)} - p_{\bar{\alpha}}^{(l)}) \times \frac{\delta}{2}\frac{1}{\Delta t} \tag{3.111}$$

where $p_{\bar{\alpha}}^{(r)}$ is the probability to interact with a filament located right of the reference filaments located at x, captured by the density $\bar{c}(x)$. Here we have dropped the $\pm$ superscripts for better readability as the expressions are identical for plus and minus filaments. Let $n^{(c,r)}$ be the number of candidate filaments with $x_k > x$, then

$$p_{\bar{\alpha}}^{(r)} = \bar{\alpha} n^{(c,r)} \Delta t \tag{3.112}$$

The probability to interact with filaments left of the reference filament $p_{\bar{\alpha}}^{(l)}$ is defined accordingly. We thus obtain for the current

$$J_{\bar{\alpha}}(x) = \bar{c}(x) \times \bar{\alpha}(n^{(c,r)} - n^{(c,l)}) \times \frac{\delta}{2} \quad . \tag{3.113}$$

The current due to passive cross-linkers is given by replacing $\bar{\alpha} \to \bar{\alpha}'$ and $\delta \to a$. The currents due to cross-linkers and motors between antiparallel filaments are given by analogous expressions.

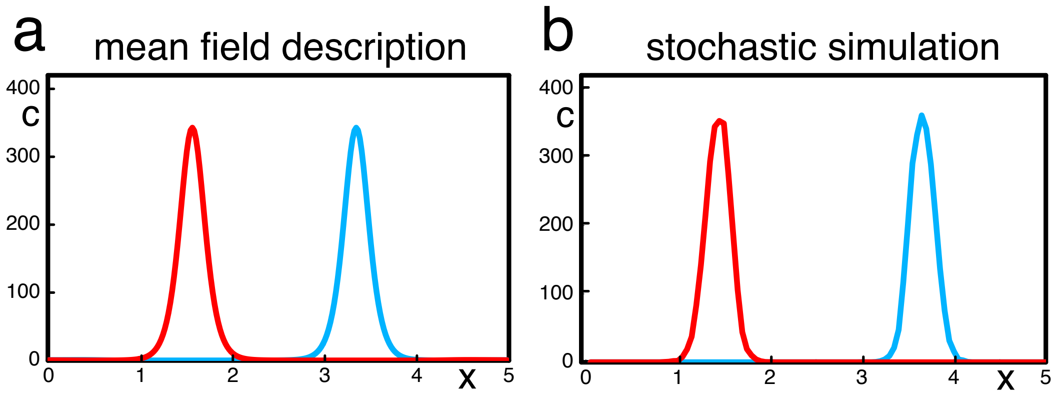

Figure 3.21: Comparision of stochastic simulations with mean field description in the absence of treadmilling. The parameters have been chosen according to Eqs. (3.117)-(3.118). (a) Asymptotic density profile obtained by numerical integration of the mean field equations. Parameters are $\alpha = 0.1$, $\beta = 0.1$, $D = 1$, $v = 0$, $L = 5$, $\int_0^L \mathrm{d}x\, c^+ = 125$, $\int_0^L \mathrm{d}x\, c^- = 125$. (b) Density profile of filaments in an active bundle obtained by stochastic simulations. Graph shows the filament densities of plus and minus filaments averaged over 100 instances in time. Parameters are $\bar{\alpha} = 40$, $\bar{\beta} = 40$, $\bar{D} = 0.5$, $N^+ = 125$, $N^- = 125$, $L = 5$, $l_{\mathrm{mot}} = 0.05$.

While these stochastic simulations are an intuitive way of gaining some understanding of the dynamics of active filament bundles, they cannot provide a thorough, mathematically rigorous insight in the system. This can be obtained by formulating the dynamics in the framework of a mean field description that is based on active filament currents, as outlined in the next section.

3.4 Relation between Stochastic Simulations and Mean Field Description

We have seen in the previous sections that the results obtained by stochastic simulations and by the mean field description are in good qualitative agreement with each other. This is comforting, yet expected, as both deal with the same physics. In this section we derive some quantitative relations between both descriptions. To this end we compare the currents in the stochastic simulations to the currents used in the mean field description and deduce relations between the corresponding coefficients.

The most simple example is the treadmilling current. If we compare this current in the mean field description (Eq. (3.43)) to the current in the stochastic simulation (Eq. (3.110)) and take into account that in the continuum limit $\Delta x \to 0$ the density of the filaments in the stochastic simulation $\bar{c}$ has to approach the mean field density $\bar{c}(x) = c(x)$, it follows that

$$v \simeq \bar{v} \quad . \tag{3.114}$$

Next we turn to the currents due to filament interactions. We start with the current due to motors between parallel filaments. In the mean field description this current for filaments of either orientation is given by Eq. (3.39). Compare this to the stochastic current Eq. (3.113), taking into account that in the continuum limit we have

$$n^{(c,r)} \simeq \int_0^l \mathrm{d}\xi c(x+\xi) \tag{3.115}$$

$$n^{(c,l)} \simeq \int_0^l \mathrm{d}\xi c(x-\xi) \quad . \tag{3.116}$$

Here $n^{(c,r)}$ and $n^{(c,l)}$ are the numbers of candidate filaments left and right of filaments at position x as introduced above Eq. (3.112). Hence the relation between coefficients in the stochastic simulation and the mean field description is given by

$$\alpha \simeq \bar{\alpha}\frac{\delta}{2} \quad . \tag{3.117}$$

Recall that δ is the length of one power stroke of one motor. Similar arguments lead to the relations

$$\beta \simeq \bar{\beta}\frac{\delta}{2}, \quad \alpha' \simeq \bar{\alpha}'\frac{a}{2}, \quad \beta' \simeq \bar{\beta}'\frac{a}{2} \quad , \tag{3.118}$$

where a is the length of one monomer.

The integral of the densities used in the mean field description taken over the whole system has to give numbers of filaments used in the stochastic simulations:

$$\int_0^L \mathrm{d}x\, c^\pm \simeq N^\pm \tag{3.119}$$

How to relate the diffusion constants D and $\bar{D}$, however, is less clear. The effective diffusion in the mean field description D includes stochastic effects due to motor action on multiple filaments that are not included in $\bar{D}$. In order to determine $\bar{D}$ we measured the density distributions for stochastic simulations with parameters chosen according to Eqs. (3.117)-(3.118) and different values for $\bar{D}$. Figure 3.21 shows an example of distributions of similar width. For this case we obtain obtain $\bar{D} \sim 0.5D$. How this relation depends on the choice of the other parameter is an interesting open topic.

3.5 Discussion

This chapter kind of provides the basis for all theories and results presented in this thesis. It allows the identification of the contributions of individual microscopic processes to the collective dynamics of active filament systems. This is of great importance when comparing theoretical results to experimental observations.

Starting from considerations concerning the action of filament polymerization, depolymerization, and filament treadmilling in the presence of passive cross-linkers as well as molecular motors we derive a description of the dynamics of active filament bundles. This description covers central cytoskeletal processes, especially filament polymerization and treadmilling.

We discuss bundle contraction and pattern formation by analyzing the stability of the homogenous state. This state can lose its stability via sub- and supercritical bifurcations that can be of the Hopf kind. Numerical integration of the system for parameters that render the homogenous state unstable reveals asymptotic, contracted states that usually take the form of traveling waves. The shape of these waves can either be constant or oscillate. In the presence of treadmilling, the localized density profiles can also be stationary. These states are also obtained by stochastic computer simulations of active filament bundles. The parameters of the stochastic simulation can be quantitatively related to those of the minimal model, allowing a deeper understanding of the contributions of the microscopic processes involved.

Bundle contraction is due to tension generated in the bundle by active processes between filament pairs, such as the action of motor dimers or passive cross-linkers in the presence of treadmilling. We derive an expression for the tension in such bundles and discuss the contribution of various microscopic processes. Motor dimers can only contribute to the tension when bound to parallel filaments. Passive, end-tracking cross-linkers in the presence of treadmilling can contribute independent of the orientation of the filaments they bind to. If they track the depolymerizing end, they increase the tension in the bundle, if they track the polymerizing end they lower it.

The minimal model is limited to the action of motors on filaments. In bacteria, rings of FtsZ protein filaments are thought to initiate cytokinesis by contraction, although no molecular motors like myosins are known to exist (Moller-Jensen and Lowe, 2005). Our description of filament treadmilling in the presence of passive cross-linkers offers a possible physical mechanism for ring contraction even in the absence of molecular motors and provides an attractive framework of thought for these processes.

As cytoskeletal waves have been found in various motile cells (Vicker, 2002; Bretschneider et al., 2004; Giannone et al., 2004; Dubin-Thaler et al., 2004; Döbereiner et al., 2004) it is tempting to link the solitary waves found in the minimal model to cell locomotion. Momentum conservation however prohibits a net filament transport by these waves. This constraint can be released by coupling the system to the environment, e.g. by allowing filaments to attach to a substrate. The minimal model with stabilized filaments has also been studied in situations where filaments were allowed to attach to a substrate (Kruse et al., 2001; Kruse and Jülicher, 2003) and with dynamics motor concentrations (Kruse and Jülicher, 2003). Attachment of filaments may change the critical value of α but the set of asymptotic states of the system remains unchanged. When the homogenous state loses stability, it evolves either to solitary or oscillatory waves. In the absence of interaction with filaments of the opposite orientation ($\beta = 0$) stationary localized states are also possible. Because of a possible momentum exchange with the substrate, the waves are now accompanied by a net filament current, $I \neq 0$,

Allowing for a dynamic motor density reproduces all types of asymptotic states presented in this chapter. In addition a few interesting new features appear. First, oriented bundles also support solitary waves. Interestingly it is only necessary to change the value (and not the sign) of the average motor velocity on filaments Γ, as introduced in Eqs. (3.13) and (3.14), in order to reverse the direction of propagation of solitary waves. Second, a new intrinsic length scale emerges: the instability of the homogenous state towards these waves can occur at wave numbers different from $2\pi/L$. Third, the homogenous state in bundles of mixed orientation, can become unstable even in the absence of an interaction between filaments of the same orientation. The generation of tension in the homogenous state however still requires interactions between filaments of the same orientation. Fourth, in bundles of mixed orientations the homogenous state can lose stability with respect to stationary localized states if $c_0^+ = c_0^-$. This is reminiscent of the stationary localized states obtained in the presence of treadmilling, cf. Fig. 3.11b.

The treatment of microscopic processes in active filament systems in more than one dimension is technically more cumbersome than for filament bundles, due to additional degrees of freedom, e.g. filament rotations. A generalization of the minimal model to higher dimensions in the absence of filament polymerization that takes rotations of filaments into account has been proposed by Liverpool and Marchetti (2003) and was subsequently developed in (Liverpool and Marchetti, 2005; Liverpool, 2005). The homogenous isotropic state is a stationary solution of the resulting equations. Assuming that friction is isotropic the linear stability of this state was analyzed (Liverpool and Marchetti, 2003; Ziebert and Zimmermann, 2004). As in one-dimension the homogenous isotropic state loses stability at a critical value α_c. For small densities, density fluctuations drive the instability, while for larger densities fluctuations in the polarization are responsible. In either case the bifurcation is stationary. If $\beta \neq 0$, the instability can be oscillatory if the density c_0 is large enough (Liverpool and Marchetti, 2003). The nature of the states beyond the instability remains to be explored. Note that a similar derivation of active filament dynamics in more than one dimension has revealed additional terms (Tanase, 2004).

It will be interesting future work to investigate how filament polymerization and especially treadmilling alters the dynamics of active systems with these extensions.

4 Stability of the Mitotic Spindle

4.1 Introduction

The mitotic and meiotic spindles that separate chromosomes during the cell cycle are fascinating dynamic cytoskeletal structures that have captured the attention of biologists and physicists alike. While aspects of aster formation and dynamics as well as spindle formation have been studied by numerical simulations (Nédélec, 2002a; Chakravarty et al., 2004; Joglekar and Hunt, 2002), a comprehensive analytical description of spindle dynamics is still lacking. Here we present first steps towards this goal developing a microscopic description for cytoskeletal spindles.

We focus on the question of what determines the length of stable spindles, as e.g. mitotic and meiotic spindles of the same organism often differ in size. Even more strikingly spindles in *Xenopus* egg extract are longer when the minus-end directed dynein-dynactin complex is inhibited. Our theory reproduces this observation. Furthermore we calculate conditions for the stability of these spindles. We are confident that this description will also be helpful in answering many other questions regarding mitotic and meiotic spindles, such as e.g. spindle oscillations (Grill et al., 2005).

4.1.1 From Filament Bundles to the Mitotic Spindle

We describe a bipolar cytoskeletal spindle consisting of two interacting microtubule asters. This corresponds to a model of mitotic spindles that is widely used in the literature. The asters are characterized by a length distribution, which determines the microtubule density as well as the densities of microtubule ends. Due to the rotational symmetry of the spindle we may project the system onto the spindle axis. This results in an effectively one-dimensional, fiber-like geometry, Fig. 4.1. We consider pair-wise filament interactions that are mediated by molecular motors. This approach is similar in spirit to the microscopic description of motor-filament systems presented in chapter 3. In addition to the concepts employed in the minimal model, here we also include a force dependent motor velocity captured by a force-velocity relation. This allows us to discuss the influence of aster movement on motor dimers bound to microtubules originating from both asters. We furthermore explicitly consider motor binding to filament ends, which has important consequences for the formation of stable spindles.

The geometry of the spindle determines the orientation of microtubules in the system. Microtubules are bound with their minus end to the aster centers, so that the plus ends always point outwards from each aster. Plus-end directed motor dimers that are bound to one MT from each aster between the asters will thus push the asters apart, while minus end directed complexes will pull them together. Furthermore due to the attachment of MTs to the aster center, molecular motors cannot induce relative filament sliding between MTs originating from the same aster. Forces generated by motors bound to MTs originating from two different asters, contribute to an effective force that acts on both asters. We calculate the resulting force between the two asters by summing up all contributions from motors bound. Assuming that this active force is balanced by viscous forces that act on

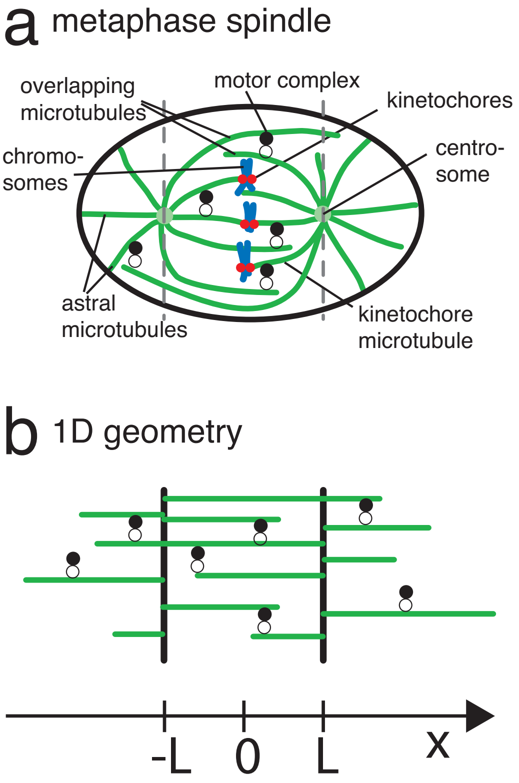

Figure 4.1: (a) Sketch of a metaphase spindle. Microtubules (green) originate from two centrosomes (light green) and form two interacting asters. Motor complexes link MTs from the two asters. The asters also interact by binding to kinetochores (red) on the same chromosome pairs (blue). (b) One-dimensional, simplified model geometry. MTs of different lengths originate from two aster centers (black) and interact via motor dimers. MTs from one aster can extend past the center of the other aster. We choose the x-axis of our description along the spindle axis and its origin in the middle between the two asters, which are then located at L and $-L$.

the asters, we write the dynamics for the spindle length. This allows us to analytically discuss criteria for spindle existence and stability.

4.1.2 Computer Simulations of Interacting Asters

Systems of two interacting filament asters have also been studied using computer simulations. Nédélec and coworkers have developed stochastic computer simulations of microtubules and motor complexes (Nédélec et al., 1997; Nédélec and Surrey, 2001; Surrey et al., 2001; Nédélec et al., 2001; Nédélec, 2002a). They investigated formation of asters, vortices and other patterns in filament motor systems and also studied the interaction of two microtubule asters. In these simulations, filaments and motors are individual objects characterized by parameters that could in principle be obtained from single molecule experiments.

In the simulations microtubules are modeled as linear, infinitely thin, polar objects (Nédélec, 2002a). The length of microtubules can change by adding or removing points at the plus end. Mechanically, the microtubules are inextensible elastic rods. Steric

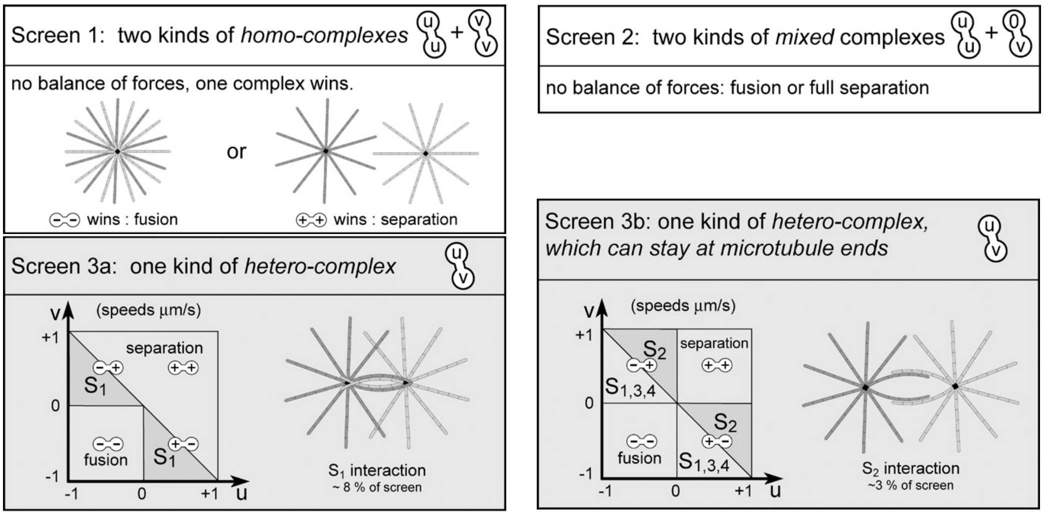
Screen 1: two kinds of homo-complexes
no balance of forces, one complex wins.
or
⊖-⊖ wins : fusion
⊕-⊕ wins : separation
Screen 2: two kinds of mixed complexes
no balance of forces: fusion or full separation
Screen 3a: one kind of hetero-complex
(speeds µm/s)
separation
fusion
S1
S1 interaction
~ 8 % of screen
Screen 3b: one kind of hetero-complex, which can stay at microtubule ends
S2
S1,3,4
S2 interaction
~3 % of screen
v
u
+1
0
-1

Figure 4.2: Diagrams of parameter space for stable interactions of microtubule asters obtained by numerical screens of parameter values. Figure adapted from (Nédélec, 2002a). S_i mark different solutions. See text for explanation of phase space.

or hydrodynamic interactions between the microtubules are neglected. Microtubules only interact when they are linked by a molecular motor complex.

Single motors can stochastically attach to and detach from microtubules. The attachment rate is the probability per unit time for a motor to bind to a microtubule at a point on that microtubule that is spatially closer than a given parameter. Motors complexes consist of two hands that are linked by a Hookean spring. The two hands of a complex move independently of each other. Two hands of the same complex are not allowed to bind to the same or two subsequent subunits of a microtubule. The two hands of a complex might either move both into the same or into opposite directions. Free complexes diffuse in the solvent.

Stochastic simulations according to these rules showed the evolution of an isotropic homogenous distribution of microtubules into asters due to the action of molecular motors, similar to what is observed in experiments (Nédélec et al., 1997; Surrey et al., 2001). Asters are only formed when a critical motor density is reached. The critical density depends on the processivity of the motors. Less processive motors require a higher density to form asters. The system evolves towards vortices instead of asters when the detachment rate of motors at the filament ends is increased beyond a critical value.

These simulation tools have also been employed to investigate the interaction of microtubule asters. This work has shed light on the prerequisites necessary to form stable spindles (Nédélec, 2002a). A single aster consists of a set of microtubules whose minus ends are connected by linear springs, mimicking a microtubule organizing center (MTOC). Neighboring microtubules are also linked some distance from this center. The structural integrity of the asters was maintained throughout the simulations. While some data is known about microtubules in spindles, the motors involved have not been characterized well enough to fix the parameters. The author thus systematically scanned the parameter space for steady states of two interacting asters. He employed different motor complexes (homo-complexes with both directionalities as well as hetero-complexes) acting alone and simultaneously on two asters and varied their number, their velocities v_m and stall forces F_s, as well as their attachment and detachment rates.

Stable bipolar aggregates depend on a balance of attracting and repelling forces between their poles. Due to the orientation of the microtubules with the plus ends away from the poles, a plus homo-complex will exert repelling forces on the poles while a minus homo-complex exerts attracting forces. In the presence of both types of complexes the asters thus will either separate or fuse depending on the relative strength and densities of motors, see Fig 4.2 (Screen 1).

The same behavior resulted from the simultaneous action of plus end directed complex together with a hetero-complex that had one minus end directed hand and one MT binding site that did not move along the microtubule (Screen2). This screen was motivated by two motors involved in spindle formation: Eg5, a plus end directed tetramer and NCD, that has a minus end directed motor domain and a nonmotor MT binding site. Screen 3 covers hetero-complexes in which the motors can have different speeds and directions. When motors detach immediately at the microtubule ends, stable spindles can form if the two motors in a complex moved towards opposite ends and the velocity towards the minus end is larger than the velocity towards the plus end, see Fig 4.2 (Screen 3b). In these solutions the attractive force between asters results from the interaction between anti-parallel microtubules while the repulsive force is due to the interaction between parallel microtubules. The two asters thus have to be close enough so that MTs from one can reach past the pole of the other and connect with MTs there. Stable spindle configurations were also found when motors were allowed to stay attached to the ends of microtubules.

4.2 Mean Field Description of Mitotic Spindles

4.2.1 Spindle Geometry

In our approach we consider the interaction of two microtubule asters, which is reminiscent of a spindle in the absence of chromosomes. The interaction of the asters is mediated by numerous proteins such as molecular motors (e.g, Eg5, Ncd, MCAK,...). We assume that these proteins as well as the microtubules can be described by densities.

Motivated by the rotational symmetry of the spindle we project these densities on the spindle axis yielding an effectively one dimensional description of the spindle, Fig. 4.1. We choose the x-axis of our description along the spindle axis and the origin in the middle of the spindle. This defines the reference system in which the center of mass is stationary. In this setting a spindle then consists of two interacting asters located at $-L$ and L, where L is the spindle half length, Fig. 4.3.

Microtubules that originate from the asters have a specific, fixed orientation. They all point their plus-ends away from their aster. In this one dimensional setting we define plus-microtubules as those pointing their $\oplus$-end to the right along the positive x-axis (blue bars in Fig. 4.3). We define forces and velocities directed to the right as positive. In the absence of external forces and due to conservation of momentum a symmetric arrangement of two asters at L and $-L$ remains symmetric, as all forces considered in our description conserve the system's symmetry, so that when the right aster moves with velocity $\dot{L}$ the left one moves with $-\dot{L}$ and the whole system is always symmetric with respect to space inversions $x \rightarrow -x$.

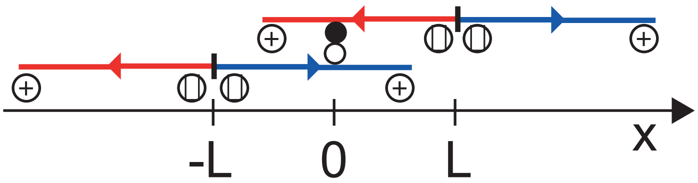

Figure 4.3: Two interacting asters of oriented microtubules. The black vertical lines in the center of each aster symbolize microtubule organizing centers such as centrosomes, which provide structural integrity to the asters. The microtubules (MTs) are fixed with their ⊖-ends to these centrosomes, the ⊕-ends are distributed in space according to a length distribution. MTs left of their centrosome are thus minus-MTs (red bars), MTs right of their centrosome are plus-MTs (blue bars). The symbols ⊖ and ⊕ mark the locations of the respective ends of the microtubules shown. The two vertically stacked disks in the center represent a motor dimer that has two heads with different properties, hence one black, one white.

4.2.2 Spindle Dynamics, Stability and Length

The actions of motor dimers between the spindle poles result in a total force F that brings the poles closer to each other or drives them apart. Cytoskeletal motion takes place in an environment that is characterized by a low Reynolds number. We can thus assume that effects due to inertia are negligible and that motion of the two asters is over-damped and viscous. If the system of two asters is symmetric with respect to the origin, it is fully characterized by the position L and the velocity $\dot{L}$ of the right aster. Because of symmetry the left aster is then at position $-L$ and has velocity $-\dot{L}$. It is thus sufficient to calculate the total force on the right aster $F(L, \dot{L})$ that depends on the spindle half length L and the pole velocity $\dot{L}$.

Spindle dynamics. The spindle poles move driven by the force $F(L, \dot{L})$ generated by the active processes in the spindle. They separate in response to a positive force and approach each other when $F(L, \dot{L})$ is negative. Assuming that the asters are situated in a highly viscous environment (low Reynolds number) so that motion is overdamped we may write

$$\dot{L} = \xi \; F(L, \dot{L}) \quad , \tag{4.1}$$

where ξ is the mobility of the two asters when dragged through the surrounding medium.

Spindle length. Two asters that interact are stationary when no force acts on them

$$F(L_s, 0) = 0 \quad , \tag{4.2}$$

where L_s is the half length of the stationary spindle. This is the condition for stationary asters, i.e. a spindle of fixed length $2L_s$. Obviously this only refers to physically a meaningful situation if the stationary spindle length is larger than zero

$$L_s > 0 \quad . \tag{4.3}$$

Spindle stability. Having determined the stationary length $2L_s$ and conditions for existence of a spindle, we calculate its stability. The stability of the spindle is determined by the systems reaction to small perturbations in length. In order to be stable, it should produce a negative force when extended to larger lengths than L_s, i.e.

$$\left. \frac{\partial F(L, 0)}{\partial L} \right|_{L=L_s} < 0 \tag{4.4}$$

is the condition for a stationary spindle of length $2L_s$ to be stable.

4.2.3 Force on Asters

The total force that acts on the right aster is the combination of the force contributions from anywhere along the spindle axis

$$F(L,\dot{L}) = \int_{-\infty}^{\infty} F(L,\dot{L},x)\ \mathrm{d}x \quad , \tag{4.5}$$

where $F(L,\dot{L},x)$ is the average force per MT hetero-dimer due to motor dimers at position x. It is the sum of the forces exerted by various motor dimers types at different locations in the spindle that are bound to the bulk or ends of microtubules:

$$F(L,\dot{L},x) = \sum_{\text{dimer type}\,i} \ \sum_{\text{zone}\,j} \ \sum_{\text{link type}\,k} d_i(x) w_{i,j,k}(x) \mathcal{F}_{i,j,k} \quad . \tag{4.6}$$

Here $i \in \{p,m,h\}$ denotes the three types of dimers: plus-plus, minus-minus, and hetero-dimers, $j \in \{(a),(b),(c)\}$ is summed over the three regions of a spindle, cf. blue regions in Fig. 4.5, and $k \in \{b,\oplus,\ominus\}$ and marks the three types of possible links: bulk-bulk, bulk-$\oplus$-end, and bulk-$\ominus$-end. The motor dimer number density of motor dimers of type i is denoted by d_i. The effective probability of a dimer of type i to form a link of type k at position x in zone j is given by $w_{i,j,k}(x)$ and the average force contribution of such dimers by $\mathcal{F}_{i,j,k}$.

4.2.4 Interaction between Filament Pairs

Let us now discuss the forces that act on two asters due to molecular motors in the spindle. Individual motors are characterized by a force-velocity relation. Depending on their position in the spindle their contribution to the total force acting on both asters can change.

Motor dimers consist of two linked motor heads that bind to MTs. We assume the bending rigidity of the microtubules to be large. Hence we neglect MT bending by motors in our one dimensional scenario. Thus we need not consider motor actions between MTs originating from the same aster. In our description we only consider asters that do at least partially overlap, so that motor dimers can bind to MTs from both asters simultaneously. When bound to two different microtubules they will not only experience forces due to the movement of the asters but they also actively exert forces on these MTs. Their contribution to the total force on the asters, which is due to the collective action of all motors, depends on their position in the spindle and also if they are attached to the bulk or the ends of the microtubules.

We investigate the force a single motor dimer can exert when interacting with both asters. This corresponds to a situation where the motor is not free to move with its unloaded velocity v_0 anymore, because it forms part of a dimer that is attached to a MT from the other aster and is thus subject to a force. In our description a single motor with unloaded velocity v_0 is characterized by a linear force-velocity curve, Eq. (3.3). If the microtubule itself moves with a velocity V with respect to the laboratory system, the motor's velocity in this system is given by

$$\dot{x} = \pm v + V \tag{4.7}$$

where the sign in front of v depends on the orientation of the microtubule (negative sign when it is a minus MT). A free $\oplus$-end directed motor on a minus-microtubule has a

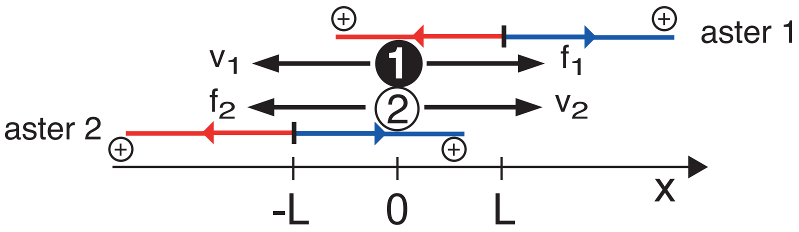

Figure 4.4: Conventions in nomenclature used in this chapter. The right aster (at L) is termed aster 1, the motor head bound to a MT emanating from that aster thus is head 1 (black disk). The motor heads experience forces due to the movement of the aster (example here f_1) and move along their respective MTs with a velocity given by Eq. (3.3) (example here v_2). Note that the positive direction for forces and velocities is given by the respective orientation of the microtubules.

negative velocity in the laboratory system of reference and thus would enter as $-v$ in Eq. (4.7).

In the following we will calculate the force f a motor dimer exerts on the right aster. This is accompanied by an opposing force of the same magnitude on the other aster as *actio=reactio*. In this sense we can speak of f as acting on both asters. If $f > 0$ it tends to increase the distance $2L$ between the asters, if it is negative, it pulls them together. The force f a motor dimer exerts on the spindle asters depends on three characteristics: first, the location of the dimer, because this defines the orientation of the MTs it binds to. Second, the type of dimer, i.e. if the dimer consists of plus-end or minus-end directed motor heads. And third if the dimer is bound to the bulk or to the end of the microtubules. These three topics are discussed in the following.

Starting from the velocity of the dimer in the lab system and using the force velocity curves of both motors, we derive an expression for the force f_1 acting on motor 1, i.e. the motor bound to a MT originating from the right aster, Fig. 4.4. As f_1 is measured with respect to the orientation of microtubule 1 and f is measured in the laboratory reference frame, the two forces have opposite signs when MT 1 is a minus-microtubule. As the force contribution of a motor dimer depends on the location and orientation of its binding, we calculate the ensemble average for every type of dimer in each of the three regions. We assume that motors that reach the ends of filaments can stall there for a short moment, i.e. the velocity of the respective motor head becomes zero. These stalled heads then do not actively contribute to the force between the asters, but still provide a structural link between them.

Motor binding to MTs from different asters can occur either between the two aster poles or on either side of these poles. The location defines the orientation of the MTs involved which in turn influences the force contribution of the motor. Outside the asters, i.e. left or right of the two asters the microtubules have the same orientation, i.e. they are either both minus-microtubules (Fig. 4.5a) or both plus-microtubules (Fig. 4.5c). Between the asters the interacting MTs have opposite orientation and motor dimers that exert forces on both asters are always bound to one plus- and one minus-microtubule (Fig. 4.5b).

Force Contribution of a Single Motor Dimer. Here we consider the force of motor dimers that bind to MTs originating from both asters. Due to the varying orientations of the two microtubules involved, the calculation differs slightly for each region in the spindle. The force a dimer exerts depends also on whether it is bound to the bulk or to the end of a MT. For concreteness we first discuss a motor bound to the bulk between the two asters

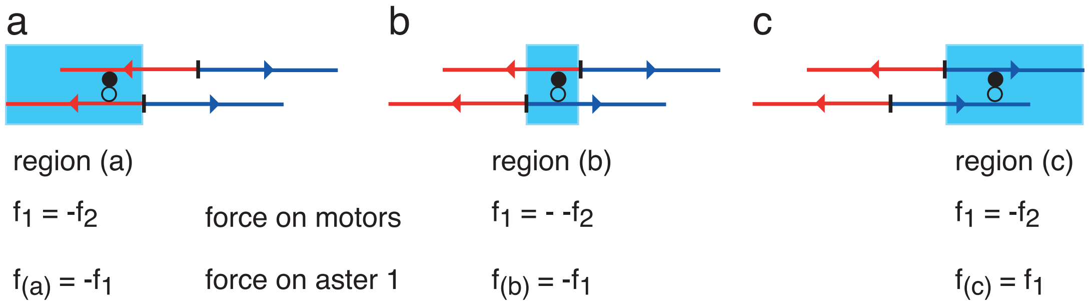

Figure 4.5: Motors can bind to the two asters in three different regions. Their influence on the spindle dynamics depends crucially on their location. The motor heads (each depicted as a black or white disk) bind to the bulk of either (a) parallel and minus-oriented microtubules (red) when left of both centrosomes, (b) antiparallel MTs between the centrosomes or (c) parallel and plus-oriented MTs (blue) when right of them. The relation between the forces on the motors heads (f_1, f_2) is determined by Newton's law *actio=reactio*. As the forces are measured with respect to the orientation of their microtubule, the explicit expression depends on the location of the motor as indicated in the figure. The force a motor dimer exerts on aster 1 can be calculated from the force f_1 as shown in the last line. Here we also need to take the orientation of MT 1 into account.

(region (b) in Fig. 4.5) and then show how to calculate the average force contribution if one head of the dimer is bound to a MT $\oplus$-end. These two examples illustrate the procedure. The remaining 25 different cases follow the same logic and are calculated explicitly in appendix C. The velocities in the laboratory frame of reference of the two heads of the dimer are described by

$$\begin{aligned} \dot{x}_1 &= -v_1 + \dot{L} && (4.8) \\ \dot{x}_2 &= v_2 - \dot{L} && (4.9) \end{aligned}$$

and $\dot{x}_1 = \dot{x}_2$, as the heads cannot separate. Note that v_1 enters with a negative sign because MT1 is a minus MT. The forces on the two motor heads are related by

$$f_1 = -(-f_2) \qquad (4.10)$$

where the first negative sign is due to the opposite orientation of MT1 (minus MT) and MT2, and the second because the two heads form a dimer (*actio=reactio*). Using this relation and the force velocity curves (3.3) of the motor dimers we can solve Eqs. (4.8) and (4.9) and obtain

$$f_1 = \frac{-v_a - v_b + 2\dot{L}}{\chi_a + \chi_b} \qquad (4.11)$$

and the force that the dimer exerts on the two asters in this case is given by

$$f = -f_1 \quad , \qquad (4.12)$$

where the negative sign in front of f_1 is due to the orientation of microtubule 1. To further illustrate this result we explicitly calculate the contribution of four types of motor dimers:

- p-p: a homo-dimer of two $\oplus$-end directed motors
- m-m: a homo-dimer of two $\ominus$-end directed motors

Complex	p-p	m-m	p-m	m-p
Fig. 4.5b				
Velocities	$v_a > 0, v_b > 0$	$v_a < 0, v_b < 0$	$v_a > 0, v_b < 0$	$v_a < 0, v_b > 0$
Forces	$f_1 = \dfrac{-v_a - v_b}{\chi_a + \chi_b}$ $f = -f_1 > 0$	$f_1 = \dfrac{-v_a - v_b}{\chi_a + \chi_b}$ $f = -f_1 < 0$	$f_1 = \dfrac{-v_a - v_b}{\chi_a + \chi_b}$ $f = -f_1$	$f_1 = \dfrac{-v_a - v_b}{\chi_a + \chi_b}$ $f = -f_1$
Effect	expansive	contractile	depends	depends
Ensemble	$\mathcal{F} = f$	$\mathcal{F} = f$	$\mathcal{F} = f$	

Table 4.1: Force contributions of different individual motor dimers bound to the bulk of two MTs between both asters. The asters are assumed to be stationary ($\dot{L} = 0$). The last line shows the average force contribution per dimer $\mathcal{F}$ of an ensemble of motor dimers.

- p-m: a hetero-dimer of a $\oplus$-end directed motor bound to MT 1 (from the right aster) and a $\ominus$-end directed motor bound to MT 2 (from the left aster)
- m-p: a hetero-dimer of a $\ominus$-end directed motor bound to MT 1 and a $\oplus$-end directed motor bound to MT 2

Table 4.1 summarizes the results for different kinds of motor dimers and stationary asters.

For an ensemble of motors bound to the bulk of filaments the average force contribution $\mathcal{F}$ is calculated by averaging the two possible ways of binding (motor head a bound either to MT1 or MT2)[1]. When both heads are bound to the bulk between the two asters as in our example here, both situations are equivalent (v_a and v_b carry the same sign in Eq. (4.11)) and contribute the same force. Thus for dimers with both heads bound to the bulk of filaments we find

$$\mathcal{F} = f \tag{4.13}$$

for the average force contribution from an ensemble of motor dimers in this case. This is different when the dimer is bound on one side of both asters (region (a) or (c)), so that the two MTs have the same orientation and v_a and v_b enter with the same sign in Eqs. (4.8) and (4.9). In this case the contributions of either case cancel out and and ensemble of motor dimers effectively acts like passive cross-linkers, cf. appendix C.1.

When one head in a motor dimer is bound to a MT end, the situation requires one more distinction in the analysis as the MT can originate from aster 1 (case i in Fig. 4.6) or from aster 2 (case ii). So when calculating the average force contribution of an ensemble of motor dimers bound to the bulk one MT and to the end of the other MT, we have to average over four configurations in total. Here we also have to take into account that motor heads can stall at the ends and thus do not contribute actively to the force anymore. The explicit expressions for four kinds of motor dimers are summarized in table 4.2.

4.2.5 Microtubule Length Distributions

An individual aster is characterized by a microtubule length distribution $P(L) \geq 0$ which is normalized $\int_0^\infty P(L)\, \mathrm{d}L = 1$. On one side of the MT organizing center of an aster in one dimension this results in a microtubule density

$$\rho(x) = \frac{N_0}{a} \int_x^\infty P(L)\, \mathrm{d}L \tag{4.14}$$

---

[1] This distinction is not necessary when both motor heads are identical, of course.

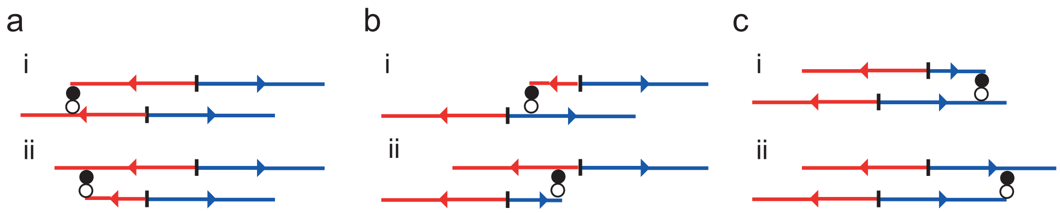

Figure 4.6: Motor dimers linking the ⊕-end of a microtubule from one aster to the bulk of a microtubule from the the second. The motors (each depicted as a black disk or a white disk) bind to either either (a) parallel and minus-microtubules (red) when left of both centrosomes, (b) antiparallel MTs between the centrosomes or (c) parallel and plus-MTs (blue) when right of them. In each of these cases we distinguish the motor bound to the end of a MT from the right aster (i) or from the left aster (ii) as the force contribution is different in each case (see text for details).

Complex	p-p	m-m	p-m	m-p
Fig. 4.6b (i)				
Velocities	$v_a = 0, v_b > 0$	$v_a < 0, v_b < 0$	$v_a = 0, v_b < 0$	$v_a < 0, v_b > 0$
Forces	$f_1 = \dfrac{-v_b}{\chi_a + \chi_b}$ $f = -f_1$	$f_1 = \dfrac{-v_a - v_b}{\chi_a + \chi_b}$ $f = -f_1$	$f_1 = \dfrac{-v_b}{\chi_a + \chi_b}$ $f = -f_1$	$f_1 = \dfrac{-v_a - v_b}{\chi_a + \chi_b}$ $f = -f_1$
Effect	expansive	contractile	contractile	depends
Fig. 4.6b (ii)				
Velocities	$v_a > 0, v_b = 0$	$v_a < 0, v_b < 0$	$v_a > 0, v_b < 0$	$v_a < 0, v_b = 0$
Forces	$f_1 = \dfrac{-v_a}{\chi_a + \chi_b}$ $f = -f_1$	$f_1 = \dfrac{-v_a - v_b}{\chi_a + \chi_b}$ $f = -f_1$	$f_1 = \dfrac{-v_a - v_b}{\chi_a + \chi_b}$ $f = -f_1$	$f_1 = \dfrac{-v_a}{\chi_a + \chi_b}$ $f = -f_1$
Effect	expansive	contractile	depends	contractile
Ensemble	$\mathcal{F} = \frac{1}{2}\frac{v_a+v_b}{\chi_a+\chi_b}$	$\mathcal{F} = \frac{v_a+v_b}{\chi_a+\chi_b}$	$\mathcal{F} = \frac{1}{2}\frac{2v_a+v_b}{\chi_a+\chi_b}$, where $v_a < 0, v_b > 0$	

Table 4.2: Force contributions of different motor dimers bound to bulk and one ⊕-end of MTs between of both asters (region(b)). The asters are assumed to be stationary ($\dot{L} = 0$). The last line shows the average force contribution per dimer $\mathcal{F}$ of an ensemble of motor dimers.

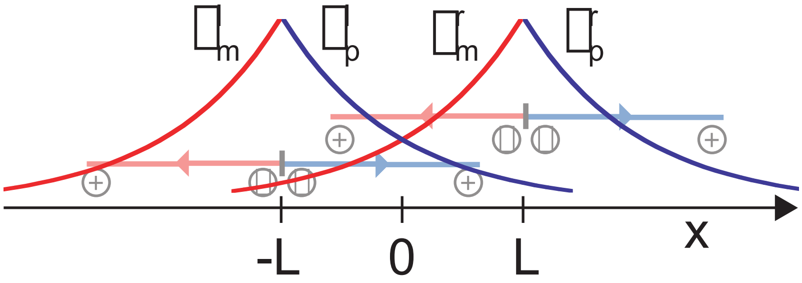

Figure 4.7: Sketch of the tubulin densities in the two microtubule asters. The superscript (l,r) for left and right indicates the aster the MTs belong to, the subscript refers to the orientation of the microtubules (m, minus, red and p, plus, blue respectively).

so that $\rho(x)$ decreases monotonously as $P(L)$ is always positive. The total number of MTs is given by N_0 and a is the length of a tubulin dimer, the basic building block of microtubules. The mass M of the aster is then given by

$$M = \int_0^\infty \mathrm{d}x \rho(x) = \int_0^\infty \mathrm{d}x \frac{N_0}{a} \int_x^\infty P(L)\ \mathrm{d}L \quad . \tag{4.15}$$

The boundary of the MT density is

$$\partial_x \rho(x) = -\frac{N_0}{a} P(x) \tag{4.16}$$

so that the density of ends $\eta(x)$ is given by

$$\eta(x) = N_0 P(x) = a |\partial_x \rho(x)| \tag{4.17}$$

where the domain of definition has to be chosen according to the ends in question (i.e. $\oplus$- or $\ominus$-ends). Furthermore $\int_{-\infty}^{\infty} \eta(x) \mathrm{d}x = N_0$, i.e. every microtubule has exactly one end of either type.

We assume the two asters to be identical (cf. Fig. 4.7). The densities of the tubulin hetero-dimers bound in filaments $\rho_{\{m,p\}}^{\{l,r\}}(x)$ have units of 1/length in our description. The superscript refers to the aster the MTs originate from (left: aster at $-L$, right: aster at L), the subscript to their orientation (minus-, plus-microtubules).

The distributions of ends of microtubules are given by densities $\eta_{\{m,p\}}^{\{l,r\},\{\oplus,\ominus\}}(x)$, where the subscript as above refers to the orientation of the microtubule, the first superscript again indicates the aster of origin and the second superscript denotes the type of the end $(\oplus, \ominus)$. Thus the $\oplus$-ends of the minus-MTs originating from the right aster are given by $\eta_m^{r,\oplus}(x)$ and $\eta_m^{r,\ominus}$ denotes the $\ominus$-ends of the minus-microtubules at that aster's center. Note that we assume that the minus ends of all microtubules coincide in one point (L or $-L$ respectively). This allows us to simplify the notation for the density of minus ends and use $\eta^{r,\ominus} = \eta_m^{r,\ominus} + \eta_p^{r,\ominus}$ and for the left aster analogously. Our findings presented in this chapter are robust against other choices, cf. appendix C.3.

Now we are in a position to discuss examples of half asters given by different types of length distributions. Half asters are asters that possess only MTs oriented towards the other aster. We will use half asters to illustrate the general ideas before discussing a system of two full asters. The extension to full asters is straightforward.

Length distribution	$P(x) = ke^{-kx}$ (exponential)	
Half aster at	L (right)	$-L$ (left)
MT density	$\rho_m^r(x) = \rho(L-x)$ $= a^{-1}N_0e^{-k(L-x)}$	$\rho_p^l(x) = \rho(L+x)$ $= a^{-1}N_0e^{-k(L+x)}$
$\oplus$-end density	$\eta_m^{r,\oplus}(x) = a\vert\partial_x\rho_m^r(x)\vert$ $= N_0ke^{-k(L-x)}$	$\eta_p^{l,\oplus}(x) = a\vert\partial_x\rho_p^l(x)\vert$ $= N_0ke^{-k(L+x)}$
$\ominus$-end density	$\eta^{r,\ominus}(x) = N_0\delta(L-x)$	$\eta^{l,\ominus}(x) = N_0\delta(-L-x)$

Table 4.3: Densities describing a system of two half asters with exponential microtubule distributions. Densities are defined on the interval $[-L; L]$ and are zero everywhere else.

Exponential half asters refer to asters that only possess microtubules on $[-L; L]$, i.e. between the two centrosomes, and whose length distribution is an exponential

$$P(x) = ke^{-kx} \tag{4.18}$$

as would result from polymerization and depolymerization of a fixed number of aligned microtubules, cf. (Dogterom and Leibler, 1993). The MT density of one half-aster with its center at $x = 0$ is then also given by an exponential distribution :

$$\rho(x) = \frac{N_0}{a}e^{-kx} \tag{4.19}$$

where N_0 is the dimensionless number of microtubules, a is the length of a hetero-dimer forming the MTs and k is the inverse of the characteristic length of the MT distribution ($[k] = 1/\text{length}$). For the aster at L we have to replace $x \to -x$ in this definition. Table 4.3 summarizes the densities that describe two exponential half asters at L and $-L$.

Motor Binding Depends on Microtubule Density. The probability to form a link is proportional to the densities involved. For simplicity we assume that the probability to form a link is independent of the type of motor dimer, so that we can write $w_{j,k}(x)$ instead of $w_{i,j,k}(x)$. For motors binding to the bulk of microtubules (link type b) between both asters (zone (b)), the probability $w_{(b),b}(x)$ is given by

$$w_{(b),b}(x) = C_b\rho_p^l(x)\rho_m^r(x) \quad , \tag{4.20}$$

where C_b is a positive constant with dimensions $[C_b] = \text{length}^2$ and $C_b \leq 1/\max_x(\rho_p^l(x)\rho_m^r(x))$. This means that with probability $w_{(b),b}(x)$ a link exists at position x and with $1 - w_{(b),b}(x)$ it does not. Note that there is no normalization condition for w when integrating over the whole system.

For dimers linking $\oplus$-ends and bulk in region (b) beetween the asters, we obtain analogously

$$w_{(b),\oplus}(x) = C_p(\rho_p^l(x)\eta_m^{r,\oplus}(x) + \eta_p^{l,\oplus}(x)\rho_m^r(x)) \tag{4.21}$$

where C_p is a positive constant with dimensions $[C_p] = \text{length}^2$ and $C_p \leq 1/\max_x(\rho_p^l(x)\eta_m^{r,\oplus}(x) + \eta_p^{l,\oplus}(x)\rho_m^r(x))$.

The probability for $w_{(b),\ominus}(x)$ is defined analogously with a constant C_m. The probability left and right of the asters are calculated with the corresponding densities.

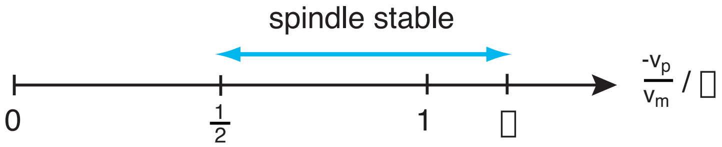

Figure 4.8: Graphical representation of the general condition for stable spindles from exponential half asters as given by Eq. (4.25).

4.3 Results

4.3.1 Spindle Stability

We demonstrate the power of the theory developed in this chapter by applying it to two interacting exponential half asters, as discussed above. The force that ensembles of motor dimers exert on such half asters is calculated explicitly in appendix C.1. The spindle is stationary if $F(L,0) = 0$. Using the expression for the total force as given by Eq. (C.41), the stationary half length L_s is given by

$$L_s = -\frac{C'_m(0)}{C'_b(0)/a + 2kC'_p(0)} \quad . \tag{4.22}$$

Here $C'_b(0)$ is the function that characterizes the effectiveness of bulk-bulk links for stationary spindles ($\dot{L} = 0$), C'_p that of bulk-$\oplus$-en-links and C'_m that of bulk-$\ominus$-end-links. This expression thus reveals that for stationary spindles of finite length to exist, it is absolutely necessary to balance the force contribution of the $\ominus$-end-bulk interactions with either one or both of the other two interactions, as $C'_m = 0$ implies $L_s = 0$. This also holds for the more general case of full asters.

A spindle furthermore only exists when the spindle length is positive $L_s > 0$. This leads to the condition for spindle existence

$$C'_m(0)\left(C'_b(0)/a + 2kC'_p(0)\right) < 0 \quad . \tag{4.23}$$

Given existence, stability is determined by Eq. (4.4). With L_s from Eq. (4.22) we obtain

$$\left[C'_b(0)/a + 2kC'_p(0)\right] > 0 \quad . \tag{4.24}$$

as the condition for a stable spindle. Note that the condition for existence (4.23) is the same as the condition for stability (4.24) when $C'_m(0) < 0$. All spindles that exist under these circumstances are thus also stable.

Now we are in a position to discuss the existence and stability of a spindle formed by two half asters as described above. We assume that in a dimer the velocity and the force-velocity curve of one motor do not depend on the details of the other motor. Moreover we assume that there are only two different kinds of motor heads (one $\oplus$-end directed with velocity $v_p > 0$ and one $\ominus$-end directed with $v_m < 0$) and replace v_a, v_b, χ_a, χ_b accordingly. This results in simplified expressions for the functions $C'_m(0)$, $C'_b(0)$, and $C'_p(0)$, cf. Eqs. (C.53)-(C.55). So in this situation stationary spindles can only exist when the velocities v_m and v_p obey the following condition (see appendix C.2.1 for detailed calculations):

$$0 < \frac{1}{2}\gamma < -\frac{v_p}{v_m} < \Gamma\gamma \tag{4.25}$$

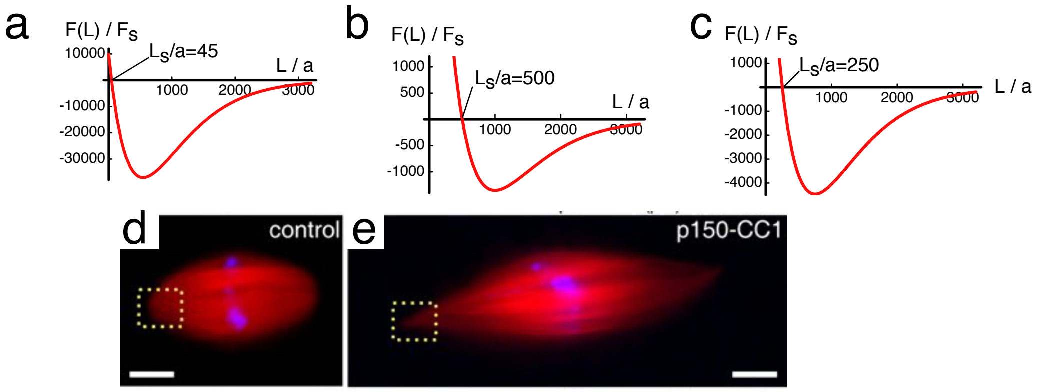

Figure 4.9: Qualitative agreement between theoretical description and experimental observation. (a,b,c) Force on asters in dependence of spindle length L as determined by our theory. Spindle is stable with a stationary length L_s. Length is measured in units of the dimer length a and forces in units of the stall force F_s as defined in Eq. (4.31). (b) Inhibiting the minus-end directed motors in our theory (1% with respect to (a)) leads to longer spindles, similar to the experimental observations. (c) F(L) like in (b), but with twice the probability to form a link with the plus end C_p. (d) Normal spindle in *Xenopus* egg extract. (e) Spindles elongate when the minus end directed dynein/dynactin complex is inhibited. (d,e) from (Gaetz and Kapoor, 2004).

where

$$\gamma := \frac{\chi_p(\chi_p m_0 + \chi_m(h_0 + m_0))}{\chi_m(\chi_m p_0 + \chi_p(h_0 + p_0))} \tag{4.26}$$

depends on the homogenous motor concentrations involved, but is independent of the motor velocities. Note that γ is always positive. Further we have defined

$$\Gamma := \frac{C_b + 2akC_p}{C_b + akC_p} \tag{4.27}$$

for the prefactor in Eq. (4.25), which defines the range of $-v_p/v_m$ in that stable spindles exist. The constants C_b and C_p describe the linking probability in the bulk and at $\oplus$-ends respectively and have been introduced in Eqs. (4.20) and (4.21). As they are always positive, Γ is always between 1 and 2. Figure 4.8 displays a graphical representation of the condition for spindle existence and stability, Eq. (4.25).

As the condition for stability of the spindle Eq. (4.24) coincides with the second condition for its existence $\left[C_b'(0)/a + 2kC_p'(0)\right] > 0$, Eq. (4.25), stationary spindles formed by two half asters under these conditions are always stable.

4.3.2 Spindle Length

Now we discuss the conditions for spindle existence and calculate the stationary length of a few instructive examples.

Dimers with heads of the same directionality. We start out with two asters that only interact via the two kinds of homo-dimers: p-p and m-m. In this case γ simplifies to

$$\gamma = \frac{\chi_p m_0}{\chi_m p_0} \quad . \tag{4.28}$$

The length dependent force is given by

$$\begin{aligned} F(L) &= \frac{N_0^2}{a^2\chi_p\chi_m}e^{-2kL}\times \\ &\quad [\chi_p(2C_bL+a(C_m+4C_pkL))m_0v_m+2\chi_m(C_bL+a(C_m+C_pkL))p_0v_p] \end{aligned} \tag{4.29}$$

and shows directly the force balance between $\oplus$- and $\ominus$-end directed motors. The stationary length simplifies to

$$L_s=-\frac{aC_m(\chi_p m_0 v_m+2\chi_m p_0 v_p)}{2(\chi_p(C_b+2akC_p)m_0v_m+\chi_m(C_b+akC_p)p_0v_p)} \quad . \tag{4.30}$$

Figure 4.9 shows graphs of $F(L)$ in the absence of hetero-dimers. For this illustration we have chosen the following dimensionless parameters: $ak = 0.001$, $N_0 = 100$, $h_0 = 0$, $\chi_m/\chi_p = 1$, $C_m/a^2 = 1$, $C_b/a^2 = 1$, $C_p/a^2 = 1$, and $-v_m m_0/v_p p_0 = 1$ for (a) and $-v_m m_0/v_p p_0 = 0.99$ for (b), which completely determine the dynamics. Force is displayed in units of the stall force of a plus-motor

$$F_s := \left|\frac{v_p}{\chi_p}\right| \quad . \tag{4.31}$$

Note that increasing the product of the density and velocity of the m-m dimers m_0v_m by just 1% decreases the stationary spindle length by a factor of 10 from $L_s/a = 500$ in (b) to $L_s/a \simeq 45$ in (a). The spindle is thus very sensitive to variations in the speed of the motors. Our choice of parameters furthermore fixes $\Gamma = 1.001$. The value of γ depends on the detailed choice of m_0 and p_0.

The stationary length is less sensitive to variations in Γ. Figure 4.9c shows the same $F(L)$ curve as before but with twice the probability to form links at $\oplus$-ends $C_p/a^2 = 2$. This halves the stationary length to $L_s/a = 250$. Doubling the probability for links at $\ominus$-ends C_m doubles the spindle length, while changing the bulk probability C_b has no effect. The spindle is thus more robust against variations in linking probabilities C_m, C_p, and C_b than against variations in the relation of motor velocities and concentrations.

In conclusion we can say that we found stable spindles formed in the presence of the two types of homo-dimers only. The observed $F(L)$ dependence and the shortening of the spindle when increasing the effectiveness of the minus end directed motors ($-v_m m_0$) are in good agreement with experimental observation as well as an intuitive understanding of the force balance in the spindle. These findings are even more interesting as no stable spindles have been found in computer simulations of interacting asters in the presence of two homo-complexes (Nédélec, 2002a). See section 4.4 for a more detailed discussion of this point.

Dimers with heads of different directionality. Figure 4.10 shows graphs of $F(L)$ in the absence of homo-dimers. In the presence of hetero-dimers only, the spindle exhibits a similar behavior as for homo-dimers only. In this case we always have

$$\gamma = 1 \tag{4.32}$$

because $p_0 = 0$ and $m_0 = 0$. The length dependent force is explicitly given by

$$\begin{aligned} F(L) &= \frac{N_0^2}{a^2(\chi_p+\chi_m)}h_0e^{-2kL}\times \\ &\quad [(aC_m+2C_bL+4akC_pL)v_m+(2aC_m+2C_bL+2akC_pL)v_p] \ . \end{aligned} \tag{4.33}$$

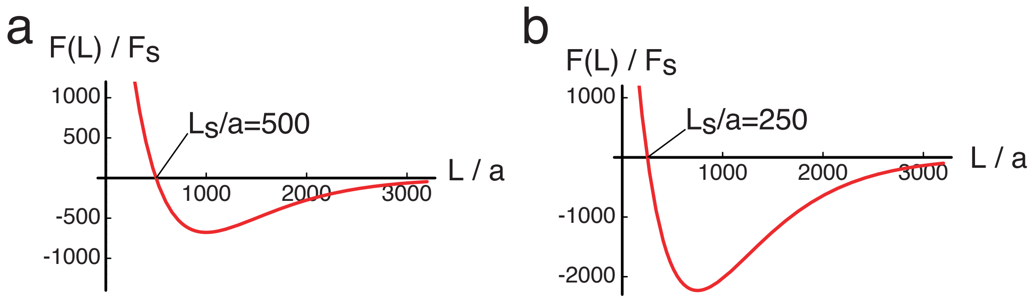

Figure 4.10: (a) Force on asters as a function of spindle half length L in the presence of hetero motor dimers only. The stationary length L_s is defined by the intersection with the horizontal axis. As the force is positive at smaller lengths and negative at larger lengths the spindle is stable at L_s. L_s is determined by the balance between plus and minus directed motor heads, but independent of the total concentration of hetero-dimers h_0. The stationary length is also directly influenced by the binding probabilities C_p, C_m, and C_p. (b) F(L) like in (a), but with C_p doubled.

This expression reveals that the concentration of hetero-dimers h_0 only scales the absolute values of $F(L)$, but does not influence its characteristics. The force balance in this case is determined by the relative motor velocities and independent of motor concentrations. The stationary length in this case is also independent of h_0

$$L_s = -\frac{aC_m(v_m + 2v_p)}{2(C_b(v_m + v_p) + akC_p(2v_m + v_p))} \quad . \tag{4.34}$$

The dimensionless parameters are: $ak = 0.001$, $N_0 = 100$, $h_0 a = 1$, $m_0 = 0$, $p_0 = 0$, $\chi_m/\chi_p = 1$, $C_m/a^2 = 1$, $C_b/a^2 = 1$, $-v_m/v_p = 1$, and $C_p/a^2 = 1$ for (a) and $C_p/a^2 = 1$ for (b), which completely determine the dynamics. Note that as before, doubling the $\oplus$-linking probability C_p halves the stationary length L_s, while doubling the $\ominus$-linking probabilityC_m halves it. Varying the bulk-bulk linking probability C_b has no effect. On the other hand the spindle is very sensitive to variations of the balance of motor velocities $-v_m/v_p$. A 1% increase causes the spindle to shorten by a factor of 10, as is the case of homo dimers only. Another interesting observation in this case is however that the total concentration of hetero-dimers has no influence on the stationary spindle length, as it does not appear in the balance of forces. This force balance is entirely determined by the motor velocities and linking probabilities.

4.3.3 State Diagrams

Having discussed the force balance in the spindle by the action of homo- or hetero-dimers alone in the previous sections, we now turn to the complete system in which all three kinds of motors are present at the same time.

We normalize the densities with the total number of motor dimers, so that

$$p_0 a + m_0 a + h_0 a = 1 \quad . \tag{4.35}$$

Solving the condition for existence of a stationary spindle, Eq. (4.25), for m_0 as function of p_0, using the normalized densities from (4.35) we can calculate the phase boundary of stable spindles. Figure 4.11 displays the result of the calculations. For clarity of presentation we

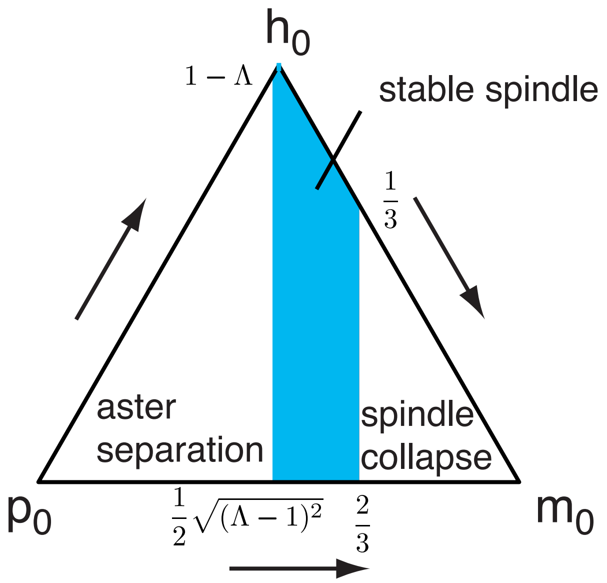

Figure 4.11: Phase diagram for spindle formation by two exponential half asters in the presence of all three types of motors. Stable, finite size spindles are formed in the blue region. Each point in the triangle represents exactly one composition of homogenous motor dimer densities. The three corners correspond to pure plus-, minus-, and hetero-dimers respectively. On an edge only the two motor types named at the bordering corners are present. The arrows along the sides point to the species whose fraction is given by the coordinate on that side, e.g. $m_0/(m_0+p_0)$ on the horizontal basis of the triangle.

assume two identical motor heads of opposite directionality, i.e. we set $-v_p/v_m = 1$ and $\chi_m = \chi_p$. It is then convenient to define

$$\Lambda := \frac{\Gamma-1}{\Gamma+1} = \frac{C_p k}{2C_b + 3akC_p} \tag{4.36}$$

with $0 \leq \Lambda \leq 1/3a$ and $\Gamma \geq 1$ as defined in Eq. (4.27). Stable spindles exist if

$$-\Lambda + p_0 < m_0 < \frac{1}{3} + p_0 \quad , \tag{4.37}$$

which results in the blue area in Fig. 4.11. To the left of this area the effect of the $\oplus$-end directed motors dominates, leading to aster separation. On the right of the blue area $\ominus$-end directed motors cause the spindle to collapse.

Until now we studied the somewhat artificial situation of two interacting half asters. Here we extend our analysis to also include interaction in regions (a) and (c). The overall structure of the calculation is not changed by these additional forces. The detailed calculations are given in appendix C.2.2. We obtain the stationary half length of the full spindle

$$L_s = -\frac{C_m'^{(a)}(0) + C_m'^{(b)}(0)}{C_b'^{(b)}(0)/a + 2kC_p'^{(b)}(0)} \quad . \tag{4.38}$$

In the presence of motor dimers made of two kinds of motor heads, as described above, a spindle can attain this state when

$$0 < \gamma < -\frac{v_p}{v_m} < \Gamma\gamma \quad , \tag{4.39}$$

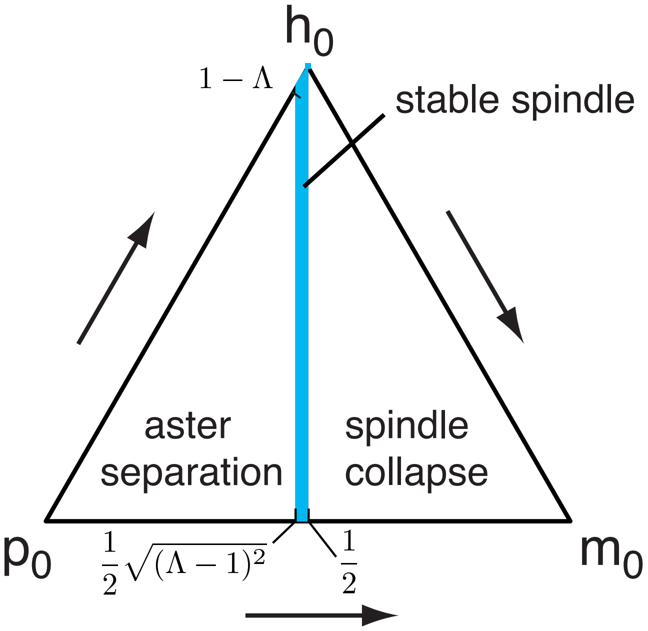

Figure 4.12: State diagram for spindle formation by two exponential full asters in the presence of all three types of motors. Stable, finite size spindles are formed in the blue region, which is smaller than for two half asters, cf. Fig. 4.11. The region of spindle collapse on the other hand has increased.

which is the same as Eq. (4.25) except that here the factor of 1/2 is missing. Also all spindles that form under this regime are stable.

Assuming two identical kinds of motor heads we can again calculate the concentration phase diagram, shown in Figure 4.12. Note that the obtained result is qualitatively similar to that obtained for half asters. The additional forces from the outside regions increase the tendency of the two asters to collapse, reducing the region in which stable spindles can form.

4.3.4 Comparison to Computer Simulations

An important theoretical study of the interaction of microtubule asters was performed with the help of computer simulations (Nédélec, 2002a). As many parameters of these simulations were not known, e.g. from experiments or independent theoretical considerations, the author employed a screening technique to discover combinations of parameters that give rise to stable interactions. The results from these screens are summarized in Fig. 4.2. Here we briefly compare them with our findings.

An important difference is brought up by screen 1: two kinds of homo-dimers. While our calculations indicate that stable spindles with finite length, Eq. (4.30), exist for a range of velocities, no such interactions were found in computer simulations. One possible explanation is that they just slipped through the mashes of parameters used in the screen. For full asters the parameter region can be narrow depending on the value of Γ (compare Figs. 4.11 and 4.12). Another possibility is that these kinds of solutions are due to special properties of our 1D description. As all microtubules are arranged aligned along a common axis and cannot bend, they might support force balances that in higher dimensions would cause these MTs to splay apart. The computer simulations are performed in 2D, so that here MTs may splay. Another important difference is that end-effects are neglected in these computer simulations, i.e. motors at filament ends detach immediately. In our description this corresponds to setting $C_p = 0$, $C_m = 0$. Under these conditions no stable spindles can be found, cf. Eq. (4.22). The precise role of end-binding cross-linkers in spindle formation and stability thus remains an important open question.

Screen 2. Motivated by the biological situation in a spindle a combination of a plus-plus dimer (Eg5) with a dimer that has one inactive and one $\ominus$-end directed head (Ncd) was investigated. No stable spindles were observed in these computer simulations. In our description an ensemble of such Ncd complexes corresponds to an ensemble of minus-minus dimers with lower velocities. When bound to two MTs only on head in an Ncd-dimer can contribute to the force on the microtubules. The situation is thus captured by the action of two homo-dimers and stable spindles are possible. We furthermore find that spindles lengthen when the velocity of minus-minus dimers is diminished.

The action of one kind of complex (screen 3a) gives rise to stable spindles. This is interesting as these spindles are formed in the absence of end-effects, i.e. motors detach immediately from microtubule ends. The complex can be of any kind (homo or hetero), depending on the combination of motor velocities chosen. We do not find finite size spindles in our description in the absence of end-effects. One possible reason for this is that the simulations model the polymerization dynamics of the aster microtubules explicitly. The smooth, idealized densities might not capture this faithfully. Microtubule densities with two intrinsic length scales on the other hand could also give rise to such stable spindles.

End-effects give rise to additional solutions (screen 3b). One kind of complex with two different heads (that need not necessarily be of different directionality), which can stay attached to the ends of MTs for a short time gives rise to additional stable spindles. This screen is the closest to our description as end-effects are included. Figure 4.13 shows the phase diagram obtained by Nédélec (2002a) and the corresponding diagram obtained analytically from our theory. The overall structure is similar, yet our theoretical description is more restrictive on the region where finite size spindles exist. The most probable reasons for this difference are the dimensionality (1D vs. 2D) and MT polymerization and depolymerization as discussed above.

4.3.5 Generality of Our Results

The results obtained within the framework of theory could depend on the specific choices of microtubule densities. Especially as the interaction with MT $\ominus$-ends plays such a prominent role (cf. e.g. Eq. (4.22)). In part C.3 of the appendix we show that stationary spindles of finite size do also exist for two different types of distributions of $\ominus$-ends as long as these distributions possess a length scale that is smaller than the length scale of the distribution of the microtubules.

The existence of finite size spindles furthermore is dependent on the length scale of the microtubules, but independent of the precise form of the MT density. In the appendix we show that finite size spindles do also exist for homogenous asters, i.e. asters in which all microtubules have the same length. The stationary length of the spindle depends on this

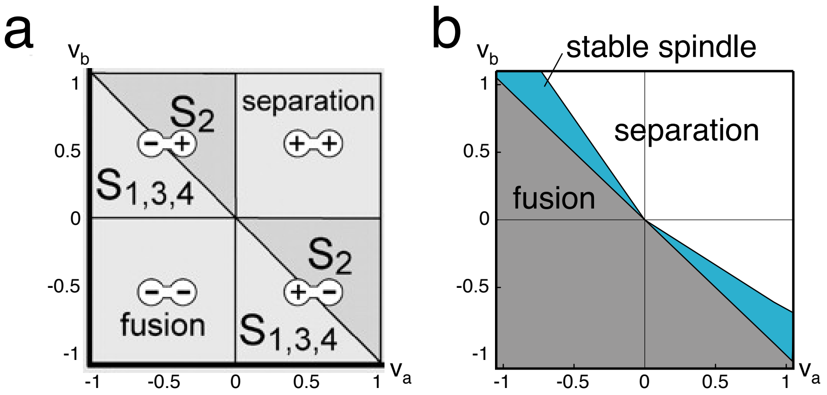

Figure 4.13: Comparision of phase diagrams for one type of motor dimers obtained by computer simulations (a, adapted from (Nédélec, 2002a)) and analytical theory (b). The regions of the stable solutions $S_1 - S_4$ obtained by computer simulations are indicated in (a), the blue region in (b) corresponds to stable spindles supported by the analytical theory.

length scale directly, be it k^{-1} as in Eq. (4.22) or the microtubule length l for homogenous asters, cf. Eq. (C.91) in the appendix.

4.3.6 Microtubule Dynamics, Chromosomes and Motor Transport

Our analytical description of two interacting stationary microtubule asters is a first step towards a theory of the mitotic spindle. Other aspects that are known about spindle structure and dynamics can be added to this theory.

One of the most prominent features of microtubules in the spindle besides dynamic instability (cf. section 2.3.1) is their continuous poleward flux (Mitchison, 1989; Mitchison and Salmon, 2001). The expression refers to a treadmilling motion of microtubules towards the spindle poles. In our description this kind of dynamics could be captured by adding a $\ominus$-end directed bias to all motor velocities. It will then depend on the size of this bias if the resulting spindles are still stable or if they collapse. Dynamic instability of microtubules on the other hand is a stochastic event of individual microtubules. In our mean field description this is accounted for by the filament densities. Its effect on the binding of motor dimers is reflected in the effective binding constants C_b, C_p and C_m. Real spindles also feature microtubules that are not attached to the spindle poles. These "free microtubules" could have interesting effects on the dynamics. They could be included in our description by a density of free mircotubules in addition to the densities of MTs that belong to the asters.

Moreover, real spindles are formed around chromosomes to which they attach via kinetochore microtubules. These kinetochore microtubules do not undergo dynamic instability and give more structural stability to the spindle. Spindles forming entirely from chromosomes in the absence of microtubule organizing centers have received a lot of attention recently (Karsenti and Nédélec, 2004). They present an interesting, complementary way of spindle formation, which is not in the scope of the theoretical approach presented here.

Another important aspect is the transport of motors and the resulting inhomogenous motor densities in the spindle. So far we have considered situations where the motor concentrations are homogenous and not influenced by the dynamics. This is the case when motors are abundant and/or when the motors are not very processive and diffuse rapidly when free. A straightforward form of the transport equations is

$$\begin{aligned} \partial_t p^{(f)}(x) &= D^{(f)}\partial_x^2 p^{(f)}(x) - \omega_{p,a} p^{(f)}(x) + \omega_{p,d} p^{(b)}(x) && (4.40) \\ \partial_t p^{(b)}(x) &= D^{(b)}\partial_x^2 p^{(b)}(x) + \omega_{p,a} p^{(f)}(x) - \omega_{p,d} p^{(b)}(x) && (4.41) \\ & \quad -\partial_x \left[\left\langle \frac{v_a^p + v_b^p}{2} \right\rangle (\rho_p(x) - \rho_m(x))\, p^{(b)}(x) \right] \end{aligned}$$

and for the other motors analogously. The superscript refers to the bound or unbound motor dimers, respectively. Free motors are subject to diffusion in the surrounding fluid and may attach to microtubule pairs with rate $\omega_{p,a}$. Detachment occurs with $\omega_{p,d}$. The mean field current due to motor interaction with the asters in the last line is proportional to the average velocity of motor heads, the difference in orientation of microtubules and of course the motor concentration. It is also possible to extend the description to motors that are attached to asters with only one head.

While it is straightforward to write down dynamic equations including motor transport, their solution is more involved and beyond the scope of this thesis.

4.4 Discussion

In this chapter we have shown how our analytic description of cytoskeletal spindles formed by two interacting asters of microtubules allows us to gain a more in depth understanding of the essential processes involved in spindle formation. A key result is that the formation of stable spindles of finite length is only possible when motor dimers stay attached to the minus end of spindle microtubules.

Our theory is based on considerations about the microscopic action of motor dimers in the spindle. It is thus an application and extension of the microscopic descriptions presented in chapter 3. We investigate two interacting filament asters that resemble a simplified mitotic spindle. The symmetry of the spindle geometry allows us to project the system on the spindle axis, yielding an effectively one-dimensional description. We explicitly take force-velocity relations of motor dimers into account.

This analytical theory of the mitotic spindle reveals interesting results about essential aspects such as forces in the spindle, spindle existence, length, and stability. Although simplified, our one dimensional mean field description already captures many central aspects of spindle dynamics. For example it puts the hypothesis and ad hoc models of how the balance of forces generated by molecular motors influences the spindle length on a firmer physical ground.

We employ the theory to discuss the length scale of mitotic spindles and conditions for the existence of stable, stationary spindles of finite length. Our theory qualitatively reproduces observations of spindle formation in *Xenopus* egg extract, that found that spindles are longer when minus-end directed motors are inhibited. It provides a framework that also facilitates the study of spindle dynamics such as spindle oscillations.

Our description of the mitotic spindle already includes many of the crucial effects for spindle formation. Although real spindles are three dimensional objects, their rotational symmetry suggests that much of the essential physics can be captured by a one dimensional description. This is even more likely, as most of the spindle material is concentrated around the spindle axis, see appendix C.4 for an example.

But the extension to higher dimensions also introduces novel physics to the problem. We already mentioned the possibility of microtubules to splay apart, i.e. MT in two or more dimensions do not necessarily support arbitrary stresses anymore. Another interesting aspect is microtubule bending. Molecular motors are strong enough to bend MTs and this is observed in spindles as well. MT bending could be captured by introducing an elastic energy in the description. Finally, molecular motors in two or more dimension induce MT rotation besides MT sliding (Liverpool and Marchetti, 2003; Tanase, 2004). This has effects on microtubule bending as well as on the distribution of MTs in the asters.

5 Continuum Theory of the Cytoskeleton

Microscopic descriptions as presented in chapter 3 present an intuitive way of approaching cytoskeletal dynamics. In real biological systems however the knowledge of the microscopic details is usually incomplete. The parameters characterizing microscopic processes in biology thus are often unknown and difficult to determine. In section 3.3 we have presented a way of tackling this biological complexity with the help of computer simulations. Physical descriptions on the other hand often take the form of microscopically inspired mean field descriptions with densities and effective parameters such as e.g. the model for active filament systems presented in section 3.1.3. The advantage of these microscopic approaches is that they are mathematically tractable and usually allow the identification of microscopic key processes for the observed dynamics. On the other hand it is often unclear if these models encompass all relevant biological details. We know that the "minimal model" as introduced in section 3.2 represents a minimal model for the contraction of bundles of stabilized filaments by molecular motors. Real protein filaments however are highly dynamic, i.e. they polymerize and depolymerize. Furthermore they will also bind other proteins such as passive cross-linkers that influence bundle dynamics. In order to understand the effect of these processes one has to include them explicitly into the microscopic description. As additional biological details can only be accounted for by additional terms. Obviously it is impractical and impracticable if not impossible to add all possible protein interactions in that way.

In this chapter we present descriptions of cytoskeletal dynamics that are not limited in this way. The behavior of systems on large length and time scales is frequently independent of the microscopic details. Rather, it is often determined by the symmetries of the system and the conserved quantities. Phenomenological descriptions of the cytoskeleton capture dynamics on length scales large compared to the filament length and on time scales large compared to typical microscopic time scales, e.g. the motor binding time. In contrast to microscopic descriptions, phenomenological, continuum descriptions do not rely on explicit microscopic details of the involved processes. They approach the problem from the other end as it were. Based on symmetries and conserved quantities of the system, they are generic in the sense that they capture the effects of all possible microscopic interactions that respect these symmetries and conservation laws. The dynamics of the distributions of cytoskeletal filaments, motors and other proteins are captured by their respective densities and continuity equations. The orientational order of filaments is described by a hierarchy of order parameters for e.g. polarization and nematic order. These order parameters are usually not conserved. For cytoskeletal systems the conserved quantities are usually the number densities of proteins and other molecules such as actin, myosin or ATP, the solvent and momentum. This conservation usually applies only to the whole system, i.e. actin in its G- and F-form together will be conserved, ATP, ADP and P_i together are conserved, and so on.

Where microscopic descriptions need to include nonlocal expressions to capture e.g. the transmission of stresses over finite distances by interactions of filaments (chapter 3), phenomenological descriptions can be local, continuum theories, see section 5.1. A prominent example for the phenomenological approach in physics is the Ginzburg-Landau theory for phase transitions (Ginzburg and Landau, 1950). The cytoskeleton however is an active system, i.e. all terms allowed by symmetry have to be included, regardless of their significance for the energy of the system. Phenomenological descriptions have been applied to cytoskeletal systems in situations, in which only motors are allowed to move in space (Lee and Kardar, 2001; Kim et al., 2003; Sankararaman et al., 2004). The filament density is taken to be homogenous at all times so that motors are influenced mainly by filament orientation. The complementary case of filaments moving freely on a plane of localized motors is reminiscent of e.g. microtubule motility assays and has also been studied (Bourdieu et al., 1995; Bassetti et al., 2000). We proposed a first phenomenological description of the cytoskeleton as an active fluid, i.e. allowing motors *and* filaments to move in Kruse et al. (2003). It is explained in greater detail in section 5.1 below.

The organization of this chapter is as follows: the following section 5.1 introduces the general ideas behind our description of active fluids or gels. We then discuss the dynamics of contractile fibers, i.e. linear aggregates of active material such as stress fibers or contractile rings formed by cytoskeletal protein filaments and motors in section 5.2. We analyze bundle contraction driven by stress release and show the emergence of sarcomere like structures by self-organization. In section 5.3 we discuss these active gels in cylindrical geometries such as found e.g. in the cell cortex. We show that rings in the cell cortex such as the contractile ring or the pre-prophase band can form by self-organization phenomena. The rings can be stationary or oscillate. Oscillating cytoskeletal rings have been observed in various different cell types (Bornens et al., 1989; Paluch et al., 2005).

5.1 Phenomenological Description of Active Fluids

In (Kruse et al., 2003) we proposed a first phenomenological description for the dynamics of the cytoskeleton as an active polar fluid. We investigated linear structures such as contractile rings or stress fibers, taking into account polar order. This one-dimensional description has been generalized to higher dimensions and nematic order (Zumdieck et al., 2005a; Banik et al., 2005), see Fig. 5.1.

5.1.1 Dynamic Equations

The general idea is as follows: We describe the dynamics of filaments and free subunits with respect to a non-moving solvent. This situation corresponds, e.g., to filaments and motors in the vicinity of a stationary surface, such as e.g. a cell wall. The concentration of subunits and motors is assumed to be homogenous and constant for all times, so that their dynamics does not appear explicitly.[1] In this case, the dynamics is completely specified by the conservation law for the filaments and the dynamic equations for orientational order parameters:

$$\partial_t c + \boldsymbol{\nabla} \cdot \boldsymbol{j} = s \tag{5.1}$$

$$\partial_t \boldsymbol{p} = \boldsymbol{\psi} \tag{5.2}$$

$$\partial_t \boldsymbol{q} = \boldsymbol{\omega} \tag{5.3}$$

where c is the filament density, $\boldsymbol{p}$ is the polar and $\boldsymbol{q}$ is the nematic order parameter. We assume local friction and neglect hydrodynamic interactions between filaments. Disregarding filament treadmilling, we can write the filament current as

$$j_\alpha = \eta^{-1} \partial_\beta \sigma_{\alpha\beta} \quad . \tag{5.4}$$

---

[1] The values of e.g. the motor concentration do of course implicitly influence the phenomenological constants of the theory.

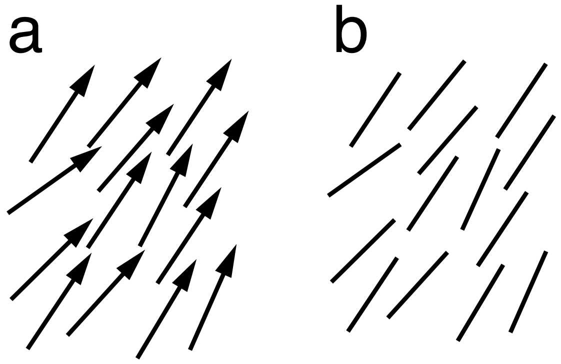

Figure 5.1: Order parameters used in this chapter. (a) Polar order captures orientations and directions of filaments. It can thus be described by a vector $\boldsymbol{p}$ which is invariant under rotations of 2π. (b) Nematic order captures only the direction of the filaments. It corresponds to rods that do not have a orientation, i.e. are invariant under rotations of π. Mathematically this can be described by a symmetric, traceless tensor.

Here, η is a parameter with dimensions of a friction coefficient and $\sigma_{\alpha\beta}$ is the stress tensor. We close the equations with a constitutive equation for the stress tensor $\boldsymbol{\sigma}$ and equations for the rates of change in the orientational order parameters $\mathbf{p}$ and $\boldsymbol{q}$. As the exact functional dependence of the stress on the filament density and the order parameters is not known, we systematically expand the stress in terms of these quantities with respect to a reference state. We treat the rates of change $\boldsymbol{\psi}$ and $\boldsymbol{\omega}$ of the orientation order parameters in the same way. The details of this calculation are given in section 5.2. In this chapter we chose the homogenous isotropic state as the reference state.

5.1.2 Order Parameters

We now briefly present the two types of order parameters used in this chapter. We start out with polar order which is characterized by a vectorial order parameter, see Fig. 5.1a. Second we discuss nematic order (Fig. 5.1b) that is familiar from the field of liquid crystals (de Gennes and Prost, 1993) and characterized by a symmetric, traceless tensor.

Polar Order

Cytoskeletal filaments such as microtubules or actin filaments are typically extended objects that thus lie in a certain direction in space. They are furthermore structurally polar, i.e. they are oriented along the direction in one of two possible ways. In a one dimensional geometry the direction is the same for all filaments, but the orientation may be different. We denoted the two different orientations "+" and "−" in the previous chapter.

In higher dimensions the direction and orientation of a filament i can be characterized by a unit vector $\boldsymbol{u}_i$ located at the filament center. Considering filaments in a volume V we can define averages of the tensor products of $\boldsymbol{u}$. The zeroth of these "moments" is the number density $c(V) = \langle \boldsymbol{u}^0 \rangle_V$, where $\langle \cdot \rangle_V$ denotes the average over the filaments located in V.

The polar order parameter is given by the next higher tensor product

$$\boldsymbol{p}(V) = \langle \boldsymbol{u} \rangle_V \quad . \tag{5.5}$$

This order has vectorial character, the direction and orientation of $\boldsymbol{p}$ are the average direction and orientation of filaments in V. The length of $\boldsymbol{p}$ is a measure of the magnitude of the order, where 0 describes a completely disordered system and 1 corresponds to perfect order (i.e. all filaments are aligned and oriented in the same way).

Nematic Order

Nematic order describes the direction of extended objects, but ignores their orientation, see Fig. 5.1b. This type of order is invariant under rotations of π. Mathematically nematic order is based on the tensor product of $\boldsymbol{u}$ that is of the next higher, i.e. quadratic order. It is represented by a symmetric and traceless tensor of rank d, where d is the dimension of space. The definition of the tensor components is given by

$$q_{\alpha\beta}(V) = \langle u_\alpha u_\beta - \frac{1}{d}\delta_{\alpha\beta}\rangle_V \tag{5.6}$$

where α, β are summed over the spatial dimension. In this thesis we only consider up to two dimensional geometries. As the nematic order is trivial in one dimension, where all filaments are aligned, we will focus on $d = 2$ for the rest of this section.

Physically nematic order describes only a direction in space (but no orientation). It is thus instructive to interpret the components of the nematic tensor $q_{\alpha\beta}$ in this way. By construction we have

$$\boldsymbol{q} = \left(\begin{array}{cc} q_{xx} & q_{xy} \\ q_{xy} & -q_{xx} \end{array}\right) \quad , \tag{5.7}$$

i.e. there are only two independent components. From these components we can derive two quantities that are more intuitive to interpret:

$$\begin{aligned} S &= 2\sqrt{q_{xx}^2 + q_{xy}^2} && (5.8) \\ \tan\phi &= \frac{S}{2q_{xy}} - \frac{q_{xx}}{q_{xy}} && (5.9) \end{aligned}$$

Here S measures the magnitude of the order with $S = 0$ for a completely disordered system and $S = 1$ for perfect order. The angle $\phi \in [-\pi/2; \pi/2]$ is the angle the nematic director forms with the x-axis. Table 5.1 shows some examples of nematic order parameters.

For both perfect horizontal and perfect vertical alignment $q_{xy} = 0$ which complicates the calculation of $\tan\phi$. We obtain the values presented in table 5.1 by expanding Eq. (5.9) up to second order in q_{xy}:

$$\begin{aligned} \tan\phi &= \frac{\sqrt{q_{xx}^2 + q_{xy}^2} - q_{xx}}{q_{xx}} \\ &\simeq \frac{|q_{xx}|\left(1 + \frac{1}{2}\frac{q_{xy}^2}{q_{xx}^2}\right) - q_{xx}}{q_{xy}} + \mathcal{O}(q_{xy}^3) && (5.10) \\ &\to \left\{ \begin{array}{ll} \frac{q_{xy}}{2\,q_{xx}} \to 0 & \text{for } q_{xx} > 0 \\ 2\frac{|q_{xx}|}{q_{xy}} + \frac{q_{xy}}{2\,|q_{xx}|} \to \pm\infty & \text{for } q_{xx} < 0 \end{array} \right. && (5.11) \end{aligned}$$

This calculation shows that the perfect horizontal and the perfect vertical orientation are determined by the sign of q_{xx}.

$\boldsymbol{n}$	q_{xx}	q_{xy}	S	$\tan\phi$	ϕ	Graphics
$\begin{pmatrix} 1 \\ 0 \end{pmatrix}$	$\frac{1}{2}$	0	1	0	0	
$\begin{pmatrix} 0 \\ 1 \end{pmatrix}$	$-\frac{1}{2}$	0	1	∞	$\frac{\pi}{2}$	
$\frac{1}{\sqrt{2}}\begin{pmatrix} 1 \\ 1 \end{pmatrix}$	0	$\frac{1}{2}$	1	1	$\frac{\pi}{4}$	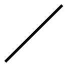

Table 5.1: A few examples illustrating the nematic order parameter. The first column gives the director of all filaments in the volume considered, i.e. the system is in perfect order. The corresponding values of the nematic order parameter in the two representations introduced in the text and a graphical representation are shown.

5.2 Active Filament Bundles

As already discussed, the one dimensional geometry of a fiber provides a good starting point for our theoretical approach. We thus first developed a one dimensional, phenomenological description of active filament bundles (Kruse et al., 2003). Here all filaments are aligned along a common axis and their movement is restricted to one dimension along that axis. In this case, the stress is a scalar σ and the polarization p is a pseudo-scalar that changes sign under the inversion of space $x \to -x$ (Kruse et al., 2003). The density c and the stress σ are even under these reflections. As the nematic order is trivial in one dimension we do not include it in our description of one dimensional filament bundles. The dynamics is given by the continuity equations

$$\begin{aligned} \partial_t c + \partial_x j &= s &(5.12)\\ \partial_t p + \partial_x j_p &= s_p \quad . &(5.13) \end{aligned}$$

The filament current in the rest frame of the fluid j is given by a tension gradient as in Eq. (5.4), which ignores filament treadmilling[2]:

$$j = \eta^{-1}\partial_x \sigma \quad . \tag{5.14}$$

We expand the constitutive equation for σ up to second order in c and p and retain derivatives up to second order:

$$\begin{aligned} \eta^{-1}\sigma = & -Dc + A_1\partial_x p + A_2\partial_x^2 c & (5.15)\\ & +B_1c^2 + B_2p^2 + E_1c\partial_x p + E_2(\partial_x c)p \\ & +F_1c\partial_x^2 c + F_2p\partial_x^2 p + F_3(\partial_x c)^2 + F_4(\partial_x p)^2 \quad . \end{aligned}$$

Here we have kept only terms that are allowed by symmetry and have truncated the expansion such that the dynamics does not generate singularities at finite times. The latter requirement furthermore imposes $F_1 > 0$ and $F_3 < 0$. The stress as given in the above equation contains the active stress generated by motor proteins.

---

[2] The density current due to filament treadmilling has the form $j = -vp$ and can thus not be written as the divergence of a stress. See also section 5.2.5

The current j_p is not induced by tension gradients, however we assume throughout this calculation that c and p fully determine the state of the system. We thus may write for the polarization current

$$\begin{aligned} j_p \;=\; & \epsilon(c^2 - p^2) - D\partial_x p + A_1\partial_x^2 c + A_2\partial_x^3 p \\ & +\bar{B}_1 c\partial_x p + \bar{B}_2(\partial_x c)p \\ & +\bar{E}_1 c\partial_x^2 c + \bar{E}_2 p\partial_x^2 p + \tilde{E}_1(\partial_x c)^2 + \tilde{E}_2(\partial_x p)^2 \\ & +\bar{F}_1 c\partial_x^3 p + \bar{F}_2(\partial_x^3 c)p + \bar{F}_3(\partial_x c)\partial_x^2 p + \bar{F}_4(\partial_x^2 c)\partial_x p \quad . \end{aligned} \tag{5.16}$$

Again we have only kept terms allowed by symmetry. Furthermore, in the case of a fully polarized fiber, polarization and density are proportional to each other, $c \propto p$. This is due to the proportionality of currents in this case: Let c^+ denote the density of plus filaments and c^- that of minus filaments. Then we can relate the density $c(x) = c^+(x) + c^-(x)$ and polarization $p(x) = c^+(x) - c^-(x)$. So in a fully polar fiber where only one orientation is present we must have $j \propto j_p$. Without loss of generality we may assume $j = j_p$. Comparing the expressions for j and j_p in the limit $c = p$ then imposes the form (5.16) of the polarization current and furthermore implies $\bar{B}_1 + \bar{B}_2 = 2(B_1 + B_2)$, $\bar{E}_1 + \bar{E}_2 = \tilde{E}_1 + \tilde{E}_2 = E_1 + E_2$, $\bar{F}_1 + \bar{F}_2 = F_1 + F_2$, and $\bar{F}_3 + \bar{F}_4 = 2(F_3 + F_4) + F_1 + F_2$.

The source and sink terms s and s_p describe effects of polymerization and depolymerization. Using the same arguments as described above, we can write simplified expressions for them:

$$s \;=\; c - \mu c^2 - \nu p^2 \tag{5.17}$$

$$s_p \;=\; p - (\mu + \nu)pc \tag{5.18}$$

Again we have used the constraint $s = s_p$ for $c = p$. This constraint remains valid in the presence of filament polymerization and depolymerization if spontaneous changes of filament orientation (filament flips) are neglected and under the assumption, that filaments of one orientation are generated by nucleation only if filaments of this orientation already exist (i.e. a fully polar fiber with $c = p$ remains fully polar at all times even in the presence of source terms). For the expressions of the source terms we have assumed that they only depend on the local density and order, which excludes the possibility of externally controlled polymerization. The system is stable for μ and ν positive.

Now we analyze these dynamic equations in two limiting cases of a fully polar and a non-polar fiber, cf. (Kruse et al., 2003), before discussing the general case.

5.2.1 Fully Polar Fibers

The dynamics of fully polarized fibers, i.e. fibers with $p = c$, in the absence of filament polymerization and depolymerization is completely determined by a single equation for the filament density

$$\partial_t c = -\eta^{-1}\partial_2^2 \sigma \quad . \tag{5.19}$$

The stress can then be written as

$$\eta^{-1}\sigma = -Dc + A\partial_x c + \frac{B}{2}\left(c^2 - \lambda^2(\partial_x c)^2\right) + Ec\partial_x c + Fc\partial_x^2 c \quad , \tag{5.20}$$

where λ is a length scale with $\lambda^2 = -(F_3+F_4)/(B_1+B_2)$, $A = A_1$, $A_2 = 0$, $B = 2(B_1+B_2)$, $E = E_1 + E_2$, and $F = (F_1 + F_2)$. Here we will neglect the A_2 term, as it is irrelevant in for the remainder of this section. We impose $F > 0$ in order to avoid instabilities on

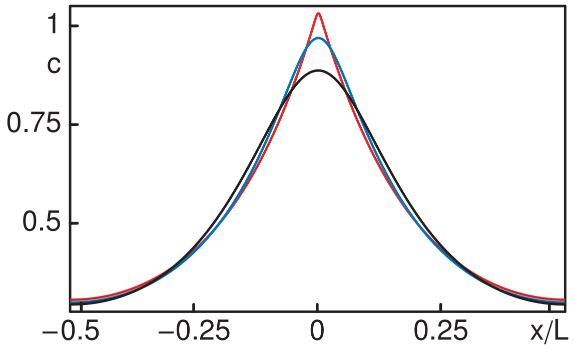

Figure 5.2: Stationary filament density profile of a fully polarized fiber with tension as given by Eq. (5.20). The curves were obtained by numerical integration with $F = 0.05$ (red), $F = 0.5$ (blue), and $F = 1$ (black). The analytic solution for $F = 0$ as given by Eq. (5.27) has a real kink at $x = 0$ (not shown). Parameters are $B = 6$, $D = 1$, $\lambda = 1$, $c_0 = 0.5$, $L = 5$, $A = 0$, $E = 0$.

small length scales. For periodic boundary conditions, the homogenous state $c = c_0$ is a stationary solution of the above equations. Here the homogenous density is determined by $c_0 = L^{-1} \int \mathrm{d}x\, c$ where L is the length of the system. The homogenous state is linearly stable as long as $B < B_c$ with

$$B_c = \frac{D}{c_0} + 4\pi^2 \frac{F}{L^2} \quad . \tag{5.21}$$

For $B > B_c$ the homogenous state becomes unstable with respect to a stationary, localized state for $A + Ec_0 = 0$, and otherwise with respect to oscillatory solutions that are solitary waves. In either case the density profile has exactly one maximum and corresponds to an accumulation of the filaments at one point (Fig. 5.2). The density profiles have been obtained by integrating the dynamic equations (5.19) and (5.20) numerically, see appendix B for details. The bifurcation can be sub- or supercritical, depending on the values of Fc_0/DL^2 and λ/L, cf. Fig. 5.3.

As stated above, the system undergoes a Hopf bifurcation for $A+Ec_0 \neq 0$. The resulting solitary wave solutions have the form $c(x,t) = u(x - vt)$. Inserting this Ansatz into the dynamic equation (5.19), we obtain an ordinary differential equation of third order for the density profile u. Integrating once with respect to space leads to

$$-vu = \partial_x \sigma + K \tag{5.22}$$

where K, the constant of integration for periodic boundary conditions is fixed by

$$-v \int_0^L \mathrm{d}x\, u = \int_0^L \mathrm{d}x\, K \iff K = \frac{-vN}{L} \quad . \tag{5.23}$$

With periodic boundary conditions, equation (5.22) has a discrete set of solutions with distinct values of v. Note, that a unique stationary solution with $v = 0$ always exists. As the system size is increased, solitary waves maintain their shapes but cease to propagate in an infinite system.

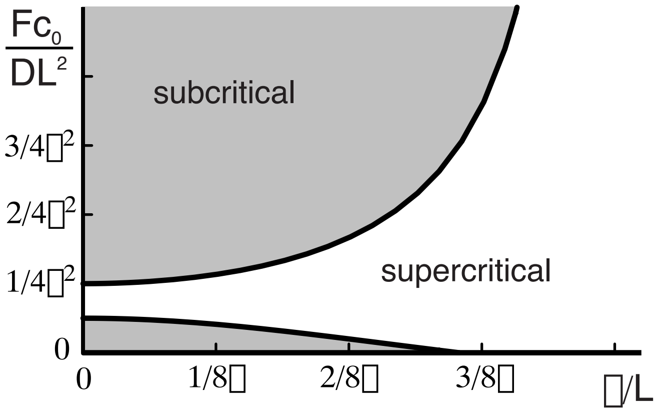

Figure 5.3: Regions of supercritical and subcritical bifurcations for oriented bundles with parameter values $A = 0$ and $E = 0$. In the case of a supercritical bifurcation at $B = B_c$, a stable nonhomogeneous state exists only for $B > B_c$. For a subcritical bifurcation such states coexist with the stable homogeneous state in an interval $[B_d, B_c]$. The character of the bifurcation is determined by the values of Fc_0/DL^2 and λ/L.

It is instructive to consider the limit $F = 0$ where the differential equations is of second order and can be represented by the pair of first order equations

$$\begin{aligned} \sigma' &= v\eta(u - c_0) && (5.24)\\ u' &= \frac{1}{\lambda^2 B}\left(Eu + A\right. \\ &\pm \left.\sqrt{(Eu + A)^2 + 2\lambda^2 B(Bu^2/2 - Du - \sigma)}\right) \quad , && (5.25) \end{aligned}$$

where the primes denote derivatives with respect to x and where we have used the condition $\sigma(0) = \sigma(L)$. The resulting solutions $u(x)$ are discontinuous in their first derivative at the extrema of u where the two branches of solutions to Eq. (5.25) are connected. For finite F, solitary wave solutions can be obtained by numerically integrating the dynamic equations. For small F these waves approach solutions to Eq. (5.25). Numerical solutions to the dynamic equations reveal that the stationary solution with $v = 0$ is unstable if solitary waves exist.

Stress release by contraction in a fully polar fiber. The homogenous state of the fiber generates a tension σ_0 with

$$\sigma_0 = \eta\left(\frac{B}{2}c_0^2 - Dc_0\right) \quad . \tag{5.26}$$

This tension is positive, i.e., contractile for $B > 2D/c_0$. Thus for $F > DL^2/4\pi^2 c_0$ the homogenous state of the fiber is stable and contractile. This regime represents a homogenous contractile ring that can contract radially as described in chapter 6.

For a stationary bifurcation ($A = 0$, $E = 0$) we can analytically calculate the density profile in the limit $F = 0$. For periodic boundary conditions of a system with length L, it is given by

$$c_s(x) = H\cosh\frac{x - L/2}{\lambda} + \frac{D}{B} \quad , \tag{5.27}$$

which has a discontinuity of c' at $x = 0$ and $x = L$. The amplitude

$$H = \frac{L(c_0 - D/B)}{2\lambda \sinh L/2\lambda} \quad . \tag{5.28}$$

is determined by the total number of filaments $c_0 L$. This state has a constant tension

$$\sigma_{\mathrm{s}} = \eta \left(\frac{B}{2} H^2 - \frac{D^2}{2B} \right) \quad . \tag{5.29}$$

which obeys $\sigma_s < \sigma_0$ for $B > B_c$. This means that tension is relaxed via fiber contraction at the instability of the homogeneous state.

5.2.2 Non-Polar Fibers

If the filaments in the fiber are disordered, so that in a small volume the average orientation is $p = 0$, we are dealing with a non-polar fiber. Note that the filaments at very short scales can be ordered regularly and still the fiber can be non-polar. This is e.g. the case in muscle myofibrils (see Fig. 2.30) for dynamics on length scales larger than a sarcomere length. It presumably also holds for contractile rings and stress fibers in animal cells and the preprophase band in plant cells (cf. section 5.3). For vanishing polarization the dynamics of the fiber is again given by one equation for the filament density only. The dependence of the tension on the filament density is of the same form as in Eq. (5.20) but the non-polarity additionally requires $A = 0$, $E = 0$, $B = 2B_1$, $F = F_1$, and $\lambda^2 = -F_3/(2B_1)$. This implies that the stationary homogenous state always looses its stability via a stationary bifurcation. Non-polarity thus suppresses oscillations. The stationary results discussed for the fully polar bundle thus also apply to non-polar fibers.

5.2.3 Partial Polarization

In the general case, i.e. for arbitrary values of the polarization, the dynamics is given by two coupled partial differential equations for c and p. The same classes of solutions as discussed above can be obtained by numerical integration.

The stability of the homogenous state (c_0, p_0) is governed by

$$\partial_t \begin{pmatrix} c \\ p \end{pmatrix} = \begin{pmatrix} A_{11} & A_{12} \\ A_{21} & A_{22} \end{pmatrix} \begin{pmatrix} c \\ p \end{pmatrix} \tag{5.30}$$

where the matrix elements are given by

$$\begin{aligned} A_{11} &= (D - 2Bc_0)\partial_x^2 - Ep_0\partial_x^3 - (A_2 + Fc_0)\partial_x^4 && (5.31) \\ A_{12} &= -2Bp_0\partial_x^2 - (A_1 + Ec_0)\partial_x^3 - Fp_0\partial_x^4 && (5.32) \\ A_{21} &= -2\epsilon c_0\partial_x - 2Bp_0\partial_x^2 - (A_1 + Ec_0)\partial_x^3 - Fp_0\partial_x^4 && (5.33) \\ A_{22} &= 2\epsilon p_0\partial_x + (D - 2Bc_0))\partial_x^2 - Ep_0\partial_x^3 - (A_2 + Fc_0)\partial_x^4 && (5.34) \end{aligned}$$

The homogenous state is again stable for $B < B_c$, a critical value, and loses its stability via a Hopf-bifurcation if $A + Ec_0 > 0$. In addition the parameter ϵ, introduced in Eq. (5.16), must be lower than a certain critical value ϵ_c. For $\epsilon > \epsilon_c$ the bifurcation is stationary.

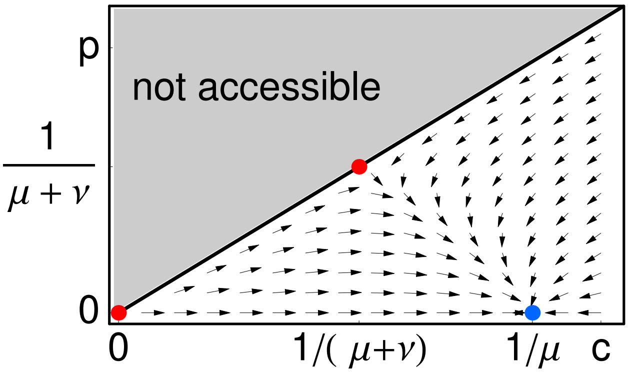

Figure 5.4: Phase space for the dynamics of the source terms alone as given by Eqs. (5.35) and (5.36). The arrowheads indicate the direction of flux in phase space. The colored dots mark the three fixed points of the dynamics. Two states are unstable against homogenous perturbations (red dots), only state (iii) with $c = 1/\mu$ and $p = 0$ is stable (blue dot).

5.2.4 Polymerization and Depolymerization of Filaments

So far we have discussed the dynamics of active fibers in the absence of polymerization and depolymerization. Here we consider this dynamics as described by the source terms (5.17) and (5.18). The dynamics of the sources alone

$$\partial_t c = s \tag{5.35}$$
$$\partial_t p = s_p \quad , \tag{5.36}$$

has three different stationary homogenous states (see Fig. 5.4):

i $c_0 = 0$, $p_0 = 0$

ii $c_0 = p_0 = 1/(\mu + \nu)$

iii $c_0 = 1/\mu$ and $p_0 = 0$.

In order to determine the stability of a stationary state (c_0, p_0) against homogenous perturbations, we perform a linear stability analysis. Up to linear order the dynamics is governed by

$$\partial_t \begin{pmatrix} c \\ p \end{pmatrix} = \begin{pmatrix} 1 - 2\mu c_0 & -2\nu p_0 \\ -(\mu + \nu) p_0 & 1 - (\mu + \nu) c_0 \end{pmatrix} \begin{pmatrix} c \\ p \end{pmatrix} \tag{5.37}$$

The eigenvalues of the stability matrix are given by

$$\lambda_{1,2} = 1 - \frac{3\mu + \nu}{2} c_0 \pm \frac{1}{2} \left((\mu - \nu)^2 c_0^2 + 8\nu(\nu + \mu) p_0^2 \right)^{\frac{1}{2}} \tag{5.38}$$

Analysis of the larger eigenvalue reveals that only state (iii) is stable with respect to homogenous perturbations for all parameter values.

Taken as the state of a homogenous fiber described by the full dynamical equations, state (iii) becomes unstable with respect to non-homogenous perturbations when $B > B_c$, a critical value. Linear stability analysis of this situation reveals that the instability occurs with respect to an unstable mode that has a finite wave vector q, which introduces a new length scale in the system, see Fig. 5.5. As discussed above for the dynamics without source terms, the instability can be stationary or of the Hopf kind, depending on the value of ϵ and F.

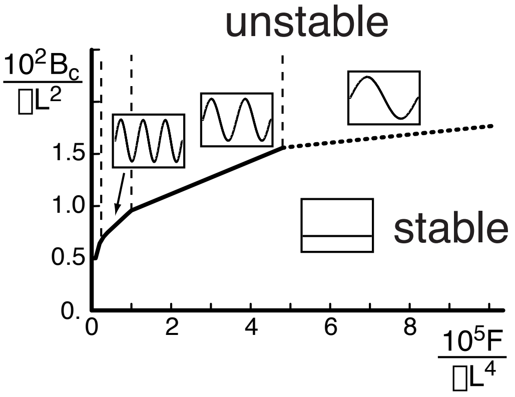

Figure 5.5: Stability boundary of the homogenous state of an active fiber in the presence of filament polymerization and depolymerization. Insets indicate the density profiles of the corresponding unstable modes. Along the solid line the homogenous state loses stability via a Hopf-bifurcation; the dotted line indicates a pitchfork-bifurcation.

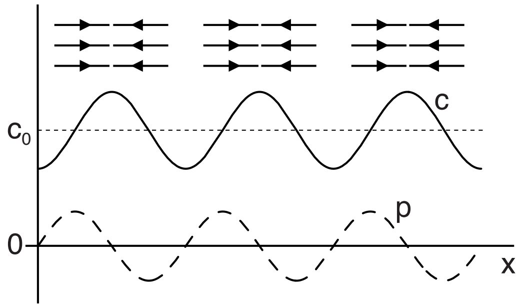

Figure 5.6: Density profile (solid line) and polarization profile (broken line) of an unstable mode of an active fiber with filament polymerization and depolymerization. The associated wavelength is smaller than the system size, leading to a periodic modulation of the unstable mode. Density and polarization display a relative phase shift of $\pi/2$. The mode corresponds to an arrangement of filaments like the one indicated schematically.

Our analysis shows that the unstable mode possesses a phase shift of $\pi/2$ between c and p. The corresponding arrangement of filaments is comparable to the periodic arrangement of filaments in a muscle myofibril, see Fig. 5.6 for an illustration.

Let us now discuss the case of a fully oriented bundle. We assume that the system consists exclusively of filaments of one orientation and that filaments of the opposite orientation are not generated by polymerization events. Therefore, the dynamic solutions satisfy the condition $c = p$ for all times. In this situation, two homogeneous states with $c = p = 0$ and $c = p = 1/(\mu + \nu)$ exist. The former is always unstable while the latter becomes unstable for $B > \bar{B}_c$ where $\bar{B}_c = \mu(2\sqrt{F/\mu} + D)$. At the bifurcation, the characteristic wave vector is given by $q^4 = (\mu + \nu)/F$ and the frequency is $\omega = A + E/(\mu + \nu)$. Therefore, as in the absence of polymerization and depolymerization, the instability of the homogeneous state occurs in general via a Hopf bifurcation.

The source terms presented and discussed above are the simplest source terms in the frame work of this generic continuum description that, when studied alone, do not have trivial dynamics. We can extend these expressions in order to accommodate the polymerization dynamics discussed in the microscopic mean field description, section 3.2.4. Neglecting explicit monomer dynamics, the corresponding expressions are

$$\partial_t c^+ = k_p - k_d c^+ \tag{5.39}$$

$$\partial_t c^- = k_p - k_d c^- \tag{5.40}$$

so that using $c = c^+ + c^-$ and $p = c^+ - c^-$ we immediately obtain

$$\partial_t c = k_c - k_d c \tag{5.41}$$

$$\partial_t p = -k_d p \tag{5.42}$$

where we define a new constant polymerization rate $k_c = 2k_p$. The only stationary state of this dynamics is given by $c = k_c/k_d$ and $p = 0$, which is globally stable.

The situation becomes more interesting when we merge these expressions with the simplified expressions in Eqs. (5.17) and (5.18):

$$\partial_t c = c - \mu' c^2 - \nu' p^2 + k'_c \tag{5.43}$$

$$\partial_t p = p - (\mu' + \nu') pc \tag{5.44}$$

where we have rescaled time and the primes mark the resulting rescaled parameters. This system has two types of fixed points

i $c = \frac{\pm 1 + \sqrt{1 + 4k'_c \mu'}}{2\mu'}$, $p = 0$

ii $c = \frac{1}{\mu+\nu}$, $p = \pm\sqrt{\frac{k'_c}{\nu} + \frac{1}{(\mu+\nu)^2}}$

The linear stability is governed by the larger eigenvalue given in Eq. (5.38) with the appropriate rescaled parameters. This reveals that fixed point (ii) is always unstable and that (i) is stable for $\mu' \neq 0$. This fixed point is qualitatively the same as point (iii) of the simplified expressions, see Fig. 5.4. Thus its properties are not different and the results presented in the previous section qualitatively hold also for these extended source terms.

5.2.5 Filament Treadmilling

As the filament current due to filament treadmilling is not induced by gradients in the tension, it cannot be included by adding terms to Eq. (5.15). We thus have to alter the currents in the theory directly by adding the following terms for treadmilling:

$$j_v = -vp \tag{5.45}$$

$$j_{p,v} = -vc \tag{5.46}$$

The dynamics of fully polar fibers in the presence of treadmilling is given by

$$\partial_t c = v\partial_x c + D\partial_x^2 c - A\partial_x^3 c - \frac{B}{2}\partial_x^2\left(c^2 - \lambda^2(\partial_x c)^2\right) + Ec\partial_x^3 c + Fc\partial_x^4 c \quad . \tag{5.47}$$

Writing c as a Fourier sum $c = \Sigma_k c_k \exp(ikx)$ reveals immediately that the treadmilling current can only contribute to the oscillation frequency of the critical mode, but not to its stability. Hence even in the presence of treadmilling the homogenous state is stable for $B < B_c$, where the critical value B_c is given by Eq. (5.21). As discussed above, we generally expect the homogenous state to loose stability via a Hopf bifurcation towards oscillation solutions. The presence of treadmilling will thus not alter the generic behavior of the system qualitatively.

The stability of unpolar fibers in the presence of treadmilling is the same as without treadmilling. As outlined above, the dynamics is described by Eq. (5.47) with $A = 0$ and $E = 0$. In addition the treadmilling term is not present, as $p = 0$ implies $j_v = 0$, cf. Eq. (5.45). Thus literally nothing changes in the presence of treadmilling, as the dynamic equation is unchanged.

For arbitrary polarization we expect the same types of solutions as discussed in section 5.2.3. The homogenous state is stable for $B < B_c$ a critical value.

5.2.6 Connection to the Minimal Model

The types of asymptotic state solutions of the generic continuum description of an active fiber presented above are the same as found in the minimal model presented in chapter 3. This is comforting as we can view the minimal model as a microscopic theory corresponding to the generic continuum description. Interestingly the minimal model seems to capture the generic behavior of active filament fibers, although it is based on simplifying assumptions and limited to pair-wise filament interactions. In appendix A we put this statement on firm grounds by coarse graining the minimal model and comparing the resulting expressions with the generic description. The ensuing expressions are of the form presented above.

When derived from the minimal model, most coefficients of the expansion (5.15) and (5.16) are non-zero. Only A_1, A_2, $\tilde{E}_1$, $\tilde{E}_2$, $\bar{F}_3$ and $\bar{F}_4$ vanish. The corresponding terms thus are either generated by higher order processes involving three or more filaments, are a consequence of anisotropy effects that manifest themselves only in higher dimensions or are due to a different form of filament-filament interactions not included in the minimal model. The equations derived from the minimal model show a higher degree of symmetry than the generic description. Some coefficients mutually depend on each other (explicit expressions given in Eqs. (A.20) - (A.25)), which further reduces the phase space of the system.

The detailed dependence of the coarse grained expansion coefficients on the parameters α and β (cf. Figs. 3.5 and 3.6) is given in tables A.2 and A.3. Here we note that B_1 and F_1 are proportional to α, while E_1 is proportional to β. This confirms the finding that instabilities in the minimal model are driven by interactions between filaments of the same orientation and that oscillatory solutions in the absence of filament treadmilling are driven by interactions between filaments of opposite orientation.

Furthermore we can compare the tension for the homogenous state with concentration c_0 and polarization p_0 derived by coarse graining the minimal model (cf. Eq. (A.26))

$$\sigma = -c_0 + \frac{l^2}{8}\left[(2(\alpha+\alpha')+\beta')c_0^2 + (2(\alpha+\alpha')-\beta')p_0^2\right] \tag{5.48}$$

and in the continuum theory derived from Eq. (5.15)

$$\eta^{-1}\sigma = -Dc_0 + B_1 c_0^2 + B_2 p_0^2 \quad . \tag{5.49}$$

These expressions agree (cf. tables A.2 and A.3) for $D = 1$ and $\eta = 1$, which are the choices made for the minimal model and the continuum description respectively.

5.3 Active Fluid in Cortical Geometry[3]

The continuum theory presented for active fibers in the last section can be extended to more general geometries and orders. The cortex in eucaryotic cells, that often have an elongated shape such as Tobacco BY2 cells, motivates a two dimensional, cylindrical geometry. Evidence from plant cells indicates that in the cortical array (CA) filaments orient in a non-polar way (Chan et al., 2003). It has been suggested that this holds for the pre-prophase band (PPB) as well (Tian et al., 2004; Dhonukshe and Gadella, 2003), see also section 2.5.3. After polar order, nematic order as introduced in section 5.1.2 is described by the next order parameter in the hierarchy. Here we present a description of an active fluid in a cylindrical (cortical) geometry with nematic order. As rings such as the contractile ring or the pre-prophase band are prominent cytoskeletal structures, we focus our attention on ring formation in the cell cortex. Neglecting influences of surface curvature, we find that nematic order is sufficient to drive self-organization phenomena that give rise to the formation of one or multiple rings. These rings can be stationary or oscillate along the cylinder axis.

5.3.1 Continuum Description in 2D

In order to derive a generic continuum description of an active fluid in two dimensions, we make the same assumptions as before, i.e. (i) all dynamics is overdamped as its origin lies in the motion of colloidal sized particles in a viscous background fluid, (ii) all mass transport is due to stresses generated in the system, and (iii) all driving terms that respect the rotational invariance of space are allowed and could be generated by active processes in the cell.

The basic structure of the system is again given by the dynamic equations (5.1)-(5.3). And the current in the filaments is again given by active stresses generated in the material:

$$\boldsymbol{j} = \eta^{-1}\boldsymbol{\nabla}\cdot\boldsymbol{\sigma} \tag{5.50}$$

Here we have assumed a system of cortical filaments that move in the vicinity of a cell wall and that friction (coefficient η) is local and isotropic. Let L denote the system length. We assume that the present state of the material completely determines the system. We can thus again expand the stress $\boldsymbol{\sigma}$ and the rates of change of the order parameters $\boldsymbol{\psi}$ and $\boldsymbol{\omega}$ in the dynamic fields c, $\boldsymbol{p}$, and $\boldsymbol{q}$. We then expand these driving forces in terms of perturbations of the dynamic fields around a homogenous reference state.

We describe the cell cortex as a two-dimensional active gel, embedded in three-dimensional space along the cell surface. Since cortical filaments orient in a non-polar way, we neglect the polarization $\boldsymbol{p}$ and only keep the nematic order $\boldsymbol{q}$. In situations where the total mass of polymerized microtubules is conserved (such as the transition from CA to PPB (Vos et al., 2004)), the source term s of Eq. (5.1) can be neglected. The cylinder axis is the x-axis of our coordinate frame, the second dimension described by the y-axis is wrapped around the cylinder with radius R, see Fig. 5.7. For simplicity, we neglect effects of surface curvature.

---

[3] This section is based on a collaboration with Marileen Dogterom, Marco Cosentino Lagomarsino, Catalin Tanase, and Bela Mulder from the AMOLF, Amsterdam. See also (Zumdieck et al., 2005a).

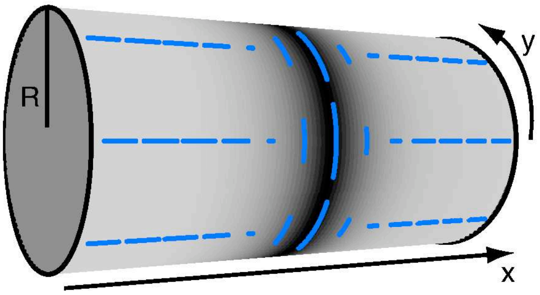

Figure 5.7: Cortical geometry. The system is described by a two dimensional gel that is wrapped on a cylinder of radius R. The x-axis corresponds to the cylinder axis, the y-axis is wrapped around the cylinder. Shown is a ring like state of the gel with no flux boundary conditions in x-direction, similar to a contractile ring or pre-prophase band in a cell's cortex. The density of filaments is represented by the grey level on the cylinder. The blue bars indicate the nematic order of filaments by their orientation and length.

We expand the stress $\boldsymbol{\sigma}$ and the rate of change $\boldsymbol{\omega}$ around a state with constant concentration c and order parameter $\boldsymbol{q}$. Up to second order in c and $\boldsymbol{q}$, and up to second order derivatives the most general expression for $\boldsymbol{\sigma}$ is

$$\begin{aligned}-\eta^{-1}\sigma_{\alpha\beta} \quad = \quad & a_1\delta_{\alpha\beta}c + a_2\delta_{\alpha\beta}c^2 + a_3\delta_{\alpha\beta}\Delta c + a_4\partial_\alpha\partial_\beta c \\ & + a_5 q_{\alpha\beta} + a_6\delta_{\alpha\beta}\partial_\gamma\partial_\delta q_{\gamma\delta} \\ & + a_7(\partial_\alpha c)(\partial_\beta c) \\ & + a_8\delta_{\alpha\beta}q_{\gamma\delta}q_{\gamma\delta} + a_9\delta_{\alpha\beta}c\partial_\alpha\partial_\beta c \quad .\end{aligned} \tag{5.51}$$

Here we have written all terms permitted by symmetry (under reflection $x \mapsto -x$ the density c and the nematic order $\boldsymbol{q}$ are even, which limits the number of possible terms). Assuming that the rate of change in the order parameter $\omega_{\alpha\beta}$ is determined by the state of the system we may expand it similarly:

$$\begin{aligned}\omega_{\alpha\beta} \quad = \quad & b_1 q_{\alpha\beta} + b_2\Delta q_{\alpha\beta} + b_3\Delta^2 q_{\alpha\beta} \\ & + b_4\left(\partial_\alpha\partial_\beta c - \frac{1}{2}\delta_{\alpha\beta}\Delta c\right) \\ & + b_5\left((\partial_\alpha c)(\partial_\beta c) - \frac{1}{2}\delta_{\alpha\beta}\left(\nabla c\right)^2\right) \\ & + b_6\left(c\partial_\alpha\partial_\beta c - \frac{1}{2}\delta_{\alpha\beta}c\Delta c\right) + b_7 q^3_{\alpha\beta}\end{aligned} \tag{5.52}$$

where we have added the term with coefficient b_7 in order to stabilize the dynamics.

5.3.2 Rotationally Invariant Equations

As we focus on the formation of rotationally symmetric objects like rings etc., we may project the above equations on the longitudinal axis so that they only depend on x and are thus essentially one dimensional. The dynamics of configurations, which are rotationally invariant, obey a set of equations projected on the cylinder axis:

$$\begin{aligned}
\eta^{-1}\sigma_{xx} &= A_1 c + A_2 c^2 + A_3 c\partial_x^2 c + A_4(\partial_x c)^2 + A_5 q_{xx} && (5.53)\\
\omega_{xx} &= -B_1 q_{xx} + B_2\partial_x^2 q_{xx} + B_3\partial_x^4 q_{xx} + B_4\partial_x^2 c && (5.54)\\
&\quad +B_5(q_{xx}^2 + q_{xy}^2)q_{xx} &&\\
\omega_{xy} &= -B_1 q_{xy} + B_2\partial_x^2 q_{xy} + B_3\partial_x^4 q_{xy} && (5.55)\\
&\quad +B_5(q_{xx}^2 + q_{xy}^2)q_{xy} &&
\end{aligned}$$

where we have neglected higher order terms.

For the following it is convenient to introduce dimensionless densities, time, space, marked with a tilde:

$$\begin{aligned}
\tilde{c} &= cL^2 && (5.56)\\
\tilde{t} &= t\tau && (5.57)\\
\tilde{x} &= x/L && (5.58)
\end{aligned}$$

The corresponding dimensionless parameters are

$$\begin{array}{lcl}
\tilde{A}_1 = \frac{A_1}{\tau L^2} & , & \tilde{B}_1 = \frac{B_1}{\tau}\\
\tilde{A}_2 = \frac{A_2}{\tau L^4} & , & \tilde{B}_2 = \frac{B_2}{\tau L^2}\\
\tilde{A}_3 = \frac{A_3}{\tau L^6} & , & \tilde{B}_3 = \frac{B_3}{\tau L^4}\\
\tilde{A}_4 = \frac{A_4}{\tau L^6} & , & \tilde{B}_4 = \frac{B_4}{\tau L^4}\\
\tilde{A}_5 = \frac{A_5}{\tau} & , & \tilde{B}_5 = \frac{B_5}{\tau} \quad .
\end{array} \qquad (5.59)$$

Here L denotes a typical length scale such as the system length, and τ has units of inverse time.

Dimensional analysis reveals that these equations contain six independent parameters. Four parameters can be fixed by measuring time in units of, say B_5 and rescaling c, q_{xx}, and q_{xy}. The values of only three of the remaining independent parameters turn out to influence the dynamics qualitatively; they can be identified with A_2, B_2, and

$$F = -A_5 B_4 \quad . \qquad (5.60)$$

The other parameters describe nonlinear terms which are required to stabilize the dynamics. We verified that stability requires $A_3 > 0$, $A_4 < 0$, $B_3 < 0$, and $B_5 < 0$. The specific values of these parameters do not qualitatively influence the asymptotic dynamics.

We study these equations with two types of boundary conditions in the x-direction, cf. Fig. 5.8:

- Periodic boundary conditions (Fig. 5.8a) are useful to gain a general insight into the problem, as they are easier to access mathematically and often allow analytical treatment.

- No flux or fixed boundary conditions (Fig. 5.8b) are biologically more realistic. They obey $\boldsymbol{j}(0) = 0$, $\boldsymbol{j}(L) = 0$, which implies that the cortical material cannot leave the cell. Additional boundary conditions have to be specified to fully determine the asymptotic solutions.

Periodic boundary conditions are discussed in section 5.3.3 and fixed boundary conditions in section 5.3.4.

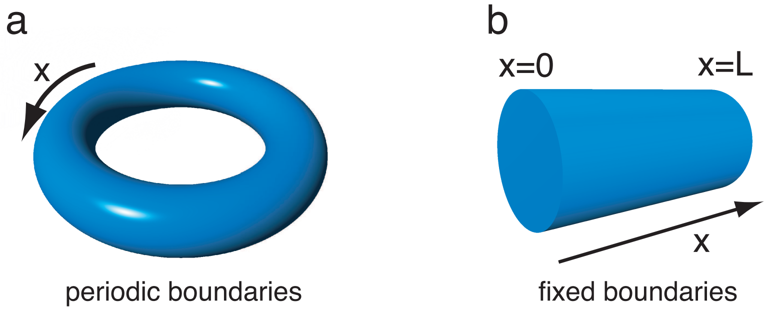

Figure 5.8: (a) Periodic boundary conditions correspond to a torus shaped cell. (b) Fixed or no flux boundary conditions are biologically more appropriate. The density flux $\boldsymbol{j}$ vanishes at $x = 0$ and $x = L$ so that no material can leave the cell.

5.3.3 Stability and Phase Diagram

Periodic Boundary Conditions

We investigate the transition from a homogenous state such as e.g. the cortical array to an inhomogenous state such as e.g. the pre-prophase band, by performing a linear stability analysis of the homogenous, isotropic state $c = c_0$, $\boldsymbol{q} = 0$. For periodic boundary conditions this state is a stationary state of the equations.

We consider small perturbations around this state $c = c_0 + \delta c$ and $\boldsymbol{q} = \delta\boldsymbol{q}$. We drop the δ for clarity of presentation. Linearizing the dynamic equations derived from the projected Eqs. (5.53)-(5.55) around $c = c_0$, $\boldsymbol{q} = 0$, the dynamic equation is

$$\frac{\mathrm{d}}{\mathrm{d}t}\begin{pmatrix} c_k \\ q_{xx,k} \\ q_{xy,k} \end{pmatrix} = \tag{5.61}$$
$$\begin{pmatrix} D\partial_x^2 - A_3 c_0 \partial_x^4 & -A_5\partial_x^2 & 0 \\ B_4\partial_x^2 & -B_1 + B_2\partial_x^2 + B_3\partial_x^4 & 0 \\ 0 & 0 & -B_1 + B_2\partial_x^2 + B_3\partial_x^4 \end{pmatrix}\begin{pmatrix} c_k \\ q_{xx,k} \\ q_{xy,k} \end{pmatrix} ,$$

where $D = -(A_1 + 2c_0A_2)$ is an effective diffusion constant.

Stability of $\boldsymbol{q}_{xy}$. We first note that at linear order the equation for $\boldsymbol{q}_{xy}$ decouples from the other two equations. We write the perturbation in a Fourier series

$$q_{xy} = \sum_n q_{xy,k} \exp(\frac{2\pi i n x}{L}) \tag{5.62}$$

where $k = 2\pi n/L$ is the wave number of the modes and $n = 0, 1, 2, \ldots$. Note that large system sizes correspond to small k, i.e. $k \to 0$ corresponds to $L \to \infty$. We then obtain the following equation for the coefficient

$$\frac{\mathrm{d}}{\mathrm{d}t} q_{xy,k} = (-B_1 - B_2k^2 + B_3k^4)q_{xy,k} \quad . \tag{5.63}$$

The isotropic state is thus unstable for $k = 0$ if $B_1 < 0$. This instability corresponds to the isotropic-nematic transitions of rod-like particles which generically sets in at high enough concentrations, or low enough temperatures. We verified that in the case of spontaneous

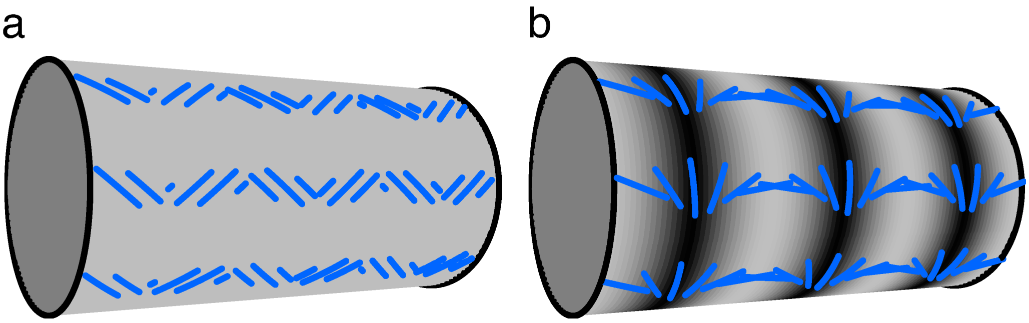

Figure 5.9: Examples of stationary solutions to the dynamic equations with periodic boundary conditions. The density of filaments is represented by the grey level on the cylinder. The blue bars indicate the nematic order of filaments by their orientation and length. (a) Chevron pattern with homogeneous filament density for $\tilde{B}_2 = -1.25$, $\tilde{D} = 0.75$, and $\tilde{F} = -1$. (b) Multiple ring pattern for $\tilde{B}_2 = -1.5$, $\tilde{D} = 1.5$, and $\tilde{F} = -1$.

nematic order, there exists a stationary homogenous state with $\mathrm{tr}(\boldsymbol{q}^2) = B_1/B_5$, that is stable against perturbations with $k = 0$.

Let us now focus on the instabilities of the isotropic state with $B_1 > 0$. In this case an instability occurs at finite wave number $k^* > 0$, if B_2 is smaller than a critical value $B_2^* < 0$. The unstable mode corresponds to periodically alternating regions with nematic order at an angle of $\pi/4$ and $-\pi/4$ with the x-axis. These structures are reminiscent of chevrons in nematic liquid crystals, cf. Fig. 5.9a (de Gennes and Prost, 1993). In the limit of infinite system size $L \to \infty$, we find

$$\begin{aligned} B_2^*(\infty) &= -2(B_1 B_3)^{1/2} && (5.64)\\ k^*(\infty) &= (B_1/B_3)^{1/4} && (5.65) \end{aligned}$$

for the critical value of B_2^* and the critical wave number k^*. For smaller system sizes, the critical value of B_2 is smaller than $B_2^*(\infty)$ and the critical mode is given by the value $k_c = 2\pi n/L$ that is closest to $(B_1/B_3)^{1/4}$.

Stability of c and q_{xx}. The linearized dynamics of the coefficients c_k and $q_{xx,k}$, as defined by $\delta c = \sum_n c_k \mathrm{e}^{2\pi i n x/L}$ and $\delta q_{xx} = \sum_n q_{xx,k} \mathrm{e}^{2\pi i n x/L}$ is given by two coupled equations

$$\frac{\mathrm{d}}{\mathrm{d}t}\begin{pmatrix} c_k \\ q_{xx,k} \end{pmatrix} = \begin{pmatrix} -Dk^2 - A_3 c_0 k^4 & +A_5 k^2 \\ -B_4 k^2 & -B_1 - B_2 k^2 + B_3 k^4 \end{pmatrix} \begin{pmatrix} c_k \\ q_{xx,k} \end{pmatrix}, \quad (5.66)$$

where $D = -(A_1 + 2c_0 A_2)$ is an effective diffusion constant. The eigenvalues of this stability matrix are

$$\begin{aligned} \lambda_{1,2} = &\frac{1}{2}\left(-B_1 - (D + B_2)k^2 + (B_3 - A_3 c_0)k^4\right) \qquad (5.67)\\ &\pm \frac{1}{2}\Big[\left(B_1 - (D - B_2)k^2\right)^2 + (4F - 2B_1(B_3 + A_3 c_0))k^4 \\ &+ 2(D - B_2)(B_3 + A_3 c_0)k^6 + (B_3 + A_3 c_0)^2 k^8\Big]^{\frac{1}{2}} \end{aligned}$$

Here we have used F as defined in Eq. (5.60). We see immediately that stability at small wave lengths (small k) is guaranteed if $A_3 > 0$ and $B_3 < 0$. For $k = 0$ the eigenvalues are 0 and $-B_1$. The homogenous mode $k = 0$ is thus unstable for $B_1 < 0$. This instability does not respect mass conservation. In the following we will concentrate on pattern formation in the case $B_1 > 0$, so that the homogenous mode is always stable.

It is instructive to study a simplified case in which we only consider terms in k up to quadratic order. Although truncated, the resulting expressions already exhibit key features of the phase space of the full system. It is thus possible to analytically identify the terms that determine the stability of the homogenous state, for example. Assuming $B_3 = -A_3 c_0$, which does not influence the results qualitatively, the eigenvalues read in the truncated form:

$$\bar{\lambda}_{1,2} = \frac{1}{2}\left(-B_1 - (D + B_2)k^2 \pm \sqrt{(B_1 - (D - B_2)k^2)^2 + 4Fk^4}\right) + \mathcal{O}(k^3) \tag{5.68}$$

As the instability is driven by the eigenvalue with the largest real part, it suffices to focus on the eigenvalue with the plus sign. For large k, terms $\propto k^2$ dominate the eigenvalue. The homogenous state can only be stable if

$$D + B_2 > 0 \iff B_2 > -D \quad , \tag{5.69}$$

because the eigenvalue can only be negative if the first term is negative (as the square root always has a positive real part by definition). In order to further discuss the stability of the homogenous state, we now discuss two cases:

1. $F > 0$: in this case the argument of the square root is always positive and the homogenous state is only stable for large k, if in addition to condition (5.69) the real part of the square root is smaller than the first term $(D + B_2)k^2$:

   $$\begin{aligned} &(D - B_2)^2 + 4F < (D + B_2)^2 \\ \Rightarrow &\begin{cases} B_2 > F/D > 0 & \text{for} \quad D > 0 \\ B_2 < F/D < 0 & \text{for} \quad D < 0 \end{cases} \end{aligned} \tag{5.70}$$

   The resulting region of stability is sketched blue in Fig. 5.10a.

2. $F < 0$: here the argument of the square root can become negative, so that it does not influence the stability but only the type of bifurcation (Hopf or stationary). Let

   $$\Gamma = (D - B_2)^2 + 4F \tag{5.71}$$

   denote the argument of the square root for large k. The homogenous state is stable for large k if $-(D + B_2) < \sqrt{\Gamma}$. We distinguish two sub-cases:

   a) $\Gamma \leq 0$: in this case $\sqrt{\Gamma}$ is purely imaginary, the homogenous state becomes unstable via a Hopf bifurcation, but the stability boundary does not depend on Γ. The criterion for negative Γ leads to the condition

   $$\begin{aligned} \Gamma \leq 0 \quad &\iff \quad |D - B_2| \leq 2\sqrt{|F|} \\ &\iff \quad D - B_2 \leq 2\sqrt{|F|} < G < D - B_2 \leq 2\sqrt{|F|} \ . \end{aligned} \tag{5.72}$$

   If this is true, the stability is determined by condition (5.69). Both conditions have to be fulfilled simultaneously. The borders of the resulting stripe-like area in the B_2-D-plane are indicated in Fig. 5.10b.

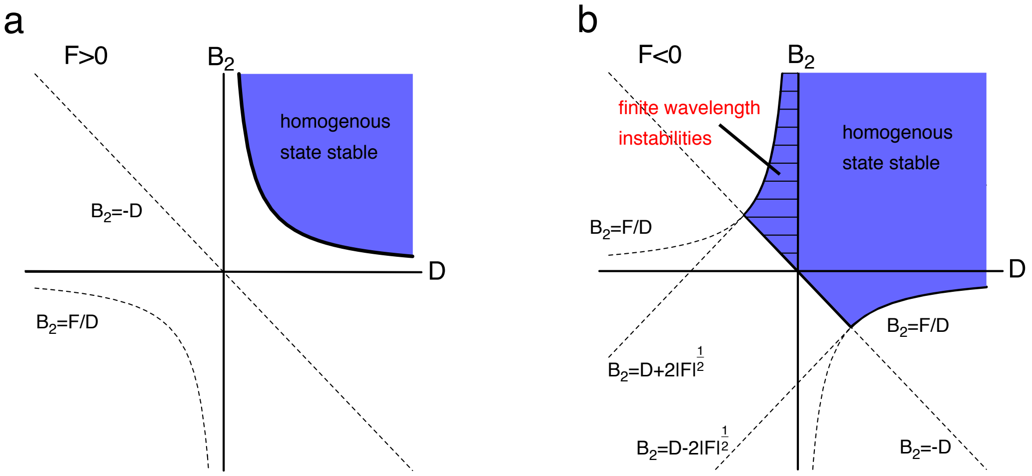

Figure 5.10: Analytic stability boundaries of the homogenous state up to quadratic order in k. The blue areas mark the regions of stability of the homogenous state against perturbations with large k in the B_2-D-plane for the two cases $F > 0$ (a) and $F < 0$ (b) in an infinite system. The dashed lines mark the various stability boundaries discussed in the text. The striped area in the right graph marks the region where instabilities with finite wave lengths can occur.

b) $\Gamma > 0$: here the root is real and directly influences the location of the stability boundaries. The condition for positive Γ is

$$\Gamma > 0 \iff B_2 > D + 2\sqrt{|F|} \quad \text{or} \quad B_2 < D - 2\sqrt{|F|} \tag{5.73}$$

which is the region outside the stripe discussed in case (a). The homogenous state is then stable if

$$\begin{aligned} & -(D+B_2) + \sqrt{(D-B_2)^2 + 4F} \\ \Rightarrow & \begin{cases} B_2 > F/D > 0 & \text{for} \quad D > 0 \\ B_2 < F/D < 0 & \text{for} \quad D < 0 \end{cases} \end{aligned} \tag{5.74}$$

The resulting region of stability is sketched blue in Fig. 5.10b.

Up to now we have discussed the stability at small wave length, i.e. large k. Small structures described by very large k are however not faithfully reproduced by our coarse grained continuum description. Instabilities of modes with a finite, not too big $k > 0$ lead to pattern formation that can be biologically meaningful if they occur in a region where large k modes are stable. A necessary condition for such finite wavelength instabilities to occur is that the slope of the eigenvalue $\lambda(k)$ at $k = 0$ is positive. We again discuss this for the analytically tractable eigenvalue $\bar{\lambda}$ given in Eq. (5.68), which is a quadratic from in k^2. This has two consequences:

1. The eigenvalue $\bar{\lambda}$ is symmetric with respect to $k = 0$. Thus its slope at $k = 0$ is zero:

$$\left.\frac{\mathrm{d}\bar{\lambda}}{\mathrm{d}k}\right|_{k=0} \tag{5.75}$$

2. Defining $l = k^2$, we see that $\bar{\lambda}(l)$ has at most two roots. For positive B_1 one of them is at $l = 0$. For stability at large wave lengths we need $\bar{\lambda}(k) < 0$ for $k \to \infty$. This

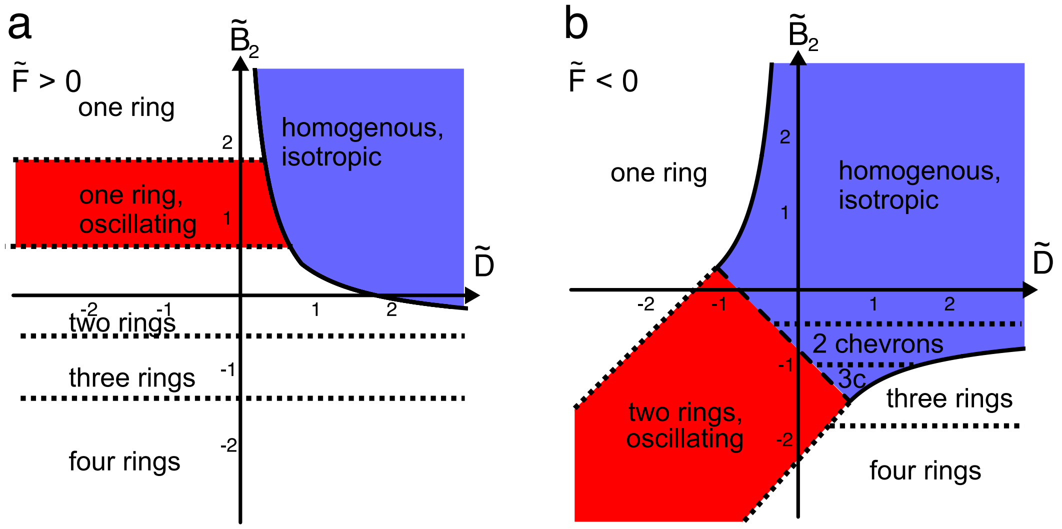

Figure 5.11: Schematic state diagrams of an active gel layer in cylindrical geometry with periodic boundary conditions in the x-direction, are shown for two values of $\tilde{F}$ as a function of two dimensionless parameters $\tilde{B}_2$ and $\tilde{D}$. Regions of linear stability of homogeneous filament distributions are shaded blue. Outside these regions, the topology of the state diagram as determined numerically is indicated by dotted lines. Asymptotic states include chevron patterns with parameter dependent spacing (regions marked 2 chevrons, and 3c for three chevrons respectively) and single or multiple rings that are either stationary or do oscillate. Regions of oscillating solutions are shown in red. The long dashed line indicates a Hopf bifurcation determined by linear stability analysis. Examples for stationary chevron and ring patterns are displayed in Fig. 5.9. Parameters are defined as $\tilde{D} = -(\tilde{A}_1 + 2\tilde{c}_0\tilde{A}_2)$, $\tilde{B}_2 = B_2/(B_1L^2)$, $\tilde{F} = F/(B_1^2L^4)$ and $\tilde{A}_2 = A_2/(B_1L^4)$. Parameter values are $\tilde{c}_0 = c_0L = 0.5$, $L(-2B_1/A_1)^{1/2} = 5$, $\tilde{A}_1 = A_1/(B_1L^2) = -2$, $A_3/(B_1L^6) = 0.1$, $A_4/(B_1L^6) = -1$, $A_5/B_1 = 1$, $B_3/(B_1L^2) = -0.05$, $B_5/B_1 = -10$ and $\tilde{F} = 1$ for (a) and $\tilde{F} = -1$ for (b). L is the period of the system.

is inconsistent with a positive root of $\bar{\lambda}$ when $B_1 > 0$ if the slope of $\bar{\lambda}$ is negative at $k = 0$. Thus we need a positive slope at the origin. The slope is given by

$$\left.\frac{\mathrm{d}\bar{\lambda}}{\mathrm{d}l}\right|_{l=0} = \begin{cases} -D & \text{for} \quad B_1 > 0 \\ -G & \text{for} \quad B_1 < 0 \end{cases} \tag{5.76}$$

Thus for $B_1 > 0$ pattern formation due to instabilities of modes with small wave lengths can only occur for $D < 0$. This also implies that for $F > 0$ we cannot observe finite wave length instabilities in regions where the homogenous state is stable for large k. The only resulting “candidate region” is marked stripes in Fig. 5.10.

State Diagram. The analytical considerations above are useful to gain an insight in the stability of the homogenous isotropic state. Here we explore the rich asymptotic behavior of the system and present a schematic state diagram, see Fig. 5.11. The corresponding asymptotic states are illustrated in Figs. 5.12, 5.13, and 5.14. Note that while the topology of the boundaries in the state diagram depends only on the value of F, the orientation of filaments in the asymptotic states depends on the values of A_5 and B_4.

The similarities between the phase diagrams shown here and the sketches shown in Fig. 5.10 are striking. The regions of stability of the homogenous state hardly change

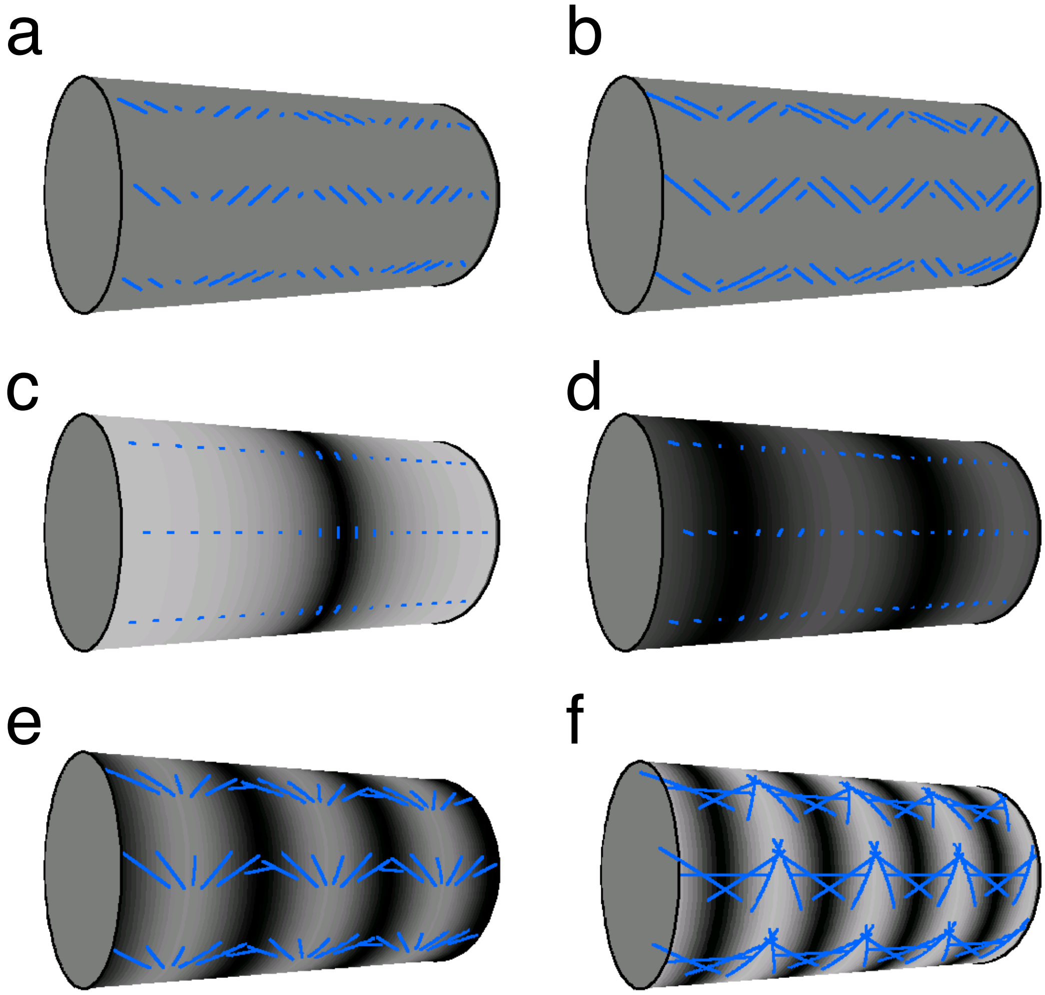

Figure 5.12: Asymptotic states obtained by numerical integration with $\tilde{F} = -1$. The density of filaments is represented by the grey level on the cylinder. The blue bars indicate the nematic order of filaments by their orientation and length. (a) Two chevrons ($\tilde{B}_2 = -0.75$, $\tilde{D} = 0.75$) (b) Three chevrons ($\tilde{B}_2 = -1.25$, $\tilde{D} = 0.75$) (c) One ring ($\tilde{B}_2 = 1$, $\tilde{D} = -1.5$) (d) Two rings ($\tilde{B}_2 = -1$, $\tilde{D} = -1$) (e) Three rings ($\tilde{B}_2 = -1.5$, $\tilde{D} = 1.5$) (f) Four rings ($\tilde{B}_2 = -2.5$, $\tilde{D} = 1.5$). Furthermore $A_5 = 1$, $B_4 = 1$, the other parameters are the same as in Fig. 5.11.

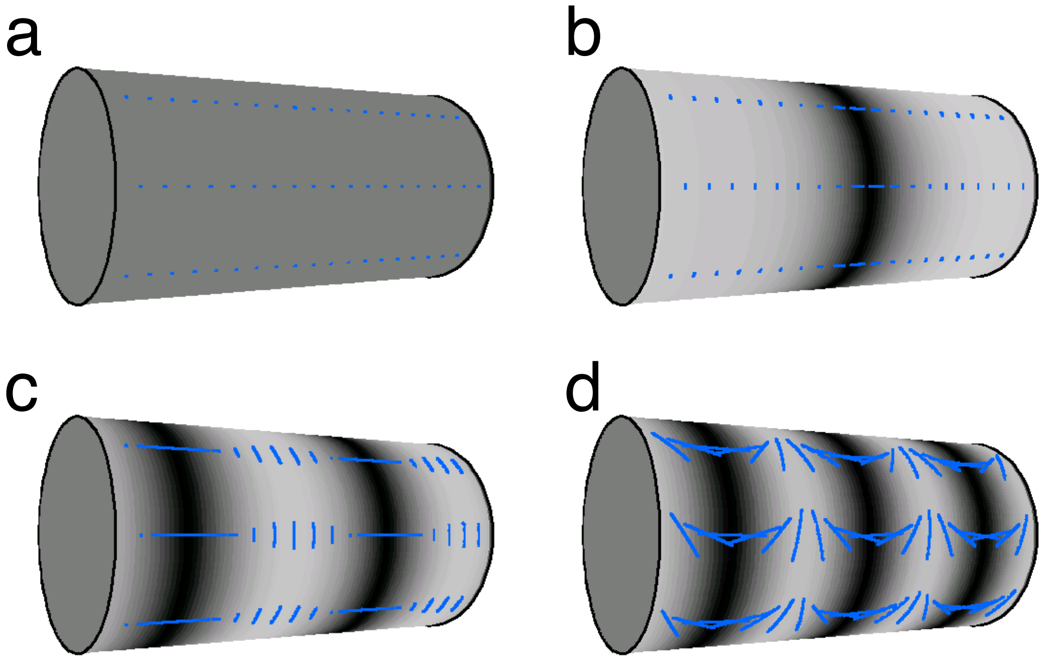

Figure 5.13: Asymptotic states obtained for $\tilde{F} = -1$. The density of filaments is represented by the grey level on the cylinder. The blue bars indicate the nematic order of filaments by their orientation and length. (a) Homogenous isotropic ($\tilde{B}_2 = 1.5$, $\tilde{D} = 1.5$) (b) One ring ($\tilde{B}_2 = -1.55$, $\tilde{D} = -1.5$) (c) Two rings ($\tilde{B}_2 = 0.25$, $\tilde{D} = -0.5$) (d) Three rings ($\tilde{B}_2 = -1$, $\tilde{D} = -0.5$). Furthermore $A_5 = 1$, $B_4 = -1$, the other parameters are the same as in Fig. 5.11.

at all. The essential physics for this stability is thus already contained in the truncated expression for $\bar{\lambda}$. An important difference is however, that for the full system (Fig. 5.11) the stability of the homogenous state against perturbations with $k = 2\pi/L$ with finite L is analyzed while the sketch of the truncated system was calculated also including $k \to 0$. The resulting shape of the stability region of the homogenouns, isotropic state in Figs.. 5.11b and 5.10b is different, as the striped part is unstable against perturbations with small k and thus does not form part of the stability region of the homogenous state for the truncated expressions.

This difference is readily accounted for by the fact that the analytical calculation allowed arbitrarily small k, corresponding to system with infinite length L, while the system length for the analysis of the full system was taken to be $L = 5$. Thus there are no k-values between $k_0 = 0$ and $k_1 = 2\pi/L$, which explains the difference in shape, see Fig. 5.15. It is thus truly remarkable how much we could learn about the full system by analyzing the simplified expression in Eq. (5.68).

The stability boundaries of the homogenous, isotropic state are obtained by linear stability analysis. When $F > 0$, stability is lost in favour of inhomogenous states. The wave-length of the critical modes is set by the values of D and B_2. The unstable modes at the instabilities towards stationary states correspond to periodic patterns of filament accumulation combined with nematic order, parallel or perpendicular to the x-axis, at the maxima of the filament density, cf. Fig. 5.9b.

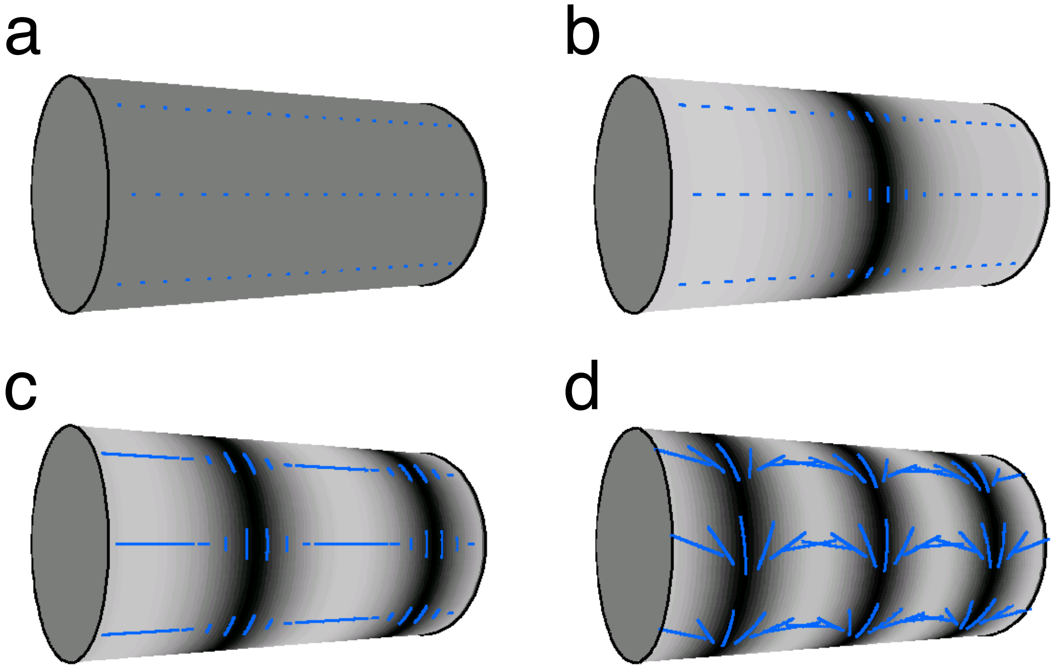

Figure 5.14: Asymptotic states obtained for $\tilde{F} = 1$. The density of filaments is represented by the grey level on the cylinder. The blue bars indicate the nematic order of filaments by their orientation and length. (a) Homogenous isotropic ($\tilde{B}_2 = 1.5$, $\tilde{D} = 1.5$) (b) One ring ($\tilde{B}_2 = -1.55$, $\tilde{D} = -1.5$) (c) Two rings ($\tilde{B}_2 = 0.25$, $\tilde{D} = -0.5$) (d) Three rings ($\tilde{B}_2 = -1$, $\tilde{D} = -0.5$). Furthermore $A_5 = -1$, $B_4 = 1$, the other parameters are the same as in Fig. 5.11.

For $F < 0$ the homogenous state looses stability not only towards stationary states but also via a Hopf bifurcation. The boundary where these oscillating critical modes occur is marked by the dashed line in Fig. 5.11b. These solutions correspond to traveling waves. Because of symmetry, these waves can propagate along the x-axis in both directions.

Although the linear stability analysis is indicative of the type of instabilities that can occur in our model, a numerical analysis of the full nonlinear equations is necessary to identify the asymptotic states. Numerical integration of the full system yields asymptotic states as shown in Figs. 5.12, 5.13, and 5.14. The system thus exhibits the formation of one or multiple rings with filaments aligned parallel or perpendicular to the cylinder axis. Furthermore nematic order can emerge even if the filament density remains constant, this is the consequence of instabilities in q_{xy} as discussed above.

Numerical analysis also reveals oscillatory rings. Here one or multiple rings form from the homogenous state and start oscillating along the x-axis. The direction of movement is determined by the initial conditions, i.e. is due to spontaneous symmetry breaking.

A peculiar situation arises for $F > 0$, see Fig. 5.11. The linear stability analysis of the homogenous isotropic state indicates a stationary bifurcation independent of parameter values, while a neighboring region is colored red, marking oscillations. Numerical integration indeed shows oscillating asymptotic states in this region. The frequency of oscillation however decreases when the parameters approach the boundary to the blue region from the left. The two apparently contradicting observations are thus consistent. The detailed

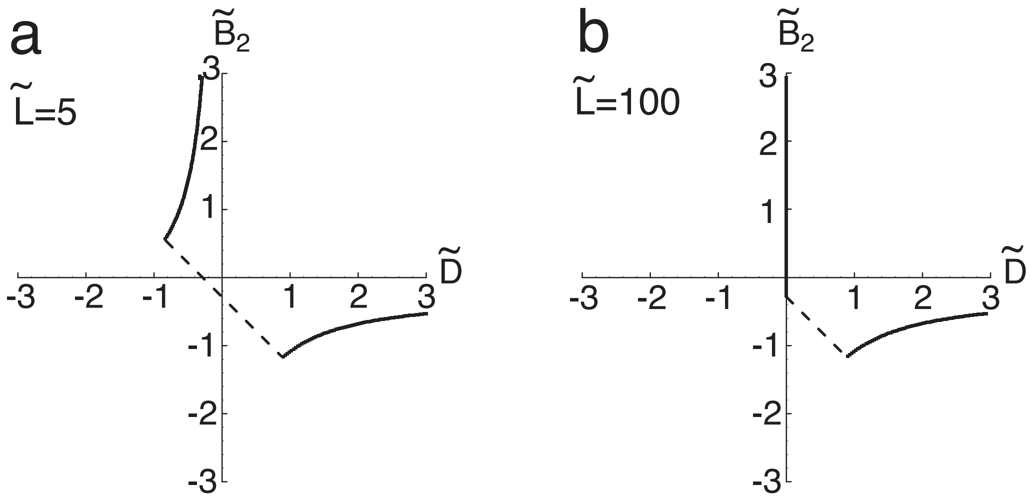

Figure 5.15: The precise location of the stability boundary of the homogenous state depends on the system length. The boundary was obtained by linear stability analysis of the full system as given by Eq. (5.66) for dimensionless system length $L/l = 5$ (a) and $L/l = 100$ (b) and $\tilde{F} = -1$. The dashed line indicates a Hopf bifurcation.

analysis of this region by numerical means unfortunately is hardly feasible, as close to the boundary the oscillation frequencies become low requiring extremely long integration times for the numerical analysis.

5.3.4 Stationary and Oscillating Rings

Up to now we discussed the system with periodic boundary conditions that are mathematically convenient but hardly biologically realistic, cf. Fig 5.8. Motivated by the situation in biological cells, we investigate a set of boundary conditions with zero flux at the boundaries $\boldsymbol{j}(0) = 0$, $\boldsymbol{j}(L) = 0$, which implies that cortical material cannot leave the cell. Additional boundary conditions have then to be specified to fully define the asymptotic solutions. It is observed that the end-faces of interphase plant cells are essentially free of microtubules. This is consistent with the absence of imposed order at the boundaries and we therefore set $\boldsymbol{q}(0) = 0$, $\boldsymbol{q}(L) = 0$. In the following we use for simplicity the boundary conditions

$$\begin{aligned} \boldsymbol{j} &= 0 && (5.77)\\ \boldsymbol{q} &= 0 && (5.78)\\ \partial_x c &= 0 && (5.79)\\ \partial_x q_{xx} &= 0 && (5.80)\\ \partial_x q_{xy} &= 0 && (5.81) \end{aligned}$$

at both $x = 0$ and $x = L$.

Figure 5.7 shows a steady state solution of Eqs. (5.53)-(5.55) with these zero flux boundary conditions. This solution corresponds to a stationary ring of filaments. The filaments are oriented in the y-direction and localized in a ring-like pattern wound around the cylinder, strongly reminiscent of a pre-prophase band or a contractile ring. The corresponding stress is anisotropic and for $\sigma_{yy} > \sigma_{xx}$ the ring solution is contractile, see section 6.5.3 below. Additional asymptotic solutions are similar to the solutions shown in Fig. 5.9

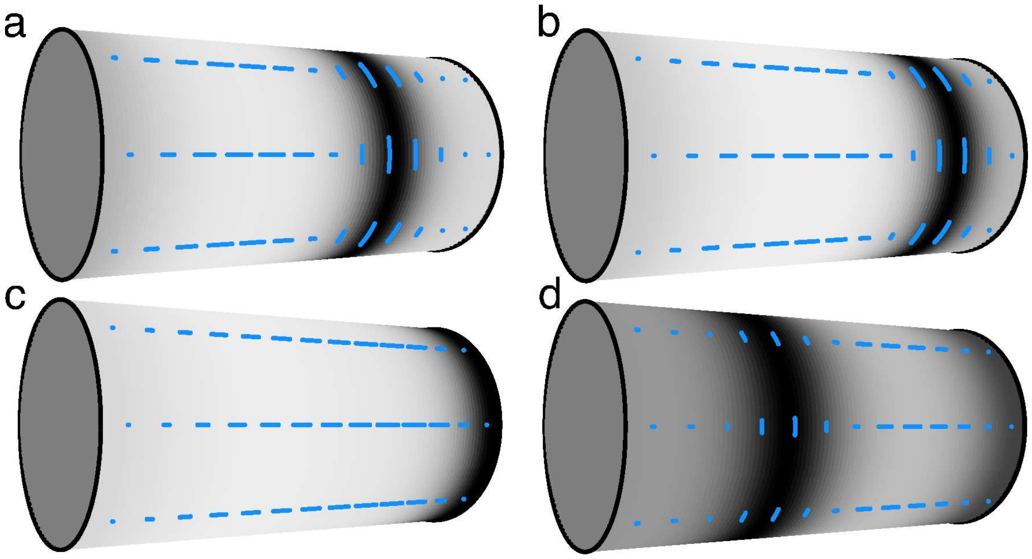

Figure 5.16: Snapshots at different times of an oscillating filament ring. The pattern consists of a filament ring which forms near the center of the cell (cylinder) (a) and moves towards the right pole (b,c), where the ring disappears. Simultaneously, a new ring is formed near the center (d) which subsequently moves to the opposite pole. The whole process is repeated periodically. The times correspond to phases $\phi = \omega t$ of the oscillation with $\phi = 0$ (a), $\phi = (4/36)2\pi$ (b), $\phi = (7/36)2\pi$ (c) and $\phi = (15/36)2\pi$ (d). The density of filaments is represented by the grey level on the cylinder. The blue bars indicate the nematic order of filaments by their orientation and length. The parameters are $\tilde{B}_2 = 1$, $\tilde{D} = 0.25$ and $\tilde{F} = 1$.

with periodic boundary conditions. Furthermore, oscillatory solutions appear along a line of Hopf-bifurcations. An example of such a state with no flux boundary conditions is shown in Fig. 5.16. The oscillating solutions for no flux boundary conditions correspond to traveling waves in the case of periodic boundary conditions. Additional states can be generated via the boundaries by imposing other boundary conditions.

Linear stability analysis of the system with no flux boundary conditions is technically difficult. Numerical investigations however indicate that the phase space topology is often similar for periodic and no-flux boundary conditions depending on the sign of F.

5.4 Discussion

In this chapter we presented generic continuum descriptions of the cytoskeleton. These are phenomenological theories that are based on symmetry considerations only and do not depend on microscopic detail. The description is formulated in the filament density and the polar as well as the nematic order parameters. While the relation between the terms in the description to biological mechanisms observable in experiments is not obvious in general, the terms can be linked to microscopical theories of cytoskeletal systems that allow an interpretation.

Applying this approach to one-dimensional filament bundles, we could observe stress release by contraction of such a bundle. Adding source terms, which can directly be identified with polymerization and depolymerization dynamics, to the evolution equation, we find unstable modes that correspond to structures reminiscent of muscle myofibrils. This could have interesting implications, e.g. for the formation of stress fibers, which are transient contractile filament bundles. In contrast to myofibrils, stress fibers seem to form without any apparent structural cues such as Z-disks.

We furthermore investigate ring formation in the cell cortex. We apply the theory to a two-dimensional geometry that corresponds to the surface of a cylinder, reminiscent of an elongated cell. We find that single as well as multiple rings can form by dynamic instabilities. The rings can be stationary or oscillate along the cylinder axis. Our theory could be extended to include filament elasticity, which probably would tend to align filaments along the cylinder axis rather than perpendicular to it. An alternative way of treating the boundaries is to write explicit evolution equations for the quantities at the boundaries.

The phenomenological descriptions of cytoskeletal dynamics presented in the previous sections all focused on the system's behavior on long time scales. They thus neglected that the cytoskeleton shows elastic behavior on short time scales (Thoumine et al., 1996; Thoumine and Ott, 1997; Fabry et al., 2001; Beil et al., 2003; Mahaffy et al., 2004; Micoulet et al., 2005; Balland et al., 2005). The viscoelastic response of an isotropic solution of entangled, polar, semiflexible polymers in the presence of motor like forces has been investigated in (Liverpool et al., 2001). Recently, a description of active gels has been presented that includes viscoelastic behavior (Kruse et al., 2004, 2005). See (Kruse, 2005) for a detailed discussion on how elastic effects can be incorporated into the theory of cytoskeletal filament systems based on this description of active polar viscoelastic gels.

6 Dynamics of the Contractile Ring

The contractile ring that cleaves the cell after mitosis is a truly fascinating structure. In this chapter we present a physical description for the dynamics of ring contraction based on a force balance equation. The ring generates tension and constricts against a restoring force. The cytoplasm of a cell is usually densly packed with organelles and cytoskeletal filaments that have to be rearranged when the ring constricts, which could give rise to such an opposing force. For the force balance equation we take into account the structure of the ring. Using parameters estimated from independent measurements, we show that our description quantitatively fits ring constriction as observed in yeast cells, see Fig. 6.1. Our theory explicitly captures filament polymerization and depolymerization of actin filaments and we can show that these processes are indispensable in order to obtain ring contraction dynamics as observed in experiments with fission yeast (Fig. 6.1).

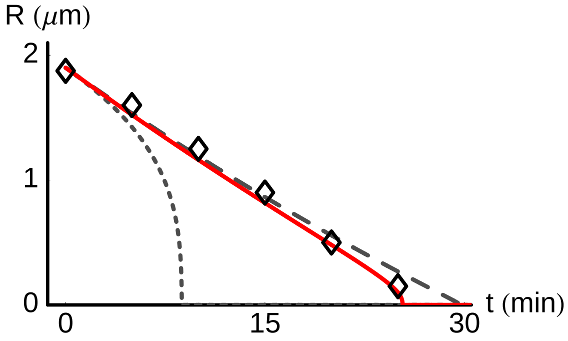

Figure 6.1: Good quantitative agreement between our theory (lines) and experimental data (diamonds). Shown is the radius over time of a contractile ring. The red line represents the dynamics with experimentally motivated values of filament turnover. Fast filament turnover leads to the long dashed, straight line, while the absence of turnover gives rise to dynamics represented by the short dashed line. Experimental data from (Pelham and Chang, 2002).

6.1 Structure of the Contractile Ring

The biology and general structure of a contractile ring was introduced in section 2.5.2. Here we briefly recall its key features. The contractile ring is essentially a band of actin filaments, myosin motors and other associated proteins that wraps around the cell at its equator and contributes to cell cleavage when it contracts. A "typical" ring is formed by $N_\mathrm{b} \sim 200$ bundles consisting of 25 aligned actin filaments so that there are about 5000 filaments in a cross-section at every point along the circumference (Maupin and Pollard, 1986; Schroeder, 1990). The ring forms in or below the cortex in an unconstricted cell with radius R_0, matures and then starts to constrict the cell, assuming radii $R < R_0$. The total number of filaments in an unconstricted ring with N_b bundles is given by

$$N = 2\pi R_0 N_\mathrm{b} c \quad , \tag{6.1}$$

where c is the instantaneous homogenous number density of filaments in one bundle, i.e. c is constant along the ring circumference. If the filaments in the ring have a typical length l the total mass of filaments in a ring with N_b bundles and radius R can be written as

$$M = Nm_l = 2\pi R N_\mathrm{b} c\, m_l \quad , \tag{6.2}$$

where m_l is the mass of a filament of length l. The number of filaments in a cross section is given by $N_b\, c\, l$. There is experimental evidence that the mass of a contractile ring is not conserved during ring constriction (Schroeder, 1972). The contractile ring appears to be losing material while constricting. A ring with a constant homogenous density c during constriction (i.e. while decreasing ring radius R) would also have to lose material.

6.2 Force Balance and Material Exchange During Ring Contraction

In this thesis we consider a contractile filament ring wrapped around a cylindrical surface with radius R_0, see Fig. 6.2a. The contractile stress Σ in the ring is generated by active processes. It characterizes the mechanical work

$$\delta W = 2\pi \Sigma \delta R \tag{6.3}$$

required to change the ring-diameter by δR and thus has units of force. The stress Σ in the ring leads to normal forces on the cylinder surface which are balanced by viscous and elastic forces generated by the cell body. This force balance can be expressed by a simplified dynamic equation for the ring radius R

$$\dot{R} = -\xi \left(\frac{\partial E}{\partial R} + 2\pi\Sigma \right) \quad . \tag{6.4}$$

Here we have assumed for simplicity that the elastic response of the cell can be described by an elastic energy $E(R)$. A typical dependence of E on R is sketched in Fig. 6.2b. The viscous forces associated with the cell constriction are characterized by a friction coefficient ξ^{-1}. We assume that the radius $R = R_0$ is locally stable and thus minimum of E. As a first approximation we use a harmonic elastic energy

$$E(R) = \frac{k}{2}(R - R_0)^2 \quad . \tag{6.5}$$

We have verified that other choices of $E(R)$ do not change our results qualitatively, see section 6.4 for details.

The active stress Σ is generated by the action of motor proteins and the polymerization and depolymerization of filaments. As we show explicitly in chapter 3, the contractile stress is the result of the interactions of filament pairs via active processes. For a filament ring consisting of N_b filament bundles, the total stress generated by filament interactions can be expressed as

$$\Sigma \simeq A N_\mathrm{b} c^2 \quad . \tag{6.6}$$

for sufficiently small filament numbers per bundle. Here A is an effective material coefficient which captures the force generation within a bundle, c denotes the number density of filaments per unit length along a bundle and has units of inverse length. As shown in chapter 3, the quadratic dependence on the filament density c corresponds to stress resulting from interactions between filament pairs within a bundle. The factor N_b signifies that

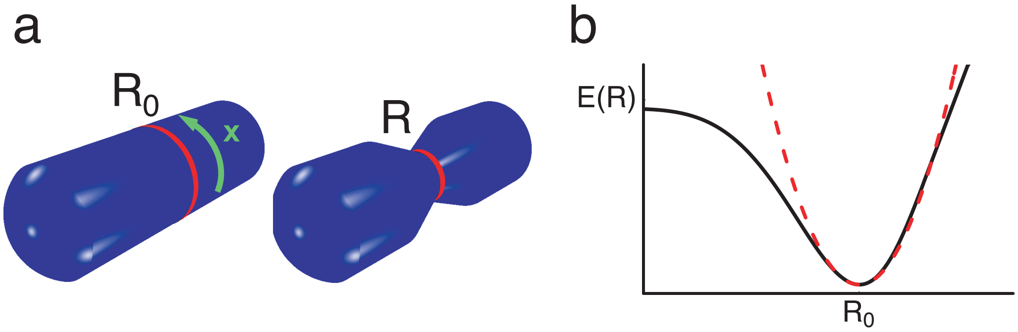

Figure 6.2: (a) Schematic representation of a cylindrical cell with a contractile ring of radius R_0 (left) and $R < R_0$ (right). (b) Energy needed to deform the cell $E(R)$. The black line shows a possible dependence of $E(R)$. We approximate this curve by a parabola centered at R_0 (dashed, red line). Figure modified from (Zumdieck et al., 2005b).

the stresses generated by different bundles in the ring add up to the total stress generated by the ring. Note that Eq. (6.6) includes the case of a single bundle forming a contractile ring as the special case $N_\mathrm{b} = 1$. In general, terms involving higher powers of c could occur if more filaments interact simultaneously in the bundle. For large densities c, the generated stress could increase proportional to the filament density $\Sigma \sim c$ as the number of pairwise interactions does not grow unbounded due to geometrical constraints. This is captured in our description by assuming N_b bundles with smaller densities c. The tension will in general saturate at a maximal value as discussed below. However, this does not affect the main results presented here.

Moreover, filaments can nucleate and polymerize from monomers and existing filaments disassemble. Monomers from the ring are continuously exchanged with reservoirs in the cytoplasm. This balance of material exchanges between ring and cytoplasm can be described as

$$\dot{c} = k_\mathrm{p} - k_\mathrm{d} c - \frac{\dot{R}}{R} c \quad . \tag{6.7}$$

Here k_p/c and k_d denote effective rates of filament assembly and disassembly. In the limit $k_\mathrm{p} = 0$, $k_\mathrm{d} = 0$ when no material is exchanged with the cytoplasm, we obtain

$$\dot{c} \simeq -\frac{\dot{R}}{R} c \qquad \Rightarrow \qquad \dot{M} = 0 \quad , \tag{6.8}$$

which describes mass conservation during ring contraction. If the filaments in the ring have a typical length l and no polymerization and depolymerization of filaments occurs, the total mass of filaments in the ring as given by Eq. (6.2) is constant. As a consequence, the filament density $c \sim 1/R$ in the ring increases with decreasing radius. Another interesting limiting case is fast polymerization dynamics. The filament density is then given by

$$c = \frac{k_p}{k_d} \qquad \Rightarrow \qquad \dot{M} = 2\pi N_b c m_l \dot{R} \tag{6.9}$$

where we have assumed in both cases that the number of bundles, N_b, does not change.

6.3 Ring Dynamics

We discuss the contraction dynamics of a contractile ring described by Eqs. (6.4)-(6.7). First we discuss the stability of an unconstricted ring with radius R_0 to better understand the onset of ring contraction, section 6.3.1. Then we show the time course of contraction determined by numerical integration and discuss the choice of parameters as well as the dependence of the dynamics on these parameters.

6.3.1 Contraction of the Ring

When a ring forms in the cell cortex it usually does not contract right away but it “matures” and then starts contraction upon a cellular signal. In the framework of the ring dynamics as presented in the previous section this means changing a parameter so that a ring with radius R_0 becomes unstable towards smaller radii. Here we discuss the linear stability of such a ring.

No Polymerization and Depolymerization

We start with the instructive case of a constricting ring in the absence of polymerization and depolymerization. In this case the total number of filaments $N = N_b 2\pi R_0 c_0$ is conserved. The filament density therefore is given by

$$c(t) = \frac{N}{2\pi R(t)} \quad . \tag{6.10}$$

The contraction velocity is thus given by

$$\dot{R} = -\xi \left[k(R - R_0) + \frac{N_\mathrm{b} A N^2}{2\pi} \frac{1}{R^2} \right] \quad . \tag{6.11}$$

The equation $\dot{R} = 0$ has three solutions in R, indicating three possible radii at which the ring stalls. Typically only one of them is real and thus physically meaningful. If $A > 0$, a ring with radius R_0 will always constrict

$$\dot{R}(R_0) = -\xi \frac{N_\mathrm{b} A N^2}{2\pi} \frac{1}{R_0^2} < 0 \quad . \tag{6.12}$$

If A is positive but smaller than some critical value A_c the ring will constrict, but stall at an radius $R(A) > 0$ at which $\dot{R} = 0$. The explicit form of $R(A)$ in the absence of polymerization and depolymerization is given in appendix D. The critical value A_c can thus be determined by $R(A_c) = 0$. As this is technically difficult, we chose a different path to obtain A_c:

$$\dot{R} < 0 \quad \Longleftrightarrow \quad A(R) > -\frac{2\pi k R^2 (R - R_0)}{N^2 N_\mathrm{b}} \tag{6.13}$$

$$\Rightarrow \quad A_\mathrm{c} = \max_{R \in [0; R_0]} \left(-\frac{2\pi k R^2 (R - R_0)}{N^2 N_\mathrm{b}} \right) = \frac{8\pi}{27} k \frac{R_0^3}{N^2 N_\mathrm{b}} \quad , \tag{6.14}$$

which defines the critical A_c that is necessary for the ring to fully contract (i.e $R \to 0$) in the absence of polymerization and depolymerization.

Fast Polymerization and Depolymerization

The other limiting case which allows us to discuss the conditions for ring contraction is that of fast polymerization and depolymerization, so that

$$c(t) = \frac{k_\mathrm{p}}{k_\mathrm{d}} \quad . \tag{6.15}$$

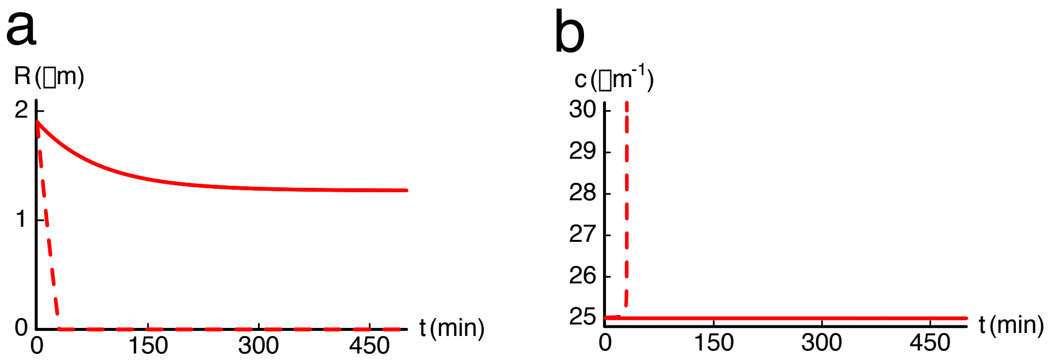

Figure 6.3: Dynamics of a contracting ring as a function of time for A larger and smaller than A_c. (a) Ring radius R as a function of time. For $A > A_\mathrm{c}$ (dashed line) the ring constricts completely in around 30 min while for $A < A_\mathrm{c}$ (solid line) it approaches a radius $R_s > 0$. (b) Corresponding filament density c as a function of time shown for the same numerical calculations as in (a). Parameters are as in Fig. 6.4, so that by Eq. (6.18) $A_\mathrm{c} \simeq 9.7 \times 10^{-15}\,\mathrm{N}\mu\mathrm{m}^2$. Plots show $A = 3.2 \times 10^{-14}\,\mathrm{N}\mu\mathrm{m}^2$ (dashed lines) and $A = 3.2 \times 10^{-15}\,\mathrm{N}\mu\mathrm{m}^2$ (solid lines). The curves are calculated as described in section 6.3.2.

This leads to a dynamic equation for the radius

$$\dot{R} = -\xi \left[k(R - R_0) + 2\pi N_\mathrm{b} A \left(\frac{k_\mathrm{p}}{k_\mathrm{d}} \right)^2 \right] \quad . \tag{6.16}$$

Therefore $\dot{R}(R_0) < 0$ for $A > 0$, so that a ring with radius R_0 would start to contract immediately. For any given A the ring contracts to the radius

$$R(A) = R_0 - \frac{2\pi N_\mathrm{b} A k_\mathrm{p}^2}{k k_\mathrm{d}^2} \quad . \tag{6.17}$$

The critical value of A is determined by the condition $R(A) = 0$:

$$A_\mathrm{c} = \frac{k k_\mathrm{d}^2 R_0}{2\pi k_\mathrm{p}^2 N_\mathrm{b}} \tag{6.18}$$

Intermediate Polymerization Rates

The general case of intermediate polymerization rates is described by Eqs. (6.4)-(6.7). As in the two limiting cases a ring with radius R_0 will start to contract as for $A > 0$ we have $\dot{R}(R_0) < 0$. The system has a fixed point at

$$c_\mathrm{s} = \frac{k_\mathrm{p}}{k_\mathrm{d}}, \qquad R_\mathrm{s} = R_0 - \frac{2\pi N_\mathrm{b} A k_\mathrm{p}^2}{k k_\mathrm{d}^2} \quad . \tag{6.19}$$

The stability of this fixed point at linear order is given by

$$\begin{pmatrix} \dot{\delta c} \\ \dot{\delta R} \end{pmatrix} = \begin{pmatrix} -k_\mathrm{d} - 6\pi N_\mathrm{b} A \xi c_\mathrm{s}^2 / R_\mathrm{s} & -\xi c_\mathrm{s} (2\pi N_\mathrm{b} A c_\mathrm{s}^2 - k)/R_\mathrm{s} \\ -2A\xi c_\mathrm{s} & -\xi k \end{pmatrix} \begin{pmatrix} \delta c \\ \delta R \end{pmatrix} \tag{6.20}$$

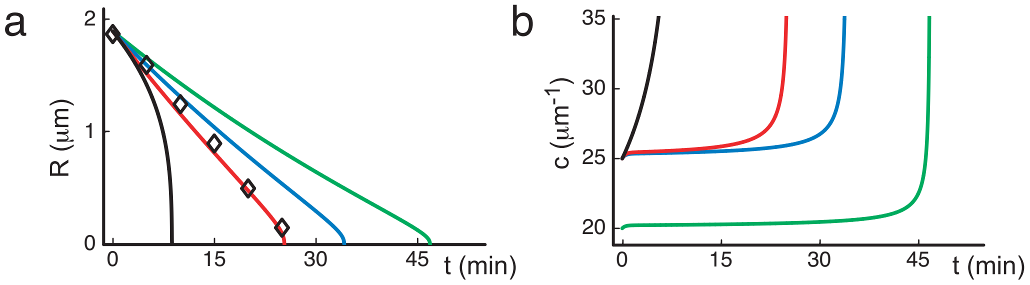

Figure 6.4: Radius and filament density of a contracting ring as a function of time obtained by numerical integration of Eqs. (6.4)-(6.7) . (a) Ring radius R as a function of time t for different choices of parameters. The solid red line agrees with experimentally obtained data for wildtype fission yeast indicated by diamonds (from ref. (Pelham and Chang, 2002)). Parameters are: filament depolymerization rate $k_d = 1/(25s)$, initial filament density $c_0 = 25\,\mu\text{m}^{-1}$, number of bundles $N_b = 200$, $R_0 = 1.9\,\mu$m, cell elastic modulus $k = 4\times10^{-9}\,\text{N}\mu\text{m}^{-1}$, friction coefficient $\xi^{-1} = 20$ Ns/m and $A = 3.2\times10^{-14}\,\text{N}\mu\text{m}^2$. The corresponding mechanical tension is $\Sigma = AN_bc^2 \simeq 4\times10^{-9}$ N. The contraction with almost constant contraction velocity $-\dot{R}$ requires rapid filament depolymerization. For $k_d = 0\,\text{s}^{-1}$, i.e. no filament turnover, the contraction becomes faster and the contraction speed increases with time (black line). In some mutants, the observed contraction velocity is smaller (Pelham and Chang, 2002). This effect can result from reduced contractile tension Σ. This can be achieved by either reducing the filament density by reducing the nucleation/polymerization rate k_p (green line, $c_0 = 20\,\mu\text{m}^{-1}$), or by reducing the active force generation in the bundle (blue line, $A = 2.6\times10^{-14}\,\text{N}\mu\text{m}^2$). (b) Filament density c as a function of time shown for the same calculations as in (a).

For the physically sensible conditions $c_\text{s} > 0$, $R_\text{s} > 0$, $k > 0$, $\xi > 0$, $A > 0$, $k_\text{d} > 0$, $N_\text{b} > 0$, the eigenvalues are always negative

$$\lambda_{1,2} < 0 \quad , \tag{6.21}$$

i.e. the fixed point is always stable and the ring does never fully contract, unless we choose $A > A_\text{c}$, so that there is no fixed point in $[0, R_0]$. The critical value of A is again given by Eq.(6.18).

In conclusion we can say that a ring of radius R_0 will always start to contract down to a radius that is determined by the balance of forces involved, see Fig. 6.3. This means that constriction upon a cell signal after a the maturation period as observed in live cells corresponds to “switching on” A at some point. If the effective force generation exceeds a critical value $A > A_\text{c}$ the ring contracts completely and cleaves the cell.

6.3.2 Numerical Analysis of Ring Contraction

Equations (6.4)-(6.7) provide a physical description of the dynamics of ring contraction. Having discussed the stability of the ring we now integrate these equations numerically in order to obtain the whole trajectories $R(t)$ and $c(t)$. We start at time $t = 0$ with $R = R_0$ and a steady state filament density $c_0 = k_\text{p}/k_\text{d}$. We assume that a cell signal activates the ring (i.e. $A > 0$ at $t = 0$), which then generates tension according to Eq. (6.6) and starts to contract as described by Eq. (6.4). The turnover time of actin filaments is given by k_d^{-1} and $k_\text{p} = c_0k_\text{d}$. If this time is long compared to the contraction time, the filament density increases during contraction, which in turn causes the contraction velocity to increase significantly for small ring radii. As a consequence the function $R(t)$ is curved downwards, see black lines in Fig. 6.4. The opposite scenario is a situation where filament turnover (measured by k_{d}^{-1}) is fast compared to the contraction time. In this case, the filament density is controlled by the assembly and disassembly kinetics of the filaments, and during contraction $c \simeq k_{\mathrm{p}}/k_{\mathrm{d}}$. As a consequence, the generated stress Σ remains constant. If contractile stresses dominate over elastic stresses, as is required for robust contraction, the contraction velocity is constant during contraction, see green lines in Fig 6.4. The parameters for the numerical integration are determined by comparison with experimental observations as explained in the following section.

6.3.3 Estimate of Parameter Values

We can compare our calculations to experiments that observe the kinetics of contraction and the turnover of the ring components in fission yeast (Pelham and Chang, 2002). In this case the initial cell radius is $R_0 \simeq 1.9\,\mu\mathrm{m}$. The total contraction time is $T \simeq 30\,\mathrm{min}$. The fluorescent signals of GFP-Cdc4 (a myosin light chain) does not change remarkably during contraction which is consistent with a scenario where the ring density is constant. The fluorescence recovery of GFP-Cdc8 (tropomyosin) is shorter than 30 s, which suggests a choice of filament turnover rate

$$k_{\mathrm{d}} \simeq \frac{1}{25}\,\mathrm{s}^{-1} \quad . \tag{6.22}$$

This estimate is consistent with the regime of constant density c and constant contraction velocity v_{R} as is indeed observed, see experimental data points in Fig. 6.4a, where $v_{\mathrm{R}} \simeq R_0/T \simeq 1.1\,\mathrm{nms}^{-1}$. This observed contraction kinetics allows us to estimate

$$\xi\Sigma \simeq \frac{v_{\mathrm{R}}}{2\pi} \simeq 0.2\,\mathrm{nm}\cdot\mathrm{s}^{-1} \tag{6.23}$$

if contractile stresses dominates, i.e. $\Sigma \gg kR_0$.

In order to estimate k_{p}, we need the number density of filaments in the ring. Electron microscopy of human HeLa cells[1] suggests that filament bundles forming the ring contain about 25 filaments each in its crossection (Maupin and Pollard, 1986). A "typical" contractile ring displays in total about 5000 filaments in its crossection (Schroeder, 1990). As a rough estimate, we thus assume that

$$N_{\mathrm{b}} \simeq 200 \tag{6.24}$$

bundles exist with 25 parallel MTs each exist.

Treadmilling exchanges all actin in a filament of length $1\,\mu\mathrm{m}$ in about 20 minutes (Pollard, 1986). This can be sped up more than 30 times by proteins such as ADF/cofilin (Carlier et al., 1999) and formins (Pollard and Borisy, 2003) that are present in the ring. Given that actin in the ring completely exchanges within 60 s, we use an average filament length of $l \simeq 1\mu\mathrm{m}$ in our description. This suggests an initial concentration

$$c(0) = c_0 \simeq 25\,\mu\mathrm{m}^{-1} \tag{6.25}$$

and thus

$$k_{\mathrm{p}} \simeq k_{\mathrm{d}} \cdot c_0 \simeq 1\,\mathrm{s}^{-1}\mu\mathrm{m}^{-1} \quad . \tag{6.26}$$

Here c_0 is the density that is established by polymerization and depolymerization without ring contraction. We choose the initial concentration $c(0) = c_0$.

---

[1] It is not obvious that HeLa cells posses the same ring structure as yeast. Equivalent data on yeast is unfortunately not available. There are however many similarities between rings in very diverse species so that Schroeder (1990) speaks of the typical ring, cf. section 2.5.2.

The elastic modulus of cells as a function of position on the cell surface has been measured by atomic force microscopy (AFM) for PtK2 cells by Matzke et al. (2001). In these experiments, the observed Young modulus was $Y_\mathrm{i} \simeq 1\,\mathrm{kPa}$ during interphase and increased during cytokinesis up to $Y_\mathrm{c} \simeq 10\,\mathrm{kPa}$ in the equatorial zone. Using the Young modulus at interphase suggests an elastic modulus of PtK2 cells of the order of

$$k \simeq Y_\mathrm{i} R_0 \simeq 4 \times 10^{-9}\,\mathrm{N}\mu\mathrm{m}^{-1} \quad , \tag{6.27}$$

where $R_0 \simeq 4\,\mu\mathrm{m}$ for PtK2 cells. The value of the Youngs modulus of the cleavage furrow during cytokinesis provides a rough estimate for the tension generated in the contractile ring of PtK2 cells:

$$\Sigma \simeq Y_\mathrm{c} R_0^2 \simeq 160 \times 10^{-9}\,\mathrm{N} \quad . \tag{6.28}$$

Motivated by these measurements and taking into account that fission yeast is smaller than PtK2 cells but could possess a more rigid cell wall, we suggest

$$k \simeq 4 \times 10^{-9}\,\mathrm{N}\mu\mathrm{m}^{-1} \tag{6.29}$$

for yeast. Note that the contractile tension $2\pi\Sigma$ must exceed $kR_0 \simeq 10\,\mathrm{nN}$. We use

$$\Sigma = 4 \times 10^{-9}\,\mathrm{N} \quad , \tag{6.30}$$

which can be compared with direct measurements of ring forces. In echinoderm eggs for example, the ring can generate contractile forces up to $3 \times 10^{-8}\,\mathrm{N}$ (Rappaport, 1967). This force was obtained by inserting glass needles in the cell and measuring their deflection. An unperturbed ring probably does not contract with maximal force. Using our estimate from above allows us to fit the inverse friction coefficient ξ and the effective material coefficient A so that the dynamics reproduces the experimental behavior. We obtain

$$\xi \;=\; 5 \times 10^{4}\,\mu\mathrm{m} \cdot \mathrm{N}^{-1}\mathrm{s}^{-1} \tag{6.31}$$

$$A \;=\; 3.2 \times 10^{-14}\,\mathrm{N}\mu\mathrm{m}^{2} \quad . \tag{6.32}$$

The contraction dynamics with these parameter corresponds to the solid red lines displayed in Fig. 6.4, and is consistent with the experimental data observed in yeast (Pelham and Chang, 2002). For comparison, the experimentally observed ring diameter as a function of time is shown as diamonds. For $k_d = 0$, i.e. no polymerization and depolymerization, the contraction velocity increases rapidly with time (Fig. 6.4, black line). Mutations and drugs that affect the rates of filament nucleation and polymerization typically lead to slower contraction velocities (Pelham and Chang, 2002). We imitate such effects by modifying the contraction mechanics via a reduction of the parameter A (Fig. 6.4, blue line) or of the polymerization rate (Fig. 6.4, green line).

6.3.4 Parameter Dependence of Ring Dynamics

In this section we discuss how the ring contraction dynamics depends on the parameters involved. The parameters that lead to the contraction dynamics shown in Fig. 6.4 have been determined directly and indirectly from various experimental sources. While some of them are set with a high confidence, others could vary considerably e.g. because they are obtained from another organism or inferred indirectly. It is thus important to investigate how changes in the parameters will affect out results.

The two parameters that have been measured with the highest confidence are the ring diameter R and the total contraction time T. Both parameters have been directly observed

Parameter	Examples of Values		
N_b	10	100	200
Total # of filaments	250	2500	5000
A ($10^{-14}\mathrm{N}\mu\mathrm{m}^2$)	64	6.4	3.2
Other parameters:	$R(t=0) = R_0 = 1.9\,\mu\mathrm{m}$, $c(t=0) = c_0 = 25\,\mu\mathrm{m}^{-1}$, $k_\mathrm{d} = (1/25)\,\mathrm{s}^{-1}$, $k_\mathrm{p} = 1\,\mathrm{s}^{-1}\mu\mathrm{m}^{-1}$, $\xi = 5 \cdot 10^4\,\mu\mathrm{m}\,\mathrm{N}^{-1}\mathrm{s}^{-1}$, $k = 4 \cdot 10^{-9}\,\mathrm{N}\mu\mathrm{m}^{-1}$, $\Sigma = 4 \cdot 10^{-9}\,\mathrm{N}$		

Table 6.1: Different numbers of filament bundles N_b. Each of the three cases (values of A and N_b) gives rise to the dynamics shown by the solid in Fig. 6.4.

in the fission yeast experiments by Pelham and Chang (2002). All other parameters are inferred from different organisms and could thus be different in fission yeast. The structure of the contractile ring as captured by c and N_b was determined in human HeLa cells. They are consistent with the sheet like appearance of a "typical" contractile ring (Schroeder, 1972, 1990). It seems likely that fission yeast contractile rings have a similar structure. In any case the number of filaments in a cross section should not vary by more than one order of magnitude. The forces per filament in rings with less than 100 filaments in a cross section would be high enough to cause filament rupture or depolymerization. It is thus unlikely that the number of filament bundles N_b varies by more than two orders of magnitude.

The values for k and Σ are obtained from AFM measurements on PtK2 cells. These cells are bigger and divide faster than *S. pombe* but do not posses a rigid cell wall. We thus assume that the elastic modulus k is essentially the same in both cells, while the tension Σ is significantly (40×) smaller in yeast. The inverse friction coefficient ξ and the effective material parameter A are parameters that have not been determined experimentally. We use them to fit the dynamics to the observed experimental behavior.

As the effective dynamics is essentially driven by the force balance between Σ and $k(R_0 - R)$ but does not depend on the details of stress generation, a change in the number of filament bundles for example can be conveniently compensated by a change in A without affecting the resulting dynamics, see table 6.1.

Now we turn to the generic features of the trajectories $R(t)$ and $c(t)$ and how they depend on parameters.

General Form of $\mathbf{R}(\mathbf{t})$

While changes in the number of bundles can easily be absorbed by other parameter without changing the ring dynamics at all, the other parameters are determined by the ring dynamics and cannot be changed without altering the time course $R(t)$. In order to facilitate the discussion we rewrite Eqs. (6.4)-(6.7) in dimensionless form:

$$\dot{\tilde{R}} = -\tilde{\alpha}(\tilde{R} - 1) - \tilde{\beta}\tilde{c}^2 \tag{6.33}$$

$$\dot{\tilde{c}} = \tilde{\gamma} - \tilde{\delta}\tilde{c} - \frac{\dot{\tilde{R}}}{\tilde{R}}\tilde{c} \tag{6.34}$$

where

$$\tilde{R} = \frac{R}{R_0}, \quad \tilde{c} = cR_0, \quad \tilde{t} = t\tau \tag{6.35}$$
$$\tilde{\alpha} = \frac{\xi k}{\tau} \tag{6.36}$$
$$\tilde{\beta} = 2\pi \frac{\xi A N_{\mathrm{b}}}{\tau R_0^3} \tag{6.37}$$
$$\tilde{\gamma} = \frac{k_{\mathrm{p}} R_0}{\tau} = \tilde{\delta} c_0 R_0 \tag{6.38}$$
$$\tilde{\delta} = \frac{k_{\mathrm{d}}}{\tau} \tag{6.39}$$

are the dimensionless quantities and parameters. We drop the tilde in this section understanding that all calculations are in dimensionless form. For the good fit to the experimental data points (solid line in Fig. 6.4) we obtain with $\tau = 1\,\mathrm{s}^{-1}$

$$\alpha = 2 \times 10^{-4}, \quad \beta \simeq 2.9 \times 10^{-7} \tag{6.40}$$
$$\gamma = 1.9, \quad \delta = \frac{1}{25} \quad . \tag{6.41}$$

The slope of $\mathbf{R}(\mathbf{t})$ is set by $\dot{R}$. For the unconstricted radius R_0, the slope is given by $-\beta c^2$ and for $R = 0$ we find $\dot{R} = \alpha - \beta c^2$, where $c = c(R,t)$ is the number density of filaments that depends on R. A constant contraction velocity thus requires

$$\alpha(R-1) \ll \beta c^2 \tag{6.42}$$

for all $R \in [0;1]$ and $c(R,t)$, which would give a straight line for $R(t)$. In this case the dimensionless total contraction time is given by

$$T = \frac{1}{\beta c^2} \quad . \tag{6.43}$$

The dynamics observed for the parameters motivated by experiments (i.e. $k_{\mathrm{d}} = 1/(25\,s)$, see solid line in Fig. 6.4), however shows a straight line for $R(t)$ that curves downward around some radius R^* and quickly reaches $R = 0$. Experimental data does not allow to measure R^*. We present an analytical estimate for R^* below.

In the absence of polymerization and depolymerization ($\gamma = 0, \delta = 0$), we have

$$c(t) = \frac{M_0}{2\pi R(t)} \tag{6.44}$$

where $M_0 = N_{\mathrm{b}} 2\pi R_0 c_0$ is the constant, dimensionless mass of the ring (cf. Eq. (6.2), $\tilde{m}_l = 1$). The dynamics is entirely determined by the contraction of the ring and we are left with one equation:

$$\dot{R} = -\alpha(R-1) - \beta \left(\frac{M_0}{2\pi}\right)^2 \frac{1}{R^2} \quad . \tag{6.45}$$

The slope at $R = 1$ is given by $-\beta M_0^2/(2\pi^2)$; at $R = 0$ it diverges towards ∞.

If the dynamics is polymerization dominated so that the density of filaments is constant

$$c = \frac{\gamma}{\delta} \quad , \tag{6.46}$$

Polymerization	Initial slope ($R = 1$)	Final slope ($R = 0$)
None	$-\beta M_0^2/(2\pi^2)$	∞
Intermediate	$-\beta c^2$	$\alpha - \beta c^2$
Fast	$-\beta\gamma^2/\delta^2$	$\alpha - \beta\gamma^2/\delta^2$

Table 6.2: Slopes of $R(t)$ for the three different cases of dynamics at the maximal and minimal radius in dimensionless units as discussed in the text.

we are also left with one equation that describes the dynamics of ring contraction in this regime

$$\dot{R} = -\alpha(R-1) - \beta\left(\frac{\gamma}{\delta}\right)^2 \quad . \tag{6.47}$$

In this case the initial slope for $R = 1$ is given by $-\beta\gamma^2/\delta^2$, and the slope for full contraction $R = 0$ is $\alpha - \beta\gamma^2/\delta^2$. Table 6.2 summarizes the slopes in the different regimes.

We present two ways to estimate the radius $\mathbf{R}^*$ at which $\mathbf{R(t)}$ curves, which is another important parameter that characterizes the time courses of $R(t)$. First we obtain R^* by matching the slopes of $R(t)$ coming from both ends, i.e. $R = 0$ and $R = R_0$. Then we determine R^* by analyzing the change over from a polymerization dominated regime to a contraction dominated regime in the mass equation.

1. Matching of slopes. The slope in the first part of the curve depends only weakly on R, which is the case if c is essentially constant. That in turn is true for polymerization dominated dynamics, when $c = \gamma\,\delta^{-1}$. We thus obtain

$$\dot{R}_1 = -\alpha(R-1) - \beta\frac{\gamma^2}{\delta^2} \tag{6.48}$$

for the slope of the first part. Towards full contraction, the mass conservation term dominates in Eq. (6.34), so that $c \propto R^{-1}$ and the slope of the second part is

$$\dot{R}_2 \simeq \alpha(R-1) - \beta\frac{1}{R^2} \quad . \tag{6.49}$$

Matching the two slopes yields

$$R^* = \frac{\delta}{\gamma} = \frac{1}{c_0 R_0} \tag{6.50}$$

This way of estimating R^* is problematic, as the dynamics can change considerably without affecting R^*. Figure 6.5 shows an example for two sets of parameters that have the same $R^* \simeq 0.02$. For the first case R^* is too small, for the second it clearly is too large.

2. Crossover in mass equation. A complementary way to estimate R^* is to determine at what radius the mass conservation term in Eq. (6.34) is of the same magnitude as the polymerization terms. This conditions marks the crossover from the regime in which the concentration c is dominated by the polymerization dynamics to the regime in which the contraction dynamics influences c most. The condition in mathematical terms is

$$\begin{aligned} -\frac{\dot{R}(R^*)}{R^*} &= \delta && (6.51) \\ \Rightarrow R^* &= \frac{\alpha - \beta {c^*}^2}{\alpha - \delta} = \frac{\alpha - \beta\left(\frac{\gamma}{\delta}\right)^2}{\alpha - \delta} && (6.52) \end{aligned}$$

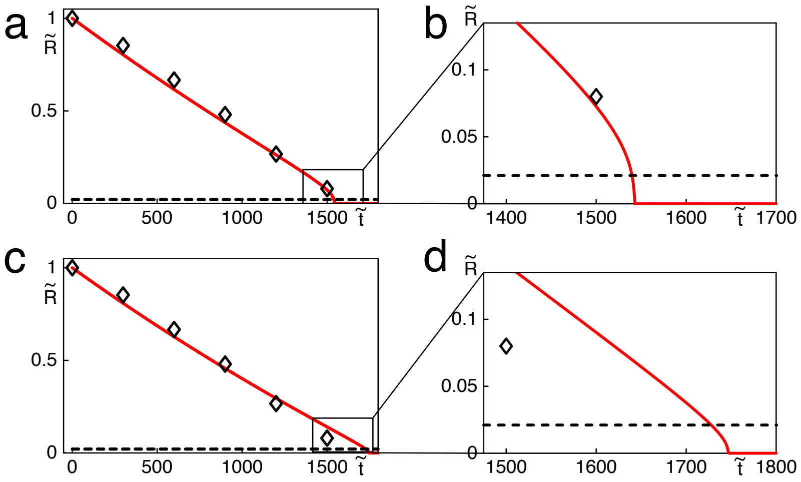

Figure 6.5: Estimate of R^* by matching slopes (Method 1, Eq. (6.50)). Shown are the contraction dynamics in dimensionless variables $(\tilde{R}, \tilde{t})$ obtained by numerical integration (red lines) and the estimated value of R^* (dashed, black line). The diamonds are experimental data points from (Pelham and Chang, 2002). The plots at the right show the relevant region in detail. Parameters are (a,b) $\gamma = 1.9$, $\delta = 1/25$ and (c,d) $\gamma = 5 \times 1.9$, $\delta = 5/25$. In both cases $\alpha = 2 \times 10^{-4}$, $\beta \simeq 2.9 \times 10^{-7}$, which leads to $R^* \simeq 0.02$.

where $c^* = \gamma/\delta$ is the solution of $\dot{\tilde{c}} = \gamma - \delta\tilde{c}^2$.

R^* is only positive if $\delta < \alpha$ and $\beta\gamma^2\delta^{-2} < \alpha$ or $\delta > \alpha$ and $\beta\gamma^2\delta^{-2} > \alpha$. If $\alpha \gg \beta\gamma^2\delta^{-2}$ and $\alpha \gg \delta$ then $R^* = 1$. Generally R^* becomes small when α is of the same order as $\beta\gamma^2\delta^{-2}$ or when $\alpha \ll \beta\gamma^2\delta^{-2} \ll 1$. Figure 6.6 shows that R^* as given in Eq. (6.52) (dashed lines) systematically underestimates the radius of cross over in the dynamics. This is due to the approximation of the density $c^* = \gamma/\delta$. The dotted line shows the values of

$$R^*_{\mathrm{c}} = \frac{\alpha - \beta c_{\mathrm{c}}^2}{\alpha - \delta} \tag{6.53}$$

where c_{c} is the solution of

$$-\frac{\dot{R}(c_{\mathrm{c}})}{R} = \delta \quad . \tag{6.54}$$

These values fit the dynamics significantly better. Despite these shortcomings, the expression for R^* can be used to explore some general dependences of parameters.

We can tune α as defined by Eq.(6.36) so that R^* assumes an arbitrary value Γ:

$$\begin{aligned} R^* &= \Gamma \\ \Rightarrow \alpha &= \frac{\beta\gamma^2 - \Gamma\delta}{1 - \Gamma} \quad . \end{aligned}$$

But because of its definition, α has always to be positive, which limits the range of available R^*:

$$\alpha = \frac{\beta\gamma^2 - \Gamma\delta}{1 - \Gamma} > 0 \tag{6.55}$$

$$\Rightarrow \Gamma < \frac{\beta\gamma^2}{\delta} \tag{6.56}$$

---

[2] This assumption is best for $R \sim 1$ but cannot be expected to hold at the cross over point. This is likely to be the biggest weakness of this approach, see Fig 6.6.

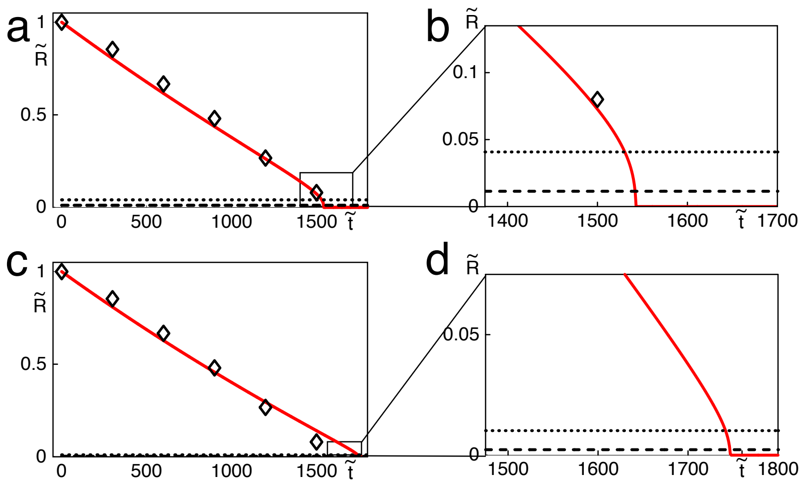

Figure 6.6: Estimate of R^* by determining the crossover in the mass equation (Method 2, Eq. (6.52)). Shown are the contraction dynamics in dimensionless variables $(\tilde{R}, \tilde{t})$ obtained by numerical integration (red lines) and the estimated value of R^* (long dashed, black line). The diamonds are the experimental data points from (Pelham and Chang, 2002) and the dotted lines are the improved estimate of R^* as given by Eq. (6.53). The plots at the right show the relevant region in detail. Parameters are $\alpha = 2 \times 10^{-4}$, $\beta \simeq 2.9 \times 10^{-7}$ and (a,b) $\gamma = 1.9$, $\delta = 1/25$ so that $R^* \simeq 0.01$ and $R_c^* \simeq 0.04$. (c,d) $\gamma = 5 \times 1.9$, $\delta = 5/25$ so that $R^* \simeq 0.002$ and $R_c^* \simeq 0.01$.

In order to reproduce the linear behavior observed in experiments, we want to choose the parameters so that $R^* < 0.1$ as the last datapoint corresponds to a dimensionless radius of 0.15:

$$\begin{array}{rcll} R^* & < & \dfrac{1}{10} & \\ \Rightarrow \alpha & > & \dfrac{10}{9}\beta\gamma^2 - \dfrac{1}{9}\delta & \text{for} \quad \alpha < \delta \\ \Rightarrow \alpha & < & \dfrac{10}{9}\beta\gamma^2 - \dfrac{1}{9}\delta & \text{for} \quad \alpha > \delta \end{array}$$

Unfortunately neither of the two ways to estimate R^* is fully satisfactory. The best approximation is given by R_c^*, but this is no analytical estimate. The considerations presented here do however allow some insight into the dynamics of the coupled partial differential equations that would be difficult to gain by numerical integration alone.

6.4 Generality of the Description

In section 6.3.4 we discussed the dependence of the ring dynamics on parameters. Here we will discuss the assumptions made for the formulation of the dynamics.

The harmonic approximation of $E(R)$ seems problematic, especially for small radii. We also investigated the dynamics using a clipped harmonic version of $E(R)$. Here $E(R)$ is constant on $[0; R_c]$ at a value $E(R_c)$ for an $R_c \in [0; R_0]$ and harmonic on the remaining interval, cf. Fig. 6.7. This did not qualitatively change the behavior. The trajectories obtained by numerical integration are usually similar to those where we used the harmonic

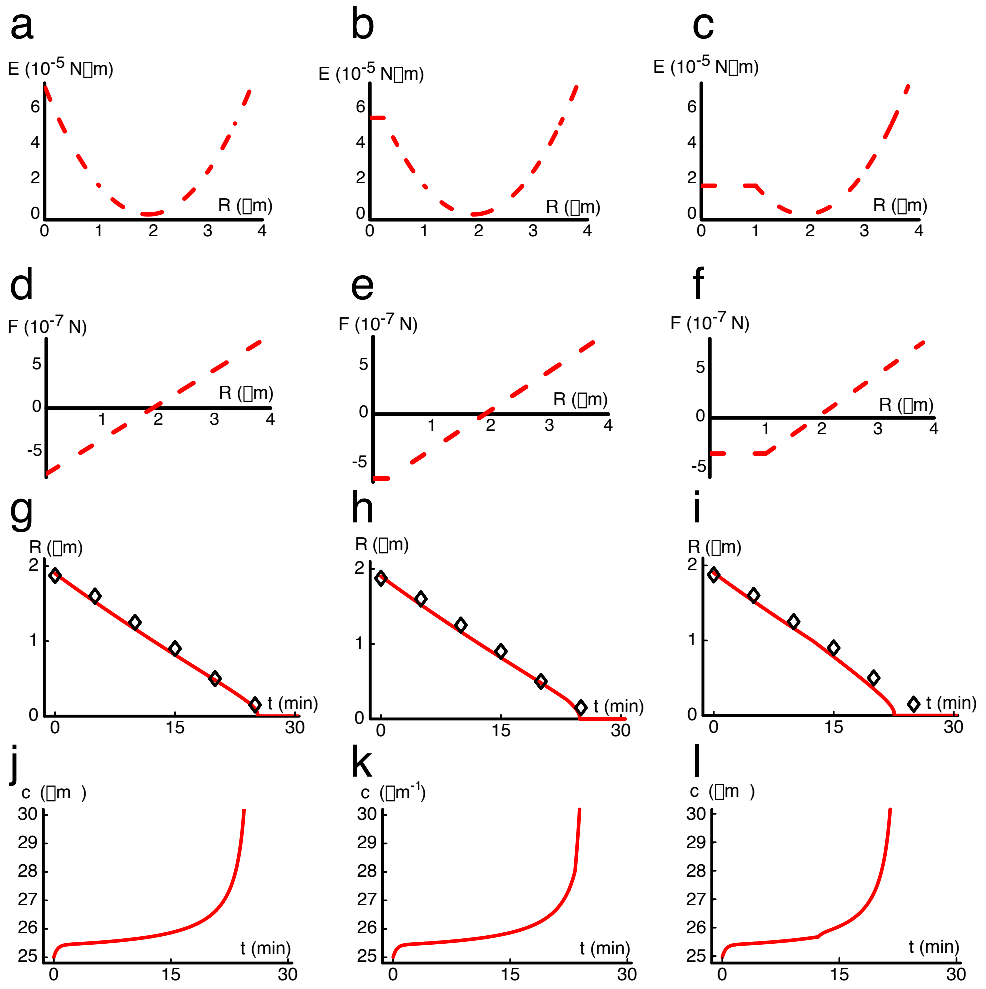

Figure 6.7: Influence of a cut off in the elastic energy $E(R)$ on the dynamics. Top row shows the elastic energy as a function of the radius without any cut (a), with a cut at $R = 0.25\,\mu$m (b) and at $R = 1\,\mu$m (c). The next line (d,e,f) gives the correscponding elastic forces. The bottom two lines give the trajectories $R(t)$ (g,h,i) and $c(t)$ (j,k,l) obtained by numerical integration. The diamonds mark the experimental data points from (Pelham and Chang, 2002). The parameters are the same as in Figure 6.4.

approximation over the whole range of R, see Fig. 6.7. This behavior can be understood if we assume that for smaller R the contraction dynamics is dominated by the active tension. In that case a change in the exact form of the potential would not have a dramatic effect on the dynamics.

This prompts us to take a closer look at the active tension. We assume that the tension is generated by active processes in the ring. Motivated by the analysis of pairwise interactions between filaments discussed in chapter 3, we propose a quadratic dependence of Σ on c. This seems sensible as long as the density of filaments is low, so that the probability of pairwise interactions is proportional to c^2. When the filament density becomes large and the filament bundle has a larger diameter, it is unlikely for filaments to interact with filaments that are spatially distant. That is why for large densities the stress will probably grow $\propto c$, simply because the probability of filament pair interactions in a thicker bundle grow linearly. The contractile ring as found e.g. in human HeLa cells appears to fit well with these considerations: the ring is a flat, band-like structure composed of many different filament bundles that are aligned next to each other. In every bundle the density of filaments can be small enough so that $\Sigma \propto c^2$ holds. The stress of the various bundles then just adds up, similar to $\Sigma \propto c$ in one thick bundle.

When the ring forms it can either form all bundles at the same time, so that N_b remains constant over the period of ring constriction. In this case the structure of the ring just leads to a rescaling of the coefficient of stress generation A as seen above. If however the ring forms with only one bundle which consecutively splits during ring contraction, then N would always increase monotonously, while $c(t)$ should increase monotonously and then decrease suddenly everytime a bundle splits. This behavior could lead to a different kind of dynamics of the ring, that is beyond the scope of this thesis.

6.5 Stresses and Ring Contraction

Throughout this chapter we assumed that radial stresses in cytoskeletal structures such as the contractile ring or the actin cortex can lead to forces normal to the cell surface, i.e. forces that could lead to the contraction of this cytoskeletal structure. In this section we briefly show how the normal forces are related to radial stresses and under which conditions an active material in cortical geometry can generate normal forces.

6.5.1 Radial Stress and Normal Force

We have seen in section 3.2.5 that a ring of active filaments and molecular motors can generate tension in the radial direction. If this ring is wound around the equator of a cell and contracts like a contractile ring, this radial stress has to lead to normal forces directed towards the center of the cell. Here we calculate this relation explicitly.

Consider a ring with radius $R = 1$ that exercises stress only in the radial direction, i.e. in polar coordinates ($x = R\cos\phi$, $y = R\sin\phi$) the stress tensor is given by

$$\boldsymbol{\sigma} = \begin{pmatrix} \sigma_{rr} & \sigma_{r\phi} \\ \sigma_{\phi r} & \sigma_{\phi\phi} \end{pmatrix} = \begin{pmatrix} 0 & 0 \\ 0 & \sigma_{\phi\phi} \end{pmatrix} \tag{6.57}$$

which in cartesian coordinates leads to

$$\boldsymbol{\sigma} = \begin{pmatrix} \sigma_{xx} & \sigma_{xy} \\ \sigma_{yx} & \sigma_{yy} \end{pmatrix} = \mathcal{R} \begin{pmatrix} 0 & 0 \\ 0 & \sigma_{\phi\phi} \end{pmatrix} \mathcal{R}^{-1} = \begin{pmatrix} y^2 & -xy \\ -xy & x^2 \end{pmatrix} \sigma_{\phi\phi} \tag{6.58}$$

where

$$\mathcal{R} = \begin{pmatrix} \cos\phi & -\sin\phi \\ \sin\phi & \cos\phi \end{pmatrix} \tag{6.59}$$

is the rotation operator. The force is given by the divergence of $\boldsymbol{\sigma}$

$$\boldsymbol{F} = \mathrm{div}\boldsymbol{\sigma} = -\frac{1}{R^2}\sigma_{\phi\phi}\boldsymbol{e}_r \quad , \tag{6.60}$$

where $\boldsymbol{e}_r$ is the unit vector pointing outward normal to the ring. The radial stress thus indeed causes a normal force, which is proportional to its magnitude.

6.5.2 Forces of Arbitrary Stress Tensor

While the example presented in the last section is instructive in order to understand radial stress generation in rings, here we consider forces pointing in arbitrary direction resulting from stress tensors of the most general form:

$$\begin{aligned}
\boldsymbol{\sigma} &= \begin{pmatrix} \sigma_{xx} & \sigma_{xy} \\ \sigma_{yx} & \sigma_{yy} \end{pmatrix} \\
&= \mathcal{R}\begin{pmatrix} \sigma_{rr} & \sigma_{r\phi} \\ \sigma_{\phi r} & \sigma_{\phi\phi} \end{pmatrix}\mathcal{R}^{-1} \\
&= \frac{1}{R^2}\begin{pmatrix} \sigma_{rr}x^2 - (\sigma_{r\phi}+\sigma_{\phi r})xy + \sigma_{\phi\phi}y^2 & \sigma_{r\phi}x^2 - (\sigma_{\phi\phi}-\sigma_{rr})xy - \sigma_{\phi r}y^2 \\ \sigma_{\phi r}x^2 - (\sigma_{rr}-\sigma_{\phi\phi})xy - \sigma_{r\phi}y^2 & \sigma_{\phi\phi}x^2 + (\sigma_{\phi r}+\sigma_{r\phi})xy + \sigma_{rr}y^2 \end{pmatrix}
\end{aligned} \tag{6.61}$$

where $(x = R\cos\phi,\ y = R\sin\phi)$ and $\mathcal{R}$ is the rotation operator introduced in Eq. (6.59). This stress gives rise to a force

$$\begin{aligned}
\boldsymbol{F} &= \mathrm{div}\boldsymbol{\sigma} \\
&= \frac{1}{R^2}\left[(\sigma_{rr}-\sigma_{\phi\phi})\boldsymbol{e}_r + (\sigma_{r\phi}+\sigma_{\phi r})\boldsymbol{e}_\phi\right]
\end{aligned} \tag{6.62}$$

where $\boldsymbol{e}_r = (\cos\phi, \sin\phi)$, $\boldsymbol{e}_\phi = (-\sin\phi, \cos\phi)$ are the unit vectors radial and tangential to the cylinder. It is then trivial to see that e.g. a ring will contract radially if

$$\sigma_{\phi\phi} > \sigma_{rr} \quad , \tag{6.63}$$

because in this case the force is oriented radially towards the cylinder axis.

6.5.3 Generic Condition for Radial Contraction

The condition for ring contraction $\sigma_{\phi\phi} > \sigma_{rr}$ (Eq. (6.63)) is a consequence of the symmetry of the system. It is thus independent of the choice of coordinate system. Here we show that this is indeed the case by presenting a generic calculation based on the symmetry properties of the stress tensor.

Without fixing a coordinate system, we split the stress tensor σ into a diagonal, symmetric part $\sigma^{\mathrm{s}}\delta_{\alpha\beta}$ that effectively describes an isotropic surface tension and a traceless part $\sigma^{\mathrm{a}}_{\alpha\beta}$ that is symmetric by construction (cf. Eq. (5.51)) and describes anisotropic tension:

$$\sigma_{\alpha\beta} = \sigma^{\mathrm{s}}\delta_{\alpha\beta} + \sigma^{\mathrm{a}}_{\alpha\beta} \tag{6.64}$$

where

$$\sigma^{\mathrm{s}} = \frac{\sigma_{11}+\sigma_{22}}{2} \tag{6.65}$$

$$\sigma^{\mathrm{a}} = \begin{pmatrix} \sigma^* & \sigma_{12} \\ \sigma_{12} & -\sigma^* \end{pmatrix} \tag{6.66}$$

$$\sigma^* = \frac{\sigma_{11}-\sigma_{22}}{2} \tag{6.67}$$

are the diagonal and traceless components of $\boldsymbol{\sigma}$ and σ^* is a constant. The ring exerts a force in the radial direction, when $\sigma^* < 0$, i.e. when $\sigma_{22} > \sigma_{11}$. For polar coordinates this argument thus leads to the same condition for radial contraction as the direct calculation in the previous section, cf. Eq. (6.63).

6.6 Discussion

In this chapter we present a phenomenological description of cytoskeletal ring contraction based on force balance arguments. We explicitly take into account filament polymerization and depolymerization and show that they are indispensable for dynamics observed in experiments. Using parameters derived from independent experiments we obtain quantitative agreement with contraction trajectories measured in fission yeast.

The stress generated in the ring can result from the interaction between cytoskeletal filaments and molecular motors as well as filament polymerization dynamics. In chapter 3 we discuss microscopic mechanisms that give rise to tension in filament rings which are of the same form as Eq. (6.6). This allows us to identify how interfering with mechanisms at work in the ring, such as actin polymerization, can influence its contraction dynamics.

The contractile ring is central for cell division in many cells. From our analysis it becomes clear that its contraction trajectory yields much information about the processes that drive contraction. Our approach can be furthered to include other effects like e.g. different pressures in and outside the cell and in various regions of the cell. These pressure gradients can give rise to currents in the cytoplasm, which might also influence the contraction dynamics. Moreover the contribution of other organelles like e.g. the mitotic spindle to ring contraction can be approached using the tools introduced here. This will allow us to gain insight into this central question of cell biology from a novel point of view.

7 Summary and Perspectives

7.1 Summary of the Results

In this thesis we studied physical aspects of active filament systems, like those that form the basis of the cytoskeleton, i.e. the protein scaffold that e.g. allows cells to move and determines their shape. The central focus of our investigations was the role of polymerization and depolymerization of protein filaments for the formation and dynamics of prominent cytoskeletal structures such as the contractile ring, stress fibers or the mitotic spindle. These structures are indispensable for vital cellular processes such as cell division and cell locomotion, which play a crucial role e.g. for the development of organisms, in wound healing, or diseases such as cancer.

The processes that drive the dynamics of these structures are far from equilibrium and depend on a constant supply of chemical energy. While the energy delivered to motors is used to generate directed motion along protein filaments, these protein filaments themselves use energy to assemble and disassemble. The filaments are structurally polar and polymerization occurs with different rates at both ends due to the supplied energy. Filament polymerization and depolymerization together with the action of molecular motors and other cross-linking proteins generates forces at the microscopic scale, whose interplay gives rise to complex phenomena on the cellular level. We exemplified explicitly how physical tools and concepts such as self-organization and dynamic instability can contribute to our understanding of these truly fascinating structures.

In chapter 3 we presented a microscopic mean field description of active filament systems. Our focus was on the role of filament polymerization and depolymerization for the dynamics of filament bundles. We showed that filament treadmilling in the presence of end-tracking cross-linkers can lead to tension in the bundle and to bundle contraction even in the absence of molecular motors. Filament polymerization and depolymerization also change the type of bifurcation by which a homogenous bundle loses its stability. A particularly striking result is that passive, end-tracking cross-linkers in the presence of filament treadmilling do always generate stress in a bundle, while molecular motors have to be bound between filaments of the same polar orientation to contribute to the stress.

The second part (chapter 4) shows an extension and application of the microscopic description developed in chapter 3 to mitotic and meiotic spindles. Meiotic and mitotic spindles of the same organism can have vastly different lengths, although in principle they fulfill the same task. We showed how the action of many proteins gives rise to interesting collective behavior such as the formation of stable, finite size spindles. Our theory allows a detailed, analytical discussion of the contributions of different microscopic aspects of cytoskeletal dynamics such as motor force-velocity curves and binding probabilities on spindle formation and dynamics. In particular we showed how the balance of motors influences the spindle length.

Chapter 5 introduced phenomenological descriptions of cytoskeletal systems based on generic symmetry considerations. These theories are helpful tools to investigate the physics of these systems, because they highlight properties independent of microscopic details, which are often unknown. We showed in particular that bundle contraction is a consequence of the system's symmetry and calculate explicitly how stress is released by contraction. We linked this phenomenological description to the microscopic mean field theory presented in chapter 3. Applying this description to a cylindrical geometry, we uncovered physical mechanisms of ring formation in the cell cortex.

Finally in the last part of this thesis (chapter 6) we studied the dynamics and mechanics of contractile actin rings, which cleave cells during cytokinesis. Quantitative comparison of experimental data from *S. pombe* with the results obtained with a phenomenological description of ring contraction allowed us to estimate the essential parameters that characterize the mechanical and dynamical properties of such a contractile ring. We related our theoretical findings to experiments, which showed that ring contraction in fission yeast proceeds with constant velocity. We found that filament turnover due to polymerization and depolymerization is indispensable for such ring contraction with constant velocity.

In summary we presented ways to approach the dynamics of active filament systems from different angles and on different length and time scales. Starting out from considerations about the microscopic processes in active filament systems we presented a theory for active bundles that explicitly takes filament polymerization and depolymerization into account. This microscopic description is helpful as it provides an intuitive way of relating theoretical results to concrete processes in the cytoskeleton. Extending this theory with force dependent motor dynamics allowed us to discuss spindle formation, stability and length in chapter 4. The following chapter showed a generic way to analyze the physics of active filament systems on larger length and time scales. The phenomenological descriptions are useful to investigate situations in which the precise nature of the microscopic details is not known, as is often the case in biological systems. The power of such phenomenological approaches is demonstrated by investigations about ring formation in the cell cortex as well as by our study of the contraction dynamics of the contractile ring in chapter 6.

7.2 Outlook and Perspectives

The physics of the cytoskeleton has attracted the attention of many physicists for years now. Many important insights have been gained, but many fundamental questions are still open. It is safe to say that most of the work still lies ahead.

In the context of the topics presented in this thesis there are two main directions in which we may further our considerations. One is to apply the tools to other cytoskeletal structures and try to uncover more physical processes underlying the observed cellular dynamics. Detailed, microscopic descriptions are getting very complex and are hard to deal with when many players are involved. Furthermore, much of the biological detail remains yet to be discovered, which makes it impossible to cover them faithfully. Phenomenological descriptions such as those presented in chapter 5 might prove to be extremely valuable tools in these settings. Being independent of microscopic details and only based on symmetry considerations, they will help to clarify the physics of complex situations involving many (even partially unknown) proteins and mechanisms.

The investigation of physical mechanisms behind biological phenomena is more than just purely academic. Concepts originally developed in a more classical physical setting, such as e.g. self-organization in systems out of equilibrium (Cross and Hohenberg, 1993), phase transitions or bifurcation have been shown to be useful also for the description of biological systems and thus changed the way we think about them. Hopf bifurcations that mark the transition to oscillations are particularly fascinating and appear often in biological systems (Kruse and Jülicher, 2005).

The other direction is relating our theoretical approaches more closely to experiments. Investigations of how the cell achieves what it does profited remarkably from advances in experimental manipulation techniques, such as optical tweezers, atomic force microscopy or micro-pipettes that allowed better controlled and more quantitative experiments *in vivo* and *in vitro*. Equally impressive advances in microscopy enabled scientists to obtain more detailed information about cellular structures, e.g. by (cryo-) electron microscopy. Light microscopy, especially in combination with fluorescence based techniques such as fluorescence resonance energy transfer (FRET), fluorescence recovery after photobleaching (FRAP) or fluorescence correlation spectroscopy (FCS) now enable us to follow the dynamic processes of individual molecules and living cells (Schwille and Kettling, 2001). They also allow us to follow microscopic details of cytoskeletal dynamics even inside living cells. The advances in manipulation and observation are furthermore complemented by advanced in reconstitution of biological systems from purified components. Biomimetic systems and *in vitro* assays now enable us to quantify more and more aspects of cellular dynamics. This allows the fruitful combination and comparison of physical descriptions with (quantitative) experiments, see e.g. (Leduc et al., 2004; Boukellal et al., 2004).

Our theories make several predictions that could be tested in real cytoskeletal systems. Prominent examples are traveling density profiles in actin rings or the observation that binding to filament minus ends is crucial for spindle formation. A crucial step will be to make these results and the theoretical considerations that lead to them more easily accessible to experimentalists, e.g. by providing them with directly measurable quantities. This should go along well with the encouraging trend towards more quantitative measurements on biological systems supported by the advent of systems biology (Sorger, 2005).

More concretely, future work should extend our theories to higher dimensions. This seems to be especially interesting for the mitotic spindle. Furthermore the elasticity and pole-ward flux of the microtubules are new aspects that could be included in the description explicitly. The same is true for chromosomes and microtubules that are not attached to asters. The spindle will also interact with other cytoskeletal structures, be it another scaffold in the central region of the spindle or with the actin cortex of cells. Moreover, it is also believed to influence ring formation and dynamics.

Our understanding of the formation of the contractile ring will profit by linking the phenomenological description explicitly with microscopic processes in higher dimensions. Considering the microscopic action of other proteins besides motors and cross-linkers will be useful to understand ring and bundle dynamics. Another open question is the influence of arbitrary filament polymerization and depolymerization, which gives rise to filaments of various lengths. To incorporate these effects explicitly into microscopic theories is an important open challenge. Microscopic descriptions also seem to be a good starting point to investigate effects of fluctuations on cytoskeletal dynamics. This will strengthen the link to real cytoskeletal systems in which e.g. motor binding and unbinding seem to be stochastic events.

Independent of the tools employed, the effects of polymerization on the dynamics of cytoskeletal structures will continue to be a fascinating topic of research. This is certainly also due to the importance of the cytoskeleton for many cellular processes such as cell locomotion, which in turn are prominent in diseases, such as metastasis formation in cancer. A better understanding of the physics of the basic and collective processes involved in cytoskeletal dynamics will contribute to a more comprehensive appreciation of the cell's toolbox and its behavior. This knowledge has a great potential for application in medicine, e.g. development of drugs that target cytoskeletal structures, or in the design of novel materials. Ultimately the physics of the cytoskeleton will also help us to understand fundamental processes in living organisms. I am sure the long quest (Frixione, 2000) for a better understanding of the cytoskeleton will go on and am happy if I could contribute a tiny bit.

A Supplementary Analytic Calculations

A.1 Minimal Model: Linear Stability Analysis

Here we present additional results concerning the linear stability of the homogenous state. First we investigate how the critical interaction strength α depends on the other parameters. In a second part we discuss the influence of creation and annihilation of entire filaments on the stability of the homogenous state.

A.1.1 Parameter Dependence of the Critical Alpha

In chapter 3 we showed that the stability boundary $\alpha_c(v)$ qualitatively and quantitatively depends on the concentrations of filaments of either orientation. In addition it also depends on the value of the interaction strength between antiparallel filaments, β, in a quantitative way, Fig. A.1. Increasing β widens and deepens the “valley” where $\alpha_c(v) < \alpha_c(0)$. It thus enlarges the interval of treadmilling speeds v in which the homogenous state is destabilized and where (for equal concentrations) a stationary bifurcation occurs. The strength of this effect seems to be independent of the filament concentrations as long as the total number of filaments in the system is identical, compare Fig. A.1a and b. Furthermore, in the absence of this interaction ($\beta = 0$) the critical value of α does not depend on v.

We obtain similar results for the stability of a homogenous bundle in the presence of passive cross-linkers, but in the absence of molecular motors, see Fig. 3.13. The combined action of motors and passive cross-linkers does not change this trend.

Another peculiar observation is that when varying c^+ and c^- while keeping their sum fixed, all resulting curves $\alpha_c(v)$ intersect at the same point (v^*, α^*), see Fig. A.2. While

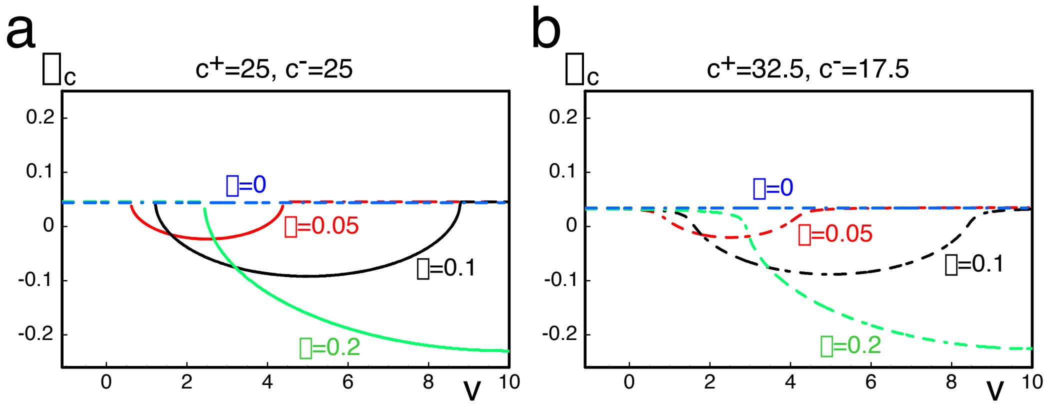

Figure A.1: Dependence of $\alpha_c(v)$ on β. Graphs show $\alpha_c(v)$ for different values of the interaction strength between antiparallel filaments β and (a) equal concentrations $c_0^+ = 25$, $c_0^- = 25$ as well as (b) for unequal concentrations $c_0^+ = 32.5$, $c_0^- = 17.5$. Increasing β deepens and widens the “valley” in $\alpha_c(v)$, which for equal concentrations also extends the region of the stationary bifurcation (solid line in (a)). Outside the valley and everywhere for unequal concentrations the bifurcation is of the Hopf kind (broken lines).

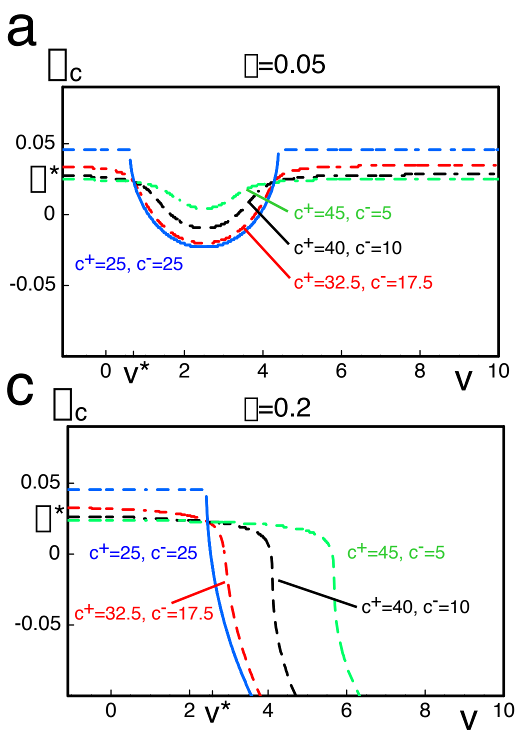

Figure A.2: Critical $\alpha_c(v)$ for $\beta = 0.5$ and varying concentrations. All curves intersect in the same point v^* with critical value α_c^*. While α_c^* is independent of β, v^* grows with increasing β, as do width and depth of the "valley" (a-c).

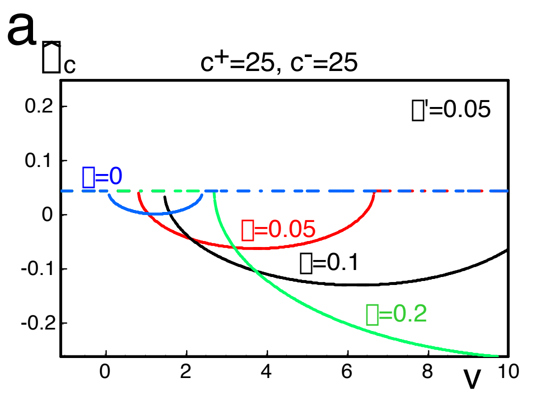

Figure A.3: Stability boundary of the homogenous state in a bundle with treadmilling, motors and passive cross-linkers. The graphs show $\hat{\alpha}_c(v)$ as defined in Eq. (3.64) for different values of the interaction strength between antiparallel filaments β and (a) equal concentrations $c_0^+ = 25$, $c_0^- = 25$ as well as (b) for unequal concentrations $c_0^+ = 32.5$, $c_0^- = 17.5$. Increasing β depends and widens the "valley" in $\alpha_c(v)$, which for equal concentrations also extends the region of the stationary bifurcation. The interaction strength of passive cross-linkers between antiparallel filaments is $\bar{\beta}' = 0.05$. Similar results are obtained when fixing β and varying β' (not shown).

(a) Motors and treadmilling		
$\beta = 0.05$	$v^* \approx 0.72$	$\alpha_c^* \approx 0.23$
$\beta = 0.10$	$v^* \approx 1.27$	$\alpha_c^* \approx 0.23$
$\beta = 0.20$	$v^* \approx 2.46$	$\alpha_c^* \approx 0.23$

(b) Treadmilling and passive cross-linkers		
$\beta' = 0.05$	$v^* \approx 0.25$	$\alpha_c'^* \approx 0.23$
$\beta' = 0.10$	$v^* \approx 0.27$	$\alpha_c'^* \approx 0.23$
$\beta' = 0.20$	$v^* \approx 0.36$	$\alpha_c'^* \approx 0.23$

(c) Treadmilling, motors and passive cross-linkers		
$\beta = 0.05, \beta' = 0.05$	$v^* \approx 0.9$	$\hat{\alpha}_c^* \approx 0.23$
$\beta = 0.10, \beta' = 0.05$	$v^* \approx 1.5$	$\hat{\alpha}_c^* \approx 0.23$
$\beta = 0.20, \beta' = 0.05$	$v^* \approx 2.74$	$\hat{\alpha}_c^* \approx 0.23$

Table A.1: Varying the interaction strength between antiparallel filaments shifts the treadmilling speed of the intersection v^* but not the critical α_c^*. This is true for the action (a) of motors alone, (b) passive cross-linkers in the absence of motors or (c) for both motors and cross-linkers acting at the same time.

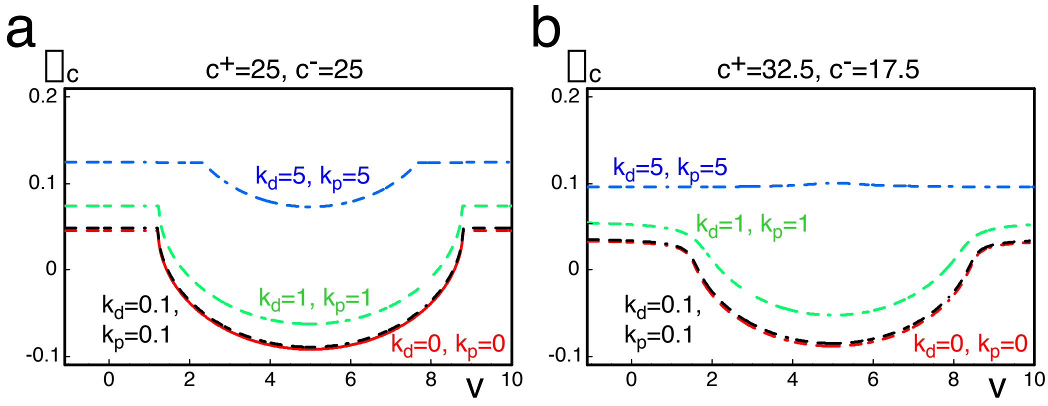

Figure A.4: Dependence of the stability of the homogenous state on the polymerization and depolymerization rates. Graphs show $\alpha_c(v)$ for different values of k_p and k_d and (a) equal concentrations $c_0^+ = 25$, $c_0^- = 25$ as well as (b) for unequal concentrations $c_0^+ = 32.5$, $c_0^- = 17.5$. Increasing the rates stabilizes the homogenous state. Parameters are $\beta = 0.1$, $L = 5$.

the value of α^* remains constant, when β is varied, v^* increases with increasing β, see table A.1. Equivalent results are found when analyzing the stability of a homogenous bundle in the presence of passive cross-linkers, but in the absence of molecular motors or in the presence of both motors and passive cross-linkers. Calculating the point (v^*, α^*) analytically, which will help to determine whether it is physically meaningful or just an artifact of the mean field description is still an open challenge.

A.1.2 Polymerization of Entire Filaments

The linear stability analysis of a system in the presence of an explicit dynamics for protein subunits as presented in section 3.2.4 reveals that the stability of the homogenous state also depends on the polymerization and depolymerization rates of the filaments, Fig. A.4. Higher turnover rates stabilize the homogenous state and destroy (for equal concentrations of plus- and minus-filaments) the stationary bifurcation in the “valley”.

A.2 Minimal Model: Interaction Integrals

The transformation of the dynamic equations (3.44) and (3.45) into their representation in Fourier space is straightforward for the diffusion and treadmilling term. The overlap integrals require more care. Here we discuss the approximation of the integral reflecting the interaction between antiparallel filaments via molecular motors (cf. Eq. (3.40)):

$$\begin{array}{rcl}
 & \beta\partial_x \int_{-l}^{l} \mathrm{d}\xi\, c^-(x+\xi)c^+(x) & \\
= & \beta\partial_x \int_{-l}^{l} \mathrm{d}\xi\, \sum_k c_k^- e^{ikx} e^{ik\xi} \sum_k c_k^+ e^{ikx} & \text{keeping only linear terms} \\
\rightsquigarrow & \beta\partial_x \int_{-l}^{l} \mathrm{d}\xi\, \sum_k c_0^- c_k^+ e^{ikx} + \sum_k c_0^+ c_k^- e^{ikx} e^{ik\xi} & \text{exchanging derivative and integral} \\
\rightsquigarrow & \beta \int_{-l}^{l} \mathrm{d}\xi\, c_0^- c_k^+ ik + c_0^+ c_k^- ik\, e^{ik\xi} & \text{using } \displaystyle\int_{-l}^{l} \mathrm{d}\xi e^{ik\xi} = \frac{1}{ik}\left[e^{ik\xi}\right]_{-l}^{l} \\
= & 2i\beta\left(c_0^- kl c_k^+ + c_0^+ \sin(kl) c_k^-\right) & \qquad (\mathrm{A.1})
\end{array}$$

The α-integral is evaluated analogously.

For the action of passive, end-tracking crosslinkers the α'-integral is identical to the α-integral. The β'-integral leads to a different expression:

$$\begin{array}{rcl}
 & \beta'\partial_x c^+(x) \int_0^l c^-(x-\xi)\mathrm{d}\xi & \\
= & \beta'\partial_x \sum_{k=-\infty}^{\infty} c_k^+ e^{ikx} \int_0^l \sum_{k=-\infty}^{\infty} c_k^- e^{ikx} e^{-ik\xi}\mathrm{d}\xi & \text{linear terms} \\
= & \beta'\partial_x (c_0^+ \int_0^l \sum_{k=-\infty}^{\infty} c_k^- e^{ikx} e^{-ik\xi}\mathrm{d}\xi + \sum_{k=-\infty}^{\infty} c_k^+ e^{ikx} \int_0^l c_0^- \mathrm{d}\xi) & \text{derivative} \\
= & \beta' (c_0^+ \int_0^l \sum_{k=-\infty}^{\infty} c_k^- ik e^{ikx} e^{-ik\xi}\mathrm{d}\xi + \sum_{k=-\infty}^{\infty} c_k^+ ik e^{ikx} \int_0^l c_0^- \mathrm{d}\xi) & \text{integrals} \\
= & \beta' (-c_0^+ \sum_{k=-\infty}^{\infty} c_k^- e^{ikx} (e^{-ikl}-1) + \sum_{k=-\infty}^{\infty} c_k^+ ik e^{ikx} l c_0^-) & \text{one mode} \\
\rightsquigarrow & \partial_t c_k^+ = \beta' ikl c_0^- c_k^+ - \beta' c_0^+ (e^{-ikl}-1) c_k^- & \qquad (\mathrm{A.2})
\end{array}$$

A.3 Continuum Limit of the Minimal Model

On length scales large compared to the length of an individual filament, the dynamics of active filament bundles can be captured by a continuum description in the filament density c and the local polarization p, cf. chapter 5. Here we calculate a coarse grained version of the more microscopic minimal model presented in chapter 3. By comparing the coefficients in the resulting expressions we show that already the pairwise interactions captured by the minimal model give rise to almost all terms considered in the symmetry based generic description.

We define

$$c(x) := c^+(x) + c^-(x) \qquad (\mathrm{A.3})$$

$$p(x) := c^+(x) - c^-(x) \qquad (\mathrm{A.4})$$

and expand

$$c^\pm(x \pm \xi) = c^\pm(x) \pm c^{\pm\prime}(x)\xi + \frac{1}{2}c^{\pm\prime\prime}(x)\xi^2 \pm \frac{1}{6}c^{\pm\prime\prime\prime}(x)\xi^3 + \dots \qquad (\mathrm{A.5})$$

in order to approximate the overlap integrals used in the minimal model (cf. chapter 3, Eqs. (3.39), (3.40), (3.58), (3.60)) as follows:

$$
\begin{aligned}
\alpha,\alpha' : \quad & c^+(x)\int_0^l (c^+(x+\xi)-c^+(x-\xi))\mathrm{d}\xi \\
\simeq\ & c^+(x)(l^2\partial_x c^+(x)+\frac{l^4}{12}\partial_x^3 c^+(x)) && \text{(A.6)} \\
\beta : \quad & c^+(x)\int_{-l}^l c^-(x+\xi)\mathrm{d}\xi \\
\simeq\ & c^+(x)(2lc^-(x)+\frac{l^3}{3}\partial_x^2 c^-(x)) && \text{(A.7)} \\
\beta' : \quad & c^+(x)\int_0^l c^-(x-\xi)\mathrm{d}\xi \\
\simeq\ & c^+(x)(lc^-(x)-\frac{l^2}{2}\partial_x c^-(x)+\frac{l^3}{6}\partial_x^2 c^-(x)-\frac{l^4}{24}\partial_x^3 c^-(x)) \quad . && \text{(A.8)}
\end{aligned}
$$

Inserting these expressions into the dynamic equations of the full minimal model (3.62),(3.63)), we obtain

$$
\begin{aligned}
\partial_t c &= \partial_t(c^+ + c^-) \\
&\simeq \partial_x^2 c - v\partial_x p - (\alpha+\alpha')\partial_x\left[\frac{l^2}{2}(c\partial_x c + p\partial_x p)+\frac{l^4}{24}(c\partial_x^3 c + p\partial_x^3 p)\right] && \text{(A.9)} \\
&\quad +\beta\partial_x\left[\frac{l^3}{6}(p\partial_x^2 c - c\partial_x^2 p)\right] \\
&\quad +\beta'\partial_x\left[-\frac{l^2}{4}(c\partial_x c - p\partial_x p)+\frac{l^3}{12}(p\partial_x^2 c - c\partial_x^2 p)-\frac{l^4}{48}(c\partial_x^3 c - p\partial_x^3 p)\right] \\
\partial_t p &= \partial_t(c^+ - c^-) \\
&\simeq \partial_x^2 p - v\partial_x c - (\alpha+\alpha')\partial_x\left[\frac{l^2}{2}(p\partial_x c + c\partial_x p)+\frac{l^4}{24}(p\partial_x^3 c + c\partial_x^3 p)\right] && \text{(A.10)} \\
&\quad +\beta\partial_x\left[l(c^2-p^2)+\frac{l^3}{6}(c\partial_x^2 c - p\partial_x^2 p)\right] \\
&\quad +\beta'\partial_x\left[\frac{l}{2}(c^2-p^2)-\frac{l^2}{4}(c\partial_x p - p\partial_x c)+\frac{l^3}{12}(c\partial_x^2 c - p\partial_x^2 p)-\frac{l^4}{48}(c\partial_x^3 p - p\partial_x^3 c)\right] \quad ,
\end{aligned}
$$

where we have used the identities

$$
\begin{aligned}
c^+c^- &= \frac{1}{4}(c^2-p^2) && \text{(A.11)} \\
c^+\partial_x c^- - c^-\partial_x c^+ &= \frac{1}{2}(p\partial_x c - c\partial_x p) && \text{(A.12)} \\
c^+\partial_x c^+ - c^-\partial_x c^- &= \frac{1}{2}(p\partial_x c + c\partial_x p) && \text{(A.13)} \\
c^+\partial_x c^+ + c^-\partial_x c^- &= \frac{1}{2}(c\partial_x c + p\partial_x p) && \text{(A.14)} \\
c^+\partial_x c^- + c^-\partial_x c^+ &= \frac{1}{2}(c\partial_x c - p\partial_x p) \quad . && \text{(A.15)}
\end{aligned}
$$

Term in current j	Factor in coarse grained microscopic model, Eq. (A.9)	Coefficient in continuum description
$\partial_x c$	1	D
$\partial_x^2 p$		$-A_1$
$\partial_x^3 c$		$-A_2$
$c\partial_x c$	$-l^2(2(\alpha+\alpha')+\beta')/4$	$-2B_1$
$p\partial_x p$	$-l^2(2(\alpha+\alpha')-\beta')/4$	$-2B_2$
$(\partial_x c)\partial_x p$		$-2(E_1+E_2)$
$c\partial_x^2 p$	$-l^3(2\beta+\beta')/12$	$-E_1$
$p\partial_x^2 c$	$l^3(2\beta+\beta')/12$	$-E_2$
$(\partial_x c)\partial_x^2 c$		$-(F_1+2F_3)$
$c\partial_x^3 c$	$-l^4(2\alpha+\beta')/48$	$-F_1$
$(\partial_x p)\partial_x^2 p$		$-(F_2+2F_4)$
$p\partial_x^3 p$	$-l^4(2\alpha-\beta')/48$	$-F_2$
p	$-v$	$-v$

Table A.2: Relation of the coefficients used in the density currents from the generic continuum description presented in chapter 5 and the coarse grained minimal model given by Eqs. (A.9) and (A.10).

This coarse grained continuum limit of the minimal model can be compared with the generic continuum description, cf. chapter 5. In that description the respective currents read (cf. Eqs. (5.14), (5.15), (5.16))

$$\begin{aligned} j &= \eta^{-1}\partial_x\sigma \\ &= D\partial_x c - A_1\partial_x^2 p - A_2\partial_x^3 c - 2B_1 c\partial_x c - 2B_2 p\partial_x p - E_1\left((\partial_x c)\partial_x p + c\partial_x^2 p\right) \\ &\quad -E_2\left((\partial_x c)\partial_x p + p\partial_x^2 c\right) - F_1\left((\partial_x c)\partial_x^2 c + c\partial_x^3 c\right) - F_2\left((\partial_x p)\partial_x^2 p + p\partial_x^3 p\right) \\ &\quad -2F_3(\partial_x c)\partial_x^2 c - 2F_4(\partial_x p)\partial_x^2 p \end{aligned} \tag{A.16}$$

and

$$\begin{aligned} j_p &= \epsilon(c^2-p^2) + D\partial_x c - A_1\partial_x^2 c - A_2\partial_x^3 p - \bar{B}_1 c\partial_x p - \bar{B}_2 p\partial_x c \\ &\quad -\bar{E}_1 c\partial_x^2 c - \bar{E}_2 p\partial_x^2 p - E_1(\partial_x c)^2 - \tilde{E}_2(\partial_x p)^2 \\ &\quad -\bar{F}_1 c\partial_x^3 p - \bar{F}_2 p\partial_x^3 c - \bar{F}_3(\partial_x c)\partial_x^2 p - \bar{F}_4(\partial_x p)\partial_x^2 c \quad . \end{aligned} \tag{A.17}$$

In addition to these currents we also have to take into account the treadmilling currents, Eqs. (5.45) and (5.46):

$$j_v = -vp \tag{A.18}$$

$$j_{p,v} = -vc \tag{A.19}$$

The tables A.2 and A.3 summarize the resulting relations between the coefficients in the coarse grained model and the continuum description.

Term in current j_p	Factor in coarse grained microscopic model, Eq. (A.10)	Coefficient in continuum description
$c^2 - p^2$	$l(2\beta + \beta')/2$	$-\epsilon$
$\partial_x p$	1	D
$\partial_x^2 c$		$-A_1$
$\partial_x^3 p$		$-A_2$
$c\partial_x p$	$-l^2(2\alpha + \beta')/4$	$-\bar{B}_1$
$p\partial_x c$	$-l^2(2\alpha - \beta')/4$	$-\bar{B}_2$
$c\partial_x^2 c$	$l^3(2\beta + \beta')/12$	$-\bar{E}_1$
$p\partial_x^2 p$	-$l^3(2\beta + \beta')/12$	$-\bar{E}_2$
$(\partial_x c)^2$		$-\tilde{E}_1$
$(\partial_x p)^2$		$-\tilde{E}_2$
$c\partial_x^3 p$	$-l^4(2\alpha - \beta')/48$	$-\bar{F}_1$
$p\partial_x^3 c$	$-l^4(2\alpha + \beta')/48$	$-\bar{F}_2$
$(\partial_x c)\partial_x^2 p$		$-\bar{F}_3$
$(\partial_x p)\partial_x^2 c$		$-\bar{F}_4$
c	$-v$	$-v$

Table A.3: Relation of the coefficients used in the polarization currents from the generic continuum description presented in chapter 5 and the coarse grained minimal model given by Eqs. (A.9) and (A.10).

We thus find the following additional relations between the expansion coefficients when derived from the coarse grained minimal model:

$$\bar{E}_1 = -\bar{E}_2 \tag{A.20}$$

$$\tilde{E}_1 = -\tilde{E}_2 \tag{A.21}$$

$$\bar{F}_3 = -\frac{1}{2}\bar{F}_1 \tag{A.22}$$

$$\bar{F}_4 = -\frac{1}{2}\bar{F}_2 \tag{A.23}$$

In the absence of passive cross-linkers ($\alpha' = 0, \beta' = 0$), additional relations exist:

$$\bar{B}_1 = \bar{B}_2 \tag{A.24}$$

$$\bar{F}_1 = \bar{F}_2 \; (= -2\bar{F}_3 = -2\bar{F}_4) \tag{A.25}$$

We use $j = \eta^{-1}\partial_x \sigma$ to write the tension for the coarse grained microscopic description:

$$\begin{aligned} \sigma \;=\; & -c + \frac{l^2}{8}\left[(2(\alpha+\alpha')+\beta')c^2 + (2(\alpha+\alpha')-\beta')p^2\right] \\ & + \frac{l^3}{12}(2\beta+\beta')(c\partial_x p - p\partial_x c) \\ & - \frac{l^4}{48}\left[(2(\alpha+\alpha')+\beta')c\partial_x^2 c + (2(\alpha+\alpha')-\beta')p\partial_x^2 p\right] \\ & + \frac{l^4}{96}\left[(2(\alpha+\alpha')+\beta')(\partial_x c)^2 + (2(\alpha+\alpha')-\beta')(\partial_x p)^2\right] \end{aligned} \tag{A.26}$$

Here the last term $\propto l^4/96$ has to be added so that Eqs. (A.22) and (A.23) are fulfilled. This expression can be directly compared with Eq. (5.15) which yields the relations listed in tables A.2 and A.3.

B Numerical Methods

B.1 Numerical Integration of the Mean Field Description

We numerically solve the equations (3.44) and (3.45) that describe the evolution of the filament densities $c^{\pm}$ in the minimal model. In this appendix we present a detailed description of the methods used to this end. For the integration in time we employ the forward Euler scheme (Press et al., 2002) in which the partial derivative of a function f is approximated by

$$\partial_t f(t) = \frac{f(t+\Delta t) - f(t)}{\Delta t} \quad . \tag{B.1}$$

This simple scheme is sufficient for the temporal integration of our system. The spatial integration of the partial integro-differential equations requires more care. We now describe the discretization scheme explicitely.

The mean field descriptions presented in chapter 3 capture linear structures of length L. We discretize space and introduce a one dimensional lattice with lattice constant Δx. The concentrations of filaments and monomers are sampled on the sites. We define the concentrations $c_i^{\pm} = c^{\pm}(i\Delta x, t)$, with $i = 0, 1, \ldots N_L = L/\Delta x$ and the monomer concentrations accordingly. Quantities with a dagger † denote the distributions at time $t + \Delta t$, i.e. $c_i^{\pm,\dagger} = c^{\pm}(i\Delta x, t + \Delta t)$. Currents in these quantities exist between sites, cf. Fig. B.1.

In the bulk, i.e. for $i \in [1; N_L - 1]$ the discretization of the various currents is then given by the following expressions:

Diffusion The diffusion current between two sites depends on the difference of the concentrations on the respective sites:

$$j_i^{(D)\pm} = \frac{D}{\Delta x}\left(c_{i-1}^{\pm} - c_i^{\pm}\right) \tag{B.2}$$

Motors between parallel filaments (Eq. (3.39)) The current is given by

$$j_i^{(\alpha)\pm\pm} = \alpha\left(c_{i-1}^{\pm} S_i^{\pm} - c_i^{\pm} S_{i-\ell+1}^{\pm}\right) \tag{B.3}$$

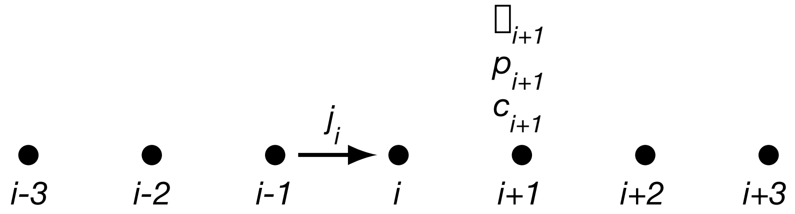

Figure B.1: Discretization scheme for mean field and continuum description. The densities, order parameters or stresses represented by c, p, σ respectively, are defined on the sites (here exemplified on site $i+1$). The currents are defined between two sites. They point to and have the same index as the site with the larger index, shown for j_i.

where

$$\ell = \left\lfloor \frac{l}{\Delta x} \right\rfloor \tag{B.4}$$

is the length of one filaments in units of Δx. The symbol $\lfloor \cdot \rfloor$ denotes the floor, i.e. the next lower integer of the argument. We only consider cases when ℓ is an integer, odd number, as an even number would leave the center of the filaments between two sites. Furthermore we define S_i, the number of filaments on sites i to $i+\ell-2$:

$$S_i^{\pm} = \sum_{j=i}^{i+\ell-2} c_j^{\pm} \Delta x \tag{B.5}$$

Here the range of $j = i \cdots + \ell - 2$ represents interval in which filaments located at site i can interact with other filaments located to their right.

Motors between antiparallel filaments (Eq. (3.40)) The direction of the current is different for either filament orientation:

$$\begin{aligned} j_i^{(\beta)+-} &= -\beta c_i^{+} \left(S_{i-\ell+1}^{-} + c_i^{-} + S_{i+1}^{-} \right) & \text{(B.6)} \\ j_i^{(\beta)-+} &= \beta c_{i-1}^{-} \left(S_{i-\ell}^{+} + c_{i-1}^{+} + S_i^{+} \right) & \text{(B.7)} \end{aligned}$$

Treadmilling (Eq. (3.43)) The treadmilling current depends on the orientation of the filaments

$$\begin{aligned} j_i^{(v)+} &= v c_{i-1}^{+} & \text{(B.8)} \\ j_i^{(v)-} &= -v c_i^{-} & \text{(B.9)} \end{aligned}$$

Passive cross-linkers between parallel filaments (Eqs. (3.58) and (3.59)) The current is identical to that for motors between parallel filaments (Eq. (B.3)) for $\alpha' = \alpha$:

$$j_i^{(\alpha')\pm\pm} = \alpha' \left(c_{i-1}^{\pm} S_i^{\pm} - c_i^{\pm} S_{i-\ell+1}^{\pm} \right) \tag{B.10}$$

Passive cross-linkers between antiparallel filaments (Eqs. (3.60) and (3.61)) The current is given by

$$\begin{aligned} j_i^{(\beta')+-} &= -\beta' c_i^{+} S_{i-\ell+1}^{-} & \text{(B.11)} \\ j_i^{(\beta')-+} &= \beta' c_{i-1}^{-} S_i^{+} & \text{(B.12)} \end{aligned}$$

All these partial currents are added up to give the effective filament current

$$j_i^{\pm} = \; = j_i^{(D)\pm} + j_i^{(\alpha)\pm\pm} + j_i^{(\beta)\pm\mp} + j_i^{(v)\pm} + j_i^{(\alpha')\pm\pm} + j_i^{(\beta')\pm\mp} \quad . \tag{B.13}$$

The new concentrations are then given by

$$\begin{aligned} c_i^{\dagger\pm} &= c_i^{\pm} + \frac{\Delta t}{\Delta x} \left[j_i^{\pm} - j_{i+1}^{\pm} \right] & \text{(B.14)} \\ &= c_i^{\pm} + \frac{\Delta t}{\Delta x} \Big[\left(j_i^{(D)\pm} - j_{i+1}^{(D)\pm} \right) + \left(j_i^{(\alpha)\pm\pm} - j_{i+1}^{(\alpha)\pm\pm} \right) \\ &\quad + \left(j_i^{(\beta)\pm\mp} - j_{i+1}^{(\beta)\pm\mp} \right) + \left(j_i^{(v)\pm} - j_{i+1}^{(v)\pm} \right) \\ &\quad + \left(j_i^{(\alpha')\pm\pm} - j_{i+1}^{(\alpha')\pm\pm} \right) + \left(j_i^{(\beta')\pm\mp} - j_{i+1}^{(\beta')\pm\mp} \right) \Big] \end{aligned}$$

B.2 Numerical Integration of the Continuum Theory

The integration of the continuum theory is not trivial and features a few caveats. Again we introduce a lattice as in section B.1 on which the concentration c and the components of the order parameter p_x, q_{xx}, q_{xy} as well as the tension $\boldsymbol{\sigma}$ are defined. Denoting $p = p_x$ in one dimension the discretization of σ defined in Eq. (5.15) is given by

$$\begin{aligned}\eta^{-1}\sigma_i &= -Dc_i + A_1\frac{p_{i+1}-p_{i-1}}{2\Delta x} + A_2\frac{c_{i+1}+c_{i-1}-2c_i}{(\Delta x)^2} \\ &\quad +B_1c_i^2 + B_2p_i^2 + E_1c_i\frac{p_{i+1}-p_{i-1}}{2\Delta x} + E_2p_i\frac{c_{i+1}-c_{i-1}}{2\Delta x} \\ &\quad +F_1c_i\frac{c_{i+1}+c_{i-1}-2c_i}{(\Delta x)^2} + F_2p_i\frac{p_{i+1}+p_{i-1}-2p_i}{(\Delta x)^2} \\ &\quad +F_3\left(\frac{c_{i+1}-c_{i-1}}{2\Delta x}\right)^2 + F_4\left(\frac{p_{i+1}-p_{i-1}}{2\Delta x}\right)^2 \quad .\end{aligned} \tag{B.15}$$

Note that here we have used the symmetric first order derivative

$$\partial_x f(x) = \frac{f(x+\Delta x) - f(x-\Delta x)}{2\Delta x} \tag{B.16}$$

for c and p to assure that σ is localized on the sites. An asymmetric derivative would lead to contributions to σ that are not located on the lattice sites. The change in the concentration for the bulk terms $i \in [1; N_L - 1]$ is then given by

$$c_i^\dagger = c_i + \Delta t\frac{\sigma_{i+1}+\sigma_{i-1}-2\sigma_i}{(\Delta x)^2} \tag{B.17}$$

for $\eta = 1$. The change in the polarization p is discretized analogously. The filament current between sites $i-1$ and i is given by

$$j_i = -\frac{\sigma_i - \sigma_{i-1}}{\Delta x} \quad . \tag{B.18}$$

B.2.1 Description with Nematic Order

The discretization of the projected tension (Eq. (5.53)) is given by

$$\begin{aligned}\eta^{-1}\sigma_{xx,i} &= A_1c_i + A_2c_i^2 + A_3c_i\frac{c_{i+1}+c_{i-1}-2c_i}{(\Delta x)^2} \\ &\quad +A_4\left(\frac{c_{i+1}-c_{i-1}}{2\Delta x}\right)^2 + A_5q_{xx,i}\end{aligned} \tag{B.19}$$

Here again we have to use the symmetric first order derivative in order to assure that σ is located on the sites. And the change in concentration c is then again given by Eq. (B.17).

For the changes in the components of the nematic order parameter, Eqs. (5.54) and (5.55), we obtain analogously:

$$\begin{aligned}\omega_{xx,i} &= -B_1q_{xx,i} + B_2\frac{q_{xx,i+1}+q_{xx,i-1}-2q_{xx,i}}{(\Delta x)^2} + B_3\frac{q^{(2)}_{xx,i+1}+q^{(2)}_{xx,i-1}-2q^{(2)}_{xx,i}}{(\Delta x)^2} \\ &\quad +B_4\frac{c_{i+1}+c_{i-1}-2c_i}{(\Delta x)^2} + B_5(q_{xx,i}^2 + q_{xy,i}^2)q_{xx,i}\end{aligned} \tag{B.20}$$

$$\begin{aligned}\omega_{xy} &= -B_1q_{xy,i} + B_2\frac{q_{xy,i+1}+q_{xy,i-1}-2q_{xy,i}}{(\Delta x)^2} + B_3\frac{q^{(2)}_{xy,i+1}+q^{(2)}_{xy,i-1}-2q^{(2)}_{xy,i}}{(\Delta x)^2} \\ &\quad +B_4\frac{c_{i+1}+c_{i-1}-2c_i}{(\Delta x)^2} + B_5(q_{xx,i}^2 + q_{xy,i}^2)q_{xy,i}\end{aligned} \tag{B.21}$$

where $q^{(2)}_{xx,i}$ is the second order derivative at site i:

$$q^{(2)}_{xx,i} = \frac{q_{xx,i+1} + q_{xx,i-1} - 2q_{xx,i}}{(\Delta x)^2} \tag{B.22}$$

and for q_{xy} analogously. The update in the order parameter is then given by

$$q^{\dagger}_{xx,i} = q_{xx,i} + \omega_{xx,i}\Delta t \tag{B.23}$$

and q_{xy} analogously.

B.2.2 Boundary Conditions

The update rules for the sites in the bulk $i \in [1; N_L - 1]$ have been given above. How to update the sites 0 and N_L depends on the boundary conditions, which can have a huge influence on the observed dynamics and asymptotic states.

Periodic Boundary Conditions

Periodic boundary conditions are readily implemented by using

$$c^{\dagger}_0 = c_0 + \Delta t \frac{\sigma_2 + \sigma_{N_L} - 2\sigma_1}{(\Delta x)^2}, \qquad c^{\dagger}_{N_L} = c_{N_L} + \Delta t \frac{\sigma_0 + \sigma_{N_L-1} - 2\sigma_{N_L}}{(\Delta x)^2}, \tag{B.24}$$

and calculating $\omega_{xx,1}$, $\omega_{xy,1}$, ω_{xx,N_L} and ω_{xy,N_L} accordingly.

No Flux Boundary Conditions

No flux boundary conditions can be more complicated to implement correctly. Their numerical application is somewhat subtle. We illustrate the approach employed here, using the boundary conditions presented in Eqs. (5.77)-(5.81):

$$\begin{aligned} \boldsymbol{j} &= 0 && \text{(B.25)}\\ \boldsymbol{q} &= 0 && \text{(B.26)}\\ \partial_x c &= 0 && \text{(B.27)}\\ \partial_x q_{xx} &= 0 && \text{(B.28)}\\ \partial_x q_{xy} &= 0 && \text{(B.29)} \end{aligned}$$

at both $x = 0$ and $x = L$.

Condition (B.25) is discretized by setting $j_0 = 0$ and $j_{N_L+1} = 0$. This can be realized by introducing virtual sites $i = -1$ and $i = N_L + 1$ and setting $\sigma_{-1} = \sigma_0$ and $\sigma_{N_L+1} = \sigma_{N_L}$ at each time step before updating the concentration. The across the boundaries currents as given by Eq. (B.18) are then zero.

Condition (B.26) is trivially implemented by setting $q_{xx,0} = 0$, $q_{xy,0} = 0$, $q_{xx,N_L} = 0$, $q_{xy,N_L} = 0$.

The remaining three conditions (B.27)-(B.29) are again captured by introducing quantities on the virtual sites. For the concentration choosing $c_{-1} = c_0$ and $c_{N_L+1} = c_{N_L}$ at each time step prior to calculating σ and ω does the trick. We treat q_{xx} and q_{xy} in the same way.

These ad-hoc choices of virtual values may seem problematic as they need not be self consistent, i.e. the choices for c and $\mathbf{q}$ on the virtual sites determine the stresses on these sites. The filament current determined by the stresses could thus be different from zero.

While this is the case for many possible choices of boundary conditions, the boundary conditions discussed above can always be made self consistent as the calculation of σ_i requires values from sites $i-1, i, i+1$, which e.g. for σ_{-1} means it depends on the virtual value of e.g. c_{i-2} that is not restricted otherwise and can always be chosen so, that all boundary conditions are fulfilled.

C Supplementary Calculations to the Spindle

C.1 Forces between Asters

The general idea of hoe to determine the force contribution of motor dimers in the spindle has been outlined in section 4.2.4. Here we complete the list of explicitly calculated instructive examples and show in detail how to calculate the force between two half and full asters. This section concludes with a concise overview of the force contributions of all kinds of motors bound at all positions to two asters in section C.1.5. Explicit calculations for all possible cases are given in section C.5 at the end of this chapter.

C.1.1 Motors Bound to the Bulk

A motor dimer can bind to parallel microtubules of either minus- or plus-orientation, regions (a) and (c) of Fig. 4.5 respectively. Because it is the easiest (as all MTs involved are plus-microtubules), we discuss region (c) first.

Region (c): parallel plus-microtubules. Here the velocity of the motor bound to the first MT (motor 1, black disk) and the second motor (motor 2, white disk) individually are given by Eq. (4.7):

$$\begin{aligned} \dot{x}_1 &= v_1 + \dot{L} \qquad (C.1) \\ \dot{x}_2 &= v_2 - \dot{L} \qquad (C.2) \end{aligned}$$

where the different signs in front of $\dot{L}$ are due to the opposing directions of movement of the two asters. Note that the subscripts $1, 2$ refer to the aster the motor is bound to.

The two motors in the dimer are referred to as a, b, so that v_a is the load-free velocity of motor head a, and v_1 is the speed of the motor bound to MT 1, which could in principle be either motor a or b. Here we assume for simplicity and without loss of generality that motor a is bound to MT 1 and and b to 2. In terms of the force-velocity curves (Eq. (3.3)):

$$\begin{aligned} v_1 &= v_a + \chi_a f_1 \qquad (C.3) \\ v_2 &= v_b + \chi_b f_2 \quad , \qquad (C.4) \end{aligned}$$

where f_1, f_2 are the forces acting on motors bound to MT 1 and 2 respectively, measured with respect to the microtubule orientation. As the motors form a dimer we know that

$$\dot{x}_1 = \dot{x}_2 \Rightarrow v_1 + \dot{L} = v_2 - \dot{L} \quad . \qquad (C.5)$$

We thus obtain

$$v_a + \chi_a f_1 + \dot{L} = v_b + \chi_b f_2 - \dot{L} \quad . \qquad (C.6)$$

Furthermore the dimer implies

$$f_1 = -f_2 \quad . \qquad (C.7)$$

Complex	p-p	m-m	p-m	m-p
Fig. 4.5c				
Velocities	$v_a > 0, v_b > 0$	$v_a < 0, v_b < 0$	$v_a > 0, v_b < 0$	$v_a < 0, v_b > 0$
Forces	$f_1 = \dfrac{v_b - v_a}{\chi_a + \chi_b}$	$f_1 = \dfrac{v_b - v_a}{\chi_a + \chi_b}$	$f_1 = \dfrac{v_b - v_a}{\chi_a + \chi_b} < 0$	$f_1 = \dfrac{v_b - v_a}{\chi_a + \chi_b} > 0$
	$f = f_1$	$f = f_1$	$f = f_1 < 0$	$f = f_1 > 0$
Effect	depends	depends	contractile	expansive

Table C.1: Force contributions of different individual motor dimers bound to the bulk of two MTs right of both asters (region (c), cf. Fig. 4.5c). The asters are assumed to be stationary ($\dot{L} = 0$).

Hence we can solve Eq. (C.6) to obtain

$$\begin{aligned} f_1 &= \frac{v_b - v_a - 2\dot{L}}{\chi_a + \chi_b} && \text{(C.8)} \\ \dot{x} &= \frac{\chi_a v_b + \chi_b v_a}{\chi_a + \chi_b} + \frac{\chi_b - \chi_a}{\chi_a + \chi_b}\dot{L} && \text{(C.9)} \end{aligned}$$

The force that this single dimer exerts on the two asters in this case is given by

$$f = f_1 = \frac{v_b - v_a - 2\dot{L}}{\chi_a + \chi_b} \quad . \tag{C.10}$$

To further illustrate this result we explicitly calculate the contribution of four types of motor dimers:

- p-p: a homo-dimer of two $\oplus$-end directed motors
- m-m: a homo-dimer of two $\ominus$-end directed motors
- p-m: a hetero-dimer of a $\oplus$-end directed motor bound to MT 1 (from the right aster) and a $\ominus$-end directed motor bound to MT 2 (from the left aster)
- m-p: a hetero-dimer of a $\ominus$-end directed motor bound to MT 1 and a $\oplus$-end directed motor bound to MT 2

Table C.1 summarizes the results for different kinds of motor dimers and stationary asters ($\dot{L} = 0$).

For the calculation above and the expressions presented in table C.1 we assumed that motor a is bound to MT 1, and b to 2. For an ensemble of motors however it is equally likely that b binds to MT 1. Thus when considering an ensemble of many motors, the average force contribution due to a single motor bound to the bulk of both MTs right of both asters is

$$\mathcal{F} = \langle f_1 \rangle = \frac{1}{2}\frac{v_b - v_a - 2\dot{L}}{\chi_a + \chi_b} + \frac{1}{2}\frac{v_a - v_b - 2\dot{L}}{\chi_a + \chi_b} = \frac{-2\dot{L}}{\chi_a + \chi_b} \tag{C.11}$$

where $\langle \cdot \rangle$ denotes the average over all possible binding configurations. On average these motors thus do not contribute to the force acting on the asters, but oppose aster movement, because they lead to forces of opposite sign than the velocity of the asters. In conclusion: an ensemble of motors right of both asters acts essentially like passive cross-linkers. Note that this result holds independent of the type of motor dimer (p-p, m-m, etc.).

Region (a): parallel minus-microtubules. The case of a dimer between two parallel minus-microtubules left of both asters is very similar to the case above. The details of the calculation are given in C.5.1. We obtain for the force that a single dimer exerts on the two asters

$$f = -f_1 = -\frac{v_b - v_a + 2\dot{L}}{\chi_a + \chi_b} \tag{C.12}$$

where the negative sign in front of f_1 is due to the orientation of microtubule 1. As f_1 is measured with respect to the microtubule orientation and f is measured in the laboratory reference frame, the two forces have opposite signs as MT 1 is a minus-microtubule. Table C.13 summarizes the resulting forces for different kinds of motor dimers and stationary asters.

Considering an ensemble of many motors the average force contribution of a single motor is given by

$$\mathcal{F} = -\langle f_1 \rangle = -\frac{1}{2}\frac{v_b - v_a + 2\dot{L}}{\chi_a + \chi_b} - \frac{1}{2}\frac{v_a - v_b + 2\dot{L}}{\chi_a + \chi_b} = \frac{-2\dot{L}}{\chi_a + \chi_b} \quad . \tag{C.13}$$

Not surprisingly the motors on the left of both asters act the same way as the motors right of both asters, i.e. an ensemble of motors left of both asters acts essentially like passive cross-linkers.

Region (b): Between the Asters: Antiparallel Microtubules Here we consider motor dimers that bind to plus-MTs originating from the left aster and to minus-MTs from the right aster. Due to the different orientations of the two microtubules involved, the calculation is slightly different than above. The equations for the velocity of the dimer read

$$\dot{x}_1 = -v_1 + \dot{L} \tag{C.14}$$

$$\dot{x}_2 = v_2 - \dot{L} \quad . \tag{C.15}$$

Note that v_1 and v_2 enter with opposite signs due to the orientation of their respective microtubules. The next important difference is that

$$f_1 = -(-f_2) \tag{C.16}$$

where the first negative sign is due to the opposite orientation of both MTs (more precisely because MT 1 is a minus-MT) and the second because the two heads form a dimer (*actio=reactio*). This yields

$$f_1 = \frac{-v_a - v_b + 2\dot{L}}{\chi_a + \chi_b} \tag{C.17}$$

$$\dot{x} = \frac{\chi_a v_b - \chi_b v_a}{\chi_a + \chi_b} + \frac{\chi_b - \chi_a}{\chi_a + \chi_b}\dot{L} \tag{C.18}$$

and the force that the dimer exerts on the two asters in this case is given by

$$f = -f_1 = \frac{v_a + v_b - 2\dot{L}}{\chi_a + \chi_b} \tag{C.19}$$

where again the negative sign in front of f_1 is due to the orientation of microtubule 1. Table C.14 summarizes the results for different kinds of motor dimers and stationary asters. For an ensemble of motors the average force contribution due to a motor bound to the bulk of both MTs and right of both asters is

$$\mathcal{F} = -\langle f_1 \rangle = -\frac{1}{2}\frac{-v_b - v_a + 2\dot{L}}{\chi_a + \chi_b} - \frac{1}{2}\frac{-v_a - v_b + 2\dot{L}}{\chi_a + \chi_b} = \frac{v_a + v_b - 2\dot{L}}{\chi_a + \chi_b} \quad . \tag{C.20}$$

This average force $\mathcal{F}$ will generally not be proportional to $-\dot{L}$. Thus, an ensemble of motors between both asters may exert an active force on the asters.

C.1.2 Motors at the $\oplus$-Ends

When one motor head of a dimer reaches the end of its MT, it may either detach and the dimer will not exert any force on the asters anymore, or it may stall at the end (at least for a short time) and provide a mechanical link between the two asters. We consider only dimers that remain attached to both MTs when reaching the end, as only they may contribute to the dynamics directly. The motion of the other motor of the dimer is assumed not to be influenced by the stalling of the first. Here we describe the contribution of dimers with one stalled head to the force on the asters.

Region (a): Left of Both Asters: Parallel Minus-Microtubules. The force contribution of a dimer between two parallel minus-microtubules when the dimer is bound to the bulk is given explicitly by Eq. (C.12). Either one of the two motor heads may be bound to an end of a MT originating from either aster, Fig. 4.6a (i) and (ii). Depending on the details of the situation this may change the force contribution. Table C.2 summarizes the results for stationary asters ($\dot{L} = 0$), which clearly reveals the effects binding to ends has on the force contributions. Being attached to an end only affects motors that have the corresponding directionality (e.g. a plus-motor at a $\oplus$-end enters with velocity 0, while the velocity of a minus-motor remains unchanged) the force contribution depends on the type of motor dimer under consideration. The motion of a dimer with two $\ominus$-end directed motors for example is not at all influenced by being attached to a $\oplus$-end, but all other types are, compare the respective columns for end-binding cross-linkers in table C.2 and for bulk-binding cross-linkers in table C.13. Especially the columns showing the results m-p and p-m dimers reveal the structure.

Ensemble averaging yields

$$\mathcal{F} = -\langle f_1 \rangle = -\frac{1}{2}\frac{v_b - v_a + 2\dot{L}}{\chi_a + \chi_b} - \frac{1}{2}\frac{v_a - v_b + 2\dot{L}}{\chi_a + \chi_b} \tag{C.21}$$

where the first term represents motor a bound to MT 1 and the second motor b bound to MT 1. As being attached to an end only affects motors that have the corresponding directionality (e.g. a plus-motor at a $\oplus$-end enters with velocity 0, while the velocity of a minus-motor remains unchanged) it depends on the type of motor dimer under consideration how we have to calculate the average of Eq. (C.21).

As an example, let us consider an ensemble of one type of hetero-dimers (w.o.l.g: $v_a \leq 0 \leq v_b$). As $v_a < 0$ the a motor is not affected by the $\oplus$-end. In case (i) the b motor is only affected when bound to MT 1:

$$\mathcal{F} = -\langle f_1 \rangle = -\frac{1}{2}\frac{v_b - v_a + 2\dot{L}}{\chi_a + \chi_b} - \frac{1}{2}\frac{v_a + 2\dot{L}}{\chi_a + \chi_b} = \frac{1}{2}\frac{-v_b - 4\dot{L}}{\chi_a + \chi_b} \tag{C.22}$$

and in case (ii) it is only affected when bound to MT2:

$$\mathcal{F} = -\langle f_1 \rangle = -\frac{1}{2}\frac{-v_a + 2\dot{L}}{\chi_a + \chi_b} - \frac{1}{2}\frac{v_a - v_b + 2\dot{L}}{\chi_a + \chi_b} = \frac{1}{2}\frac{v_b - 4\dot{L}}{\chi_a + \chi_b} \tag{C.23}$$

Complex	p-p	m-m	p-m	m-p
Fig. 4.6a (i)			$v_a > 0 \rightsquigarrow 0$	$v_a < 0$
Velocities	$v_a = 0, v_b > 0$	$v_a < 0, v_b < 0$	$v_b < 0$	$v_b > 0$
Forces	$f_1 = \dfrac{v_b}{\chi_a + \chi_b} > 0$	$f_1 = \dfrac{v_b - v_a}{\chi_a + \chi_b}$	$f_1 = \dfrac{v_b}{\chi_a + \chi_b} < 0$	$f_1 = \dfrac{v_b - v_a}{\chi_a + \chi_b} > 0$
	$f = -f_1 < 0$	$f = -f_1$	$f = -f_1 > 0$	$f = -f_1 < 0$
Effect	contractile	depends	expansive	contractile
$\mathcal{F} =$	$-\dfrac{1}{2}\dfrac{v_a + v_b}{\chi_a + \chi_b} < 0$	0		
Effect	contractile	passive		
Fig. 4.6a (ii)			$v_a > 0$	$v_a < 0$
Velocities	$v_a > 0, v_b = 0$	$v_a < 0, v_b < 0$	$v_b < 0$	$v_b > 0 \rightsquigarrow 0$
Forces	$f_1 = \dfrac{-v_a}{\chi_a + \chi_b} < 0$	$f_1 = \dfrac{v_b - v_a}{\chi_a + \chi_b}$	$f_1 = \dfrac{v_b - v_a}{\chi_a + \chi_b} < 0$	$f_1 = \dfrac{-v_a}{\chi_a + \chi_b} > 0$
	$f = -f_1 > 0$	$f = -f_1$	$f = -f_1 > 0$	$f = -f_1 < 0$
Effect	expansive	depends	expansive	contractile
$\mathcal{F} =$	$-\dfrac{1}{2}\dfrac{-v_a - v_b}{\chi_a + \chi_b} > 0$	0		
Effect	expansive	passive		

Table C.2: Force contributions of different motor dimers bound to the bulk and one ⊕-end of MTs left of both asters (Fig. 4.6 region a). The asters are assumed to be stationary ($\dot{L} = 0$).

Averaging over both situations (i) and (ii) thus yields

$$\mathcal{F} = \frac{1}{4}\left(\frac{-v_b - 4\dot{L}}{\chi_a + \chi_b} + \frac{v_b - 4\dot{L}}{\chi_a + \chi_b}\right) = \frac{-2\dot{L}}{\chi_a + \chi_b} \quad . \tag{C.24}$$

Thus these hetero-dimers act like passive cross-linkers, i.e. they do on average not contribute to the total force on the asters. This result holds for all types of motor dimers, cf. Eq. (C.21). We can thus conclude: an ensemble of motors left of both asters acts essentially like passive cross-linkers, even when bound to one ⊕-end.

Region (b): Between Both Asters: Antiparallel Microtubules. The force contribution of a dimer between two antiparallel microtubules is given by Eq. (C.17). Either one of the two motors may be bound to an end of a MTs originating from either aster (Fig. 4.6b (i) and (ii)). The force contributions for the four types of motor dimers are summarized in table C.15. Averaging over an ensemble of motors yields

$$\mathcal{F} = -\langle f_1 \rangle = -\frac{1}{2}\frac{-v_a - v_b + 2\dot{L}}{\chi_a + \chi_b} - \frac{1}{2}\frac{-v_b - v_a + 2\dot{L}}{\chi_a + \chi_b} \tag{C.25}$$

where the first term represents motor a bound to MT 1 and the second motor b bound to MT 1.

For a hetero-dimer as described above, we obtain (see section C.5.2 for details)

$$\mathcal{F} = \frac{1}{4}\left(\frac{2v_a + v_b - 4\dot{L}}{\chi_a + \chi_b} + \frac{2v_a + v_b - 4\dot{L}}{\chi_a + \chi_b}\right) = \frac{v_a + \frac{1}{2}v_b - 2\dot{L}}{\chi_a + \chi_b} \quad . \tag{C.26}$$

This result holds qualitatively for all types of motor dimers. We can thus conclude: an ensemble of motors between both asters exerts a force on both asters, even when bound to one ⊕-end.

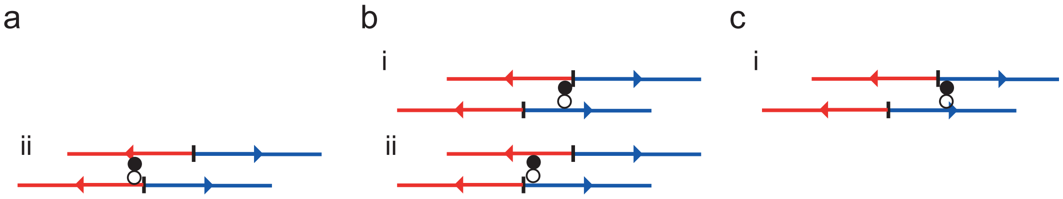

Figure C.1: Motor dimers linking the ⊖-end of a microtubule from one aster to the bulk of a microtubule from the the second. The motor heads bind to (a) the bulk of a minus-microtubule (red) and a minus end when left of both centrosomes, (b) a MT of either orientation and a minus end between the centrosomes or (c) a plus-MT (blue) and a minus end when right of them. Other combinations are not possible due to the geometry of the system. In each of these cases we distinguish the motor bound to an end of a MT from the right aster (i) or from the left aster (ii) as the force contribution is different in each case).

Region (c): Right of Both Asters: Parallel Plus-Microtubules. This case is qualitatively equal to region (a) due to symmetry. Motors bound to the bulk and ⊕-end in this region effectively act like passive cross-linkers. The results and details of the calculation are given in C.5.2.

C.1.3 Motors at the ⊖-Ends

The situation when one motor head reaches a ⊖-end of a microtubule is similar to the case when it reaches a ⊕-end, described in the previous section. Again the motor head may detach and not contribute to the dynamics of the asters anymore or it may stay attached and then work like a passive cross-link. The number of possible situations are reduced due to geometry as shown in Fig. C.1. Trivially only ⊖-end directed motors are effected when bound to a minus end. Tables summarizing the results for motors bound to minus ends are given in C.5.3. Here we illustrate the character of the force contributions and calculate the average forces due to an ensemble of hetero-dimers (p-m, m-p).

For region (a) left of both asters the force contribution of an ensemble of hetero-dimers is given by (w.o.l.g: $v_a \leq 0 \leq v_b$):

$$\mathcal{F} = -\langle f_1 \rangle = -\frac{1}{2}\frac{v_b - v_a + 2\dot{L}}{\chi_a + \chi_b} - \frac{1}{2}\frac{-v_b + 2\dot{L}}{\chi_a + \chi_b} = \frac{\frac{1}{2}v_a - 2\dot{L}}{\chi_a + \chi_b} \tag{C.27}$$

Interestingly motors bound to the minus end can contribute forces to the total force. This is in contrast to motors bound to the bulk or plus ends only in region (a).

For region (b) between the asters the force contribution of an ensemble of hetero-dimers is given by

$$\mathcal{F} = \frac{1}{2}\left(\frac{\frac{1}{2}v_a + v_b - 2\dot{L}}{\chi_a + \chi_b} + \frac{\frac{1}{2}v_a + v_b - 2\dot{L}}{\chi_a + \chi_b}\right) = \frac{\frac{1}{2}v_a + v_b - 2\dot{L}}{\chi_a + \chi_b} \tag{C.28}$$

Like above, motors between both asters contribute to the total force on the asters.

Dimer type	Velocities of heads	Density
p: plus-plus	$0 \leq v_a^p \leq v_b^p$	$p(x)$
m: minus-minus	$v_a^m \leq v_b^m \leq 0$	$m(x)$
h: hetero-dimer	$v_a^h \leq 0 \leq v_b^h$ or $v_b^h \leq 0 \leq v_a^h$	$h(x)$

Table C.3: Three different kinds of motor dimers. The densities of the two homo-dimers in which both heads move towards the same end are marked by $p(x)$ and $m(x)$ respectively. As it is impossible to distinguish an m-p from a p-m complex in solution they are described by only one density for hetero-dimers $h(x)$. We assume that a hetero-dimer binds with equal probability either way to the two MTs.

For region (c) right of both asters the force contribution of an ensemble of hetero-dimers is given by

$$\mathcal{F} = \langle f_1 \rangle = \frac{1}{2}\frac{v_b - 2\dot{L}}{\chi_a + \chi_b} + \frac{1}{2}\frac{v_a - v_b - 2\dot{L}}{\chi_a + \chi_b} = \frac{\frac{1}{2}v_a - 2\dot{L}}{\chi_a + \chi_b} \tag{C.29}$$

Like the motors bound left of both asters, also motors bound to the minus end right of both asters contribute to the total force. In conclusion: motors bound to minus ends do always contribute to the total force.

An overview of the force contributions of ensembles of the three different types of motor dimers (p-p, m-m, p-m/m-p) under the three different ways of attachment (bulk-bulk, bulk-$\oplus$-end, bulk-$\ominus$-end) in all three zones of a spindle (a, b, and c) is given in C.1.5.

C.1.4 Example: Forces Between two Half Asters

As given by Eq. (4.6) the total force on both asters is the sum of the forces exerted by all the motor dimers bound to MTs from both asters. In order to demonstrate the procedure we calculate the forces acting on two half asters for three different types of motor dimers: homo-dimers p and m, and hetero-dimers h, cf. table C.3. The constraint to half asters eliminates all interactions left or right of both aster poles (zones (a) and (c)). It turns out that the essential physics is already contained in this simplified scenario. The extension to full asters is straightforward and discussed in section C.2.2. We furthermore discuss here only the forces between asters with an exponential microtubule distribution. An application to homogenous asters is given in C.3.2.

Forces due to bulk-bulk bound motors. The forces per MT dimer on two half asters characterized by L and $\dot{L}$ due to *bulk-bulk*-interactions at x are given by (cf. Eq. (C.19)):

$$\begin{aligned} F_b(L,\dot{L},x) &= -C_b\rho_p^l(x)\rho_m^r(x)\left(p(x)\frac{-v_a^p - v_b^p + 2\dot{L}}{\chi_a^p + \chi_b^p}\right. \\ &\quad \left. +m(x)\frac{-v_a^m - v_b^m + 2\dot{L}}{\chi_a^m + \chi_b^m} + h(x)\frac{-v_a^h - v_b^h + 2\dot{L}}{\chi_a^h + \chi_b^h}\right) \\ &= -C_b\rho_p^l(x)\rho_m^r(x)\left(p(x)f_p' + m(x)f_m' + h(x)f_h'\right. \\ &\quad \left. +2\dot{L}[p(x)f_p'' + m(x)f_m'' + h(x)f_h'']\right) \end{aligned} \tag{C.30}$$

where the superscripts on the velocities denote the dimer type as introduced in table C.3 and we have introduced the following variables:

$$f'_p = \frac{-v_a^p - v_b^p}{\chi_a^p + \chi_b^p} \leq 0 \quad , \quad f''_p = \frac{1}{\chi_a^p + \chi_b^p} > 0 \tag{C.31}$$

$$f'_m = \frac{-v_a^m - v_b^m}{\chi_a^m + \chi_b^m} \geq 0 \quad , \quad f''_m = \frac{1}{\chi_a^m + \chi_b^m} > 0 \tag{C.32}$$

$$f'_h = \frac{-v_a^h - v_b^h}{\chi_a^h + \chi_b^h} \begin{cases} \leq 0 & v_a^h + v_b^h \geq 0 \\ \geq 0 & v_a^h + v_b^h \leq 0 \end{cases} \quad , \quad f''_h = \frac{1}{\chi_a^h + \chi_b^h} > 0 \tag{C.33}$$

The constants f' describe the force on the 1st head of a dimer between stationary asters.

For homogenous motor densities $p(x) = p_0 \geq 0$, $m(x) = m_0 \geq 0$, $h(x) = h_0 \geq 0$ and exponential MT-densities as given by the equations in table 4.3 we obtain

$$\begin{aligned} F_b(L, \dot{L}, x) &= -C_b a^{-2} N_0^2 e^{-2kL} \big(p_0 f'_p + m_0 f'_m + h_0 f'_h \\ &\quad + 2\dot{L}[p_0 f''_p + m_0 f''_m + h_0 f''_h]\big) \quad . \end{aligned} \tag{C.34}$$

This expression is independent of the position x. The force on both asters is thus given by

$$\begin{aligned} F_b(L, \dot{L}) &= \int_{-L}^{L} F_b(L, \dot{L}, x) \mathrm{d}x = 2L F_b(L, \dot{L}, x) \\ &= -2C_b a^{-2} N_0^2 L e^{-2kL} \Big(p_0 f'_p + m_0 f'_m + h_0 f'_h + 2\dot{L}[p_0 f''_p + m_0 f''_m + h_0 f''_h]\Big) \quad . \end{aligned} \tag{C.35}$$

As $2C_b a^{-2} N_0^2 L e^{-2kL}$ is always strictly positive, we can only have a stationary spindle if the term in the brackets is zero. This does not depend on the spindle length $2L$, so that half asters which only interact via motors bound to the bulk can form stable, stationary ($\dot{L} = 0$) spindles when $p_0 f'_p + m_0 f'_m + h_0 f'_h = 0$.

Forces due to bulk-$\oplus$-end bound motors. The same procedure can be applied to dimers linking the bulk and the $\oplus$-end of their two microtubules. For homogenous motor densities $p(x) = p_0 \geq 0$, $m(x) = m_0 \geq 0$, $h(x) = h_0 \geq 0$ and exponential MT-densities as given by the equations in table 4.3 we obtain

$$\begin{aligned} F_p(L, \dot{L}, x) &= -2C_p a^{-1} k N_0^2 e^{-2kL} \Big(\frac{1}{2} p_0 f'_p + m_0 f'_m + \frac{1}{2} h_0 f'_h \\ &\quad + \frac{1}{2} h_0 \min(v_a^h, v_b^h) f''_h + 2\dot{L}[p_0 f''_p + m_0 f''_m + h_0 f''_h]\Big) \end{aligned} \tag{C.36}$$

This expression is again independent of the position x. The force on both asters is thus given by

$$\begin{aligned} F_p(L, \dot{L}) &= \int_{-L}^{L} F_p(L, \dot{L}, x) \mathrm{d}x = 2L F_p(L, \dot{L}, x) \\ &= -4C_p a^{-1} k N_0^2 L e^{-2kL} \Big(\frac{1}{2} p_0 f'_p + m_0 f'_m + \frac{1}{2} h_0 f'_h \\ &\quad + \frac{1}{2} h_0 \min(v_a^h, v_b^h) f''_h + 2\dot{L}[p_0 f''_p + m_0 f''_m + h_0 f''_h]\Big) \end{aligned} \tag{C.37}$$

The structure of this expression is similar to that in Eq. (C.35). As always $2C_p a^{-1} k N_0^2 L e^{-2kL} > 0$, a stationary spindle can only exist if the term in the brackets is zero. This does not depend on the spindle length $2L$, so that half asters which only interact via motors bound to the bulk of the MTs of one spindle and the $\oplus$-ends of MTs from the other can form stable, stationary spindles when
$\frac{1}{2}p_0 f_p' + m_0 f_m' + \frac{1}{2}h_0 f_h' - \frac{1}{2}h_0 \min(v_a^h, v_b^h) f_h'' = 0$.

The forces due to bulk-$\ominus$-end bound motors are calculated analogously. We obtain

$$\begin{aligned} F_m(L,\dot{L},x) &= -C_m a^{-1} N_0^2 \left(e^{-k(L+x)}\delta(L-x) + e^{-k(L-x)}\delta(-L-x)\right)\Big(p_0 f_p' + \frac{1}{2}m_0 f_m' \\ &\quad + \frac{1}{2}h_0 f_h' + \frac{1}{2}h_0 \max(v_a^h, v_b^h) f_h'' + 2\dot{L}[p_0 f_p'' + m_0 f_m'' + h_0 f_h'']\Big) \qquad \text{(C.38)} \end{aligned}$$

for homogenous motor densities and exponential microtubule densities. The force on both asters is thus given by

$$\begin{aligned} F_m(L,\dot{L}) &= \int_{-L}^{L} F_p(L,\dot{L},x)\mathrm{d}x \qquad \text{(C.39)} \\ &= -2C_m a^{-1} N_0^2 e^{-2kL}\Big(p_0 f_p' + \frac{1}{2}m_0 f_m' + \frac{1}{2}h_0 f_h' \\ &\quad + \frac{1}{2}h_0 \max(v_a^h, v_b^h) f_h'' + 2\dot{L}[p_0 f_p'' + m_0 f_m'' + h_0 f_h'']\Big) \end{aligned}$$

And again we can only have stationary spindles when
$p_0 f_p' + \frac{1}{2}m_0 f_m' + \frac{1}{2}h_0 f_h' - \frac{1}{2}h_0 \max(v_a^h, v_b^h) f_h''$=0.

Thus none of the forces due to one specific type of binding is sufficient to define the spindle length. We will see in section 4.2.2 that their combined action however gives rise to a spindle with well defined length $2L$ and transparent conditions for spindle stability.

The total force per dimer length on the two half asters is the sum of the three forces calculated in Eqs. (C.35), (C.37), (C.39):

$$\begin{aligned} F(L,\dot{L},x) &= F_b(L,\dot{L},x) + F_p(L,\dot{L},x) + F_m(L,\dot{L},x) \qquad \text{(C.40)} \\ &= -C_b'(x,\dot{L})\rho_p^l(x)\rho_m^r(x) - C_p'(x,\dot{L})\left(\rho_p^l(x)\eta_m^{r,\oplus}(x) + \eta_p^{l,\oplus}(x)\rho_m^r(x)\right) \\ &\quad -C_m'(x,\dot{L})\left(\rho_p^l(x)\eta_m^{r,\ominus}(x) + \eta_p^{l,\ominus}(x)\rho_m^r(x)\right) \end{aligned}$$

where we have introduced three new functions $C_b'(x,\dot{L}), C_p'(x,\dot{L}), C_m'(x,\dot{L})$, see Eqs. (C.44)-(C.46) for details. For homogenous motor densities these variables do not depend on space. So when discussing homogenous motor densities we will write $C'(\dot{L})$ instead of $C'(x,\dot{L})$ to reflect this. Integrating Eq. (C.40) over the whole system we thus obtain for homogenous motor densities and the exponential MT densities (cf. table 4.3):

$$\begin{aligned} F(L,\dot{L}) &= -2C_b'(\dot{L})a^{-2}LN_0^2 e^{-2kL} - 4C_p'(\dot{L})a^{-1}kLN_0^2 e^{-2kL} - 2C_m'(\dot{L})a^{-1}N_0^2 e^{-2kL} \\ &= -2a^{-1}N_0^2 e^{-2kL}\left([C_b'(\dot{L})/a + 2kC_p'(\dot{L})]L + C_m'(\dot{L})\right) \qquad \text{(C.41)} \end{aligned}$$

We will now put this expression to use and determine the emergent length scale of the spindle and the conditions under which the spindle will be stable.

C.1.5 Overview of Force Contributions from Ensembles of Motors

For an ensemble of one kind of motor dimers we can write the force contribution as

$$\mathcal{F} = \frac{1}{\chi_a^j + \chi_b^j} \vec{v} \cdot \vec{f} \tag{C.42}$$

where $\vec{v} = \left(v_a^j \ , \ v_b^j \ , \ \dot{L} \right)$ is a 1×3 vector and $j \in \{p, m, h\}$ labels the three different types of motor dimers, cf. table C.3. For each region we can thus calculate $\vec{f}$ for each type of dimers explicitly:

Region (a)	bulk-bulk	bulk-⊕-end ($\frac{1}{2}$(i+ii))	bulk-⊖-end
p-p	$\begin{pmatrix} 0 \\ 0 \\ -2 \end{pmatrix}$	$\frac{1}{2}\begin{pmatrix} -1 \\ -1 \\ -2 \end{pmatrix} + \frac{1}{2}\begin{pmatrix} 1 \\ 1 \\ -2 \end{pmatrix} = \begin{pmatrix} 0 \\ 0 \\ -2 \end{pmatrix}$	$\begin{pmatrix} 0 \\ 0 \\ -2 \end{pmatrix}$
m-m	$\begin{pmatrix} 0 \\ 0 \\ -2 \end{pmatrix}$	$\begin{pmatrix} 0 \\ 0 \\ -2 \end{pmatrix}$	$\frac{1}{2}\begin{pmatrix} 1 \\ 1 \\ -4 \end{pmatrix}$
hetero	$\begin{pmatrix} 0 \\ 0 \\ -2 \end{pmatrix}$	$\frac{1}{2}\begin{pmatrix} 0 \\ -1 \\ -2 \end{pmatrix} + \frac{1}{2}\begin{pmatrix} 0 \\ 1 \\ -2 \end{pmatrix} = \begin{pmatrix} 0 \\ 0 \\ -2 \end{pmatrix}$	$\frac{1}{2}\begin{pmatrix} 1 \\ 0 \\ -4 \end{pmatrix}$

Table C.4: Force contributions $\vec{f}$ of different kinds of motor dimers in region (a).

Region (b)	bulk-bulk	bulk-⊕-end	bulk-⊖-end
p-p	$\begin{pmatrix} 1 \\ 1 \\ -2 \end{pmatrix}$	$\frac{1}{2}\begin{pmatrix} 1 \\ 1 \\ -4 \end{pmatrix}$	$\begin{pmatrix} 1 \\ 1 \\ -2 \end{pmatrix}$
m-m	$\begin{pmatrix} 1 \\ 1 \\ -2 \end{pmatrix}$	$\begin{pmatrix} 1 \\ 1 \\ -2 \end{pmatrix}$	$\frac{1}{2}\begin{pmatrix} 1 \\ 1 \\ -4 \end{pmatrix}$
hetero	$\begin{pmatrix} 1 \\ 1 \\ -2 \end{pmatrix}$	$\frac{1}{2}\begin{pmatrix} 2 \\ 1 \\ -4 \end{pmatrix}$	$\frac{1}{2}\begin{pmatrix} 1 \\ 2 \\ -4 \end{pmatrix}$

Table C.5: Force contributions $\vec{f}$ of different kinds of motor dimers in region (b).

Region (c)	bulk-bulk	bulk-⊕-end ($\frac{1}{2}$(i+ii))	bulk-⊖-end
p-p	$\begin{pmatrix} 0 \\ 0 \\ -2 \end{pmatrix}$	$\frac{1}{2}\begin{pmatrix} 1 \\ 1 \\ -2 \end{pmatrix} \frac{1}{2}\begin{pmatrix} -1 \\ -1 \\ -2 \end{pmatrix} = \begin{pmatrix} 0 \\ 0 \\ -2 \end{pmatrix}$	$\begin{pmatrix} 0 \\ 0 \\ -2 \end{pmatrix}$
m-m	$\begin{pmatrix} 0 \\ 0 \\ -2 \end{pmatrix}$	$\begin{pmatrix} 0 \\ 0 \\ -2 \end{pmatrix}$	$\frac{1}{2}\begin{pmatrix} 1 \\ 1 \\ -4 \end{pmatrix}$
hetero	$\begin{pmatrix} 0 \\ 0 \\ -2 \end{pmatrix}$	$\frac{1}{2}\begin{pmatrix} 0 \\ 1 \\ -2 \end{pmatrix} \frac{1}{2}\begin{pmatrix} 0 \\ -1 \\ -2 \end{pmatrix} = \begin{pmatrix} 0 \\ 0 \\ -2 \end{pmatrix}$	$\frac{1}{2}\begin{pmatrix} 1 \\ 0 \\ -4 \end{pmatrix}$

Table C.6: Force contributions of $\vec{f}$ different kinds of motor dimers in region (c).

So that the forces are explicitely given by:

Region (a)	$F(L, \dot{L}, x)$
bulk-bulk	$= C_b \rho_m^l(x) \rho_m^r(x) \left(p(x) \frac{-2\dot{L}}{\chi_a^p + \chi_b^p} + m(x) \frac{-2\dot{L}}{\chi_1^m + \chi_2^m} + h(x) \frac{-2\dot{L}}{\chi_a^h + \chi_b^h} \right)$
bulk-⊕-end	$= C_p \Big[\rho_m^l(x) \eta_m^{r,\oplus}(x) \left(p(x) \frac{1}{2} \frac{-v_a^{\mathrm{p}} - v_b^{\mathrm{p}} - 2\dot{L}}{\chi_a^p + \chi_b^p} + m(x)(-2\dot{L}) + h(x) \frac{1}{2} \frac{-v_b^{\mathrm{h}} - 2\dot{L}}{\chi_a^h + \chi_b^h} \right)$ $+ \eta_m^{l,\oplus}(x) \rho_m^r(x) \left(p(x) \frac{1}{2} \frac{v_a^{\mathrm{p}} + v_b^{\mathrm{p}} - 2\dot{L}}{\chi_a^p + \chi_b^p} + m(x)(-2\dot{L}) + h(x) \frac{1}{2} \frac{v_b^{\mathrm{h}} - 2\dot{L}}{\chi_a^h + \chi_b^h} \right) \Big]$
bulk-⊖-end	$= C_m \eta^{l,\ominus}(x) \rho_m^r(x) \left(p(x) \frac{-2\dot{L}}{\chi_a^p + \chi_b^p} + m(x) \frac{1}{2} \frac{v_a^{\mathrm{m}} + v_b^{\mathrm{m}} - 4\dot{L}}{\chi_1^m + \chi_2^m} + h(x) \frac{1}{2} \frac{v_a^{\mathrm{h}} - 4\dot{L}}{\chi_a^h + \chi_b^h} \right)$

Table C.7: Force contributions of different kinds of motor dimers in region (a).

Region (b) is the region where the asters overlap most and is the only important region for calculations regarding half asters. Table C.8 displays the force contributions from motor dimers in this region.

Region (b)	$F(L, \dot{L}, x)$
bulk-bulk	$= C_b \rho_p^l(x) \rho_m^r(x) \left(p(x) \frac{v_a^p + v_b^p - 2\dot{L}}{\chi_a^p + \chi_b^p} + m(x) \frac{v_a^m + v_b^m - 2\dot{L}}{\chi_a^m + \chi_b^m} + h(x) \frac{v_a^h + v_b^h - 2\dot{L}}{\chi_a^h + \chi_b^h} \right)$
bulk-⊕-end	$= C_p \left[\rho_p^l(x) \eta_m^{r,\oplus}(x) + \eta_p^{l,\oplus}(x) \rho_m^r(x) \right]$ $\times \left(p(x) \frac{1}{2} \frac{v_a^{\mathrm{p}} + v_b^{\mathrm{p}} - 4\dot{L}}{\chi_a^p + \chi_b^p} + m(x) \frac{v_a^m + v_b^m - 2\dot{L}}{\chi_a^m + \chi_b^m} + h(x) \frac{1}{2} \frac{2v_a^{\mathrm{h}} + v_b^{\mathrm{h}} - 4\dot{L}}{\chi_a^h + \chi_b^h} \right)$
bulk-⊖-end	$= C_m \eta^{l,\ominus}(x) \rho_m^r(x) \left(p(x) \frac{v_a^p + v_b^p - 2\dot{L}}{\chi_a^p + \chi_b^p} + m(x) \frac{1}{2} \frac{v_a^{\mathrm{m}} + v_b^{\mathrm{m}} - 4\dot{L}}{\chi_1^m + \chi_2^m} + h(x) \frac{1}{2} \frac{v_a^{\mathrm{h}} + 2v_b^{\mathrm{h}} - 4\dot{L}}{\chi_a^h + \chi_b^h} \right)$

Table C.8: Force contributions of different kinds of motor dimers in region (b).

Region (c)	$F(L,\dot{L},x)$
bulk-bulk	$= C_b \rho_p^l(x)\rho_p^r(x)\left(p(x)\frac{-2\dot{L}}{\chi_a^p+\chi_b^p} + m(x)\frac{-2\dot{L}}{\chi_1^m+\chi_2^m} + h(x)\frac{-2\dot{L}}{\chi_a^h+\chi_b^h}\right)$
bulk-$\oplus$-end	$= C_p\Big[\rho_p^l(x)\eta_p^{r,\oplus}(x)\left(p(x)\frac{1}{2}\frac{v_a^{\mathrm{p}}+v_b^{\mathrm{p}}-2\dot{L}}{\chi_a^p+\chi_b^p} + m(x)(-2\dot{L}) + h(x)\frac{1}{2}\frac{v_b^{\mathrm{h}}-2\dot{L}}{\chi_a^h+\chi_b^h}\right)$ $+\eta_p^{l,\oplus}(x)\rho_p^r(x)\left(p(x)\frac{1}{2}\frac{-v_a^{\mathrm{p}}+-v_b^{\mathrm{p}}-2\dot{L}}{\chi_a^p+\chi_b^p} + m(x)(-2\dot{L}) + h(x)\frac{1}{2}\frac{-v_b^{\mathrm{h}}-2\dot{L}}{\chi_a^h+\chi_b^h}\right)\Big]$
bulk-$\ominus$-end	$= C_m \eta_m^r(x)\rho_p^l(x)\left(p(x)\frac{-2\dot{L}}{\chi_a^p+\chi_b^p} + m(x)\frac{1}{2}\frac{v_a^{\mathrm{m}}+v_b^{\mathrm{m}}-4\dot{L}}{\chi_1^m+\chi_2^m} + h(x)\frac{1}{2}\frac{v_a^{\mathrm{h}}-4\dot{L}}{\chi_a^h+\chi_b^h}\right)$

Table C.9: Force contributions of different kinds of motor dimers in region (c).

This notation reflects clearly that the force action of motor dimers is a priori independent of the density of microtubules. The MT density enters in form of densities in the prefactor only, but not in the motor parts. A particularly important example of a microtubule density is given by asters with an exponential length distribution, cf. Eq. (4.38). As the asters are symmetric in this case, the prefactors for the different endbinding cases (i) and (ii) are identical as shown explicitly in the following table:

Binding	Region (a)	Region (b)	Region (c)
bulk-bulk	$C_b\frac{N_0^2}{a^2}e^{2kx}$	$C_b\frac{N_0^2}{a^2}e^{-2kL}$	$C_b\frac{N_0^2}{a^2}e^{-2kx}$
bulk-$\oplus$-end	$C_p\frac{N_0^2}{a}ke^{2kx}$	$C_p\frac{N_0^2}{a}ke^{-2kL}$	$C_p\frac{N_0^2}{a}ke^{-2kx}$
bulk-$\ominus$-end	$C_m\frac{N_0^2}{a}e^{-k(L-x)}$ $\times\delta(-L-x)$	$C_m\frac{N_0^2}{a}\times$ $\big(e^{-k(L+x)}\delta(L-x)$ $+e^{-k(L-x)}\delta(-L-x)\big)$	$C_m\frac{N_0^2}{a}e^{-k(L+x)}$ $\times\delta(L-x)$

Table C.10: Prefactors of force expressions for exponential asters, cf. Eq. (4.20) etc..

C.2 Existence and Stability of Spindles

C.2.1 Half Asters

Here we present supplementary calculations to the example of two interacting half asters with exponential microtubule densities as discussed in sections C.1.4 and 4.3.1.

The total force per dimer length on the two half asters is the sum of the three forces calculated in Eqs. (C.34), (C.36), and (C.38):

$$
\begin{aligned}
F(L,\dot{L},x) &= F_b(L,\dot{L},x)+F_p(L,\dot{L},x)+F_m(L,\dot{L},x) \qquad \text{(C.43)}\\
&= -C_b\rho_p^l(x)\rho_m^r(x)\left(p(x)f_p'+m(x)f_m'+h(x)f_h'\right.\\
&\quad \left.+2\dot{L}[p(x)f_p''+m(x)f_m''+h(x)f_h'']\right)\\
&\quad -C_p(\rho_p^l(x)\eta_p^r(x)+\eta_p^l(x)\rho_m^r(x))\left(\frac{1}{2}p(x)f_p'+m(x)f_m'+\frac{1}{2}h(x)f_h'\right.\\
&\quad \left.+\frac{1}{2}h(x)\min(v_a^h,v_b^h)f_h''+2\dot{L}[p(x)f_p''+m(x)f_m''+h(x)f_h'']\right)\\
&\quad -C_m(\rho_p^l(x)\eta_m^r(x)+\eta_m^l(x)\rho_m^r(x))\left(p(x)f_p'+\frac{1}{2}m(x)f_m'+\frac{1}{2}h(x)f_h'\right.\\
&\quad \left.+\frac{1}{2}h(x)\max(v_a^h,v_b^h)f_h''+2\dot{L}[p(x)f_p''+m(x)f_m''+h(x)f_h'']\right)\\
&= -C_b'(x,\dot{L})\rho_p^l(x)\rho_m^r(x)-C_p'(x,\dot{L})\left(\rho_p^l(x)\eta_p^r(x)+\eta_p^l(x)\rho_m^r(x)\right)\\
&\quad -C_m'(x,\dot{L})\left(\rho_p^l(x)\eta_m^r(x)+\eta_m^l(x)\rho_m^r(x)\right)
\end{aligned}
$$

in the last step we have introduced three new functions $C_b'(x,\dot{L}), C_p'(x,\dot{L}), C_m'(x,\dot{L})$:

$$
\begin{aligned}
C_b'(x,\dot{L}) &:= C_b\left(p(x)f_p'+m(x)f_m'+h(x)f_h'\right. \qquad \text{(C.44)}\\
&\quad \left.+2\dot{L}[p(x)f_p''+m(x)f_m''+h(x)f_h'']\right)\\
C_p'(x,\dot{L}) &:= C_p\left(\frac{1}{2}p(x)f_p'+m(x)f_m'+\frac{1}{2}h(x)f_h'\right. \qquad \text{(C.45)}\\
&\quad \left.+\frac{1}{2}h(x)\min(v_a^h,v_b^h)f_h''+2\dot{L}[p(x)f_p''+m(x)f_m''+h(x)f_h'']\right)\\
C_m'(x,\dot{L}) &:= C_m\left(p(x)f_p'+\frac{1}{2}m(x)f_m'+\frac{1}{2}h(x)f_h'\right. \qquad \text{(C.46)}\\
&\quad \left.+\frac{1}{2}h(x)\max(v_a^h,v_b^h)f_h''+2\dot{L}[p(x)f_p''+m(x)f_m''+h(x)f_h'']\right)
\end{aligned}
$$

The stability of this system is determined by the derivative of $F(L,\dot{L})$ (cf. Eq. (4.4)). For exponential half asters we obtain:

$$
\frac{\partial}{\partial L}F(L,\dot{L}) = -2a^{-1}N_0^2e^{-2kL}\Big((1-2kL)\Big[C_b'(\dot{L})/a+2kC_p'(\dot{L})\Big]-2kC_m'(\dot{L})\Big) \qquad \text{(C.47)}
$$

so that with L_s from Eq. (4.22)

$$
\begin{aligned}
&\left.\frac{\partial}{\partial L}F(L,\dot{L})\right|_{L=L_s} \qquad \text{(C.48)}\\
&= -2a^{-1}N_0^2e^{+2k\frac{C_m'(0)}{C_b'(0)/a+2kC_p'(0)}}\\
&\times\Bigg(\Bigg((1+2k\frac{C_m'(0)}{C_b'(0)/a+2kC_p'(0)}\Bigg)\Big[C_b'(\dot{L})/a+2kC_p'(\dot{L})\Big]-2kC_m'(\dot{L})\Bigg)\\
&= -2a^{-1}N_0^2e^{+2k\frac{C_m'(0)}{C_b'(0)/a+2kC_p'(0)}}\Big[C_b'(\dot{L})/a+2kC_p'(\dot{L})\Big] \quad .
\end{aligned}
$$

This directly gives the condition for spindle stability, Eq. (4.24).

Existence and stability of a spindle formed by two exponential half asters. We assume homogenous motor densities and two types of motor heads (one $\oplus$-end directed with velocity $v_p > 0$ and one $\ominus$-end directed with $v_m < 0$) and replace v_a, v_b, χ_a, χ_b accordingly:

$$v_a^p = v_b^p = v_b^h = v_p > 0 \tag{C.49}$$
$$v_a^m = v_b^m = v_a^h = v_m < 0 \tag{C.50}$$
$$\chi_a^p = \chi_b^p = \chi_b^h = \chi_p > 0 \tag{C.51}$$
$$\chi_a^m = \chi_b^m = \chi_a^h = \chi_m > 0 \quad . \tag{C.52}$$

We obtain simplified expressions for the functions $C_m'(0)$, $C_b'(0)$, and $C_p'(0)$:

$$C_b'(0) = C_b\left(-p_0\frac{v_p}{\chi_p} - m_0\frac{v_m}{\chi_m} - h_0\frac{v_p+v_m}{\chi_p+\chi_m}\right) \tag{C.53}$$
$$C_p'(0) = C_p\left(-\frac{1}{2}p_0\frac{v_p}{\chi_p} - m_0\frac{v_m}{\chi_m} - h_0\frac{\frac{1}{2}v_p+v_m}{\chi_p+\chi_m}\right) \tag{C.54}$$
$$C_m'(0) = C_m\left(-p_0\frac{v_p}{\chi_p} - \frac{1}{2}m_0\frac{v_m}{\chi_m} - h_0\frac{v_p+\frac{1}{2}v_m}{\chi_p+\chi_m}\right) \tag{C.55}$$

so that it is straight forward to discuss the signs of all terms we need:

$$C_b'(0) > 0 \iff 0 < v_p < -v_m\frac{\chi_p(\chi_p m_0 + \chi_m(h_0+m_0))}{\chi_m(\chi_m p_0 + \chi_p(h_0+p_0))} =: -v_m\gamma \tag{C.56}$$
$$C_p'(0) > 0 \iff 0 < v_p < -v_m\frac{2\chi_p(\chi_p m_0 + \chi_m(h_0+m_0))}{\chi_m(\chi_m p_0 + \chi_p(h_0+p_0))} = -v_m 2\gamma \tag{C.57}$$
$$C_m'(0) > 0 \iff 0 < v_p < -v_m\frac{\chi_p(\chi_p m_0 + \chi_m(h_0+m_0))}{2\chi_m(\chi_m p_0 + \chi_p(h_0+p_0))} = -v_m\frac{1}{2}\gamma \tag{C.58}$$
$$\begin{aligned}\left[C_b'(0)/a + 2kC_p'(0)\right] > 0 \iff\ & 0 < v_p \\ & < -v_m\left(\frac{C_b+2akC_p}{C_b+akC_p}\right)\frac{\chi_p(\chi_p m_0 + \chi_m(h_0+m_0))}{\chi_m(\chi_m p_0 + \chi_p(h_0+p_0))} \\ & = -v_m\left(\frac{C_b+2akC_p}{C_b+akC_p}\right)\gamma \\ & =: -v_m\Gamma\gamma\end{aligned} \tag{C.59}$$

which defines two positive constants γ and Γ as introduced in Eqs. (4.26) and (4.27).

There are in principle two ways to fulfill the conditions for the existence of a spindle consisting of two half asters (Eq. (4.23)):

1. $C_m'(0) > 0$ and $\left[C_b'(0)/a + 2kC_p'(0)\right] < 0$
   $\Rightarrow \frac{-v_p}{v_m} < \frac{\gamma}{2}$ and $\frac{-v_p}{v_m} > \Gamma\gamma$
   $\Rightarrow$ **No spindle possible** as $\Gamma \geq 1 > \frac{1}{2}$.

2. $C_m'(0) < 0$ and $\left[C_b'(0)/a + 2kC_p'(0)\right] > 0$
   $\Rightarrow \frac{-v_p}{v_m} > \frac{\gamma}{2}$ and $\frac{-v_p}{v_m} < \Gamma\gamma$
   $\Rightarrow$ **Spindle can exist** for $0 < \frac{1}{2}\gamma < \frac{-v_p}{v_m} < \Gamma\gamma$.

The second case forms the basis of the existence and stability discussion in section 4.3.1.

C.2.2 Full Asters

In the preceding section we studied spindle formation by two half asters, i.e. we have only calculated forces due to interactions that occur in region (b), i.e. $x \in [-L, L]$. We will now extend this approach to two full asters. Thus we will also consider force contributions due to interactions in regions (a) and (c).

General Forces The force between the asters in region (b) is given by (cf. Eq. (C.40))

$$\begin{aligned} F^{(b)}(L,\dot{L},x) &= -C_b'^{(b)}(x,\dot{L})\rho_p^l(x)\rho_m^r(x) - C_p'^{(b)}(x,\dot{L})\left(\rho_p^l(x)\eta_m^{r,\oplus}(x) + \eta_p^{l,\oplus}(x)\rho_m^r(x)\right) \\ &\quad -C_m'^{(b)}(x,\dot{L})\left(\rho_p^l(x)\eta_m^{r,\ominus}(x) + \eta_p^{l,\ominus}(x)\rho_m^r(x)\right) \end{aligned} \tag{C.60}$$

where the superscript (b) of the functions F and $C'_{\{b,p,m\}}$ reflects their corresponding region. Analogously we can write for the force from region (a)

$$\begin{aligned} F^{(a)}(L,\dot{L},x) &= -C_b'^{(a)}(x,\dot{L})\rho_m^l(x)\rho_m^r(x) - C_p'^{(a)}(x,\dot{L})\left(\rho_m^l(x)\eta_m^{r,\oplus}(x) + \eta_m^{l,\oplus}(x)\rho_m^r(x)\right) \\ &\quad -C_m'^{(a)}(x,\dot{L})\left(\eta^{l,\ominus}(x)\rho_m^r(x)\right) \end{aligned} \tag{C.61}$$

and region (c)

$$\begin{aligned} F^{(c)}(L,\dot{L},x) &= -C_b'^{(c)}(x,\dot{L})\rho_p^l(x)\rho_p^r(x) - C_p'^{(c)}(x,\dot{L})\left(\rho_p^l(x)\eta_p^{r,\oplus}(x) + \eta_p^{l,\oplus}(x)\rho_p^r(x)\right) \\ &\quad -C_m'^{(c)}(x,\dot{L})\left(\eta^{r,\ominus}(x)\rho_p^l(x)\right) \quad . \end{aligned} \tag{C.62}$$

The total force between two asters is thus given by

$$F(L,\dot{L},x) = F^{(a)}(L,\dot{L},x) + F^{(b)}(L,\dot{L},x) + F^{(c)}(L,\dot{L},x) \quad . \tag{C.63}$$

The force functions $C'^{(b)}_{\{b,p,m\}}(x,\dot{L})$ for region (b) are given explicitly in Eqs. (C.44)-(C.46). For region (a) we find

$$C_b'^{(a)}(x,\dot{L}) = C_b\left(2\dot{L}[p(x)f_p'' + m(x)f_m'' + h(x)f_h'']\right) \tag{C.64}$$

$$C_p'^{(a)}(x,\dot{L}) = C_p\left(2\dot{L}[p(x)f_p'' + m(x)f_m'' + h(x)f_h'']\right) \tag{C.65}$$

$$\begin{aligned} C_m'^{(a)}(x,\dot{L}) &= C_m\left(\frac{1}{2}m(x)f_m' + \frac{1}{2}h(x)\min(v_a^h, v_b^h)f_h''\right. \\ &\qquad \left. +2\dot{L}[p(x)f_p'' + m(x)f_m'' + h(x)f_h'']\right) \end{aligned} \tag{C.66}$$

and for region (c) the same expressions, compare tables C.4 and C.6. Note that as $C_b'^{(a)}(x,0) = 0$ and $C_p'^{(a)}(x,0) = 0$, motors in the bulk and at $\oplus$-ends on average do not contribute to the forces in stationary asters and only act like passive crosslinkers.

Having these expressions under our belts, we now turn to investigate the influence of the microtubule densities in regions (a) and (c) on the spindle dynamics.

Forces on Exponential Full Asters. The densities of two full asters with exponential length distribution $P(L)$ located at $\pm L$ are given table C.11. Making use of the prefactors

Length dist.	$P(L) = ke^{-kL}$	
Aster at	L	$-L$
MT densities	$\rho_p^r(x) = \rho(-L+x)$ $= a^{-1}N_0 e^{-k(-L+x)}$ on $\mathcal{D} = [L;\infty[$ $\rho_m^r(x) = \rho(L-x)$ $= a^{-1}N_0 e^{-k(L-x)}$ on $\mathcal{D} =]-\infty;L]$	$\rho_p^l(x) = \rho(L+x)$ $=a^{-1}N_0 e^{-k(L+x)}$ on $\mathcal{D} = [-L;\infty[$ $\rho_m^l(x) = \rho(-L-x)$ $= a^{-1}N_0 e^{-k(-L-x)}$ on $\mathcal{D} =]-\infty;-L]$
$\oplus$-end densities	$\eta_p^{r,\oplus}(x) = a\lvert\partial_x\rho_p^r(x)\rvert$ $= N_0 k e^{-k(-L+x)}$ on $\mathcal{D} = [L;\infty[$ $\eta_m^{r,\oplus}(x) = a\lvert\partial_x\rho_m^r(x)\rvert$ $= N_0 k e^{-k(L-x)}$ on $\mathcal{D} =]-\infty;L]$	$\eta_p^{l,\oplus}(x) = a\lvert\partial_x\rho_p^l(x)\rvert$ $= N_0 k e^{-k(L+x)}$ on $\mathcal{D} = [-L;\infty[$ $\eta_m^{l,\oplus}(x) = a\lvert\partial_x\rho_m^l(x)\rvert$ $= N_0 k e^{-k(-L-x)}$ on $\mathcal{D} =]-\infty;-L]$
$\ominus$-end densities	$\eta^{r,\ominus}(x) = N_0\delta(L-x)$ on $\mathcal{D} = [-\infty;\infty]$	$\eta^{l,\ominus}(x) = N_0\delta(-L-x)$ on $\mathcal{D} = [-\infty;\infty]$

Table C.11: Densities describing a system of two full asters with exponential microtubule densities. $\mathcal{D}$ denotes the domain of definition. Densities are zero outside their domain.

given in table C.10 and assuming w.o.l.g. $v_a^h < 0 < v_b^h$ we can directly write the force on two stationary asters due to motors in region (a):

$$F^{(a)}(L,0,x) = C_m \frac{N_0^2}{a} e^{-k(L-x)} \delta(-L-x) \left(m(x) \frac{1}{2} \frac{v_a^{\mathrm{m}} + v_b^{\mathrm{m}}}{\chi_1^m + \chi_2^m} + h(x) \frac{1}{2} \frac{v_a^{\mathrm{h}}}{\chi_a^h + \chi_b^h} \right), \tag{C.67}$$

which integrated over region (a) results in

$$\begin{aligned} F^{(a)}(L,0) &= \int_{-\infty}^{\infty} F^{(a)}(L,0,x)\mathrm{d}x \qquad \text{(C.68)} \\ &= \frac{1}{2} C_m \frac{N_0^2}{a} e^{-2kL} \left(m(-L) \frac{v_a^{\mathrm{m}} + v_b^{\mathrm{m}}}{\chi_1^m + \chi_2^m} + h(-L) \frac{v_a^{\mathrm{h}}}{\chi_a^h + \chi_b^h} \right) \quad . \end{aligned}$$

For region (c) we find analogously

$$F^{(c)}(L,0,x) = C_m \frac{N_0^2}{a} e^{-k(L+x)} \delta(L-x) \left(m(x) \frac{1}{2} \frac{v_a^{\mathrm{m}} + v_b^{\mathrm{m}}}{\chi_1^m + \chi_2^m} + h(x) \frac{1}{2} \frac{v_a^{\mathrm{h}}}{\chi_a^h + \chi_b^h} \right) \tag{C.69}$$

which integrated leads to

$$\begin{aligned} F^{(c)}(L,0) &= \int_{-\infty}^{\infty} F^{(c)}(L,0,x)\mathrm{d}x \qquad \text{(C.70)} \\ &= \frac{1}{2} C_m \frac{N_0^2}{a} e^{-2kL} \left(m(L) \frac{v_a^{\mathrm{m}} + v_b^{\mathrm{m}}}{\chi_1^m + \chi_2^m} + h(L) \frac{v_a^{\mathrm{h}}}{\chi_a^h + \chi_b^h} \right) \end{aligned}$$

So that the total additional force contribution of full asters to the forces between two half asters as given by Eq. (C.41) is

$$\begin{aligned} F^{(a)+(c)}(L,0) &= \frac{1}{2} C_m \frac{N_0^2}{a} e^{-2kL} \qquad \text{(C.71)} \\ &\times \left((m(L) + m(-L)) \frac{v_a^{\mathrm{m}} + v_b^{\mathrm{m}}}{\chi_1^m + \chi_2^m} + (h(L) + h(-L)) \frac{v_a^{\mathrm{h}}}{\chi_a^h + \chi_b^h} \right) \end{aligned}$$

For homogenous motor densities this expression simplifies further and leads to

$$F^{(a)+(c)}(L,0) \quad = \quad C_m \frac{N_0^2}{a} e^{-2kL} \left(m_0 \frac{v_a^{\mathrm{m}} + v_b^{\mathrm{m}}}{\chi_1^m + \chi_2^m} + h_0 \frac{v_a^{\mathrm{h}}}{\chi_a^h + \chi_b^h} \right) \tag{C.72}$$

The total force on two stationary full asters with exponential microtubule distribution due to homogenous motor from all three regions is then

$$F(L,0) \quad = \quad -2\frac{N_0^2}{a} e^{-2kL} \left([C_b^{\prime(b)}(0)/a + 2kC_p^{\prime(b)}(0)]L + C_m^{\prime(a)}(0) + C_m^{\prime(b)}(0) \right) \tag{C.73}$$

The conditions for existence and stability of stationary finite size spindles are thus only quantitatively changed with respect to the half asters discussed in section 4.3.1. The stationary half length L_s of the spindle is given by

$$F(L,0) = 0 \iff L_s = -\frac{C_m^{\prime(a)}(0) + C_m^{\prime(b)}(0)}{C_b^{\prime(b)}(0)/a + 2kC_p^{\prime(b)}(0)} \quad . \tag{C.74}$$

Again this expression reveals that in order for stationary spindles of finite length to exist, it is absolutely necessary to balance the force contribution of the ⊖-end-bulk interactions with either one or both of the other two interactions. A spindle furthermore only exists when

$$L_s > 0 \iff \left(C_m^{\prime(a)}(0) + C_m^{\prime(b)}(0) \right) \left(C_b^{\prime(b)}(0)/a + 2kC_p^{\prime(b)}(0) \right) < 0 \quad . \tag{C.75}$$

The stability of the spindle is again determined by Eq. (4.4). For the exponential asters we obtain from Eq. (C.73):

$$\frac{\partial}{\partial L} F(L,0) \tag{C.76}$$
$$= -2\frac{N_0^2}{a} e^{-2kL} \left((1-2kL) \left[C_b^{\prime(b)}(0)/a + 2kC_p^{\prime(b)}(0) \right] - 2k \left[C_m^{\prime(a)}(0) + C_m^{\prime(b)}(0) \right] \right)$$

so that with Eq. (4.38)

$$\left. \frac{\partial}{\partial L} F(L,0) \right|_{L=L_s} = -2\frac{N_0^2}{a} e^{+2kL_s} \tag{C.77}$$
$$\times \left(((1+2kL_s) \left[C_b^{\prime(b)}(0)/a + 2kC_p^{\prime(b)}(0) \right] - 2k \left[C_m^{\prime(a)}(0) + C_m^{\prime(b)}(0) \right] \right)$$
$$= -2a^{-1} N_0^2 e^{+2k \frac{C_m^{\prime(a)}(0) + C_m^{\prime(b)}(0)}{C_b^{\prime(b)}(0)/a + 2kC_p^{\prime(b)}(0)}} \left[C_b^{\prime(b)}(0)/a + 2kC_p^{\prime(b)}(0) \right] \quad .$$

As the prefactor is always negative, the sign is determined by the expression in the square brackets. A stationary spindle is stable if

$$\left[C_b^{\prime(b)}(0)/a + 2kC_p^{\prime(b)}(0) \right] > 0 \quad . \tag{C.78}$$

The conditions for existence and stability of spindles in the presence of motor dimers made of two different motor heads, i.e. motor characteristics as given by Eqs. (C.49)-(C.52) do hardly change with respect to the case of half asters. The same calculation as detailed in section 4.3.1 leads to

$$0 < \gamma < -\frac{v_p}{v_m} < \Gamma\gamma \tag{C.79}$$

which is the same as Eq. (4.25) except for missing the factor of 1/2 on the left. Again all spindles formed are stable.

C.3 Generality of Our Description

In chapter 4 we applied our description to asters with exponential MT densities, which interact via motor dimers that stay attached to the ends of the microtubules. For the emergence of a stationary spindle length, motors that stall at $\ominus$-ends were particularly important. In this section we show that this effect is independent of a specific choice of a distribution of $\ominus$-ends, as long as the intrinsic length scale of the distribution is small compared to k^{-1}, the length scale of the exponential distribution of aster MTs.

Furthermore we show that the scale of the stationary length is set by the length scale of the MT density. For exponential asters this is given by k^{-1} (Eq. 4.38). In section C.3.2 we present calculations regarding homogenous asters, i.e. asters in which all MTs have the same length l and show that this is sufficient for stable, finite size spindles to exist.

C.3.1 Various distributions of $\ominus$-ends

In chapter 4 we consider asters in which the $\ominus$-ends are precisely aligned in space, mathematically described by a δ-distribution, which is singular and represents a special case. Here we investigate if the phenomena described above persist for two half asters when the density of $\ominus$-ends has a different form. We consider half a Gaussian distribution with half width λ:

$$\eta^{r,\ominus}(x) = \frac{2N_0}{\lambda\sqrt{2\pi}} e^{-(L-x)^2/2\lambda^2} \quad , \quad \eta_m^{l,\ominus}(x) = \frac{2N_0}{\lambda\sqrt{2\pi}} e^{-(L+x)^2/2\lambda^2} \tag{C.80}$$

both defined on $\mathcal{D} = [-L; L]$, and an exponential distribution:

$$\eta^{r,\ominus}(x) = N_0 k_m e^{-k_m(L-x)} \quad , \quad \eta^{l,\ominus}(x) = N_0 k_m e^{-k_m(L+x)} \tag{C.81}$$

also both defined $\mathcal{D} = [-L; L]$. The MT density as well as the $\oplus$-end distribution of the half asters are exponential as given in table 4.3. The domains of definition assure that there are no MTs of the left half aster at $x < -L$ and no MTs of the right half aster at $x > L$. The forces due to bulk-bulk and bulk-$\oplus$-end interactions as calculated in Eqs. (C.34) and (C.36) remain unchanged.

Motivated by the biological system where the centrosome is small compared to the spindle, we assume the characteristic lengths of both distributions to be small compared to the length of the MTs. The perturbation of the microtubule density due to the distribution of $\ominus$-ends is thus taken to be negligible:

$$\lambda \ll k^{-1} \quad \text{and} \quad k_m^{-1} \ll k^{-1} \quad \text{respectively.} \tag{C.82}$$

Now we calculate the overlap for bulk-$\ominus$-end interactions as given in Eq. (C.38). We begin with the **Gaussian distributions**, Eq. (C.80):

$$\begin{aligned} & \int_{-\infty}^{\infty} \mathrm{d}x \; (\rho_p^l(x)\eta^{r,\ominus}(x) + \eta^{l,\ominus}(x)\rho_m^r(x)) \qquad \text{(C.83)} \\ = & \int_{-\infty}^{\infty} \mathrm{d}x \; \frac{N_0}{a}\frac{2N_0}{\lambda\sqrt{2\pi}} \left(e^{-k(L-x)} e^{-(L+x)^2/2\lambda^2} + e^{-k(L+x)} e^{-(L-x)^2/2\lambda^2} \right) \\ = & \frac{N_0^2}{a} e^{-2kL+\frac{1}{2}k^2\lambda^2} \left(\operatorname{erf}(\frac{k\lambda}{\sqrt{2}}) + \operatorname{erf}(\frac{2L-k\lambda^2}{\sqrt{2}\lambda}) \right) \\ = & a^{-1} N_0^2 e^{-2kL+\frac{1}{2}k^2\lambda^2} E(k,\lambda,L) \end{aligned}$$

where we have introduced $E(k,\lambda,L) := \operatorname{erf}(\frac{k\lambda}{\sqrt{2}}) + \operatorname{erf}(\frac{2L-k\lambda^2}{\sqrt{2}\lambda})$. As generally $k \ll L$ and $\lambda \ll L$, we may approximate $E(k,\lambda,L) \approx 1$ and $-2kL + \frac{1}{2}k^2\lambda^2 \approx -2kL$ and thus obtain

$$F(L,\dot{L}) \approx C_m' N_0^2 e^{-2kL}/a \quad . \tag{C.84}$$

Length distribution	$P(x) = \delta(l)$ (homogenous)	
Half aster at	L (right)	$-L$ (left)
MT density	$\rho^r_m(x) = \rho(L-x) = N_0/a$ on $\mathcal{D} = [L-l; L]$ ($\ominus$-MTs)	$\rho^l_p(x) = \rho(L+x) = N_0/a$ on $\mathcal{D} = [-L; -L+l]$ ($\oplus$-MTs)
$\oplus$-end density	$\eta^{r,\oplus}_m(x) = N_0\delta(L-l-x)$ on $\mathcal{D} = [-L; L-l/2]$	$\eta^{l,\oplus}_p(x) = N_0\delta(-L+l-x)$ on $\mathcal{D} = [-L+l/2; L]$
$\ominus$-end density	$\eta^{r,\ominus}(x) = N_0\delta(L-x)$ on $\mathcal{D} = [L-l/2; L]$	$\eta^{l,\ominus}(x) = N_0\delta(-L-x)$ on $\mathcal{D} = [-L; L+l/2]$

Table C.12: Densities describing a system of two half asters with homogenous microtubule densities. $\mathcal{D}$ denotes the domain of definition. Densities are zero outside their domain.

The most important characteristic of this expression is, that $F(L, \dot{L})$ is not proportional to Le^{-2kL} and thus the structure of Eq. (4.22) remains unchanged.

For exponential distributions we calculate:

$$\begin{aligned}
& \int_{-\infty}^{\infty} \mathrm{d}x \; (\rho^l_p(x)\eta^{r,\ominus}(x) + \eta^{l,\ominus}(x)\rho^r_m(x)) && \text{(C.85)} \\
= & \int_{-\infty}^{\infty} \mathrm{d}x \; N_0^2 a^{-1} k_m \left(e^{-k(L-x)}e^{-k_m(L+x)} + e^{-k(L+x)}e^{-k_m(L-x)}\right) \\
= & \; 2\frac{N_0^2 k_m}{a(k-k_m)}\left(e^{-2kL} - e^{-2k_m L}\right)
\end{aligned}$$

So this expression is neither proportional to Le^{-2kL} and thus does not lead to a qualitatively different expression for L_s.

In conclusion: the importance of the interaction by motors linked to the bulk and $\ominus$-ends for the emergence of finite size spindles of two half asters is a generic feature of this theory and does not depend on a special choice of the distribution of $\ominus$-ends $\eta_m(x)$.

C.3.2 Homogenous Half Asters

In chapter 4 we studied the interaction of two half asters with exponential microtubule densities. This choice was motivated by considerations of aligned MTs undergoing catastrophes and rescue events (cf. (Dogterom and Leibler, 1993)). In order to test the robustness of our approach we repeat the calculations for homogenous half asters, i.e. half asters with MTs of the same length. For homogenous motor densities the functions C'_b, C'_p and C'_m as defined in Eqs. (C.44)-(C.46) are not changed by a change of MT densities. Only the overlap integrals are different.

Let $P(l) = \delta(l)$ be the distribution of MT lengths. Then l is the length of all MTs of one half-aster with its center at $x = 0$. Its microtubule distribution is then given by

$$\rho(x) = \begin{cases} N_0/a & \text{for } 0 < x < l \\ 0 & \text{else} \end{cases} \tag{C.86}$$

where N_0 is the dimensionless number of microtubules and a is the length of a heterodimer forming the MTs. Table C.12 summarizes the quantities used to describe a system of two half asters at L and $-L$.

We obtain the following results for overlap of bulk-bulk, bulk-$\oplus$-ends, and bulk-$\ominus$-ends:

$$\int_{-L}^{L} \mathrm{d}x\ \rho_p^l(x)\rho_m^r(x) = \begin{cases} 2(N_0/a)^2(l-L) & \text{for} \quad L \le l \le 2L \\ 2(N_0/a)^2 L & \text{for} \quad l > 2L \\ 2(N_0/a)l & \text{for} \quad l < L \end{cases} \tag{C.87}$$

$$\int_{-L}^{L} \mathrm{d}x\ \left(\rho_p^l(x)\eta_p^r(x) + \eta_p^l(x)\rho_m^r(x)\right) = \begin{cases} 2N_0^2/a & \text{for} \quad L \le l \le 2L \\ 0 & \text{else} \end{cases} \tag{C.88}$$

$$\int_{-L}^{L} \mathrm{d}x\ \left(\rho_p^l(x)\eta_m^r(x) + \eta_m^l(x)\rho_m^r(x)\right) = \begin{cases} 2N_0^2/a & \text{for} \quad l > 2L \\ 0 & \text{else} \end{cases} \tag{C.89}$$

For our discussion, we distinguish three cases:

1. $l < L$: the half asters do not overlap, no interaction due to motors, no formation of spindles

2. $L \le l < 2L$: the half asters overlap but the MTs of one asters do not overlap with MT organizing center (centrosome) of the other half aster. In this case an overlap exists only in region (b) and the total force between the two asters is given by (cf. Eq. (C.41))

$$F(L,\dot{L}) = 2\frac{N_0^2}{a}\left(C_b'(\dot{L})(l-L)/a + C_p'(\dot{L})\right) \tag{C.90}$$

$$\Rightarrow L_s = l + a\frac{C_p'(0)}{C_b'(0)} \tag{C.91}$$

$$\text{and} \quad \frac{\partial F(L,\dot{L})}{\partial L} = -2\frac{N_0^2}{a^2}C_b'(\dot{L}) \quad . \tag{C.92}$$

   This leads to the following condition for a stationary spindle to exist (as we need $L \le l < 2L$):

$$-L_s < a\frac{C_p'(0)}{C_b'(0)} \le 0 \tag{C.93}$$

   and for stability we obtain

$$C_b'(0) > 0 \quad . \tag{C.94}$$

3. $2L \le l$: the half asters overlap completely, i.e. no interaction between the bulk and the $\oplus$-ends.

   In this case the total force is given by

$$F(L,\dot{L}) = 2\frac{N_0^2}{a}\left(LC_b'(\dot{L})/a + C_m'(\dot{L})\right) \tag{C.95}$$

$$\Rightarrow L_s = -a\frac{C_m'(0)}{C_b'(0)} \tag{C.96}$$

$$\text{and} \quad \frac{\partial F(L,\dot{L})}{\partial L} = 2\frac{N_0^2}{a^2}C_b'(\dot{L}) \quad . \tag{C.97}$$

   This leads to the following condition for a stationary spindle to exist (as we need $2L \le l$):

$$0 < a\frac{C_m'(0)}{C_b'(0)} \le \frac{l}{2} \tag{C.98}$$

   and for stability we obtain

$$C_b'(0) < 0 \quad . \tag{C.99}$$

Example: Two Types of Motor Heads. We consider two asters in the presence of motor dimers made up of two types of motor heads with velocities v_p and v_m only. Using Eqs. (C.49)-(C.52) we can now discuss conditions for the existence of stable, finite size spindles.

Case 2: $L \leq l < 2L$ The condition for a stable, finite size spindle is

$$\begin{aligned} & C_b'(0) > 0 \text{ and } C_p'(0) \geq 0 \text{ and } a\frac{C_p'(0)}{C_b'(0)} > -L_s \\ \iff \quad & 0 < \frac{-v_p}{v_m} < \gamma \text{ and } l > 0 \end{aligned} \tag{C.100}$$

Stable spindles thus can exist in this case.

Case 3: $l \geq 2L$ The condition for a stable, finite size spindle is

$$C_b'(0) < 0 \text{ and } C_m'(0) > 0 \tag{C.101}$$

which can never be fulfilled. In this case the asters do not form stable spindles.

In conclusion we have shown that homogenous asters do also support finite size spindles. The existence of spindles is thus robust against the choice of different microtubule length distributions.

C.4 Microtubule Distributions in 2D

Finally, we extend the description of microtubule asters to two spatial dimensions. Like in section 4.2.5 asters are primarily characterized by a distribution of microtubule lengths. An aster in two dimensions is characterized by a MT length distribution $P(L,\theta)$ which is normalized

$$\int_0^\infty \mathrm{d}L\; L \int_0^{2\pi} \mathrm{d}\theta\; P(L,\theta) = 1 \quad . \tag{C.102}$$

The angle θ determines the direction in space, L the length of the microtubules. For any given direction θ the MT density is given by

$$\rho(r,\theta) = \frac{N_0}{a} \int_r^\infty \mathrm{d}L\; P(L,\theta) \tag{C.103}$$

so that the MT density on a circle of radius r is given by

$$\rho(r) = \int_0^{2\pi} \mathrm{d}\theta\; r\rho(r,\theta) \tag{C.104}$$

and the mass of the aster by

$$M = \int_0^\infty \mathrm{d}r \int_0^{2\pi} \mathrm{d}\theta\; r\rho(r,\theta) = \frac{N_0}{a} \int_0^\infty \mathrm{d}r \int_0^{2\pi} \mathrm{d}\theta\; r \int_r^\infty \mathrm{d}L\; P(L,\theta) \quad . \tag{C.105}$$

Isotropic Distributions. We assume that the 2D length distribution $P(L)$ of microtubules is independent of the direction. The normalization condition Eq. (C.102) then yields

$$\int_0^\infty \mathrm{d}L\ 2\pi L\ P(L) = 1 \quad . \tag{C.106}$$

The MT density $\rho(r,\theta)$ is again given by Eq. (C.103). We furthermore obtain

$$\rho(r) = 2\pi r \frac{N_0}{a} \int_r^\infty \mathrm{d}L P(L) \quad , \tag{C.107}$$

so that the 2D $\rho(r)$ differs from the 1D $\rho(x)$ as given by Eq. (4.14) only by a factor of $2\pi r$.

The mass is given by

$$M = \int_0^\infty \mathrm{d}r \rho(r) = 2\pi \frac{N_0}{a} \int_0^\infty \mathrm{d}r\ r \int_r^\infty \mathrm{d}L\ P(L) \quad . \tag{C.108}$$

Let us assume a two-dimensional isotropic, exponential length distribution:

$$P(L) = \frac{k^2}{2\pi} e^{-kL} \quad , \tag{C.109}$$

which fulfills the normalization condition $\int_0^\infty \mathrm{d}L \int_0^{2\pi} \mathrm{d}\theta\ L\ P(L) = 1$. Then the isotropic MT density is given by (cf. Eq. (C.107))

$$\begin{aligned} \rho(r,\theta) &= \frac{N_0}{a} \int_r^\infty \mathrm{d}\ L\ P(L) = \frac{N_0}{a} \frac{k}{2\pi} e^{-kr} & \text{(C.110)} \\ \rho(r) &= 2\pi r \frac{N_0}{a} \int_r^\infty \mathrm{d}\ L\ P(L) = \frac{N_0}{a} r k e^{-kr} & \text{(C.111)} \end{aligned}$$

and the aster's mass is

$$M = \int_0^\infty \mathrm{d}r\ \rho(r) = \frac{N_0}{ak} \tag{C.112}$$

like in one spatial dimension. The Distribution of ends is given by

$$\begin{aligned} \eta^{\oplus}(r) &= 2\pi r \int_0^\infty \mathrm{d}L P(L) = r k^2 e^{-kr} & \text{(C.113)} \\ \eta^{\ominus}(r) &= \delta(r) & \text{(C.114)} \end{aligned}$$

This describes an aster centered around the origin in polar coordinates. We transform the density $\rho(r,\theta)$ to cartesian coordinates by substituting $r = \sqrt{x^2+y^2}$:

$$\rho(x,y) = \frac{N_0}{a} \frac{k}{2\pi} e^{-k\sqrt{x^2+y^2}} \tag{C.115}$$

Thus we can define the densities of two asters at $(\pm L, 0)$:

$$\begin{aligned} (-L,0): \quad \rho^l(x,y) &= \frac{N_0}{a} \frac{k}{2\pi} e^{-k\sqrt{(x+L)^2+y^2}} & \text{(C.116)} \\ (L,0): \quad \rho^r(x,y) &= \frac{N_0}{a} \frac{k}{2\pi} e^{-k\sqrt{(x-L)^2+y^2}} & \text{(C.117)} \end{aligned}$$

and calculate the total density of microtubules

$$\begin{aligned} & \rho(x,y) & \text{(C.118)} \\ = \ & \rho^l(x,y) \rho^r(x,y) \\ = \ & \frac{N_0^2}{a^2} \frac{k^2}{2\pi^2} e^{-k\left(\sqrt{(x+L)^2+y^2} + \sqrt{(x-L)^2+y^2}\right)} \end{aligned}$$

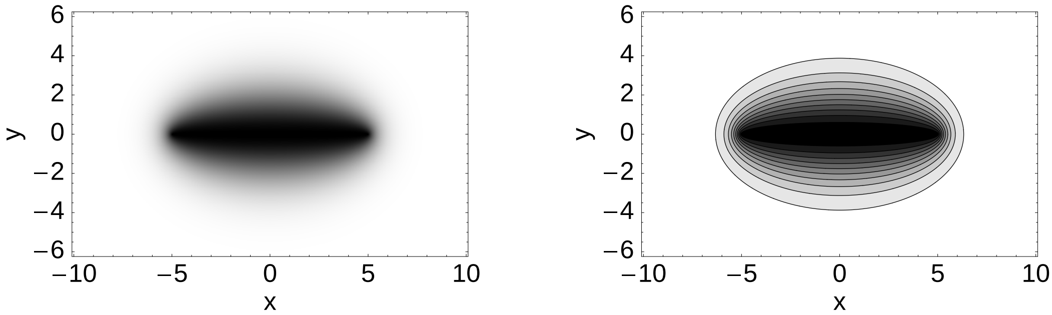

Figure C.2: Most material in a spindle is centered along the spindle axis. Left: microtubule density of two isotropic asters centered at $x \pm L, y = 0$ respectively. Darker shading represents higher density. Right: contour plot of the same arrangement.

It is not trivial to integrate this expression analytically over space. We can however easily gain a feeling for the density by plotting the total density like in Fig. C.2. It is obvious that the MT density is highest around the spindle axis between the two centers of the asters.

The analytical 1D description presented in chapter 4 seems thus to be a sensible approximation to the two dimensional case, as it covers most of the spindle material.

C.5 Additional Force Contributions of Motor Dimers

Here we present the calculations for the remaining kinds of motor dimers bound to two asters.

C.5.1 Motors bound in the Bulk

The calculation for motors bound to the bulk right of both asters (region (c)) is detailed in section C.1.1. Here we present the derivation of the explicit expressions for the other two regions (a) and (b).

Parallel minus-microtubules (region (a)). Left of both asters the velocities are given by

$$\dot{x}_1 = -v_1 + \dot{L} \tag{C.119}$$

$$\dot{x}_2 = -v_2 - \dot{L} \tag{C.120}$$

where the negative sign in front of v_1 and v_2 is due to the orientation of the microtubules. Repeating the calculation outlined by Eqs. (C.1)-(C.7) for this case yields

$$f_1 = \frac{v_b - v_a + 2\dot{L}}{\chi_a + \chi_b} \tag{C.121}$$

$$\dot{x} = -\frac{\chi_a v_b + \chi_b v_a}{\chi_a + \chi_b} + \frac{\chi_b - \chi_a}{\chi_a + \chi_b}\dot{L} \quad , \tag{C.122}$$

which directly leads to the force exerted by the dimer as given in Eq. (C.12). The resulting force contributions for different motor dimers between stationary asters are summarized in table C.13. Averaging over the possible binding configurations we obtain the expression for $\mathcal{F}$ given in Eq. (C.13).

Complex	p-p	m-m	p-m	m-p
Fig. 4.5a				
Velocities	$v_a > 0, v_b > 0$	$v_a < 0, v_b < 0$	$v_a > 0, v_b < 0$	$v_a < 0, v_b > 0$
Forces	$f_1 = \frac{v_b - v_a}{\chi_a + \chi_b}$	$f_1 = \frac{v_b - v_a}{\chi_a + \chi_b}$	$f_1 = \frac{v_b - v_a}{\chi_a + \chi_b} < 0$	$f_1 = \frac{v_b - v_a}{\chi_a + \chi_b} > 0$
	$f = -f_1$	$f = -f_1$	$f = -f_1 > 0$	$f = -f_1 < 0$
Effect	depends	depends	expansive	contractile

Table C.13: Force contributions of different motor dimers bound to the bulk of two MTs left of both asters (region (a)). The asters are assumed to be stationary ($\dot{L} = 0$).

Complex	p-p	m-m	p-m	m-p
Fig. 4.5b				
Velocities	$v_a > 0, v_b > 0$	$v_a < 0, v_b < 0$	$v_a > 0, v_b < 0$	$v_a < 0, v_b > 0$
Forces	$f_1 = \frac{-v_a - v_b}{\chi_a + \chi_b}$	$f_1 = \frac{-v_a - v_b}{\chi_a + \chi_b}$	$f_1 = \frac{-v_a - v_b}{\chi_a + \chi_b}$	$f_1 = \frac{-v_a - v_b}{\chi_a + \chi_b}$
	$f = -f_1 > 0$	$f = -f_1 < 0$	$f = -f_1$	$f = -f_1$
Effect	expansive	contractile	depends	depends

Table C.14: Force contributions of different individual motor dimers bound to the bulk of two MTs between both asters. The asters are assumed to be stationary ($\dot{L} = 0$).

Between the Asters: Antiparallel Microtubules (region (b)) The detailed calculation for this region is given by Eqs. (C.14)-(C.20). Table C.14 gives the explicit force contributions for the various kinds of motor dimers.

C.5.2 Forces due to Interactions between Bulk and $\oplus$-end

The results for motors left of both asters in region (a) is given in the main text in table C.2 and Eq. (C.21). Here we present the explicit results for the remaining two regions (b) and (c).

Between Both Asters: Antiparallel Microtubules (region (b)). The explicit expressions for four kinds of motor dimers are summarized in table C.15.

Complex	p-p	m-m	p-m	m-p
Fig. 4.6b (i)				
Velocities	$v_a = 0, v_b > 0$	$v_a < 0, v_b < 0$	$v_a = 0, v_b < 0$	$v_a < 0, v_b > 0$
Forces	$f_1 = \frac{-v_b}{\chi_a + \chi_b}$ $f = -f_1$	$f_1 = \frac{-v_a - v_b}{\chi_a + \chi_b}$ $f = -f_1$	$f_1 = \frac{-v_b}{\chi_a + \chi_b}$ $f = -f_1$	$f_1 = \frac{-v_a - v_b}{\chi_a + \chi_b}$ $f = -f_1$
Effect	expansive	contractile	contractile	depends
Fig. 4.6b (ii)				
Velocities	$v_a > 0, v_b = 0$	$v_a < 0, v_b < 0$	$v_a > 0, v_b < 0$	$v_a < 0, v_b = 0$
Forces	$f_1 = \frac{-v_a}{\chi_a + \chi_b}$ $f = -f_1$	$f_1 = \frac{-v_a - v_b}{\chi_a + \chi_b}$ $f = -f_1$	$f_1 = \frac{-v_a - v_b}{\chi_a + \chi_b}$ $f = -f_1$	$f_1 = \frac{-v_a}{\chi_a + \chi_b}$ $f = -f_1$
Effect	expansive	contractile	depends	contractile

Table C.15: Force contributions of different motor dimers bound to bulk and one $\oplus$-end of MTs between of both asters (region(b)). The asters are assumed to be stationary ($\dot{L} = 0$).

We have to exercise some care as the force contribution generally depends on which of the two binding possibilities (i) or (ii) the motor is in, cf. Fig. 4.6. We illustrate this point considering a hetero-dimer (w.o.l.g: $v_a \le 0 \le v_b$). As $v_a < 0$ the a motor is not affected by the $\oplus$-end. In case (i) the b motor is only affected when bound to MT 1:

$$\mathcal{F} = -\langle f_1 \rangle = -\frac{1}{2}\frac{-v_a - v_b + 2\dot{L}}{\chi_a + \chi_b} - \frac{1}{2}\frac{-v_a + 2\dot{L}}{\chi_a + \chi_b} = \frac{1}{2}\frac{2v_a + v_b - 4\dot{L}}{\chi_a + \chi_b} \tag{C.123}$$

and in case (ii):

$$\mathcal{F} = -\langle f_1 \rangle = -\frac{1}{2}\frac{-v_a + 2\dot{L}}{\chi_a + \chi_b} - \frac{1}{2}\frac{-v_a - v_b + 2\dot{L}}{\chi_a + \chi_b} = \frac{1}{2}\frac{2v_a + v_b - 4\dot{L}}{\chi_a + \chi_b} \tag{C.124}$$

Averaging over these two cases leads to the average force contribution of a heterodimer bound to a $\oplus$-end in region (b):

$$\mathcal{F} = \frac{1}{2}\left(\frac{1}{2}\frac{2v_a + v_b - 4\dot{L}}{\chi_a + \chi_b} + \frac{1}{2}\frac{2v_a + v_b - 4\dot{L}}{\chi_a + \chi_b}\right) = \frac{v_a + \frac{1}{2}v_b - 2\dot{L}}{\chi_a + \chi_b} \tag{C.125}$$

Right of Both Asters: Parallel Plus-Microtubules (region (c)). The force contribution of a dimer between two parallel $\oplus$-microtubules is given by Eq. (C.8). Either one of the two motors may be bound to an end of a MTs originating from either aster (cf. Fig. 4.6c (i) and (ii)). Table C.16 summarizes the results:

Complex	p-p	m-m	p-m	m-p
Fig. 4.6c (i)				
Velocities	$v_a = 0, v_b > 0$	$v_a < 0, v_b < 0$	$v_a = 0, v_b < 0$	$v_a < 0, v_b > 0$
Forces	$f_1 = \frac{v_b}{\chi_a + \chi_b}$ $f = f_1$	$f_1 = \frac{v_b - v_a}{\chi_a + \chi_b}$ $f = f_1$	$f_1 = \frac{v_b}{\chi_a + \chi_b}$ $f = f_1$	$f_1 = \frac{v_b - v_a}{\chi_a + \chi_b}$ $f = f_1$
Effect	expansive	depends	contractile	depends
Fig. 4.6c (ii)				
Velocities	$v_a > 0, v_b = 0$	$v_a < 0, v_b < 0$	$v_a > 0, v_b < 0$	$v_a < 0, v_b = 0$
Forces	$f_1 = \frac{-v_a}{\chi_a + \chi_b}$ $f = f_1$	$f_1 = \frac{v_b - v_a}{\chi_a + \chi_b}$ $f = f_1$	$f_1 = \frac{v_b - v_a}{\chi_a + \chi_b}$ $f = f_1$	$f_1 = \frac{-v_a}{\chi_a + \chi_b}$ $f = f_1$
Effect	contractile	depends	depends	expansive

Table C.16: Force contributions of different motor dimers bound to bulk and one $\oplus$end of MTs right of both asters (region (c)). The asters are assumed to be stationary ($\dot{L} = 0$).

And for the heterodimers we otain (w.o.l.g: $v_a \leq 0 \leq v_b$):

$$\mathcal{F} = \langle f_1 \rangle = \frac{1}{2}\frac{v_b - v_a - 2\dot{L}}{\chi_a + \chi_b} + \frac{1}{2}\frac{v_a - 2\dot{L}}{\chi_a + \chi_b} = \frac{1}{2}\frac{v_b - 4\dot{L}}{\chi_a + \chi_b} \tag{C.126}$$

and in case (ii):

$$\mathcal{F} = \langle f_1 \rangle = +\frac{1}{2}\frac{-v_a - 2\dot{L}}{\chi_a + \chi_b} + \frac{1}{2}\frac{v_a - v_b - 2\dot{L}}{\chi_a + \chi_b} = \frac{1}{2}\frac{-v_b - 4\dot{L}}{\chi_a + \chi_b} \tag{C.127}$$

and combined

$$\mathcal{F} = \frac{1}{2}\left(\frac{1}{2}\frac{v_b - 4\dot{L}}{\chi_a + \chi_b} + \frac{1}{2}\frac{-v_b - 4\dot{L}}{\chi_a + \chi_b}\right) = \frac{-2\dot{L}}{\chi_a + \chi_b} \quad , \tag{C.128}$$

which means that heterodimers right of both asters effectively act as passive crosslinkers.

C.5.3 Forces due to Interactions between Bulk and $\ominus$-end

Complex	p-p	m-m	p-m	m-p
Fig. C.1a				
Velocities	$v_a > 0, v_b > 0$	$v_a < 0, v_b = 0$	$v_a > 0, v_b = 0$	$v_a < 0, v_b > 0$
Forces	$f_1 = \frac{v_b - v_a}{\chi_a + \chi_b}$ $f = -f_1$	$f_1 = \frac{-v_a}{\chi_a + \chi_b} > 0$ $f = -f_1 < 0$	$f_1 = \frac{-v_a}{\chi_a + \chi_b} < 0$ $f = -f_1 > 0$	$f_1 = \frac{v_b - v_a}{\chi_a + \chi_b} > 0$ $f = -f_1 < 0$
$\mathcal{F} =$	0	$-\frac{1}{2}\frac{-v_a - v_b}{\chi_a + \chi_b} < 0$	n.a.	n.a.
Effect	passive	contractile	expansive	contractile

Table C.17: Force contributions of different motor dimers bound to bulk and one $\ominus$-end of MTs left of both centrosomes (region (a)). The asters are assumed to be stationary ($\dot{L} = 0$).

Left of Both Asters: Parallel Minus-Microtubules (region (a)).

Complex	p-p	m-m	p-m	m-p
Fig. C.1b (i)				
Velocities	$v_a > 0, v_b > 0$	$v_a = 0, v_b < 0$	$v_a > 0, v_b < 0$	$v_a = 0, v_b > 0$
Forces	$f_1 = \frac{-v_a - v_b}{\chi_a + \chi_b}$	$f_1 = \frac{-v_b}{\chi_a + \chi_b}$	$f_1 = \frac{-v_a - v_b}{\chi_a + \chi_b}$	$f_1 = \frac{-v_b}{\chi_a + \chi_b}$
	$f = -f_1 > 0$	$f = -f_1 < 0$	$f = -f_1$	$f = -f_1 > 0$
Effect	expansive	contractile	depends	expansive
Fig. C.1b (ii)				
Velocities	$v_a > 0, v_b > 0$	$v_a < 0, v_b = 0$	$v_a > 0, v_b = 0$	$v_a < 0, v_b > 0$
Forces	$f_1 = \frac{-v_a - v_b}{\chi_a + \chi_b}$	$f_1 = \frac{-v_a}{\chi_a + \chi_b}$	$f_1 = \frac{-v_a}{\chi_a + \chi_b}$	$f_1 = \frac{-v_a - v_b}{\chi_a + \chi_b}$
	$f = -f_1 > 0$	$f = -f_1 < 0$	$f = -f_1 > 0$	$f = -f_1$
Effect	expansive	contractile	expansive	depends

Table C.18: Force contributions of different motor dimers bound to bulk and one $\ominus$-end of MTs between of both centrosomes (region (b)). The asters are assumed to be stationary ($\dot{L} = 0$).

Between Both Asters: Antiparallel Microtubules (region (b)).

Complex	p-p	m-m	p-m	m-p
Fig. C.1c				
Velocities	$v_a > 0, v_b > 0$	$v_a = 0, v_b < 0$	$v_a > 0, v_b < 0$	$v_a = 0, v_b > 0$
Forces	$f_1 = \frac{v_b - v_a}{\chi_a + \chi_b}$	$f_1 = \frac{v_b}{\chi_a + \chi_b}$	$f_1 = \frac{v_b - v_a}{\chi_a + \chi_b}$	$f_1 = \frac{v_b}{\chi_a + \chi_b}$
	$f = f_1$	$f = f_1 < 0$	$f = f_1 < 0$	$f = f_1 > 0$
$\mathcal{F} =$	0	$\frac{1}{2}\frac{v_a + v_b}{\chi_a + \chi_b} < 0$	n.a.	n.a.
Effect	passive	contractile	contractile	expansive

Table C.19: Force contributions of different motor dimers bound to bulk and one $\ominus$-end of MTs right of both centrosomes (region (c)). The asters are assumed to be stationary ($\dot{L} = 0$).

Right of Both Asters: Parallel Plus-Microtubules (region (c)).

D Stability of the Contractile Ring

The contractile ring forms on a cell with radius R_0 and starts to contract in response to a cellular signal. In our description this signal corresponds to changing the parameter corresponding to stress generation from $A = 0$ to some $A > 0$, see Eq. 6.6. The value of A determines how much stress is generated by active processes in the ring and how far the ring can contract. For the two limiting cases of

i no polymerization and depolymerization and

ii fast polymerization and depolymerization

in the ring we obtain analytic expressions for the minimal radii in dependence of A.

(i) In the absence of polymerization and depolymerization the radius in dependence of A is given by

$$\begin{aligned} R(A) \;=\;& \frac{1}{6}\Bigg(2R_0 \\ &+\frac{(2\cdot 2^{2/3}k\pi^{1/3}R_0^2)}{(-27Ak^2N^2N_\mathrm{b}+4k^3\pi R_0^3+3\sqrt{3}\sqrt{Ak^4N^2N_\mathrm{b}(27AN^2N_\mathrm{b}-8k\pi R_0^3)})^{1/3}} \\ &+\frac{1}{k\pi^{1/3}}\left[-54Ak^2N^2N_\mathrm{b}+8k^3\pi R_0^3+6\sqrt{3}\sqrt{Ak^4N^2N_\mathrm{b}(27AN^2N_\mathrm{b}-8k\pi R_0^3)}\right]^{1/3}\Bigg)\,. \end{aligned} \tag{D.1}$$

(ii) When polymerization and depolymerization are fast compared to the contraction dynamics, the radius $R(A)$ is given by

$$R(A) = R_0 - \frac{2\pi N_\mathrm{b} A k_\mathrm{p}^2}{k k_\mathrm{d}^2} \quad . \tag{D.2}$$

The ring thus fully contracts (R(A)=0) for values of A larger than a critical value $A \geq A_c$ with $R(A_c) = 0$. The radius $R(A) \in [0; R_0]$ is always stable.

Bibliography

Akhmanova, A. and Hoogenraad, C. (2005). Microtubule plus-end-tracking proteins: mechanisms and functions. *Curr Opin Cell Biol*, 17(1):47–54.

Alberts, B., Johnson, A., Lewis, J., Raff, M., Roberts, K., and Walter, P. (2002). *Molecular Biology of the Cell*. Garland Science.

Andersen, S. (2000). Spindle assembly and the art of regulating microtubule dynamics by MAPs and Stathmin/Op18. *Trends Cell Biol*, 10(7):261–7.

Anderson, D., Gueiros-Filho, F., and Erickson, H. (2004). Assembly dynamics of FtsZ rings in Bacillus subtilis and Escherichia coli and effects of FtsZ-regulating proteins. *J Bacteriol*, 186(17):5775–81.

Asbury, C. (2005). Kinesin: world's tiniest biped. *Curr Opin Cell Biol*, 17(1):89–97.

Badoual, M., Julicher, F., and Prost, J. (2002). Bidirectional cooperative motion of molecular motors. *Proc Natl Acad Sci U S A*, 99(10):6696–701.

Balasubramanian, M., Bi, E., and Glotzer, M. (2004). Comparative analysis of cytokinesis in budding yeast, fission yeast and animal cells. *Curr Biol*, 14(18):R806–18.

Balland, M., Richert, A., and Gallet, F. (2005). The dissipative contribution of myosin II in the cytoskeleton dynamics of myoblasts. *Eur Biophys J*, 34(3):255–61.

Bamburg, J., McGough, A., and Ono, S. (1999). Putting a new twist on actin: ADF/cofilins modulate actin dynamics. *Trends Cell Biol*, 9(9):364–70.

Banik, S., Kruse, K., and Jülicher, F. (2005). Ring Formation by Polar Order. *in preparation*.

Bassetti, B., Cosentino-Lagomarsino, M., and Jona, P. (2000). A model for the self-organization of microtubules driven by molecular motors. *Eur. Phys. J. B*, 15:483–492.

Beil, M., Micoulet, A., von Wichert, G., Paschke, S., Walther, P., Omary, M., Van Veldhoven, P., Gern, U., Wolff-Hieber, E., Eggermann, J., Waltenberger, J., Adler, G., Spatz, J., and Seufferlein, T. (2003). Sphingosylphosphorylcholine regulates keratin network architecture and visco-elastic properties of human cancer cells. *Nat Cell Biol*, 5(9):803–11.

Bi, E., Maddox, P., Lew, D., Salmon, E., McMillan, J., Yeh, E., and Pringle, J. (1998). Involvement of an actomyosin contractile ring in Saccharomyces cerevisiae cytokinesis. *J Cell Biol*, 142(5):1301–12.

Biron, D., Alvarez-Lacalle, E., Tlusty, T., and Moses, E. (2005). Molecular Model of the Contractile Ring. *Phys Rev Lett*, 95:098102.

Blanchoin, L. and Pollard, T. (1999). Mechanism of interaction of Acanthamoeba actophorin (ADF/Cofilin) with actin filaments. *J Biol Chem*, 274(22):15538–46.

Blanchoin, L. and Pollard, T. (2002). Hydrolysis of ATP by polymerized actin depends on the bound divalent cation but not profilin. *Biochemistry*, 41(2):597–602.

Block, S., Asbury, C., Shaevitz, J., and Lang, M. (2003). Probing the kinesin reaction cycle with a 2D optical force clamp. *Proc Natl Acad Sci U S A*, 100(5):2351–6.

Block, S., Goldstein, L., and Schnapp, B. (1990). Bead movement by single kinesin molecules studied with optical tweezers. *Nature*, 348(6299):348–52.

Bornens, M., Paintrand, M., and Celati, C. (1989). The cortical microfilament system of lymphoblasts displays a periodic oscillatory activity in the absence of microtubules: implications for cell polarity. *J Cell Biol*, 109(3):1071–83.

Boukellal, H., Campas, O., Joanny, J., Prost, J., and Sykes, C. (2004). Soft Listeria: actin-based propulsion of liquid drops. *Phys Rev E Stat Nonlin Soft Matter Phys*, 69(6):061906.

Bourdieu, L., Duke, T., Elowitz, M., Winkelmann, D., Leibler, S., and Libchaber, A. (1995). Spiral defects in motility assays: A measure of motor protein force. *Phys Rev Lett*, 75(1):176–179.

Bray, D. (2001). *Cell movements: from molecules to motility*. Garland, New York, 2nd edition.

Bretschneider, T., Diez, S., Anderson, K., Heuser, J., Clarke, M., Muller-Taubenberger, A., Kohler, J., and Gerisch, G. (2004). Dynamic actin patterns and Arp2/3 assembly at the substrate-attached surface of motile cells. *Curr Biol*, 14(1):1–10.

Bringmann, H., Skiniotis, G., Spilker, A., Kandels-Lewis, S., Vernos, I., and Surrey, T. (2004). A kinesin-like motor inhibits microtubule dynamic instability. *Science*, 303(5663):1519–22.

Bucciarelli, E., Giansanti, M., Bonaccorsi, S., and Gatti, M. (2003). Spindle assembly and cytokinesis in the absence of chromosomes during Drosophila male meiosis. *J Cell Biol*, 160(7):993–9.

Burton, K. and Taylor, D. (1997). Traction forces of cytokinesis measured with optically modified elastic substrata. *Nature*, 385(6615):450–4.

Carlier, M. and Pantaloni, D. (1986). Direct evidence for ADP-Pi-F-actin as the major intermediate in ATP-actin polymerization. Rate of dissociation of Pi from actin filaments. *Biochemistry*, 25(24):7789–92.

Carlier, M., Pantaloni, D., Evans, J., Lambooy, P., Korn, E., and Webb, M. (1988). The hydrolysis of ATP that accompanies actin polymerization is essentially irreversible. *FEBS Lett*, 235(1-2):211–4.

Carlier, M., Ressad, F., and Pantaloni, D. (1999). Control of actin dynamics in cell motility. Role of ADF/cofilin. *J Biol Chem*, 274(48):33827–30.

Chakravarty, A., Howard, L., and Compton, D. (2004). A mechanistic model for the organization of microtubule asters by motor and non-motor proteins in a mammalian mitotic extract. *Mol Biol Cell*, 15(5):2116–32.

Chan, J., Calder, G., Doonan, J., and Lloyd, C. (2003). EB1 reveals mobile microtubule nucleation sites in Arabidopsis. *Nat Cell Biol*, 5(11):967–71.

Chan, J., Calder, G., Fox, S., and Lloyd, C. (2005). Localization of the Microtubule End Binding Protein EB1 Reveals Alternative Pathways of Spindle Development in Arabidopsis Suspension Cells. *Plant Cell*, 17(6):1737–48.

Condeelis, J. and Taylor, D. (1977). The contractile basis of amoeboid movement. V. The control of gelation, solation, and contraction in extracts from Dictyostelium discoideum. *J Cell Biol*, 74(3):901–27.

Cooper, J. and Schafer, D. (2000). Control of actin assembly and disassembly at filament ends. *Curr Opin Cell Biol*, 12(1):97–103.

Cosentino-Lagomarsino, M. (2004). *Biologically Inspired Problems Concerning Semiflexible Filaments*. PhD thesis, Univ. Leiden.

Cramer, L., Siebert, M., and Mitchison, T. (1997). Identification of novel graded polarity actin filament bundles in locomoting heart fibroblasts: implications for the generation of motile force. *J Cell Biol*, 136(6):1287–305.

Cross, M. and Hohenberg, P. C. (1993). Pattern formation outside of equilibrium. *Rev Mod Phys*, 65:851–1112.

Cytrynbaum, E., Rodionov, V., and Mogilner, A. (2004). Computational model of dynein-dependent self-organization of microtubule asters. *J Cell Sci*, 117:1381–97.

de Gennes, P. and Prost, J. (1993). *The Physics of Liquid Crystals*. Clarendon Press, Oxford, 2nd edition.

De La Cruz, E., Ostap, E., Brundage, R., Reddy, K., Sweeney, H., and Safer, D. (2000). Thymosin-beta(4) changes the conformation and dynamics of actin monomers. *Biophys J*, 78(5):2516–27.

DeBiasio, R., LaRocca, G., Post, P., and Taylor, D. (1996). Myosin II transport, organization, and phosphorylation: evidence for cortical flow/solation-contraction coupling during cytokinesis and cell locomotion. *Mol Biol Cell*, 7(8):1259–82.

Desai, A. (2000). Kinetochores. *Curr Biol*, 10(14):R508.

Desai, A. and Mitchison, T. (1997). Microtubule polymerization dynamics. *Annu Rev Cell Dev Biol*, 13:83–117.

Dewar, H., Tanaka, K., Nasmyth, K., and Tanaka, T. (2004). Tension between two kinetochores suffices for their bi-orientation on the mitotic spindle. *Nature*, 428(6978):93–7.

Dhonukshe, P. and Gadella, Jr, T. (2003). Alteration of microtubule dynamic instability during preprophase band formation revealed by yellow fluorescent protein-CLIP170 microtubule plus-end labeling. *Plant Cell*, 15(3):597–611.

DiBella, L. and King, S. (2001). Dynein motors of the Chlamydomonas flagellum. *Int Rev Cytol*, 210:227–68.

Dickinson, R., Caro, L., and Purich, D. (2004). Force generation by cytoskeletal filament end-tracking proteins. *Biophys J*, 87(4):2838–54.

Didry, D., Carlier, M., and Pantaloni, D. (1998). Synergy between actin depolymerizing factor/cofilin and profilin in increasing actin filament turnover. *J Biol Chem*, 273(40):25602–11.

Döbereiner, H., Dubin-Thaler, B., Giannone, G., Xenias, H., and Sheetz, M. (2004). Dynamic phase transitions in cell spreading. *Phys Rev Lett*, 93(10):108105.

Dogterom, M., Janson, M., Faivre-Moskalenko C., van der Horst, A., Kerssesmakers J.W.J., Tanase, C., and Mulder, B. (2002). Force generation by polymerizing microtubules. *Appl Phys A*, 75:331–336.

Dogterom, M., Kerssemakers, J., Romet-Lemonne, G., and Janson, M. (2005). Force generation by dynamic microtubules. *Curr Opin Cell Biol*, 17(1):67–74.

Dogterom, M. and Leibler, S. (1993). Physical aspects of the growth and regulation of microtubule structures. *Phys Rev Lett*, 70(9):1347–1350.

Dogterom, M. and Yurke, B. (1997). Measurement of the force-velocity relation for growing microtubules. *Science*, 278(5339):856–60.

dos Remedios, C., Chhabra, D., Kekic, M., Dedova, I., Tsubakihara, M., Berry, D., and Nosworthy, N. (2003). Actin binding proteins: regulation of cytoskeletal microfilaments. *Physiol Rev*, 83(2):433–73.

dos Remedios, C. and Thomas, D. (2001). *Molecular Interactions of Actin. Actin Structure and Actin Binding Proteins*. Springer Verlag, Heidelberg.

Dubin-Thaler, B., Giannone, G., Döbereiner, H., and Sheetz, M. (2004). Nanometer analysis of cell spreading on matrix-coated surfaces reveals two distinct cell states and STEPs. *Biophys J*, 86(3):1794–806.

Duke, T. (1999). Molecular model of muscle contraction. *Proc Natl Acad Sci U S A*, 96(6):2770–5.

Duke, T. (2002a). *Modelling Motor Protein Systems*, chapter 3, pages 95–143. Les Houches Lecture Notes, Springer.

Duke, T. (2002b). Push or pull? Teams of motor proteins have it both ways. *Proc Natl Acad Sci U S A*, 99(10):6521–3.

Fabry, B., Maksym, G., Butler, J., Glogauer, M., Navajas, D., and Fredberg, J. (2001). Scaling the microrheology of living cells. *Phys Rev Lett*, 87(14):148102.

Faruki, S., Cole, R., and Rieder, C. (2002). Separating centrosomes interact in the absence of associated chromosomes during mitosis in cultured vertebrate cells. *Cell Motil Cytoskeleton*, 52(2):107–21.

Feierbach, B. and Chang, F. (2001). Cytokinesis and the contractile ring in fission yeast. *Curr Opin Microbiol*, 4(6):713–9.

Finer, J., Simmons, R., and Spudich, J. (1994). Single myosin molecule mechanics: piconewton forces and nanometre steps. *Nature*, 368(6467):113–9.

Fishkind, D. and Wang, Y. (1993). Orientation and three-dimensional organization of actin filaments in dividing cultured cells. *J Cell Biol*, 123(4):837–48.

Frixione, E. (2000). Recurring views on the structure and function of the cytoskeleton: a 300-year epic. *Cell Motil Cytoskeleton*, 46(2):73–94.

Fujiwara, K. and Pollard, T. (1976). Fluorescent antibody localization of myosin in the cytoplasm, cleavage furrow, and mitotic spindle of human cells. *J Cell Biol*, 71(3):848–75.

Gadde, S. and Heald, R. (2004). Mechanisms and molecules of the mitotic spindle. *Curr Biol*, 14(18):R797–805.

Gaetz, J. and Kapoor, T. (2004). Dynein/dynactin regulate metaphase spindle length by targeting depolymerizing activities to spindle poles. *J Cell Biol*, 166(4):465–71.

Galjart, N. (2005). CLIPs and CLASPs and cellular dynamics. *Nat Rev Mol Cell Biol*, 6(6):487–98.

Gerisch, G. and Weber, I. (2000). Cytokinesis without myosin II. *Curr Opin Cell Biol*, 12(1):126–32.

Giannone, G., Dubin-Thaler, B., Döbereiner, H., Kieffer, N., Bresnick, A., and Sheetz, M. (2004). Periodic lamellipodial contractions correlate with rearward actin waves. *Cell*, 116(3):431–43.

Gibbons, I. (1981). Cilia and flagella of eukaryotes. *J Cell Biol*, 91(3 Pt 2):107s–124s.

Ginzburg, V. and Landau, L. (1950). On the theory of superconductivity. *Zh Eksp Teor Fiz*, 20:1064.

Glotzer, M. (2004). Cleavage furrow positioning. *J Cell Biol*, 164(3):347–51.

Glotzer, M. (2005). The molecular requirements for cytokinesis. *Science*, 307(5716):1735–9.

Gonczy, P., Grill, S., Stelzer, E., Kirkham, M., and Hyman, A. (2001). Spindle positioning during the asymmetric first cell division of *Caenorhabditis elegans* embryos. *Novartis Found Symp*, 237:164–75; discussion 176–81.

Goshima, G. and Vale, R. (2003). The roles of microtubule-based motor proteins in mitosis: comprehensive RNAi analysis in the Drosophila S2 cell line. *J Cell Biol*, 162(6):1003–16.

Grill, S., Gonczy, P., Stelzer, E., and Hyman, A. (2001). Polarity controls forces governing asymmetric spindle positioning in the *Caenorhabditis elegans* embryo. *Nature*, 409(6820):630–3.

Grill, S., Howard, J., Schaffer, E., Stelzer, E., and Hyman, A. (2003). The distribution of active force generators controls mitotic spindle position. *Science*, 301(5632):518–21.

Grill, S. and Hyman, A. (2005). Spindle positioning by cortical pulling forces. *Dev Cell*, 8(4):461–5.

Grill, S., Kruse, K., and Jülicher, F. (2005). Theory of mitotic spindle oscillations. *Phys Rev Lett*, 94(10):108104.

Gruenheid, S. and Finlay, B. (2003). Microbial pathogenesis and cytoskeletal function. *Nature*, 422(6933):775–81.

Guertin, D., Trautmann, S., and McCollum, D. (2002). Cytokinesis in eukaryotes. *Microbiol Mol Biol Rev*, 66(2):155–78.

Guha, M., Zhou, M., and Wang, Y. (2005). Cortical actin turnover during cytokinesis requires myosin II. *Curr Biol*, 15(8):732–6.

He, X. and Dembo, M. (1997). On the mechanics of the first cleavage division of the sea urchin egg. *Exp Cell Res*, 233(2):252–73.

Heald, R., Tournebize, R., Blank, T., Sandaltzopoulos, R., Becker, P., Hyman, A., and Karsenti, E. (1996). Self-organization of microtubules into bipolar spindles around artificial chromosomes in Xenopus egg extracts. *Nature*, 382(6590):420–5.

Heald, R., Tournebize, R., Habermann, A., Karsenti, E., and Hyman, A. (1997). Spindle assembly in Xenopus egg extracts: respective roles of centrosomes and microtubule self-organization. *J Cell Biol*, 138(3):615–28.

Heald, R. and Walczak, C. (1999). Microtubule-based motor function in mitosis. *Curr Opin Struct Biol*, 9(2):268–74.

Hill, T. (1987). *Linear Aggregation Theory in Cell Biology.* Springer Series in Molecular Biology. Springer.

Hinz, B. and Gabbiani, G. (2003). Mechanisms of force generation and transmission by myofibroblasts. *Curr Opin Biotechnol*, 14(5):538–46.

Hodge, T. and Cope, M. (2000). A myosin family tree. *J Cell Sci*, 113:3353–4.

Hodgkin, A. L. and Huxley, A. F. (1952). A quantitative description of membrane current and its application to conduction and excitation in nerve. *J Physiol*, 117:500–544.

Holmes, K., Popp, D., Gebhard, W., and Kabsch, W. (1990). Atomic model of the actin filament. *Nature*, 347(6288):44–9.

Howard, J. (2001). *Mechanics of Motor Proteins and the Cytoskeleton.* Sinauer Press, Sunderland, MA.

Howard, J., Hudspeth, A., and Vale, R. (1989). Movement of microtubules by single kinesin molecules. *Nature*, 342(6246):154–8.

Hudspeth, A. (2005). How the ear's works work: mechanoelectrical transduction and amplification by hair cells. *C R Biol*, 328(2):155–62.

Huxley, A. and Niedergerke, R. (1954). Structural changes in muscle during contraction; interference microscopy of living muscle fibres. *Nature*, 173(4412):971–3.

Huxley, H. (1963). Electron Microscope Studies on the Structure of Natural and Synthetic Protein Filaments from Striated Muscle. *J Mol Biol*, 77:281–308.

Hyman, A. and Karsenti, E. (1996). Morphogenetic properties of microtubules and mitotic spindle assembly. *Cell*, 84(3):401–10.

Ichetovkin, I., Han, J., Pang, K., Knecht, D., and Condeelis, J. (2000). Actin filaments are severed by both native and recombinant dictyostelium cofilin but to different extents. *Cell Motil Cytoskeleton*, 45(4):293–306.

Inoue, S. and Salmon, E. (1995). Force generation by microtubule assembly/disassembly in mitosis and related movements. *Mol Biol Cell*, 6(12):1619–40.

Janmey, P., Euteneuer, U., Traub, P., and Schliwa, M. (1991). Viscoelastic properties of vimentin compared with other filamentous biopolymer networks. *J Cell Biol*, 113(1):155–60.

Janson, M., de Dood, M., and Dogterom, M. (2003). Dynamic instability of microtubules is regulated by force. *J Cell Biol*, 161(6):1029–34.

Janson, M. and Dogterom, M. (2004a). A bending mode analysis for growing microtubules: evidence for a velocity-dependent rigidity. *Biophys J*, 87(4):2723–36.

Janson, M. and Dogterom, M. (2004b). Scaling of microtubule force-velocity curves obtained at different tubulin concentrations. *Phys Rev Lett*, 92(24):248101.

Joglekar, A. and Hunt, A. (2002). A simple, mechanistic model for directional instability during mitotic chromosome movements. *Biophys J*, 83(1):42–58.

Jülicher, F., Ajdari, A., and Prost, J. (1997). Modeling molecular motors. *Rev Mod Phys*, 69(4):1269–1281.

Jülicher, F. and Prost, J. (1995). Cooperative molecular motors. *Phys Rev Lett*, 75(13):2618–2621.

Jülicher, F. and Prost, J. (1997). Spontaneous Oscillations of Collective Molecular Motors. *Phys Rev Lett*, 78(23):4510–4513.

Jurgens, G. (2005). Plant cytokinesis: fission by fusion. *Trends Cell Biol*, 15(5):277–83.

Kabsch, W., Mannherz, H., Suck, D., Pai, E., and Holmes, K. (1990). Atomic structure of the actin:DNase I complex. *Nature*, 347(6288):37–44.

Kapitein, L., Peterman, E., Kwok, B., Kim, J., Kapoor, T., and Schmidt, C. (2005). The bipolar mitotic kinesin Eg5 moves on both microtubules that it crosslinks. *Nature*, 435(7038):114–8.

Kapoor, T. and Mitchison, T. (2001). Eg5 is static in bipolar spindles relative to tubulin: evidence for a static spindle matrix. *J Cell Biol*, 154(6):1125–33.

Karki, S. and Holzbaur, E. (1999). Cytoplasmic dynein and dynactin in cell division and intracellular transport. *Curr Opin Cell Biol*, 11(1):45–53.

Karsenti, E. and Nédélec, F. (2004). The mitotic spindle and actin tails. *Biol Cell*, 96(3):237–40.

Khodjakov, A., Cole, R., Oakley, B., and Rieder, C. (2000). Centrosome-independent mitotic spindle formation in vertebrates. *Curr Biol*, 10(2):59–67.

Kim, J., Park, B., Kahng, B., and Lee, H. (2003). Self-organized patterns in mixtures of microtubules and motor proteins. *J Korean Phys Soc*, 42:162.

Kline-Smith, S., Sandall, S., and Desai, A. (2005). Kinetochore-spindle microtubule interactions during mitosis. *Curr Opin Cell Biol*, 17(1):35–46.

Kodama, A., Lechler, T., and Fuchs, E. (2004). Coordinating cytoskeletal tracks to polarize cellular movements. *J Cell Biol*, 167(2):203–7.

Koka, S., Neudauer, C., Li, X., Lewis, R., McCarthy, J., and Westendorf, J. (2003). The formin-homology-domain-containing protein FHOD1 enhances cell migration. *J Cell Sci*, 116:1745–55.

Kolomeisky, A. and Fisher, M. (2001). Force-velocity relation for growing microtubules. *Biophys J*, 80(1):149–54.

Kovar, D., Kuhn, J., Tichy, A., and Pollard, T. (2003). The fission yeast cytokinesis formin Cdc12p is a barbed end actin filament capping protein gated by profilin. *J Cell Biol*, 161(5):875–87.

Kovar, D. and Pollard, T. (2004). Progressing actin: Formin as a processive elongation machine. *Nat Cell Biol*, 6(12):1158–9.

Kreis, T. and Vale, R., editors (1999). *Guidebook to the Cytoskeletal and Motor Proteins*. Oxford UP, 2nd edition.

Kruse, K. (2005). Physical Aspects of Pattern Formation and Force Generation in the Cytoskeleton. *Habilitationsschrift TU Dresden*.

Kruse, K., Camalet, S., and Jülicher, F. (2001). Self-propagating patterns in active filament bundles. *Phys Rev Lett*, 87(13):138101.

Kruse, K., Joanny, J., Jülicher, F., Prost, J., and Sekimoto, K. (2004). Asters, vortices, and rotating spirals in active gels of polar filaments. *Phys Rev Lett*, 92(7):078101.

Kruse, K., Joanny, J., Jülicher, F., Prost, J., and Sekimoto, K. (2005). Generic theory of active polar gels: a paradigm for cytoskeletal dynamics. *Eur Phys J E Soft Matter*, 16(1):5–16.

Kruse, K. and Jülicher, F. (2000). Actively contracting bundles of polar filaments. *Phys Rev Lett*, 85(8):1778–81.

Kruse, K. and Jülicher, F. (2003). Self-organization and mechanical properties of active filament bundles. *Phys Rev E Stat Nonlin Soft Matter Phys*, 67:051913.

Kruse, K. and Jülicher, F. (2005). Oscillations in cell biology. *Curr Opin Cell Biol*, 17(1):20–6.

Kruse, K. and Sekimoto, K. (2002). Growth of fingerlike protrusions driven by molecular motors. *Phys Rev E Stat Nonlin Soft Matter Phys*, 66(3):031904.

Kruse, K., Zumdieck, A., and Jülicher, F. (2003). Continuum theory of contractile fibres. *Europhys Lett*, 64(5):716–722.

Kuchnir Fygenson, D., Flyvbjerg, H., Sneppen, K., Libchaber, A., and Leibler, S. (1995). Spontaneous nucleation of microtubules. *Phys Rev E Stat Nonlin Soft Matter Phys*, 51(5):5058–5063.

Lawrence, C., Dawe, R., Christie, K., Cleveland, D., Dawson, S., Endow, S., Goldstein, L., Goodson, H., Hirokawa, N., Howard, J., Malmberg, R., McIntosh, J., Miki, H., Mitchison, T., Okada, Y., Reddy, A., Saxton, W., Schliwa, M., Scholey, J., Vale, R., Walczak, C., and Wordeman, L. (2004). A standardized kinesin nomenclature. *J Cell Biol*, 167(1):19–22.

Leduc, C. (2005). *Système biomimétique d'intermédiares de transport tubulaires: Etude quantitative*. PhD thesis, Université Paris 7.

Leduc, C., Campàs, O., Zeldovich, K., Roux, A., Jolimaitre, P., Bourel-Bonnet, L., Goud, B., Joanny, J., Bassereau, P., and Prost, J. (2004). Cooperative extraction of membrane nanotubes by molecular motors. *Proc Natl Acad Sci U S A*, 101(49):17096–101.

Lee, H. and Kardar, M. (2001). Macroscopic equations for pattern formation in mixtures of microtubules and molecular motors. *Phys Rev E Stat Nonlin Soft Matter Phys*, 64(5):056113.

Lin, H., Schneider, M., and Kachar, B. (2005). When size matters: the dynamic regulation of stereocilia lengths. *Curr Opin Cell Biol*, 17(1):55–61.

Liverpool, T. (2005). Some aspects of the dynamics of active filament solutions. *J Phys: Condens Matter*, 17:S1153–S1163.

Liverpool, T., Maggs, A., and Ajdari, A. (2001). Viscoelasticity of solutions of motile polymers. *Phys Rev Lett*, 86(18):4171–4.

Liverpool, T. and Marchetti, M. (2003). Instabilities of isotropic solutions of active polar filaments. *Phys Rev Lett*, 90(13):138102.

Liverpool, T. and Marchetti, M. (2005). Bridging the microscopic and the hydrodynamic in active filament solutions. *Europhys Lett*, 69:846–852.

Lombillo, V., Stewart, R., and McIntosh, J. (1995). Minus-end-directed motion of kinesin-coated microspheres driven by microtubule depolymerization. *Nature*, 373(6510):161–4.

Lutkenhaus, J. (2003). Another cytoskeleton in the closet. *Cell*, 115(6):648–50.

Machesky, L., Mullins, R., Higgs, H., Kaiser, D., Blanchoin, L., May, R., Hall, M., and Pollard, T. (1999). Scar, a WASp-related protein, activates nucleation of actin filaments by the Arp2/3 complex. *Proc Natl Acad Sci U S A*, 96(7):3739–44.

Maciver, S., Pope, B., Whytock, S., and Weeds, A. (1998). The effect of two actin depolymerizing factors (ADF/cofilins) on actin filament turnover: pH sensitivity of F-actin binding by human ADF, but not of Acanthamoeba actophorin. *Eur J Biochem*, 256(2):388–97.

Maciver, S., Zot, H., and Pollard, T. (1991). Characterization of actin filament severing by actophorin from Acanthamoeba castellanii. *J Cell Biol*, 115(6):1611–20.

Mahadevan, L. and Mitchison, T. (2005). Cell biology: powerful curves. *Nature*, 435(7044):895–7.

Mahaffy, R., Park, S., Gerde, E., Käs, J., and Shih, C. (2004). Quantitative analysis of the viscoelastic properties of thin regions of fibroblasts using atomic force microscopy. *Biophys J*, 86(3):1777–93.

Maiato, H., Sampaio, P., and Sunkel, C. (2004). Microtubule-associated proteins and their essential roles during mitosis. *Int Rev Cytol*, 241:53–153.

Mallik, R., Carter, B., Lex, S., King, S., and Gross, S. (2004). Cytoplasmic dynein functions as a gear in response to load. *Nature*, 427(6975):649–52.

Mallik, R. and Gross, S. (2004). Molecular motors: strategies to get along. *Curr Biol*, 14(22):R971–82.

Marsland, D. (1970). *High Pressure Effects on Cellular Processes*, pages 259–312. Academic Press, New York.

Marsland, D. and Landau J.V. (1954). The Mechanisms of Cytokinesis: Temperatur-Pressure Studies on the Cortical Gel System in various Marine Eggs. *J Exp Zool*, 125:507–539.

Matzke, R., Jacobson, K., and Radmacher, M. (2001). Direct, high-resolution measurement of furrow stiffening during division of adherent cells. *Nat Cell Biol*, 3(6):607–10.

Maupin, P. and Pollard, T. (1986). Arrangement of actin filaments and myosin-like filaments in the contractile ring and of actin-like filaments in the mitotic spindle of dividing HeLa cells. *J Ultrastruct Mol Struct Res*, 94(1):92–103.

McGough, A., Pope, B., Chiu, W., and Weeds, A. (1997). Cofilin changes the twist of F-actin: implications for actin filament dynamics and cellular function. *J Cell Biol*, 138(4):771–81.

Miao, L., Vanderlinde, O., Stewart, M., and Roberts, T. (2003). Retraction in amoeboid cell motility powered by cytoskeletal dynamics. *Science*, 302(5649):1405–7.

Micoulet, A., Spatz, J., and Ott, A. (2005). Mechanical response analysis and power generation by single-cell stretching. *Chemphyschem*, 6(4):663–70.

Mitchison, T. (1989). Polewards microtubule flux in the mitotic spindle: evidence from photoactivation of fluorescence. *J Cell Biol*, 109(2):637–52.

Mitchison, T., Maddox, P., Gaetz, J., Groen, A., Shirasu, M., Desai, A., Salmon, E., and Kapoor, T. (2005). Roles of Polymerization Dynamics, Opposed Motors and a Tensile Element in Governing the Length of Xenopus Extract Meiotic Spindles. *Mol Biol Cell*.

Mitchison, T. and Salmon, E. (2001). Mitosis: a history of division. *Nat Cell Biol*, 3(1):E17–21.

Mogilner, A. and Oster, G. (1996). Cell motility driven by actin polymerization. *Biophys J*, 71(6):3030–45.

Mogilner, A. and Oster, G. (1999). The polymerization ratchet model explains the force-velocity relation for growing microtubules. *Eur Biophys J*, 28:235–242.

Moller-Jensen, J. and Lowe, J. (2005). Increasing complexity of the bacterial cytoskeleton. *Curr Opin Cell Biol*, 17(1):75–81.

Moore, A. and Wordeman, L. (2004). The mechanism, function and regulation of depolymerizing kinesins during mitosis. *Trends Cell Biol*, 14(10):537–46.

Mullins, R., Heuser, J., and Pollard, T. (1998). The interaction of Arp2/3 complex with actin: nucleation, high affinity pointed end capping, and formation of branching networks of filaments. *Proc Natl Acad Sci U S A*, 95(11):6181–6.

Murthy, K. and Wadsworth, P. (2005). Myosin-II-Dependent Localization and Dynamics of F-Actin during Cytokinesis. *Curr Biol*, 15(8):724–31.

Nakazawa, H. and Sekimoto, K. (1996). Polarity sorting in a bundle of actin filaments by two-headed myosins. *J Phys Soc Jpn*, 65:2404–2407.

Nédélec, F. (2002a). Computer simulations reveal motor properties generating stable antiparallel microtubule interactions. *J Cell Biol*, 158(6):1005–1015.

Nédélec, F. (2002b). Studying the balance of forces in the mitotic spindle with computer simulations. *Mol Biol Cell*, 13:445a–445a.

Nédélec, F. and Surrey, T. (2001). Dynamics of Microtubule Aster Formation by Motor Complexes. *CR Acad Sci Paris*, pages 841–847.

Nédélec, F., Surrey, T., and Karsenti, E. (2003). Self-organisation and forces in the microtubule cytoskeleton. *Curr Opin Cell Biol*, 15(1):118–24.

Nédélec, F., Surrey, T., and Maggs, A. (2001). Dynamic concentration of motors in microtubule arrays. *Phys Rev Lett*, 86(14):3192–5.

Nédélec, F., Surrey, T., Maggs, A., and Leibler, S. (1997). Self-organization of microtubules and motors. *Nature*, 389(6648):305–8.

Niebuhr, K., Ebel, F., Frank, R., Reinhard, M., Domann, E., Carl, U., Walter, U., Gertler, F., Wehland, J., and Chakraborty, T. (1997). A novel proline-rich motif present in ActA of Listeria monocytogenes and cytoskeletal proteins is the ligand for the EVH1 domain, a protein module present in the Ena/VASP family. *EMBO J*, 16(17):5433–44.

Nurse, P. (2003). The great ideas of biology. *Clin Med*, 3(6):560–8.

Oiwa, K. and Sakakibara, H. (2005). Recent progress in dynein structure and mechanism. *Curr Opin Cell Biol*, 17(1):98–103.

Oosawa, F. and Asakura, S. (1975). *Thermodynamics of the Polymerization of Proteins.* Molecular Biology. Academic Press, London.

Otto, J. and Schroeder, T. (1990). Association of actin and myosin in the contractile ring. *Ann N Y Acad Sci*, 582:179–84.

Paluch, E. (2005). *Motilité cellulaire sur des systèmes simplifiés: de l'oscillation au mouvement dirigé.* PhD thesis, Université Paris 7.

Paluch, E., Piel, M., Prost, J., Bornens, M., and Sykes, C. (2005). Cortical actomyosin breakage triggers shape oscillations in cells and cell fragments. *Biophys J*, 89(1):724–33.

Pantaloni, D., Boujemaa, R., Didry, D., Gounon, P., and Carlier, M. (2000). The Arp2/3 complex branches filament barbed ends: functional antagonism with capping proteins. *Nat Cell Biol*, 2(7):385–91.

Pantaloni, D., Le Clainche, C., and Carlier, M. (2001). Mechanism of actin-based motility. *Science*, 292(5521):1502–6.

Pardo, M. and Nurse, P. (2003). Equatorial retention of the contractile actin ring by microtubules during cytokinesis. *Science*, 300(5625):1569–74.

Pelham, R. and Chang, F. (2002). Actin dynamics in the contractile ring during cytokinesis in fission yeast. *Nature*, 419(6902):82–6.

Peskin, C., Odell, G., and Oster, G. (1993). Cellular motions and thermal fluctuations: the Brownian ratchet. *Biophys J*, 65(1):316–24.

Peterson, L., Rajfur, Z., Maddox, A., Freel, C., Chen, Y., Edlund, M., Otey, C., and Burridge, K. (2004). Simultaneous stretching and contraction of stress fibers in vivo. *Mol Biol Cell*, 15(7):3497–508.

Piehl, M. and Cassimeris, L. (2003). Organization and dynamics of growing microtubule plus ends during early mitosis. *Mol Biol Cell*, 14(3):916–25.

Piel, M. and Bornens, M. (2001). Centrosome reproduction in vitro: mammalian centrosomes in Xenopus lysates. *Methods Cell Biol*, 67:289–304.

Plastino, J., Lelidis, I., Prost, J., and Sykes, C. (2004). The effect of diffusion, depolymerization and nucleation promoting factors on actin gel growth. *Eur Biophys J*, 33(4):310–20.

Plastino, J. and Sykes, C. (2005). The actin slingshot. *Curr Opin Cell Biol*, 17(1):62–6.

Pollard, T. (1986). Rate constants for the reactions of ATP- and ADP-actin with the ends of actin filaments. *J Cell Biol*, 103(6):2747–54.

Pollard, T. (2003). The cytoskeleton, cellular motility and the reductionist agenda. *Nature*, 422(6933):741–5.

Pollard, T. and Beltzner, C. (2002). Structure and function of the Arp2/3 complex. *Curr Opin Struct Biol*, 12(6):768–74.

Pollard, T., Blanchoin, L., and Mullins, R. (2000). Molecular mechanisms controlling actin filament dynamics in nonmuscle cells. *Annu Rev Biophys Biomol Struct*, 29:545–76.

Pollard, T. and Borisy, G. (2003). Cellular motility driven by assembly and disassembly of actin filaments. *Cell*, 112(4):453–65.

Pollard, T. D. and Earnshaw, W. C. (2002). *Cell Biology*. Elsevier Science (USA).

Press, W. H., Teukolsky, S. A., Vetterling, W. T., and Flannery, B. P. (2002). *Numerical Recipes in C*. Cambridge UP.

Rafelski, S. and Theriot, J. (2004). Crawling toward a unified model of cell mobility: spatial and temporal regulation of actin dynamics. *Annu Rev Biochem*, 73:209–39.

Rappaport, R. (1967). Cell division: direct measurement of maximum tension exerted by furrow of echinoderm eggs. *Science*, 156(779):1241–3.

Rappaport, R. (1996). *Cytokinesis in animal cells*. Cambridge UP.

Reichl, E., Effler, J., and Robinson, D. (2005). The stress and strain of cytokinesis. *Trends Cell Biol*, 15(4):200–6.

Reimann, P. (2002). Brownian Motors: Noisy transport far from equilibrium. *Phys Rep*, 361:57–265.

Ressad, F., Didry, D., Xia, G., Hong, Y., Chua, N., Pantaloni, D., and Carlier, M. (1998). Kinetic analysis of the interaction of actin-depolymerizing factor (ADF)/cofilin with G- and F-actins. Comparison of plant and human ADFs and effect of phosphorylation. *J Biol Chem*, 273(33):20894–902.

Revenu, C., Athman, R., Robine, S., and Louvard, D. (2004). The co-workers of actin filaments: from cell structures to signals. *Nat Rev Mol Cell Biol*, 5(8):635–46.

Robinson, D. and Spudich, J. (2000). Towards a molecular understanding of cytokinesis. *Trends Cell Biol*, 10(6):228–37.

Robinson, D. and Spudich, J. (2004). Mechanics and regulation of cytokinesis. *Curr Opin Cell Biol*, 16(2):182–8.

Rodionov, V. and Borisy, G. (1997a). Microtubule treadmilling in vivo. *Science*, 275(5297):215–8.

Rodionov, V. and Borisy, G. (1997b). Self-centring activity of cytoplasm. *Nature*, 386(6621):170–3.

Rogers, G., Rogers, S., Schwimmer, T., Ems-McClung, S., Walczak, C., Vale, R., Scholey, J., and Sharp, D. (2004). Two mitotic kinesins cooperate to drive sister chromatid separation during anaphase. *Nature*, 427(6972):364–70.

Romero, S., Le Clainche, C., Didry, D., Egile, C., Pantaloni, D., and Carlier, M. (2004). Formin is a processive motor that requires profilin to accelerate actin assembly and associated ATP hydrolysis. *Cell*, 119(3):419–29.

Rosenblatt, J., Peluso, P., and Mitchison, T. (1995). The bulk of unpolymerized actin in Xenopus egg extracts is ATP-bound. *Mol Biol Cell*, 6(2):227–36.

Roux, A., Cappello, G., Cartaud, J., Prost, J., Goud, B., and Bassereau, P. (2002). A minimal system allowing tubulation with molecular motors pulling on giant liposomes. *Proc Natl Acad Sci U S A*, 99(8):5394–9.

Rzadzinska, A., Schneider, M., Davies, C., Riordan, G., and Kachar, B. (2004). An actin molecular treadmill and myosins maintain stereocilia functional architecture and self-renewal. *J Cell Biol*, 164(6):887–97.

Safer, D. and Nachmias, V. (1994). Beta thymosins as actin binding peptides. *Bioessays*, 16(8):590.

Sanger, J. and Sanger, J. (1980). Banding and polarity of actin filaments in interphase and cleaving cells. *J Cell Biol*, 86(2):568–75.

Sankararaman, S., Menon, G., and Kumar, P. (2004). Self-organized pattern formation in motor-microtubule mixtures. *Phys Rev E Stat Nonlin Soft Matter Phys*, 70(3):031905.

Satterwhite, L. and Pollard, T. (1992). Cytokinesis. *Curr Opin Cell Biol*, 4(1):43–52.

Saunders, W., Lengyel, V., and Hoyt, M. (1997). Mitotic spindle function in Saccharomyces cerevisiae requires a balance between different types of kinesin-related motors. *Mol Biol Cell*, 8(6):1025–33.

Schafer, D., Jennings, P., and Cooper, J. (1996). Dynamics of capping protein and actin assembly in vitro: uncapping barbed ends by polyphosphoinositides. *J Cell Biol*, 135(1):169–79.

Schluter, K., Jockusch, B., and Rothkegel, M. (1997). Profilins as regulators of actin dynamics. *Biochim Biophys Acta*, 1359(2):97–109.

Schroeder, T. (1970). The contractile ring. I. Fine structure of dividing mammalian (HeLa) cells and the effects of cytochalasin B. *Z Zellforsch Mikrosk Anat*, 109(4):431–49.

Schroeder, T. (1972). The Contractile Ring - II. Determining its Brief Existence, Volumetric Changes, and Vital Role in Cleaving Arabica Eggs. *J Cell Biol*, 53:419–434.

Schroeder, T. (1973). Actin in dividing cells: contractile ring filaments bind heavy meromyosin. *Proc Natl Acad Sci U S A*, 70(6):1688–92.

Schroeder, T. (1975). Dynamics of the contractile ring. *Soc Gen Physiol Ser*, 30:305–34.

Schroeder, T. (1990). The contractile ring and furrowing in dividing cells. *Ann N Y Acad Sci*, 582:78–87.

Schwille, P. and Kettling, U. (2001). Analyzing single protein molecules using optical methods. *Curr Opin Biotechnol*, 12(4):382–6.

Sekimoto, K. and Nakazawa, H. (2000). Contraction of a Bundle of Actin Filaments: 50 years after Szent-Gyorgyi. *arXiv:physics*, page 0004044.

Sheterline, P., Clayton, J., and Sparrow, J., editors (1998). *Actin.* Protein Profile. Oxford, 4th edition.

Smilenov, L., Mikhailov, A., Pelham, R., Marcantonio, E., and Gundersen, G. (1999). Focal adhesion motility revealed in stationary fibroblasts. *Science*, 286(5442):1172–4.

Smith, L. (2001). Plant cell division: building walls in the right places. *Nat Rev Mol Cell Biol*, 2(1):33–9.

Sorger, P. (2005). A reductionist's systems biology: opinion. *Curr Opin Cell Biol*, 17(1):9–11.

Stricker, J., Maddox, P., Salmon, E., and Erickson, H. (2002). Rapid assembly dynamics of the Escherichia coli FtsZ-ring demonstrated by fluorescence recovery after photobleaching. *Proc Natl Acad Sci U S A*, 99(5):3171–5.

Sun, H., Yamamoto, M., Mejillano, M., and Yin, H. (1999). Gelsolin, a multifunctional actin regulatory protein. *J Biol Chem*, 274(47):33179–82.

Surrey, T., Nédélec, F., Leibler, S., and Karsenti, E. (2001). Physical properties determining self-organization of motors and microtubules. *Science*, 292(5519):1167–71.

Svitkina, T. and Borisy, G. (1999). Arp2/3 complex and actin depolymerizing factor/cofilin in dendritic organization and treadmilling of actin filament array in lamellipodia. *J Cell Biol*, 145(5):1009–26.

Svitkina, T., Verkhovsky, A., McQuade, K., and Borisy, G. (1997). Analysis of the actin-myosin II system in fish epidermal keratocytes: mechanism of cell body translocation. *J Cell Biol*, 139(2):397–415.

Svoboda, K. and Block, S. (1994). Force and velocity measured for single kinesin molecules. *Cell*, 77(5):773–84.

Takiguchi, K. (1991). Heavy meromyosin induces sliding movements between antiparallel actin filaments. *J Biochem*, 109(4):520–7.

Tanaka, K., Mukae, N., Dewar, H., van Breugel, M., James, E., Prescott, A., Antony, C., and Tanaka, T. (2005). Molecular mechanisms of kinetochore capture by spindle microtubules. *Nature*, 434(7036):987–94.

Tanaka-Takiguchi, Y., Kakei, T., Tanimura, A., Takagi, A., Honda, M., Hotani, H., and Takiguchi, K. (2004). The elongation and contraction of actin bundles are induced by double-headed myosins in a motor concentration-dependent manner. *J Mol Biol*, 341(2):467–76.

Tanase, C. (2004). *Physical Modeling of Micortubule Force Generation and Self-Organization*. PhD thesis, Wageningen Universiteit.

Thoumine, O. and Ott, A. (1997). Time scale dependent viscoelastic and contractile regimes in fibroblasts probed by microplate manipulation. *J Cell Sci*, 110:2109–16.

Thoumine, O., Ott, A., and Louvard, D. (1996). Critical centrifugal forces induce adhesion rupture or structural reorganization in cultured cells. *Cell Motil Cytoskeleton*, 33(4):276–87.

Tian, G., Smith, D., Gluck, S., and Baskin, T. (2004). Higher plant cortical microtubule array analyzed in vitro in the presence of the cell wall. *Cell Motil Cytoskeleton*, 57(1):26–36.

Tournebize, R., Popov, A., Kinoshita, K., Ashford, A., Rybina, S., Pozniakovsky, A., Mayer, T., Walczak, C., Karsenti, E., and Hyman, A. (2000). Control of microtubule dynamics by the antagonistic activities of XMAP215 and XKCM1 in Xenopus egg extracts. *Nat Cell Biol*, 2(1):13–9.

Toyoshima, Y., Kron, S., McNally, E., Niebling, K., Toyoshima, C., and Spudich, J. (1987). Myosin subfragment-1 is sufficient to move actin filaments in vitro. *Nature*, 328(6130):536–9.

Vale, R. (2003). The molecular motor toolbox for intracellular transport. *Cell*, 112(4):467–80.

van Doorn, G., Tanase, C., Mulder, B., and Dogterom, M. (2000). On the stall force for growing microtubules. *Eur Biophys J*, 29(1):2–6.

Veigel, C., Bartoo, M., White, D., Sparrow, J., and Molloy, J. (1998). The stiffness of rabbit skeletal actomyosin cross-bridges determined with an optical tweezers transducer. *Biophys J*, 75(3):1424–38.

Veigel, C., Coluccio, L., Jontes, J., Sparrow, J., Milligan, R., and Molloy, J. (1999). The motor protein myosin-I produces its working stroke in two steps. *Nature*, 398(6727):530–3.

Verkhovsky, A., Svitkina, T., and Borisy, G. (1999). Network contraction model for cell translocation and retrograde flow. *Biochem Soc Symp*, 65:207–22.

Vicker, M. (2002). Eukaryotic cell locomotion depends on the propagation of self-organized reaction-diffusion waves and oscillations of actin filament assembly. *Exp Cell Res*, 275(1):54–66.

Vinson, V., De La Cruz, E., Higgs, H., and Pollard, T. (1998). Interactions of Acanthamoeba profilin with actin and nucleotides bound to actin. *Biochemistry*, 37(31):10871–80.

Vorobjev, I., Malikov, V., and Rodionov, V. (2001). Self-organization of a radial microtubule array by dynein-dependent nucleation of microtubules. *Proc Natl Acad Sci U S A*, 98(18):10160–5.

Vos, J., Dogterom, M., and Emons, A. (2004). Microtubules become more dynamic but not shorter during preprophase band formation: a possible "search-and-capture" mechanism for microtubule translocation. *Cell Motil Cytoskeleton*, 57(4):246–58.

Voter, W. and Erickson, H. (1984). The kinetics of microtubule assembly. Evidence for a two-stage nucleation mechanism. *J Biol Chem*, 259(16):10430–8.

Walker, D., Wang, D., Jin, Y., Rath, U., Wang, Y., Johansen, J., and Johansen, K. (2000). Skeletor, a novel chromosomal protein that redistributes during mitosis provides evidence for the formation of a spindle matrix. *J Cell Biol*, 151(7):1401–12.

Wang, H. and Nogales, E. (2005). Nucleotide-dependent bending flexibility of tubulin regulates microtubule assembly. *Nature*, 435(7044):911–5.

Wasteneys, G. (2002). Microtubule organization in the green kingdom: chaos or self-order? *J Cell Sci*, 115:1345–54.

Watanabe, N., Madaule, P., Reid, T., Ishizaki, T., Watanabe, G., Kakizuka, A., Saito, Y., Nakao, K., Jockusch, B., and Narumiya, S. (1997). p140mDia, a mammalian homolog of Drosophila diaphanous, is a target protein for Rho small GTPase and is a ligand for profilin. *EMBO J*, 16(11):3044–56.

Waterman-Storer, C., Desai, A., Bulinski, J., and Salmon, E. (1998). Fluorescent speckle microscopy, a method to visualize the dynamics of protein assemblies in living cells. *Curr Biol*, 8(22):1227–30.

Weaver, A., Young, M., Lee, W., and Cooper, J. (2003). Integration of signals to the Arp2/3 complex. *Curr Opin Cell Biol*, 15(1):23–30.

Weber, I. (2001). On the mechanism of cleavage furrow ingression in Dictyostelium. *Cell Struct Funct*, 26(6):577–84.

Welch, M., Rosenblatt, J., Skoble, J., Portnoy, D., and Mitchison, T. (1998). Interaction of human Arp2/3 complex and the Listeria monocytogenes ActA protein in actin filament nucleation. *Science*, 281(5373):105–8.

Wolfe, B. and Gould, K. (2005). Split decisions: coordinating cytokinesis in yeast. *Trends Cell Biol*, 15(1):10–8.

Wolpert (1960). The Mechanics and Mechanism of Cleavage. *Int Rev Cytol*, 10:163–216.

Woodrum, D., Rich, S., and Pollard, T. (1975). Evidence for biased bidirectional polymerization of actin filaments using heavy meromyosin prepared by an improved method. *J Cell Biol*, 67(1):231–7.

Wordeman, L. (2005). Microtubule-depolymerizing kinesins. *Curr Opin Cell Biol*, 17(1):82–8.

Wordeman, L. and Mitchison, T. (1995). Identification and partial characterization of mitotic centromere-associated kinesin, a kinesin-related protein that associates with centromeres during mitosis. *J Cell Biol*, 128(1-2):95–104.

Wu, J., Kuhn, J., Kovar, D., and Pollard, T. (2003). Spatial and temporal pathway for assembly and constriction of the contractile ring in fission yeast cytokinesis. *Dev Cell*, 5(5):723–34.

Zhang, D. and Nicklas, R. (1995). The impact of chromosomes and centrosomes on spindle assembly as observed in living cells. *J Cell Biol*, 129(5):1287–300.

Zhang, W. and Robinson, D. (2005). Balance of actively generated contractile and resistive forces controls cytokinesis dynamics. *Proc Natl Acad Sci U S A*, 102(20):7186–91.

Ziebert, F. and Zimmermann, W. (2004). Comment on "Instabilities of isotropic solutions of active polar filaments". *Phys Rev Lett*, 93(15):159801; author reply 159802.

Zigmond, S., Evangelista, M., Boone, C., Yang, C., Dar, A., Sicheri, F., Forkey, J., and Pring, M. (2003). Formin leaky cap allows elongation in the presence of tight capping proteins. *Curr Biol*, 13(20):1820–3.

Zumdieck, A., Cosentino Lagomarsino, M., Tanase, C., Kruse, K., Mulder, B., Dogterom, M., and Julicher, F. (2005a). Continuum description of the cytoskeleton: ring formation in the cell cortex. *Phys Rev Lett*, 95(25):258103.

Zumdieck, A., Kruse, K., and Jülicher, F. (2005b). Quantitative description of ring constriction during cytokinesis: The role of filament polymerization. *in preparation.*

Versicherung

Hiermit versichere ich, daß ich die vorliegende Arbeit ohne unzulässige Hilfe Dritter und ohne Benutzung anderer als der angegebenen Hilfsmittel angefertigt habe; die aus fremden Quellen direkt oder indirekt übernommenen Gedanken sind als solche kenntlich gemacht. Die Arbeit wurde bisher weder im Inland noch im Ausland in gleicher oder ähnlicher Form einer anderen Prüfungsbehörde vorgelegt.

Die vorgelegte Arbeit wurde vom 1.10.2002 bis 25.08.2005 unter wissenschaftlicher Betreung durch Prof. Dr. Frank Jülicher am Max-Planck-Institut für Physik komplexer Systeme in Dresden durchgeführt.

Ich versichere, daß ich bisher keine erfolglosen Promotionsverfahren unternommen habe. Ich erkenne die Promotionsordnung der Fakultät Mathematik und Naturwissenschaften der Technischen Universität Dresden an.

Dresden, den 25.08.2005,

Alexander Zumdieck